Investigating Optoelectronic Properties in Three-Dimensional and Layered Metal Halide Perovskites

Manuel Kober-Czerny

St. Peter's College

A thesis submitted for the degree of

Doctor of Philosophy

at the University of Oxford

Trinity Term 2023

This DPhil felt like a long marathon,

Things got tedious, but I kept moving on.

Making it all the way

So that now I can say:

“Here is my thesis, I am finally done!”

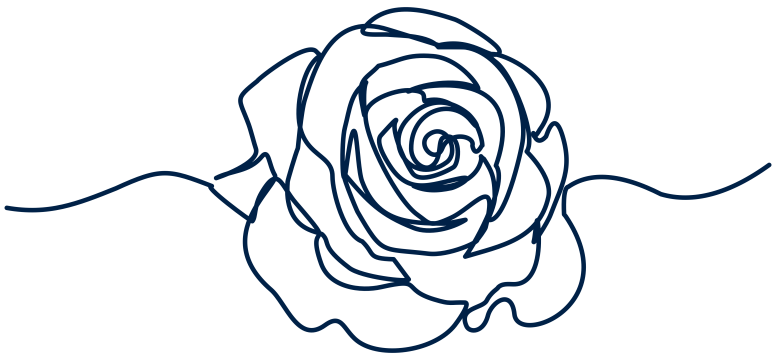

ACKNOWLEDGEMENTS

My first thanks goes out to Professor Henry J. Snaith, who has been my DPhil supervisor throughout my time in Oxford. Many times I left a meeting with him full of enthusiasm about my work and ready to tackle new research questions.
Henry's ever-expanding research group could not function without the unwavering support of Clare Moloney to who I would like to express my greatest admiration and thank her for helping me at all ends throughout my entire DPhil program.

A great thank you goes out to all the members of the Snaith group! To me, living in the UK was difficult and has become more so over the years, but having you as a group made it all worth it! Many people from the group have made an impact on my journey, but before I name some of them I first want to express my gratitude to Jongchul, who was my mentor when I arrived in Oxford. He maintained a regular supervision all these years despite the fact that he started his own research group in Korea in 2020 and I want to thank him for that.
For his everlasting supply of research ideas, enthusiasm and generally being a good person and friend I want to thank Joel, who has helped guide my research many times. Akash and Flo, both of who I value greatly as friends, have challenged me to further my understanding of the time-resolved PL and have been listening to my rants about the struggles and joys of coding for a long time. Both, Heon and Amit have become friends and academic partners of mine with who I can share and discuss many research ideas. The friday mood would have caught me multiple times, if it was not for Harry and Jake with their endless joy and requests for Pubs.

Thank you to my year-mates Jarla, Emil, Ben and Spencer. We had some good times before, during and after the pandemic. Unfortunately, Jarla went to Germany during the first lockdown in 2020 and never returned, even though Emil and I had many chocolate bars prepared to leave on her desk. I hope we will stay friends in the future.
And Bernard, who has helped me greatly during my initial struggles of taking care of the Optics

Lab of the Snaith group, deserves my praise and thanks. Most of what I know about optics, spectroscopy and the fundamentals of perovskites stems from discussions with Bernard and Jongchul. Bernard also offered me the opportunity to work at Helio Display Materials during the first year of the pandemic. Nobuya, Suer, Joe, I want to thank you for the fun times we had in the small, cold lab up in Begbroke to initiate some of Helios materials.

Yes, the pandemic also had an impact on this thesis as it resulted in limited access to the lab and many hours and days at home. While I read most of the relevant perovskite literature during that time, it was not an easy time. I know, I would have been much worse off without my friends Cat, Sarah, Sanja, JB, Piyush and Stephanos. Having you around made the life outside the lab so much fun and I am hoping that our friendship will last beyond the time in Oxford and across all borders!

A special shout-put goes to Maria, who I have known since my time in Switzerland and who has shown me all the secret locations and most importantly good food in London. I am happy that we manage to maintain this friendship (if you want to call it that...). I am happy to have maintained my long-lasting friendship with Eli, Oli, Felix, and more recently Lisa and Jasmine, who have reminded me of life outside of research whenever we met in-person or online. I can't imagine a life without them anymore.

I also cannot imagine a life without Pia anymore, my partner in life and an unlimited source of happiness throughout my DPhil. The day she moved to the UK to start her own research has been one of the happiest moments of my life. Now I enjoy every morning, evening, weekend, etc. with her in our little flat near Cowley road. I want to thank her for being so amazing and keeping up with my weirdness and late working hours. I would have not finished this DPhil without her.

Lastly, I want to thank my family, the Ohana and the and Czernys, for their everlasting support, encouragement and belief. I am sure that they still don not understand what the hell I am actually working on, but they never failed to express their admiration. During the pandemic, we had weekly facetime calls that helped me cope with the situation in the UK. The annual summer vacations with the Ohana have been important for me to recharge for the research that I wanted to embark on. I doubt I could have finished my thesis without knowing that my family was always there for me. There will be a time where we can meet more regularly and are not separated by the channel and I am looking forward to that!

Thank you all for making me happy and encouraging me to keep moving forwards with this degree. This thesis is for you...

ABSTRACT

In this thesis, several different optoelectronic techniques are used to investigate the transient behaviour of photo-generated charge carriers in metal halide perovskites. The overarching objective is to gain a greater understanding of the fundamental properties of both three-dimensional and layered perovskite structures. The first two chapters introduce the field of research of metal halide perovskites for photovoltaic applications and provide the theoretical background necessary to evaluate the results presented in this thesis. All experimental methods used throughout the entire thesis are described in detail in the third chapter so that the results can be replicated.

Chapter four discusses the difficulties of measuring charge carrier mobilities with precision, with an emphasis on the role played by early-time recombination and exciton formation. The lateral, long-range charge carrier mobilities of different perovskite thin films are then reliably determined by performing transient photo-conductivity measurements and simulating a transient free-carrier fraction. The findings highlight the impact of the fabrication route on the long-range optoelectronic properties of the resulting thin films.

The fundamental properties of two-dimensional layered perovskites are investigated in Chapter five. The sum of the electron and hole mobilities for PEA_2PbI_4 and related two-dimensional perovskites are estimated using the approach described in the prior chapter. For PEA_2PbI_4, a remarkable long-range mobility of 8.0 ± 0.6 $cm^2\,V^{-1}\,s^{-1}$ is found. This tenfold improvement in mobility over a typical 3D perovskite demonstrates the potential single-crystal-like charge trans-

port properties of 2D polycrystalline thin films.

In the final chapter, an exciting, novel approach for analysing time-resolved photo-luminescence data is presented, by making use of Bayesian inference and a Markov-Chain Monte-Carlo algorithm. Using a $FAPbI_3$ thin film as a case study, a number of parameters, including diffusion, and recombination constants can be accurately inferred. The findings provide new perspectives on the physics underlying observed optoelectronic properties. For some of the systems illustrated in this chapter, for instance, the distinction between surface and bulk appears to be less clear than previously assumed. Validation of the method is provided by comparisons to other experimental data, such as intensity-dependent PLQE and transient photo-conductivity.

Overall, this thesis contributes powerful analytical tools that can be applied to future studies of a wide range of metal halide perovskites.

CONTENTS

CHAPTER 1

INTRODUCTION

Throughout this introduction, quotes of highly cited researchers of the field of metal halide perovskites are presented. They were chosen to encourage a critical view of the results presented in this thesis and the metal halide perovskite research literature in general. In no means do they represent the personal opinion of the author of this thesis.

1.1 PEROVSKITE RESEARCH OVER THE YEARS

Metal halide perovskites (MHP) have been termed "the rising star of photovoltaic" research and have achieved some outstanding performances in photovoltaic and other optoelectronic applications. The unique combination of material properties, easy processability and promising device performances have sparked interest across the research areas of materials science, physics, chemistry, engineering and many other.[1] After the material discovery and initial characterization by H.L. Wells, C.K. Møller and D. Weber, metal halide perovskites (MHP) were not investigated much, until D. Mitzi reported on their unique optoelectronic properties around the early 2000s.[2–7] Despite early findings on the optoelectronic properties of this material class, it took until 2009 to demonstrate their use in a photovoltaic application with an initial power conversion efficiency (PCE) of 3.8%.[8] Already two years later, the group of N.G. Parks build a photovoltaic device based on perovskite quantum dots with a PCE of 6.5%.[9] It took only one year, to achieve the first important milestone for every novel photovoltaic technology: a PCE of $> 10\%$, mainly due to a surprisingly high open-circuit voltage of > 1.1 V.[10] Due to this unprecedented rate of performance improvement, thousands of new publications have been added to the field annually in recent years.[1] An important factor for this vast expansion of the research field may have been the relatively simple, solution-based fabrication of MHPs that made the material easily accessible across the world.[11].

> *"Getting high performance isn't easy, but it's very easy to get started, enabling research groups to jump in and get moving quickly."*[11]

The early MHP research concerned itself mainly with the question:

How could this material work so well in photovoltaic applications?

First fundamental studies were directed towards understanding the optoelectronic properties of this material class and revealed high absorption coefficients and photo-luminescence, low exciton binding energies and long charge carrier diffusion, all of which are highly beneficial for photovoltaic applications.[12–18] It was realized that the MHP material could not only absorb sunlight,

but also efficiently transport charges, making previous device architectures based on scaffolding obsolete.[19,20] The ability to alter perovskite composition and processing to tune bandgap, absorption properties, and resulting devices was also recognised as a benefit of the MHP material class.[21–23] The field started to become more diverse, with fundamental questions emerging alongside the surge of photovoltaic device performance.

> *"Solution processing is the essence of chemistry, while properties of perovskite semiconductors are the playground of physics."*[24]

For instance, the origin of the energetic band structure from the atomic orbitals of the metal and halide ions was an early area of research.[23,25] Further research revealed that many imperfections (defects) could form within the perovskite structure without impacting the overall PV device performance. Hence, the material was termed "defect-tolerant".[26,27] However, a significant number of defects would remain in the material and still limit the device performance by inducing non-radiative losses.[28] In addition, hysteresis was observed in MHP photovoltaic devices, where the measurement of a solar cell device was dependent on how it was measured.[29–31] It was postulated to be related to the presence of mobile, ionic species and surface defects, which would result in a screening of the electric field and performance losses.[30] This realization started a still ongoing exploration into the use of different solvent routes, molecular additives and fabrications methods to obtain a MHP material with reduced intrinsic defect density and high material quality.[32–38] Alongside these material improvements, fundamental research was targeted toward understanding their impact on the long-range transport properties and optoelectronic performance.[17,39,205?] While it is widely agree upon that the transport of charge carriers is initially governed by their interaction with crystal lattice vibrations, it is much more debated what happens at grain boundaries and extended crystalline defects in polycrystalline thin films.[40–42]

> *"[Engineers] have their place, but without basic science, they will be lost."*[43]

Then, the field of MHP-based photovoltaic research slowly shifted towards investigating and understanding the parameters that influence long-term stability of the material.[44,45] To this day it is one of the most pressing challenges facing the research field. The early improvements in the bulk material have resulted in improved performance, but also improved material stability.[46]

Unfortunately, this does not necessarily translate to an improved long-term stability of photovoltaic devices, as interfaces with adjacent layers play a crucial role as well.[47] The understanding of the impact of inhomogeneities and microstructure on material and device stability has become a hot topic in recent years.[48–50] Also, the mobile ions are under more active investigation again, specifically their impact on photovoltaic performance losses and long-term stability.[51–53]

> *"[U]sually when we come up with a way we think we are going to make the solar cell better, it does not work."*[54]

MHP-based solar cells are now getting close to their detailed balance limit and have shown > 30% PCEs in perovskite-silicon tandem applications.[55] Despite this diverse and ever-expanding research and the outstanding achievements, there still remain many open questions. For instance, the impact of reabsorption on the final material performance is not understood and often simply ignored.[56] Likewise, there is still an ongoing debate about the nature and impact of defects, especially shallow defects in this material class.[57] Finally, the initial question as to why these materials yield such promising performance in the first place is still not fully answered. A lot has been discovered, but there is a lot more to come.

1.2 STRUCTURE OF THIS THESIS

This thesis is organized into 5 main chapters.

Chapter 2 introduces the theoretical background needed to understand and challenge the results shown in this thesis.

Chapter 3 details all experimental methods used throughout this thesis that led to the results shown in the following chapters.

Chapter 4 introduces a developed methodology to accurately determine the lateral, long-range charge carrier mobility in MHPs. In this chapter, transient photo-conductivity was combined with a post-measurement analysis to reveal the strong dependence of different fabrication routes on the long-range charge carrier transport. This will allow to address open questions surrounding the nature of long-range charge transport and its limitations in these materials.

Chapter 5 applies the methodology to assess long-range charge carrier mobility of two-dimensional, layered perovskites. Fundamentally, this material class is much less investigated than the three-dimensional counterpart. In this chapter the behaviour of free charge carriers and their impact on the optoelectronic properties is investigated. It is understood that control over orientation and morphology of two-dimensional thin films is crucial for predictable material performance.

Chapter 6 demonstrates a different approach to understand the transient photo-luminescence behaviour in MHPS. There, Bayesian inference is coupled with a Markov-Chain Monte-Carlo algorithm and a physical model from already existing theory to be able to study interplay of parameters that result in the observed photo-luminescence response. $FAPbI_3$ is studied as a model system to illustrate the power of the method and validate the accuracy of inferred parameters.

This thesis presents results, which further the research discussion surrounding long-range charge carrier transport properties as well as the fundamental physics of two-dimensional MHPs. The most important outcome however is the development of novel and improved analysis methodologies, which empower others to further their own research into the fundamental properties of this fascinating material class.

CHAPTER

2 THEORETICAL BACKGROUND

In this chapter, the theoretical foundation required for the subsequent results is presented. The chapter begins with a brief background on solar radiation. Then, metal halide perovskites, a semiconductor material with an unusual set of characteristics, are introduced. This will be completed by a summary of properties that are special to two-dimensional, layered perovskites. In the end of the chapter, all optoelectronic concepts used throughout this thesis are detailed.

2.1 THE SOLAR SPECTRUM

Black Body Radiation

In order to understand why semiconductors can be used as solar cell absorber materials, one has to understand the solar spectrum which can be approximated as a black body. Any object can be described as a black body if it absorbs all the incident radiation - so the absorptance $A(h\nu) = 1$. $h\nu$ is the energy of the photons, with h being the Planck constant and ν the frequency of the photon.[58] The absorption is in thermal equilibrium with emission, called "black body (thermal) radiation", which only depends on the temperature T of the emitter. When considering photons as a gas of non-interacting particles (bosons), the distribution of the number of photons at a given energy state will follow Bose-Einstein statistics::

$$f_\gamma(h\nu, T) = \frac{1}{\exp \frac{(h\nu)}{k_B T} - 1} \tag{2.1}$$

which only depend on the energy of the photon ($h\nu$) and the temperature of the system (T), with k_B being the Boltzmann constant.[58] Generally, the energy distribution is a function of the temperature and the chemical potential of the gas. However, as the number of photons is not conserved in a black body, this chemical potential is zero, so the spectrum becomes a function of temperature alone. The resulting occupation of energy levels can be seen schematically in **Figure 2.1(a)**.

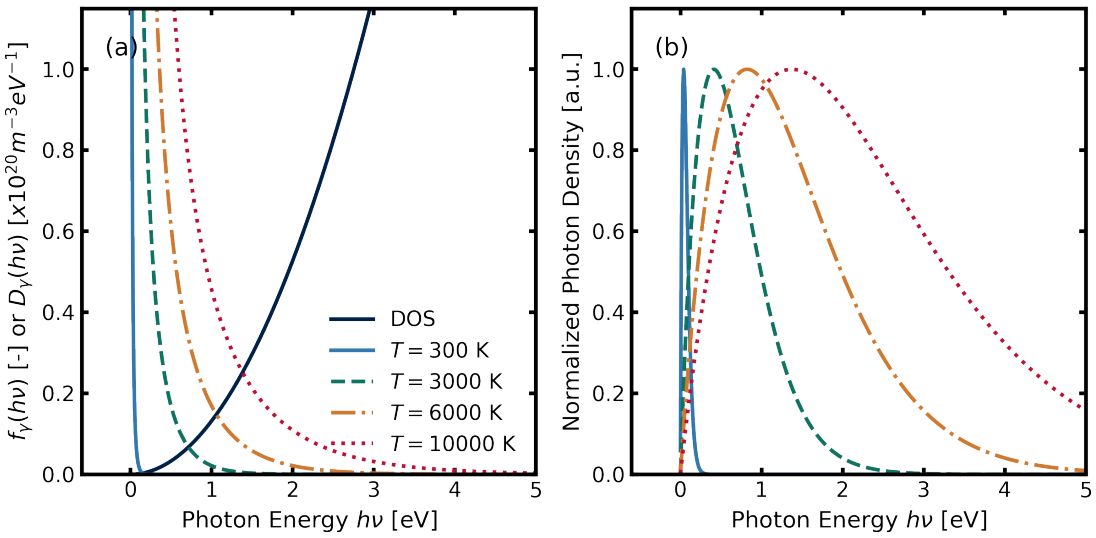

Figure 2.1: (a) The calculated density of states (DOS) as well as the photon occupation $f_\gamma(h\nu, T)$ for different temperatures ($T = 300$ K, 3000 K, 6000 K and 10000 K) are shown (b) The resulting calculated, normalized photon density is shown for each temperature. The spectrum for $T = 6000$ K is closest to the spectrum of the sun.

The density of possible states at a given energy level can be estimated from the volume of a single state in momentum space, as well as the spin-direction of the photon (up or down). The density of states is lower for lower energy levels, because the entropy is reduced. This is described in

$$D_\gamma(h\nu) = 8\pi \cdot \frac{(h\nu)^2}{h^3 \cdot c^3} \tag{2.2}$$

with c being the speed of light inside the material ($c = \frac{c_0}{n_\mathrm{r}}$, with c_0: speed of light in vaccum, and n_r: refractive index of the material). $D_\gamma(h\nu)$ is shown schematically in **Figure 2.1(a)**. Now the emitted photon density at each energy level can be calculated by multiplying the occupation statistics and the density of states.

$$\frac{dn_{\gamma,\mathrm{BB}}(h\nu, T)}{dh\nu} = \frac{1}{4\pi} \cdot D_\gamma(h\nu) \cdot f_\gamma(h\nu, T) = \frac{2 \cdot (h\nu)^2}{h^3 \cdot c^3} \cdot \frac{1}{\exp\frac{(h\nu)}{k_\mathrm{B}T} - 1}, \tag{2.3}$$

where the factor $\frac{1}{4\pi}$ is needed to describe isotropic emission of radiation.[59] For systems other than vacuum ($n_\mathrm{r} \neq 1$), the internal and external radiation of a black body are different, due to total internal reflections at the boundaries of the material. Thus, when a black body with larger n_r is interfaced with a material with lower n_r (for example air), a significant part of the radiation is reflected back into the black body as the density of states is higher there.[58] The internal photon density spectra in energy for different temperatures T are shown in **Figure 2.1(b)**. Photon

density can be turned into power density per unit energy ($\frac{\rho(h\nu,T)}{dh\nu}$) by multiplying $\frac{dn_{\gamma,\mathrm{BB}}(h\nu,T)}{dh\nu}$ with c. It is often referred to as irradiance.

In a first approximation, the sun can be described as a black body with a temperature $T = 6000$ K.[58] Not all the photons generated by the sun can reach earth to be used in photovoltaic applications. Therefore, the irradiance emitted by the sun needs to be further corrected before it can be used to predict and compare photovoltaic performances.

The AM1.5 Spectrum

As light travels from the sun to earth it first has to traverse empty space, where it continuously spreads. This leads to a reduction in irradiance which can be approximated via

$$\frac{\rho_{\mathrm{earth}}(h\nu, 6000K)}{dh\nu} = \pi \cdot \frac{R_{\mathrm{sun}}^2}{d_{\mathrm{sun-earth}}^2} \cdot \frac{\rho_{\mathrm{sun}}(h\nu, 6000K)}{dh\nu} \tag{2.4}$$

where R_{sun} is the radius of the sun and $d_{\mathrm{sun-earth}}$ is the distance between sun and earth.[60] The irradiance spectrum can then be plotted in energy or wavelength. It is important to keep the Jacobian transformation ($dh\nu = -\frac{hc}{\lambda^2}\, d\lambda$) in mind, when switching between the two, so that integration over a range of energies or wavelengths allows for the accurate determination of total power density.[61]

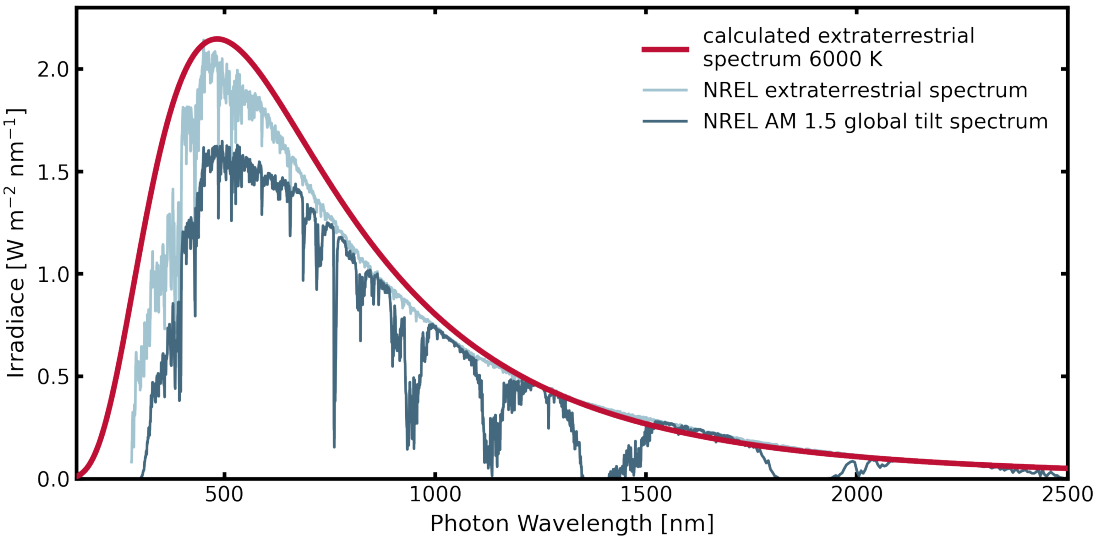

Figure 2.2: The NREL reference spectra for one sun outside the atmosphere (sun spectrum) and after travelling trough 1.5 air mass (AM1.5 Spectrum) are shown together with the wavelength spectrum calculated for a black body at $T = 6000$ K.[62]

The resulting calculated irradiance spectrum in wavelength for a black body at 6000 K is shown in **Figure 2.2** and compared to the measured extraterrestrial spectrum.[62] It can be observed that the measured spectrum has several lines of lower intensity when compared to the calculated one. These are known as "Fraunhofer lines" and correspond to absorption lines of atomic species within the outer layer of the sun, for example sodium and potassium.[63,64]

As the light travels through the atmosphere its intensity is reduced due to scattering and absorption events. Small molecules, particles and aerosols in the atmosphere can scatter and absorb photons and further reduce the irradiance reaching the surface of the earth.[65] It becomes apparent from **Figure 2.2** that the largest fraction of power density of the solar spectrum is located within the visible range (approx. 400 to 700 nm). Materials, which are able to absorb this part of the solar spectrum can hence be useful for photovoltaic energy generation. As they do not absorb all light anymore, they are called grey bodies.

Grey Bodies

Even though a large number of objects and materials can be approximated as black bodies, the materials needed for photovoltaic applications would be considered grey bodies, as they only absorb a part of the total incident radiation. Their absorptance is defined as

$$A(h\nu) = 1 - t(h\nu) - r(h\nu) \tag{2.5}$$

where $t(h\nu)$ is the transmittance and $r(h\nu)$ the reflectance. According to Kirchhoff's Law, the irradiance emitted by a grey body simply becomes[58,64]

$$\frac{\rho_{\mathrm{GB}}(h\nu, T)}{dh\nu} = A(h\nu, T) \cdot \frac{\rho_{\mathrm{BB}}(h\nu, T)}{dh\nu} \tag{2.6}$$

This relationship is also known as *reciprocity relation*. It describes the radiation emitted by a grey body as the result of an absorption process and the black body radiation at the temperature of the grey body.[58]

The Basics of a Solar Cell

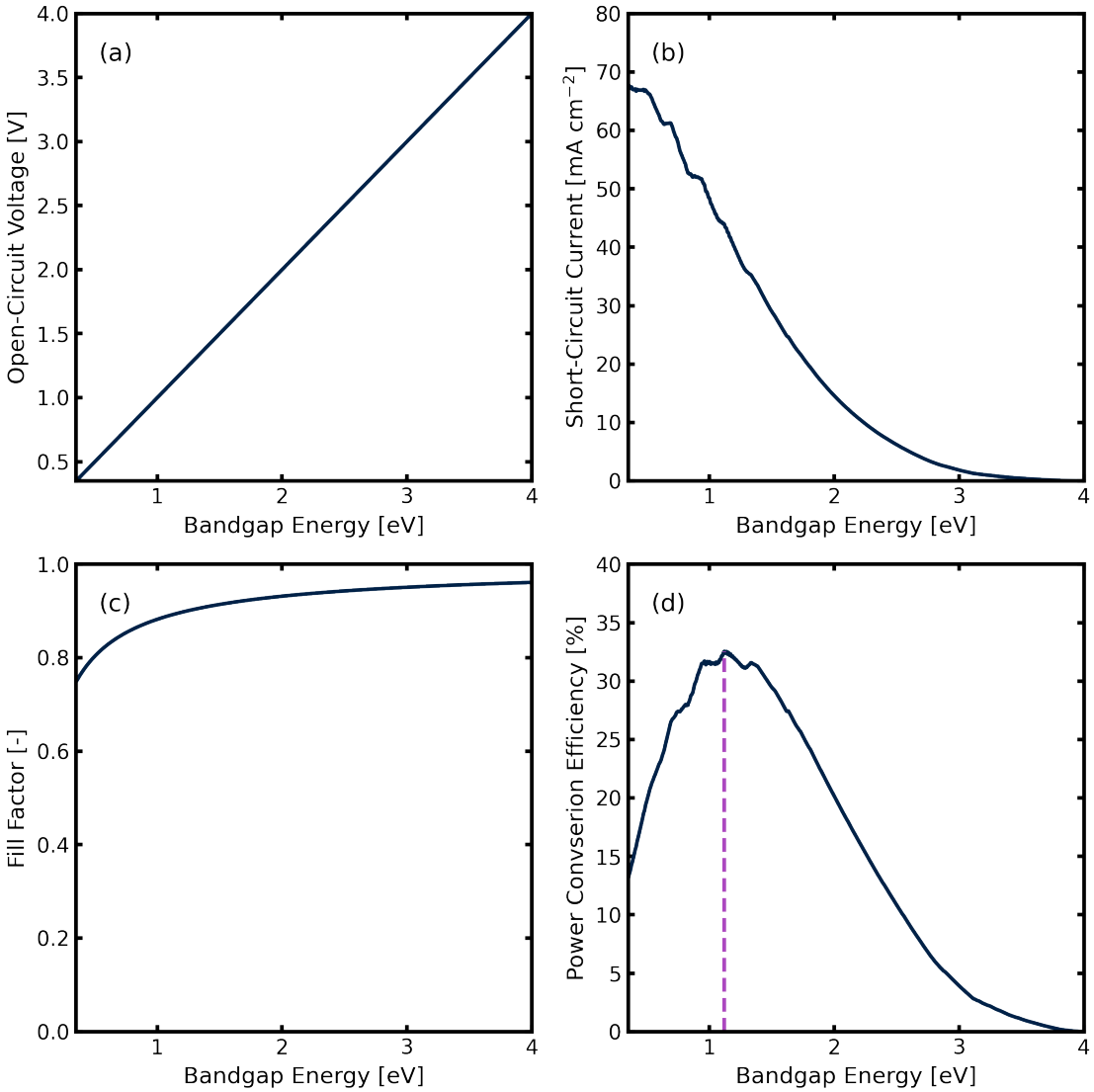

Figure 2.3: The theoretical maximum values are shown for (a) the open-circuit voltage (V_{oc}), (b) the short-circuit current density (J_{sc}), and (c) the fill-factor (FF). According to the detailed-balance limit they yield a (d) maximum power conversion efficiency (η) that changes as a function of the bandgap of the semiconductor material.

The most important class of materials for photovoltaic applications are semiconductors. A solar cell can be constructed by a semiconductor material that is sandwiched in between charge-selective contacts. The semiconductor needs to be designed to allow for the absorption of the visible part of the irradiance spectrum. The power generated by a solar cell is defined by the current (J) and voltage (V), which depend on the properties of the absorber material and full device stack. As will be introduced later, a bulk semiconductor, such as metal halide perovskites, can absorb any photon with an energy larger than its energetic bandgap. Semiconductors with small bandgaps

will thereby absorb more photons, resulting in increased currents, but also sustain lower voltages. In a first approximation the maximum voltage generated by a solar cell (open-circuit voltage or V_{oc}) is equal to the bandgap E_{g} of the absorbing semiconductor (see **Figure 2.3(a)**).

Similarly, the maximum current density (short-circuit current density or J_{sc}) is related to the absorbed photon flux and is shown in **Figure 2.3(b)**. The ideal power output is then the product of V_{oc} and J_{sc}. In reality this power can never be reached due to transport losses within the semiconductor material and the fact that the solar cell is typically at 300 K, while the absorbed photons will stem from a black body at 6000 K. The ratio between the ideal power output and the maximum power output is known as fill-factor (FF, **Figure 2.3(c)**) or impedance-matching factor. It can be estimated from an empirical equation.[60,66] The resulting maximum power conversion efficiency (η_{max}) known as "detailed balance limit" is given by

$$\eta_{\mathrm{max}}(E_{\mathrm{g}}) = \frac{V_{\mathrm{oc}}(E_{\mathrm{g}}) \cdot J_{\mathrm{sc}}(E_{\mathrm{g}}) \cdot FF(E_{\mathrm{g}})}{\rho_{\mathrm{AM1.5}}}, \tag{2.7}$$

where $\rho_{\mathrm{AM1.5}}$ is the power density obtained by integration of the AM1.5 irradiance spectrum (from **Figure 2.2**) over all energies (or wavelengths). The resulting $\eta_{\mathrm{max}}(E_{\mathrm{g}})$ is shown in **Figure 2.3(d)**. It can be seen that a maximum η of approx. 33% can be achieved with an energetic bandgap of 1.13 eV. Until now, a few materials like silicon (1.1 eV, $\eta_{\mathrm{record}} = 26.1\%$), gallium arsenide (1.42 eV, $\eta_{\mathrm{record}} = 29.1\%$), CIGS (1.12 eV, $\eta_{\mathrm{record}} = 23.6\%$) and cadmium telluride (1.42 eV, $\eta_{\mathrm{record}} = 22.3\%$) have been successful candidates for photovoltaic applications, because their energetic bandgaps are close to this ideal value.[67,68] In addition, metal halide perovskites can also have bandgaps below 1.6 eV and have hence joined this list. In the following their most important properties will be introduced.

2.2 METAL HALIDE PEROVSKITES

The Perovskite Crystal Structure

Metal halide perovskites are organic-inorganic materials with AMX_3 stoichiometry, where A^+ is a monovalent cation, typically methylammonium (MA^+), formamidinium (FA^+) or cesium (Cs^+), (M^{2+}) is a bivalent metal cation, like lead (Pb^{2+}) or tin (Sn^{2+}), and (X^-) is a monovalent anion, most commonly a halide (iodide (I^-), bromide (Br^-) or chloride (Cl^-)).[8,69]

The idealised perovskite crystal structure is cubic (α-phase; $Pm\bar{3}m$), which is the highest-temperature phase in all metal halide perovskite compositions (see **Figure 2.4(a)**).[70,71] The metal and halides form a network of corner-sharing $MX_6{}^{4-}$ octahedra and the A-site cation occupies the octahedral voids. The octahedra can collectively rotate about the c-axis into the tetragonal (β-phase; $I4/mcm$ or $P4/mbm$) crystal structure, where they are now more closely packed along the ab-plane. Additionally the octahedra can slightly tilt out of the ab-plane and distort into an orthorhombic ($Pnma$, γ-phase) phase.[70] Depending on the arrangement, the optoelectronic properties change considerably. Metal halide perovskites have a unique combination of structural and optoelectronic properties, which are summarized in the following sections.

Electronic Band Structure of Perovskites

The optoelectronic properties of this structure are determined mainly by the metal-halide bonding, which has a mixed ionic-covalent character. The electronic configurations for Pb^{2+} and I^- in $APbI_3$ perovskites are $5d^{10}6s^26p^0$ and $5s^25p^6$, respectively. The valence band (VB) consists of the filled, s-p anti-bonding orbital formed by the Pb $6s$ and I $5p$ orbitals, while the conduction band (CB) consists of a mixture of anti-bonding p-s and p-p orbitals formed by the Pb $6p$ orbitals with the I $5s$ and $5p$, respectively.[25,72] It is worth mentioning the band structure near the band edge is strongly influenced by spin-orbit coupling effects, such as the Rashba- or Dresselhaus effect.[25,73,74] These effects occur more strongly in the presence of heavy atoms, like Pb^{2+} or Sn^{2+}, hence their influence on the band structure cannot be neglected for perovskites. As is shown schematically in **Figure 2.4(b)**, the parabolic valence band maximum has strong iodide character (approx.

75%), while the conduction band minimum has a mixed lead-iodide character. The latter will therefore be more impacted by spin-orbit coupling effects. It can be seen as well that metal halide perovskites are direct bandgap semiconductors, as the valence band maximum and conduction band minimum appear at the same point (R) in momentum-space.

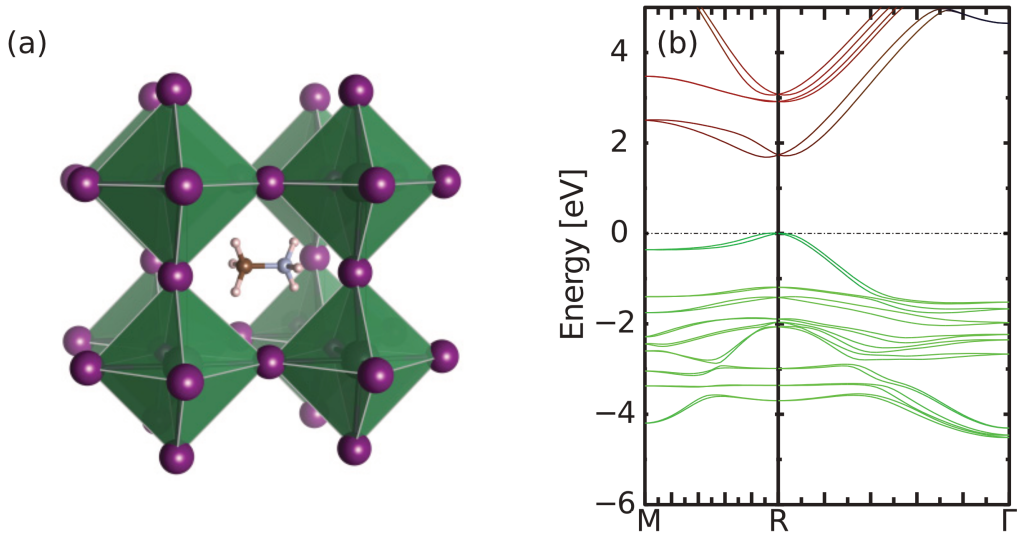

Figure 2.4: (a) Schematic of the cubic crystal structure of $MAPbI_3$. The purple spheres indicate iodide (halide), the center of the green octahedra is the lead (metal) and in the octahedral void, a methylammonium cation is shown. (b) Band structure for $MAPbI_3$ as calculated from quasi-particle self-consistent GW theory, where green represents orbitals with iodide- and red orbitals with lead-character. (a) and (b) were reproduced with permission from Ref.25

Next to the $MX_6{}^{4-}$ octahedral network, the A-site cation has mainly a structurally stabilizing function, by forcing corner-sharing octahedra instead of face-sharing (A-site too large) or edge-sharing (A-site too small) arrangements. It can indirectly influence the band structure as well, by changing the overlap of the atomic orbitals of Pb^{2+} and I^-, where a larger overlap results in a smaller bandgap.[23,75,76] For example, in the idealized cubic structure, the Pb^{2+} ions are linearly aligned, optimizing the overlap of the Pb^{2+} and I^- orbitals. This generates a bandgap of 1.45-1.55 eV in the case of $APbI_3$ perovskites, which is ideal for single-junction solar cell absorber materials.[36,77]

In addition to the chemical bonding, there are electrostatic interactions collectively shared over the entire structure as well as many-body effects between charge carriers moving through the material.[23,78] The highly ionic character of the perovskite structure affects properties such as the dielectric permittivity, exciton binding energy and low ionization potential.[23,79]

Excitons in Perovskites

Photons with energies larger than the electronic bandgap will be absorbed by the perovskite material and form a photo-excited electron-hole-pair, known as exciton.[80] A fast exciton dissociation into free charge carriers can be beneficial for photovoltaic applications. The energy needed to separate the exciton is known as exciton binding energy E_B and is a property of the underlying material. Metal halide perovskites show desirably low exciton binding energies of $E_B \leq k_B T$ ($\leq$ 26 meV at r.t.), hence they mainly generate free charge carriers upon photo-excitation. This is due to the aforementioned high dielectric constant, strong coupling of electrons to optical (LO) phonons and large polarizability. Both absorption and photo-luminescence are thought to be governed by free charge carriers, hence metal halide perovskites generally have small Stokes' shifts, which in turn can enable efficient photon recycling.[81]

There have been many attempts to measure E_B accurately, but even for $MAPbI_3$, the most studied perovskite composition, values range from 2 meV to 62 meV, depending on the method used.[82] For this thesis, the exciton binding energy was determined from absorption spectra using Elliott's method.[83]

Intrinsic Semiconductors

At this point it is important to mention that lead-based metal halide perovskites are often classified as intrinsic semiconductors. As such, the number of electrons and holes inside the material are equal in equilibrium. This will become important when time-resolved behaviour is simulated later.

Charge Carriers Effective Masses

The effective mass is the mass of a charge carrier (electron or hole) within a solid. It can be much smaller than the mass of a free electron. In metal halide perovskites, the strong hybridization of the lead orbitals result in low effective masses.[23,25] Some values for typical perovskite compositions are summarized in **Table 2.1**. The relatively low effective masses are thought to result in high charge carrier mobilities and hence long diffusion lengths.[13]

Table 2.1: Effective masses of typical perovskite compositions, where m_e is the mass of a free electron of approx. 9.11×10^{-31} kg.

Composition	**Effective Mass (x m_e)** electrons	holes	Source	Study
$MAPbI_3$	0.150	0.120	25	theoretical
	0.104		84	experimental
$FAPbI_3$	0.090		84	experimental
PEA_2PbI_4	0.091		85	experimental
BA_2PbI_4	0.150		86	experimental

Defect Tolerance of the Perovskite Material

A real material is not perfect. Even the most carefully grown single crystal has phase impurities and defects, because perfect crystals are unstable at finite temperatures due to the entropic stabilization of imperfect crystals.[87–89] These imperfections in the structure as well as stoichiometric impurities are often summarized under the term *point defects*. Common point defects are (1) vacancies, where an ion is missing from the crystal lattice, (2) interstitials, where an ion is inserted into a crystal lattice or (3) substitutions, where an ion is occupying a wrong lattice site. In metal halide perovskites, extended defects, like dislocations or stacking faults may also appear, especially at or near grain boundaries.[48] Some defects can generate energetic states within the bandgap of a material. These can act as recombination centres (see **Section 2.6** for more details), effectively narrowing the bandgap at that specific location. In the semiconductor literature, these types of defects are therefore often called 'trap-states' as well.

Early work on band structure calculations of different possible point defects in metal halide perovskites has concluded, that most of them are less detrimental for the optoelectronic properties

than in other semiconductor materials. Metal halide perovskites have hence been termed a "defect-tolerant" material class.[27,90–93]

Thus, even though the trap density in $MAPbI_3$ has been estimated in the range of 10^{16} to 10^{17} cm^{-3} for thin-films (and 10^9 to 10^{10} cm^{-3} for single crystals), this material exhibits good properties for optoelectronic devices.[94–96] It shall be noted that trap densities may be much larger near grain boundaries or at interfaces, which will be important when assessing longer-range effects, such as charge transport or recombination at later times.[97]

Mobile Ions

Another unique property of perovskites is their soft crystal lattice leading to increased ionic conductivity. The ions can screen the electric field within the semiconductor, which leads to performance losses and has been linked to hysteresis, due to their slow motion.[30,52,53,98,99] The ions migrating in an electric field may lead to degradation of the photovoltaic devices as they react with adjacent layers.[100,101] It has been estimated that the density of mobile ions is on the order of 10^{17} to 10^{19} cm^{-3} and their diffusion rather slow due to the size of the ions.[51,102]

Halide migration, in particular iodide migration, has been understood as one of the main pathways for the degradation of the perovskite material as its reduction can result in iodine formation, which can subsequently sublime from the perovskite material or induce interface reactions.[103–106]

It is worth noting that iodide has been found to be the most mobile ion through iodide-vacancy-mediated diffusion.[107] Halide interstitials can also result in mid-gap trap states, limiting the bulk properties of the perovskite material. As such, the research field is in agreement that reduced defects within the perovskite material will result in improved long-term stability as well.[46]

In fact it may be that the "defect tolerant" nature of the perovskite material resulting in good optoelectronic properties may not apply to the effects of the same defects on long-term stability

Not only do ions affect the performance and stability of perovskite-based optoelectronic devices, they can also result in segregated phases in mixed-composition metal halide perovskites. Both A-site and X-site segregation has been observed.[108–113] The movement of the anions is typically through to lead to performance losses of the optoelectronic devices, but it has been shown that it does not affect charge carrier transport properties significantly and that it can even result in a "healing" of defects within the perovskite material.[114,115]

For the work presented in this thesis it is important to keep the effects of mobile ions in mind for two reasons: 1) perovskite compositions with high Br-contents can phase segregate under illumination and hence are not useful for the fundamental work presented here. Thus, mostly I-based perovskites were used throughout the thesis. 2) During steady-state illumination in an electric field, mobile ions can readily move and screen the electric field. Especially in **Chapter 4** it was important to use a pulsed excitation and low electric fields to reduce the impact of this effect on the measurements.

2.3 TWO-DIMENSIONAL, LAYERED PEROVSKITES

Nomenclature

Beyond the three-dimensional perovskites, two-dimensional Ruddlesden-Popper (RP) and Dion-Jacobson (DJ) structures are considered to be possible alternatives to increase the stability of the perovskite layer and allow for the band-gap and optical properties to be adjusted by varying the quantum well width and confinement.[116–121] The RP-phase has a stoichiometry of $A'_2A_{n-1}M_nX_{3n+1}$, where A‘ is now a larger organic ion (most commonly butylammonium (BA^+) or phenylethylammonium (PEA^+)).[122] The organic cation induces the formation of a layered, quantum-well structure by separating n-stacks of MX_6^{4-} octahedra that are often oriented parallel to an underlying substrate.[123] The quantum confinement directly affects the electronic band structure and hence optoelectronic properties.[124] In **Figure 2.5** the crystal structures of two-dimensional perovskites of the $BA_2MA_{1-n}Pb_nI_{3n+1}$ stoichiometry for n = 1 to n = 4 are shown schematically.[125]

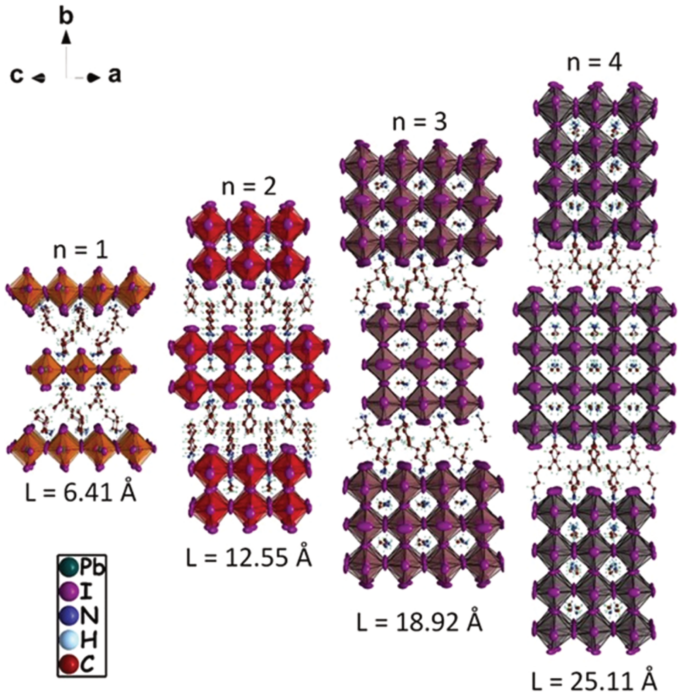

Figure 2.5: The crystal structure of $BA_2MA_{1-n}Pb_nI_{3n+1}$ ruddlesden-popper structures is shown for n = 1 to n = 4. The figure is adapted from Ref. 125.

It is noteworthy that thin films made from stoichiometries with n > 1 yield mixed phases of several n-values in most cases.[126] Improving control over the phase purity is part of ongoing research.[127,128] For this reason, only the phase-pure n = 1 compositions were studied in **Chapter 5**. In the following, the most important properties of two-dimensional, layered metal halide perovskites are summarized.

Effect of Quantum Confinement and Exciton Formation in Lower-Dimensional Materials

The reduced dimensionality in the crystal structure of two-dimensional perovskites results in a quantum confinement in the direction parallel to the inorganic layers. Dielectric confinement is the increase in electrostatic force between charge carriers in a material with a high dielectric constant that is layered between a material with a lower dielectric constant.[129,130] The electric field is only screened within the high dielectric material, but less so in the low-dielectric material. This effectively enhances the interaction between electrons and holes and hence the exciton binding energy of the material.[130] In addition, the electronic bandgap is increased as both the conduction and valence band get shifted.[129]

In two-dimensional perovskites, the MX_6^{4-} octahedra form the high-dielectric, while the large organic spacer cations form the low-dielectric. Hence, the excitons are primarily located in the inorganic layers. Two-dimensional RP perovskites with n < 5 have reported exciton binding energies on the order of or greater than 100 meV. They are considered to be *excitonic materials* and generate a significant fraction of excitons following photo-excitation.[131] Hence, excitons dominate the optoelectronic properties of confined materials (see **Section 2.6**). The exciton is further stabilized by the structure of the inorganic layer. As described in **Section 2.2**, the bandgap of perovskites is formed by the Pb-X bonding, thus the exciton stability is greatly influenced by the Pb-X-Pb angle: the closer the angle to 180°, the smaller the exciton binding energy with the lowest one reported recently being E_B = 48 meV for an n = 1 RP perovskite.[132]

Recently, it was demonstrated that excitons in the two-dimensional perovskite PEA_2PbI_4 can be highly mobile with diffusion coefficients reaching up to 2 $cm^2\,s^{-1}$ (μ_x of up to 80 $cm^2\,V^{-1}\,s^{-1}$) at room temperature with an effective exciton mass of 0.44 x m_e.[133,134] Little was understood about

the long-range transport of free charge carriers in this material class, but this will be discussed in more detail in **Chapter 5**.

Dynamic Exciton-to-Free-Carrier Fraction

The rate of exciton dissociation into free carriers is balanced by the rate of exciton formation from free charge carriers. An equilibrium can be calculated between the two for each charge carrier density (n) using the Saha equation[135]

$$\frac{\phi^2}{1-\phi} = \frac{1}{n} \cdot \left(\frac{2\pi \cdot m_i^* \cdot k_\mathrm{B} T}{h^2} \right)^{3/2} \cdot e^{-\frac{E_\mathrm{B}}{k_\mathrm{B} T}}, \tag{2.8}$$

where ϕ is the free-carrier fraction. In **Figure 2.6(a)** and **(b)** ϕ is shown for different exciton binding energies as a function of n and T, respectively.

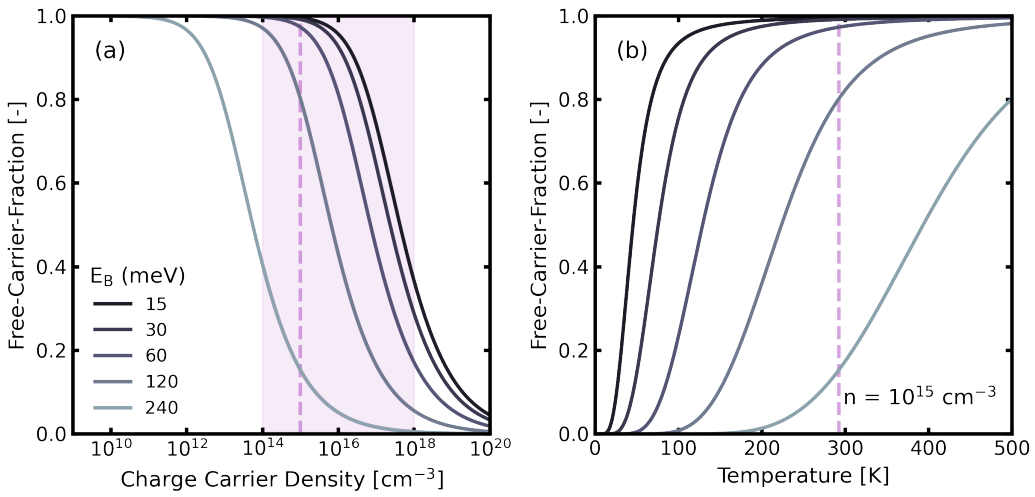

Figure 2.6: (a) The equilibrium free-carrier fraction ϕ is shown as a function of charge carrier density n for different exciton binding energies. The marked area (pink) are the typical charge carrier densities associated with most optoelectronic characterization techniques. The pink dotted line marks the charge carrier density used in (b). (b) ϕ is shown as a function of temperature T for the same exciton binding energies as in (a). The charge carrier density was fixed to 10^{15} cm^{-3}. The pink, dotted line marks the room temperature measured for this thesis of 292 K. The reduced mass m_i^* was fixed to $0.1 \times m_\mathrm{e}$ in accordance with **Table 2.1**.

In the case of two-dimensional materials, the anisotropy of charge carrier transport complicates the use of **Equation 2.8**. In general, another version of the Saha equation exists for two-dimensional materials, taking this into account, by estimating a fluence F (in cm^{-2}well^{-1}) per quantum well

thickness d_{qw} instead of the excitation density[136]

$$\frac{\phi^2}{1-\phi} = \frac{d_{\mathrm{qw}}}{F} \cdot \left(\frac{2\pi \cdot m_i^* \cdot k_{\mathrm{B}} T}{h^2} \right) \cdot e^{-\frac{E_{\mathrm{B}}}{k_{\mathrm{B}} T}}. \tag{2.9}$$

For **Chapter 5** a quantum well thickness of $d_{\mathrm{qw}} = 15$ nm yielded a good agreement between **Equations 2.8** and **2.9** for PEA_2PbI_4. For better comparability with the three-dimensional perovskite **Equation 2.8** was used for all materials investigated in that chapter.

A Note on Free Charge Carriers

Although the term "free carrier" will be used extensively throughout this thesis, it is important to note that the precise nature of charge carriers in a two-dimensional perovskite is still the subject of active investigation. Any unpaired charge carrier will be probed by the techniques used in **Chapter 5** and is thus included in the presented results, regardless of whether they are true free charge carriers, polarons, or something else entirely.

2.4 ABSORPTION

Absorption of Direct and Indirect bandgap Semiconductors

Solid state materials form energy bands rather than discrete energy levels.[80,137] Absorption of light can occur whenever a photon with energy equal or larger than the bandgap interacts with a solid material. The absorption spectra of solids are continuous above a certain energy (see **Figure 2.7(a)** and **(b)**), in contrast to the discrete lines and peaks that are observed for for atomic and molecular absorption spectra, respectively.[137]

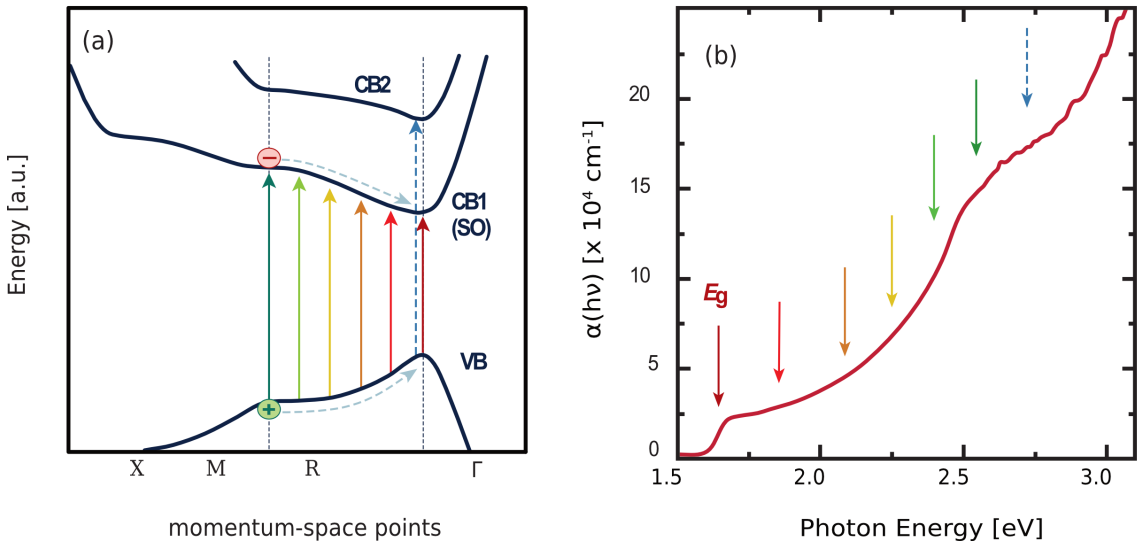

Figure 2.7: (a) Simplified band structure of $MAPbI_3$ as shown in Figure 2.4. The colored arrows represent absorption of photons at different energies. The conduction band (CB) is split into CB1 and CB2 due to the spin-orbit coupling. Between the R and M point in momentum space, electrons can be excited from the valence band (VB) to the conduction band (CB1) by absorption of visible light. Higher-energy transitions are allowed between VB and CB2 and are indicated by the dashed blue arrow. It is indicated that charge carriers with excited by higher energies will relax back to the R point, where subsequently recombination happens. (b) The absorption spectrum of $MAPbI_3$ is shown with colored arrows indicating the transitions from VB to CB1 from (a). The resulting spectrum is a continuum of absorbing states. (a) & (b) were adapted with permission from ref. 138.

Not every absorption process of a photon will lead to the formation of an electron-hole pair. The reason for that can be understood from an energetic as well as structural point of view and both will be briefly mentioned here: energetically, an excited electron will need to occupy an empty state within the conduction band. This process hence depends on the density of states in the

conduction band. During the excitation process the momentum of the electron will need to be conserved. In a molecule this can be achieved by a change in vibrations (or momentum), but in a solid it depends strongly on the interaction of the excited electron with the underlying lattice vibrations, called phonons.[80,139] Two scenarios can be differentiated: 1) a direct bandgap, in which no additional phonon-interaction is necessary to conserve the momentum during excitation of an electron. This is the case for metal halide perovskites, for example. 2) an indirect bandgap, where an electron also needs to interact with a phonon in order to conserve the momentum during excitation. This process is a second-order process and much less likely than the direct transition. An example for this type of material is crystalline silicon.

A direct bandgap semiconductor should hence show an absorptance $A(h\nu)$ of 1 for photons with energies larger than the bandgap. In reality this is not the case and an absorption coefficient α can be defined as

$$\alpha(h\nu) = \frac{1}{d} \cdot \ln\left(\frac{1 - R(h\nu)}{T(h\nu)}\right), \tag{2.10}$$

where d is the thickness of the material.[58] For a strongly absorbing semiconductor, $\alpha(h\nu) >> 1$ for photon energies above the bandgap. In **Figure 2.8(a)** the absorption coefficient is shown for common semiconductor materials that have been used in photovoltaic applications. It can be seen that all examples, except crystalline silicon (c-Si) show $\alpha(h\nu) >> 1$ at high photon energies, indicating that these materials have direct energy bandgaps. In addition the onset of the absorption is different between the materials. It can indicate the energetic disorder at the band edge and below the bandgap, due to for example defect states.[140] As these states effectively narrow the bandgap they will also directly affect the possible V_{oc} of the resulting device. The "steepness" of the absorption onset can therefore be correlated to losses in V_{oc}. It can be seen in **Figure 2.8(a)** that $MAPbI_3$ has a steep onset, indicating a low defect density, owing to the defect tolerance of the material, as well as a good overall material quality.

Charge Generation Rate

With the knowledge of the absorption coefficient of a material, one can estimate the absorption properties of a material. When photons interact with the material the likelihood of absorption increases with the the thickness of the sample. This effect is known as the Beer-Lambert law.[141] It is used in **Equation 2.11** to estimate the density of photo-generated electron-hole pairs inside a semiconductor material after a single excitation pulse

$$G(0,d) = \frac{F(h\nu)}{d} \cdot (1 - r(h\nu)) \cdot \left(1 - e^{-\alpha(h\nu)d}\right). \tag{2.11}$$

where $F(h\nu)$ is the fluence of the excitation source. The exponential part follows the Beer-Lambert law and can be used to describe the excitation profile within a semiconductor slab. In **Figure 2.8(b)** the normalized charge carrier density over the thickness of 500 nm of a given semiconductor sample is presented for different absorption coefficients following

$$n_{\text{norm}}(0,z) = 1 - e^{-\alpha(h\nu)z}. \tag{2.12}$$

It can be observed that all absorption coefficients result in an exponentially decaying profile over the thickness of the absorber material.

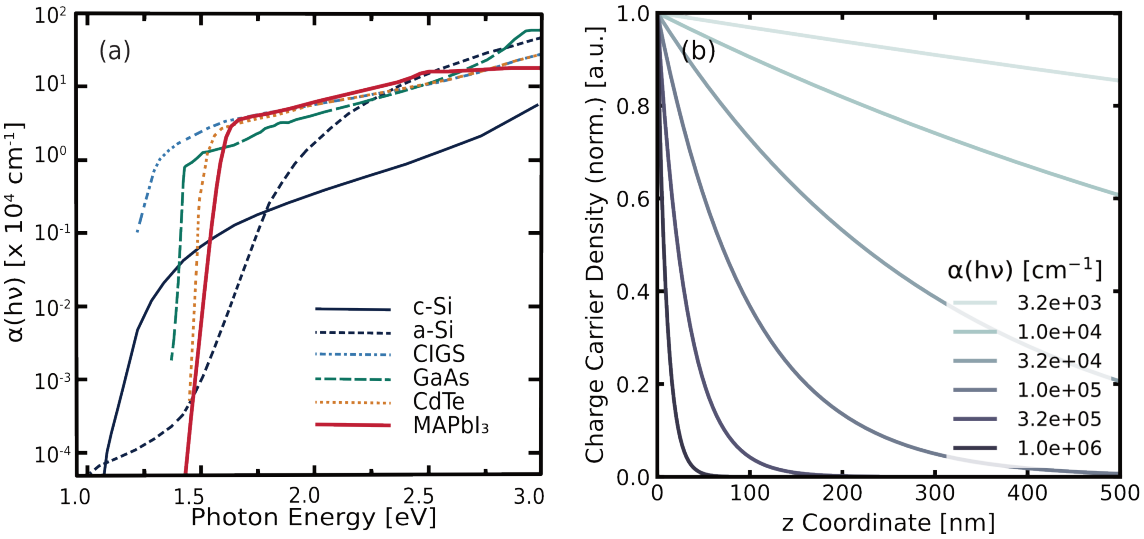

Figure 2.8: (a) The absorption coefficient of $MAPbI_3$ is shown alongside other semiconductor technologies for photovoltaic applications: crystalline silicon (c-Si), amorphous silicon (a-Si), Copper indium gallium selenide (CIGS), gallium arsenide (GaAs) and cadmium telluride (CdTe). (b) The normalized charge carrier density as a function of z coordinate is shown for different absorption coefficients. All show an exponential absorption profile over the thickness of 500 nm. (a) was adapted with permission from Ref. 18.

In agreement with **Figure 2.8(b)** it becomes apparent that high energy photons are absorbed much closer to the incident surface than lower energy ones. This effects is often used to compare surface- and bulk processes. In **Chapter 6** this effect will be leveraged to probe the surface recombination of a thin film sample and study the diffusion of charge carriers after highly inhomogeneous charge carrier generation. It is important to keep in mind that the generation profile described by **Equations 2.11** and **2.12** is more relevant for pulsed excitation, while during continuous excitation a steady-state generation rate G is calculated instead.

Comment: Reproducibility and the "one sun" Condition

At this point it is worth emphasizing the importance of reproducible experiments. When performing spectroscopic characterization it is crucial to keep the amount of photons incident on a sample as well as the density of photo-generated charge carriers in mind. This is especially important when investigating perovskite materials, where seemingly small changes to the processing can have significant impact on the final material quality.[142]

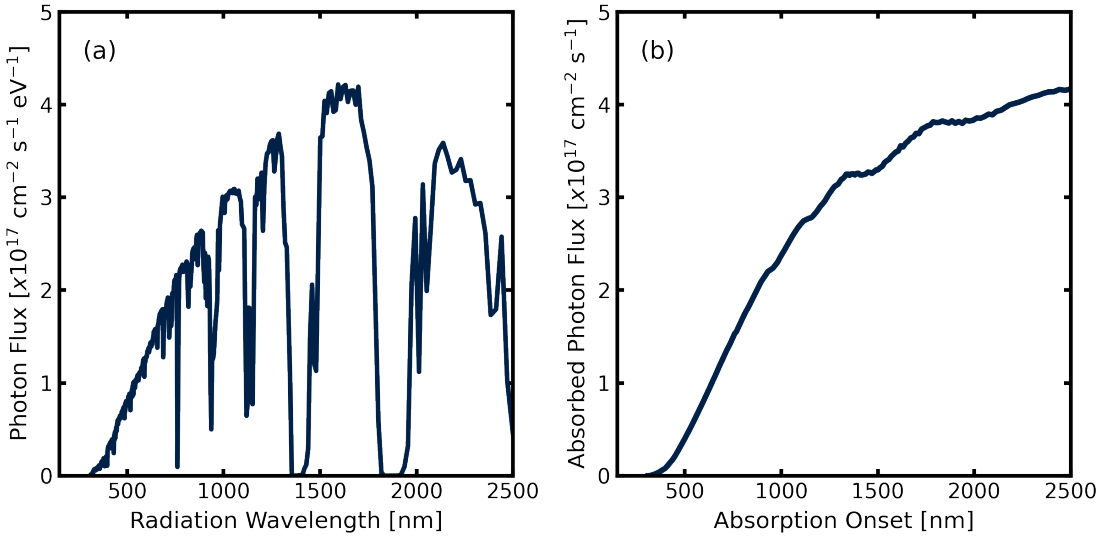

Figure 2.9: The AM1.5 global tilt spectrum is shown as (a) converted to photon flux per energy level and (b) integrated up to the absorption edge wavelength assuming a step-like absorption profile. The latter is the absorbed photon flux that is called 'one sun condition'.

Hence, the "one sun" condition has been defined as the excitation condition at which the same number of electron-hole pairs are generated per second as under AM1.5 illumination.[143] It corresponds to a power density of approx. 100 mW cm^{-2} This condition can be calculated from the AM1.5 photon flux spectrum (shown in **Figure 2.9(a)**), by integrating the photon flux above a certain bandgap energy. This assumes, that the absorption spectrum is step-like and $A(h\nu) =$

1 above the bandgap, both of which are approximately true for a direct bandgap semiconductor with low below-bandgap disorder, such as metal halide perovskites. The resulting absorbed photon flux for each bandgap energy (shown in wavelength) is presented in **Figure 2.9(b)**. This approach now allows the comparison of measurements made with different monochromatic or broadband light sources as well as continuous or pulsed excitation. In addition it allows for a better correlation of spectroscopic investigations of semiconductor materials with measurements of full photovoltaic device stacks, which are typically assessed using a lamp with a simulated AM1.5 spectrum.[144,145]

The Continuity Equation

After the generation of electron-hole pairs, their transient behaviour is described by the continuity equation

$$\frac{\partial n(t,z)}{\partial t} = G(0,z) - R(t,z) - \frac{1}{q}\frac{\partial J(t,z)}{\partial z}, \tag{2.13}$$

with $n(t,z)$ being the charge carrier density over time and space, $G(t,z)$ the generation, $R(t)$ the total recombination rate, q the electric charge and $J(t,z)$ the current density related to charge carrier transport, such as drift in an electric field and diffusion. **Equation (2.13)** is written for electrons here, but a similar equation can be written for holes. In an intrinsic semiconductor, like many perovskites, the two are linked via $n(t) = p(t)$. This relation will become important when non-radiative recombination is taken into account.

Over then next sections the different parts of the continuity equation will be introduced in more detail.

2.5 CHARGE TRANSPORT

Following photo-excitation, charges are now in the conduction band, which is delocalized over the crystal lattice and hence allows for charges to move around. There are two main processes, diffusion and drift, where the latter is only relevant in the presence of an electric field. Both are however dependent on the interaction of the charge carriers and excitons with the surrounding crystal lattice. This interaction is quantified by the mobility μ.

Mobility

In a semiconductor the mobility of electronic charge carriers is defined as

$$\mu_i = \frac{e \cdot \tau_{\mathrm{sc}}}{m_i^*} \tag{2.14}$$

using the reduced mass of the carrier type inside the crystal lattice m_i^* (i = n, p for electrons and holes) and the average time taken until the charge carrier is scattered by the lattice again (τ_{sc}). It follows that charge carriers with a higher effective mass, which are hence more localized in momentum-space, will have a lower mobility.[146] Therefore, the mobility also becomes a property of the underlying crystal lattice and is an important material parameter. In an ideal semiconductor material, it is independent of the charge carrier density until carrier-carrier scattering effects become relevant.[147]

In an electric field E charges will be accelerated along the electric field lines. Due to the m_i^* and τ_{sc} in **Equation 2.14** this acceleration slows down until it becomes a constant drift velocity v_{d}[80,146]

$$v_{\mathrm{d}}(V) = \mu_i \cdot E(V). \tag{2.15}$$

In a single crystal materials an electric field can hence be used to probe the impact of the lattice on the mobility.[148] It could be shown via temperature-dependent mobility measurements that the charge carrier transport inside the perovskite material is limited by charge carriers scattering off acoustic phonons.[39] In a polycrystalline thin film the simple relations described in Equations

(2.14) and (2.15) become dependent on the distance the charge carriers have to move. This is due to morphological or compositional changes within the thin film. Alongside the polycrystalline nature of the thin films this leads to additional scattering and trapping processes within the grains at also at grain boundaries.[13,17,147,149]

In **Chapter 4** the differences between long- and short-range mobility will be explored in more detail.

Diffusion

In the absence of an electric field, photo-generated charge carriers will diffuse inside a semiconductor material according to their density gradients. This will result in a homogeneous charge carrier distribution after some time, if recombination can be neglected. Diffusion can be described by the one-dimensional heat equation[150–152]

$$\frac{\partial n(t,z)}{\partial t} = -D_i \frac{\partial^2 n}{\partial z}. \tag{2.16}$$

Here, D is the diffusion coefficient, which is related to the mobility via

$$D_i = \frac{\mu_i k_\mathrm{B} T}{e}. \tag{2.17}$$

Often, diffusion is not characterized by the underlying mobility that governs the charge transport, but by the diffusion length L_D. It can be calculated as

$$L_{\mathrm{D},i} = \sqrt{D_i \cdot \tau_\mathrm{tot}}, \tag{2.18}$$

where τ_tot is the lifetime related to the total recombination rate R_{tot} as introduced in **Section 2.6**. It is important to keep in mind that μ_i and thereby D_i is dependent on the distance the charge carrier can move during a measurement. Additionally, there is some ambiguity in the field to how τ_tot is defined.[57]

Equation 2.16 can only be solved numerically, without further assumptions. Common methods include the foward- or backward-Euler method, the Crank-Nicolson method or the trigonometric solution as described by Ahrenkiel.[150,153] A more detailed description of the latter is presented in **Chapter 6**. Regardless of the method chosen, the behaviour at the edges $z = 0$ and $z = d$

need to be introduced via boundary conditions. This can be done by defining a net velocity of charge carriers out of the boundaries on both sides. They are referred to as 'surface recombination velocities' (SRVs) and are introduced as Neumann boundary conditions, meaning they are introduced via their first derivative[154]

$$\begin{aligned} (a) \quad & S_0 \cdot n(t,0) = D \cdot \frac{\partial n(t,0)}{\partial z} \\ (b) \quad & S_\mathrm{d} \cdot n(t,d) = -D \cdot \frac{\partial n(t,d)}{\partial z}. \end{aligned} \tag{2.19}$$

In **Section 2.6** it is described that the surface recombination can occur, if trap states are present at the surface of a thin film or single crystal. In addition, interface recombination between a semiconductor absorber and for example a charge transport layer can occur and is also described by **Equations (2.16)** and **(2.19)**. This is true because S has the units of velocity and describes a net-flow from the absorber through the surfaces. The exchange of charge carrier at an interface (extraction and re-injection) can thus be understood as a net-surface recombination rate.

Drift

The mobility, as a measure for charge transport, can also be directly linked to photovoltaic performance parameters, such as the steady-state current density or the fill factor.[80,155] The steady-state current density is defined as

$$J_\mathrm{drift}(V) = \sigma \cdot E(V) \tag{2.20}$$

and is also known as 'drift current'. Here, σ is the conductivity of the material and is linked directly to the mobility via

$$\sigma = e \cdot (n \cdot \mu_\mathrm{n} + p \cdot \mu_\mathrm{p}) = e \cdot n \cdot \Sigma\mu_i, \tag{2.21}$$

where the right side of the equation is only true for intrinsic semiconductors, where $n = p$.[149,156] In **Chapter 4** this relation will be used to estimate the sum-mobility $\Sigma\mu_i$ from photo-conductivity measurements at different length scales.

Charge Extraction

In a full solar cell device stack, charges that have moved from the absorber to a transport layer, can be extracted by the metal contacts. In such a situation, the perovskite semiconductor can no longer be assumed to be intrinsic across the entire thickness d. At this point, the charge carrier transport can no longer be described by diffusion or drift alone, but becomes a mixed system of both, that also depends on the intrinsic electric field. In perovskites, the presence of mobile ionic species further complicate this. The detailed description of such a system goes beyond the work presented here, but has been subject of previous research in the field.[157,158] It is however worth mentioning that charge extraction in the absence of electronic contacts is still covered by the surface recombination. In this regard it is not possible to decouple charge extraction and re-injection from interface recombination.

2.6 RECOMBINATION

During absorption of photons, excitons and free charge carriers are generated in the conduction and valence band. While diffusing or drifting through the material they can recombine via a variety of processes, as shown schematically in **Figure 3.1**. In the following sections, all recombination processes relevant for this thesis are introduced in detail.

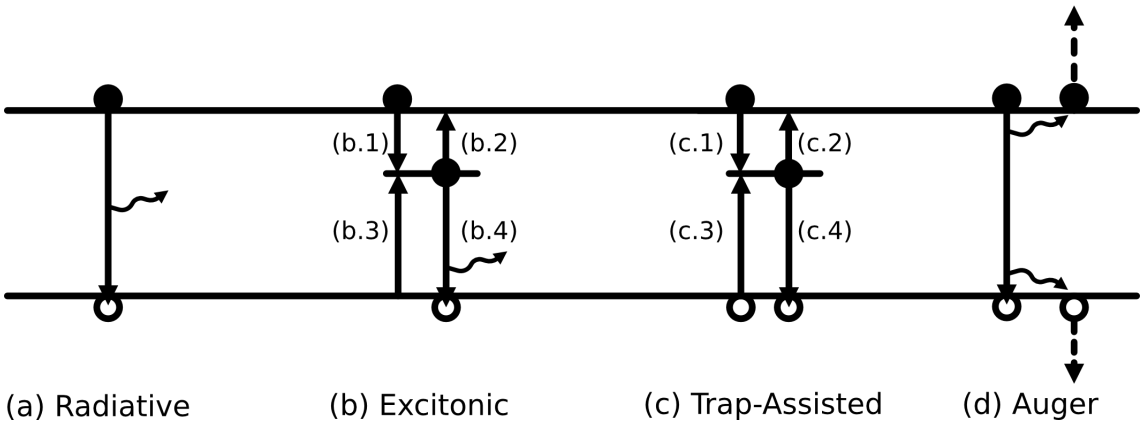

Figure 2.10: All recombination processes relevant for this thesis: (a) radiative, band-to-band recombination, (b) radiative, excitonic recombination, (c) non-radiative, trap-assisted recombination, and (d) non-radiative, Auger recombination. The straight, solid arrows indicate electron movement, the wavy arrows indicate photon emission and the straight, dotted arrows indicate the Auger process.

Radiative Recombination

Radiative recombination describes all recombination processes that result in the emission of a photon at the energy (or close to the energy) of the bandgap.

bi-molecular, Band-to-Band Recombination

The band-to-band, radiative recombination of photo-excited, free charge carriers is shown schematically in **Figure 3.1(a)** and can be described via

$$R_{\mathrm{rad}}(t) = k_{\mathrm{rad}} \cdot ((\Delta n(t) + n_{\mathrm{eq}}) \cdot (\Delta p(t) + p_{\mathrm{eq}}) - n_{\mathrm{eq}} p_{\mathrm{eq}}) \,, \tag{2.22}$$

where n_{eq} and p_{eq} are the equilibrium, background electron and hole densities, which should be equal in an intrinsic semiconductor.[81,151,159] Similarly, Δn and Δp are equal in an intrinsic semiconductor. k_{rad} is the intrinsic, radiative recombination constant. **Equation 2.22** describes that the band-to-band recombination depends on the square of the photo-generated charge carrier density.

When measuring the transient photo-luminescence of perovskites, **Equation 2.22** is often simplified to

$$R_{\mathrm{rad}} = k_{\mathrm{rad}} \cdot \Delta n^2 \tag{2.23}$$

as n_{eq} and p_{eq} are usually much smaller than the density of photo-generated charge carriers. In **Chapter 6** it will be seen under which circumstances these might become important again.

Since radiative recombination results in the generation of photons, it can be used to calculate the photo-luminescence response of a semiconductor. After pulsed excitation the photo-luminescence intensity is defined as

$$PL(t) = \int_0^d R_{\mathrm{rad}}(t,z) \cdot (1 - P_{\mathrm{reabs}}) \; dz = k_{\mathrm{rad,eff}} \cdot \int_0^d ((\Delta n(t) + n_{\mathrm{eq}}) \cdot (\Delta p(t) + p_{\mathrm{eq}}) - n_{\mathrm{eq}} p_{\mathrm{eq}}) \; dz, \tag{2.24}$$

where $k_{\mathrm{rad,eff}} = k_{\mathrm{rad}}(t,z) \cdot (1 - P_{\mathrm{reabs}})$ is the effective, radiative recombination rate, with P_{reabs} being the probability of reabsorption of emitted photons before being detected. Further below it is introduced, how the impact of P_{reabs} was handled in this thesis.

Mono-Molecular Exciton Decay

In addition to the bi-molecular, band-to-band recombination, there exists also mono-molecular exciton recombination as shown schematically in **Figure 3.1(b)**. In a full physical model description there will be rates related to the (b.1) recombination of free charge carriers to excitons, (b.2) the dissociation of an exciton into free carriers, (b.3) the decay of an exciton to the ground state resulting in the emission of a photon, and (b.4) the absorption of a photon by the excitonic bandgap.[81,160–162]

It was shown that the ratio of (b.2) to (b.1) could be approximated via the Saha-Equation (**Equation 2.8**), with high accuracy for high exciton binding energies, where (b.1) was the dominating process.[163] As was introduced in **Section 2.3**, excitons are the dominating species in two-dimensional perovskites and define the optoelectronic properties. Under the assumption that (b.1) is fast enough, the absorption rate (b.4) can be neglected as well. Then, the model can be simplified by assuming that most of the photo-luminescence comes from the decay of an exciton to the ground state (b.3). It can be described as a modification to the bi-molecular, band-to-band recombination rate as

$$k_{\mathrm{rad,eff}} = k_{\mathrm{rad}} \cdot (1 - P_{\mathrm{reabs}}) + k_{\mathrm{x}} \cdot \frac{1-\phi}{\phi^2}, \tag{2.25}$$

where k_{x} is the mono-molecular rate of the exciton decaying to the ground state (b.3).[136] For this thesis the simplified model according to **Equation 2.25** was sufficient to be used in **Chapter 5**.

Non-Radiative Recombination

Via Bulk Trap States

As introduced in **Section 2.2**, defects will exist in any material, which can act as recombination centres. The reason for this is that most defects generate energetic trap states within the bandgap. Recombination via these trap states is shown schematically in **Figure 3.1(c)** for an electron trap, but the recombination rates will be the same for a hole trap in an intrinsic semiconductor. The recombination can be described via four coupled rate equations:

$$\begin{aligned}
(c.1)\quad & R_{\mathrm{c,n}} = v \cdot \sigma_{\mathrm{n}} \cdot \Delta n \cdot N_{\mathrm{t}} \cdot (1 - f_{\mathrm{t}}) \\
(c.2)\quad & R_{\mathrm{e,n}} = e_n \cdot N_{\mathrm{t}} \cdot f_{\mathrm{t}} \\
(c.3)\quad & R_{\mathrm{e,p}} = e_p \cdot N_{\mathrm{t}} \cdot (1 - f_{\mathrm{t}}) \\
(c.4)\quad & R_{\mathrm{c,p}} = v \cdot \sigma_{\mathrm{p}} \cdot \Delta n \cdot N_{\mathrm{t}} \cdot f_{\mathrm{t}}
\end{aligned} \tag{2.26}$$

with $R_{\mathrm{c},i}$ and $R_{\mathrm{e},i}$ being the capture and emission rates of electrons ($i = n$) and holes ($i = p$), v the thermal velocity, σ_i the capture cross section ($i = n, p$ for electrons and holes), N_{t} the trap state density and f_{t} the trap state occupation.[151,164,165] **Equations 2.26(c.1)** to **(c.4)**
As the emitted energy from this recombination process is now much lower than the bandgap it will be lost to thermalisation. Hence, this type of recombination is termed non-radiative recombination.

In the perovskite literature $v\sigma_{\mathrm{n}}N_{\mathrm{t}} = v\sigma_{\mathrm{p}}N_{\mathrm{t}}$ is often summarized as a single constant k_{nr} - the non-radiative recombination constant. This is valid under the assumptions that there is negligible de-trapping and that both trapping and recombination happen on similar time scales so that $n = p$ is still conserved. In most cases, this is a good approximation and leads to the simple, non-radiative recombination rate

$$R_{\mathrm{SRH}} = k_{\mathrm{nr}} \cdot \Delta n. \tag{2.27}$$

The rates $R_{\mathrm{e},i}$ of emission of charge carriers from the trap only become significant once the energy of the trap is close to the conduction (in the case of an electron trap). In that case the density of

re-emitted charge carriers into the band can be estimated via

$$n_{\mathrm{e},i} = N_{\mathrm{C}} \cdot e^{-\frac{\Delta E_{\mathrm{t}}}{k_{\mathrm{B}} T}}, \tag{2.28}$$

where N_{C} is the density of states in the conduction band and ΔE_{t} is the depth of the trap with respect to the conduction band edge.[164] It can then be used to approximate the non-radiative recombination rate via any trap as

$$R_{\mathrm{SRH}} = k_{\mathrm{nr}} \cdot \frac{\Delta n(t)^2}{2 \cdot \Delta n(t) + n_{\mathrm{e},i}} \tag{2.29}$$

again assuming that $k_{\mathrm{nr}} = k_{\mathrm{nr,n}} = k_{\mathrm{nr,p}}$. The non-radiative recombination rate now scales with Δn for low $n_{\mathrm{e},i}$ (deep traps) or with Δn^2 for $n_{\mathrm{e},i}$ approaching Δn (shallow traps).[57]

The non-radiative recombination treated here is a property of the bulk material and is therefore termed 'bulk non-radiative recombination'. In the next section the 'surface non-radiative recombination' will be introduced.

Via Surface and Interface Recombination

Similar to bulk trap states due to imperfections within the material lattice, there can also be recombination centers at the surface. These are most often dangling bonds or under coordinated ions generating trap states with energies within the bandgap again.[166,167] In single crystal materials, the surface recombination can often be ignored as it doesn't determine the overall optoelectronic properties, but in thin films is becomes a significant contribution to the overall recombination. Again, four coupled rate equations similar to the ones for bulk-trap-assisted recombination can be formulated for the capture of an electron or hole into a surface trap and the emission of an electron or hole from the surface trap. Alternatively, it can be understood in terms of interface processes, where an electron or hole is extracted into the adjacent material or re-injected into the absorber material. As mentioned in **Section 2.5** the two descriptions are equivalent, if a net-surface recombination velocity (SRV) is defined. In this thesis surface recombination was implemented only in **Chapter 6** using the approach described in **Section 2.5**.

Comment: Via a bi-molecular Process

In the field some reports have postulated a non-radiative, bi-molecular process with the recombination constant $k_{2,\mathrm{nr}}$.[168,169] It is often needed to accurately describe intensity-dependent PLQE and TRPL data with the same parameters. The physical nature of this process is thus far not understood. Recent work points towards a possible connection to non-radiative recombination via shallow trap states, which then becomes a bi-molecular process, as shown in **Equation 2.29**.[57] It is worth noting that this non-radiative process won't have an impact on the time-resolved fitting shown in this thesis, as it cannot be disentangled from $k_{\mathrm{rad,eff}}$ unless in the case of intensity-dependent PLQE measurements. In this thesis $k_{2,\mathrm{nr}}$ was hence used to improve the agreement between intensity-dependent TRPL and PLQE measurements without further investigating its physical nature.

Via the Auger Process

In addition to the recombination processes introduced so far, there is also the possibility for the Auger recombination process, which is shown schematically in **Figure 3.1(d)**. In general, it involves three charge carriers (either two electrons and one hole or the other way around), two of which recombine and transfer the emitted energy onto the third one. In all cases the newly excited charge carrier looses its extra energy to thermalisation making it a non-radiative process.[170] As the process follows third-order kinetics, it is only probable at high charge carrier densities. The Auger recombination rate can be written as

$$R_{\mathrm{Aug}} = (k_{\mathrm{Aug,n}} + k_{\mathrm{Aug,p}}) \cdot ((\Delta n + n_{\mathrm{eq}}) \cdot (\Delta p + p_{\mathrm{eq}}) - n_{\mathrm{eq}} p_{\mathrm{eq}}) \,, \tag{2.30}$$

where $k_{\mathrm{Aug,n}}$ and $k_{\mathrm{Aug,p}}$ are the Auger recombination constants. In the case of perovskites, they are often combined into $k_{\mathrm{Aug,eff}} = k_{\mathrm{Aug,n}} + k_{\mathrm{Aug,p}}$.[152] It was shown that the Auger recombination can be influenced by the presence of trap states, as it temporarily locates one or two of the charge carriers, which increases the probability of the process.[170,171] It was postulated that the Auger recombination diverges from a third-order process, only if the trap density exceeds $10^{18}\mathrm{cm}^{-3}$ and the trap state has a large ΔE_{t}. For most perovskite materials it is hence unlikely to be the source of the unknown, non-radiative, bi-molecular recombination. In addition, typical values for $k_{\mathrm{Aug},i}$ are in the range of 10^{-27} to 10^{-32} $\mathrm{cm}^6\mathrm{s}^{-1}$, which makes the Auger process in general

only a relevant process for charge carrier densities $\geq 10^{17}\mathrm{cm}^{-3}$, which are barely reached in typical photo-luminescence measurements.[172] Therefore, Auger recombination was neglected for all TRPL-related processing in this thesis, but included for intensity-dependent PLQE analysis (see Chapter 3).

Reabsorption Effects

An additional effect, which can impact the observed recombination behaviour is the reabsorption (as mentioned P_{reabs}).[56,173–175] It was shown through simulations that reabsorption affected the earlier time processes.[56] Hence, its impact is often reduced to a pre-factor, which is then included in $k_{\mathrm{rad,eff}}$.[169] In a full ray-tracing simulation it could be shown that proper inclusion of reabsorption processes allows the extraction of k_{rad} from TRPL measurements.[173,175] The complete description of reabsorption effects goes beyond the scope of this thesis, nevertheless it is an important parameter when assessing TRPL data (as will be discussed in detail in **Chapter 6**). At this point it is worth mentioning that reabsorption can affect all parameters that impact the early-time processes during a TRPL measurement, which includes the radiative recombination, but also diffusion.[174,176] It appears to be unclear at this point how reabsorption and diffusion are connected other than via the diffusion length: The diffusion length can appear longer when reabsorption effects are present.[174,177,178] This would result in an over-estimation of the charge carrier mobility. The possible correlation between mobility and reabsorption has not been studied, yet, but will be discussed in **Chapter 6**.

2.7 STEADY-STATE PHOTOLUMINESCENCE

The steady-state photo-luminescence is the result of electron-hole pairs recombining and releasing the energy as a photon. It is thus the inverse process of absorption.[81] This is known as the reciprocity-relation between absorption and emission, which is true as long as both processes are connected to the same energetic states.[179] Hence, it is possible to gain insights into the underlying material properties from the photo-luminescence. For instance, the reciprocity relation can be leveraged to estimate below-bandgap absorption from ss-PL measurements.[180]
One can also estimate the photo-luminescence quantum efficiency (PLQE, η_{QE}), which is generally defined as the ratio of emitted photons to absorbed photons

$$\eta_{\mathrm{QE}} = \frac{\text{emitted}}{\text{absorbed}} \tag{2.31}$$

The PLQE can then be interpreted using the continuity equation (**Equation 2.13**), where all processes are in equilibrium and $\frac{dn(t,z)}{dt} = 0$. An internal and external PLQE can be defined as

$$\begin{aligned} (a) \quad & \eta_{\mathrm{QE,int}} = \frac{R_{\mathrm{rad}}}{R_{\mathrm{rad}} + R_{\mathrm{nr}}} \\ (b) \quad & \eta_{\mathrm{QE,ext}} = \frac{P_{\mathrm{esc}} \cdot \eta_{\mathrm{QE,int}}}{1 - \eta_{\mathrm{QE,int}} + P_{\mathrm{esc}} \cdot \eta_{\mathrm{QE,int}}}, \end{aligned} \tag{2.32}$$

where $\eta_{\mathrm{QE,int}}$ can be calculated with the knowledge of the radiative and non-radiative recombination rates (R_{rad} and R_{nr}). Importantly, $\eta_{\mathrm{QE,ext}}$ is also dependent on the escape probability P_{esc} and is the parameter that can be measured experimentally.[169] This is especially important to consider when measuring thin film samples on a substrate, where generated photons can be absorbed by adjacent layers or be trapped via total internal reflections.[169,175] Because of this effect it is possible to have a system, where all absorbed photons are re-emitted and still the measured $\eta_{\mathrm{QE,ext}}$ is not 100%.[173,175] Still, the PLQE is a measure of the ratio of radiative- and non-radiative processes and can hence give insights about the defect density in a material. As with the absorption, the PL emission can hence be used to assess V_{oc} losses in semiconductors in contact with transport layers and full device stacks.[143,181,182]

CHAPTER

3 EXPERIMENTAL DETAILS

This chapter summarizes all experimental techniques used for the work presented in this thesis. Both thin film fabrication, as well as extensive optoelectronic characterization are covered. Additionally, computational methods like fitting algorithms and transient behaviour simulations were applied to analyse the data.

3.1 CHEMICALS AND MATERIALS

Unless otherwise stated, the following materials were used throughout this thesis:
Precursor salts to form the perovskite material included Lead(II) iodide (PbI_2, TCI Chemicals, 99.999%, trace metals basis or sigma-PbI_2, Sigma-Aldrich, 99%), lead(II) bromide ($PbBr_2$, Afla Aesar, ultra dry, 99.999%, metals basis), lead(II) chloride ($PbCl_2$, Sigma-Aldrich, powder, 98%), lead(II) acetate ($PbAc_2$ x 3 H_2O, Sigma-Aldrich, $\geq$ 99%), formamidinium iodide (FAI, GreatCell Solar, $\geq$ 99.99% or dyenamo, 99.99%, trace elements basis), cesium iodide (sigma-CsI, Sigma-Aldrich, 99.999%, metals basis or Alfa Aesar, 99.9%, metals basis), methylammonium iodide (MAI, GreatCell Solar, $\geq$ 99.99%), methylammonium bromide (MABr, GreatCell Solar, $\geq$ 99.99%) and methylammonium chloride (MACl, GreatCell Solar, $\geq$ 99.99%).

To form the two-dimensional, layered perovskite materials, phenethylammonium iodide (PEAI, Sigma-Aldrich, 98%), 4-fluoro-phenethyl-ammonium iodide (F-PEAI, Greatcell Solar), 4-methoxy-phenethylammonium iodide (MeO-PEAI, Greatcell Solar) and 4-methyl-phenethylammonium iodide (Me-PEAI, Greatcell Solar) were used.

The solvents used where 2-isopropanol (IPA, Sigma-Aldrich, ACS reagent, $\geq$ 99.5% for cleaning), acetone (Sigma-Aldrich, ACS reagent, $\geq$ 99.5% for cleaning), toluene (Sigma-Aldrich, anhyrdous, 99.8%), acetronitrile (Sigma-Aldrich, anhydrous, $\geq$ 99.8%), dimethylformamide (DMF, Sigma-Aldrich, anhyrous, 99.8%), dimethylsulforxide (DMSO, Sigma-Aldrich, anhydrous, $\geq$ 99.9%), N-methyl-2-pyrrolidone (NMP, Sigma-Aldrich, anhydrous, 99.5%), gamma-butyrlactone (GBL, Alfa Asear, 99%), anisole (Sigma-Aldrich, anhydrous, 99.5%), methylamine (Sigma-Aldrich, 33 wt.% in absolute ethanol), hydrophosphorous acid (HPA, Sigma-Aldrich, 50 wt% in H_2O) and formic acid (FAH, Sigma-Aldrich, $\geq$ 95%).
All chemicals were used without further treatment or purification.

3.2 SUBSTRATES

Types of Substrates

The substrates used in this thesis were glass (Lumtec LT-G000 or biosigma), z-cut quartz, or fluorinated indium-tin-oxide (FTO) on glass (latech, 8Ω per square). Generally, for optoelectronic characterization thin film samples on glass or z-cut quartz were used. To measure half-stack samples FTO was used.

Substrate Cleaning

All substrates used in this thesis were cleaned using the same protocol: First, the substrates were scrubbed with a toothbrush and Decon90 detergent and rinsed with deionized water. Then the substrates were placed in a beaker in Decon90. The beaker was placed in an Ultrasonicator (Grant, Xuba3) at 50 °C for 30 min. Then, the substrates were rinsed with deionized water at least three times before being sonicated sequentially with acetone and IPA at 50 °C for 10 to 15 min. each. The substrates were then blow dried with a compressed dry air (CDA) gun and kept in a case covered with aluminum foil until use.

Right before using, the substrates were treated with UV-Ozone Cleaner (Jetlight Company Inc., Model 30) for 15 min. and used immediately, unless stated otherwise.

3.3 SAMPLE FABRICATION

Spin-Coating

All samples prepared for the work shown in this thesis were fabricated using Laurell-Technology spin-coaters. The spin-coating was either done inside a nitrogen-filled glovebox (< 1ppm H_2O, < 1 ppm O_2, 5 to 7 mbar over-pressure), a dry-box (ambient pressure) filled with nitrogen or compressed dried air (CDA) to control the humidity inside or using an ambient spin-coater in the the atmosphere of a cleanroom lab (approx. 50%RH, approx. 20 °C).

Thin Film- and Single Crystal Samples for Chapter 4

All thin films for this work were deposited on glass substrates.

Preparation of $FA_{0.83}Cs_{0.17}Pb(I_{0.9}Br_{0.1})_3$ and $(FA_{0.83}MA_{0.17})_{0.95}Cs_{0.05}Pb(I_{0.9}Br_{0.1})_3$ thin films[4,34,35]

CsI-alpha, FAI, MAI , PbI_2 and $PbBr_2$ were combined to the exact stoichiometry for the desired $(FA_{0.83}MA_{0.17})_{0.95}Cs_{0.05}Pb(I_{0.9}Br_{0.1})_3$ (termed FAMACs) or $FA_{0.83}Cs_{0.17}Pb(I_{0.9}Br_{0.1})_3$ (termed FACs) compositions and then stirred with a 4:1 solvent mixture of DMF and DMSO to obtain a 1.4 M solution. The fabrication of the thin films was carried out via spin-coating using a 2-step protocol: 1) 1000 rpm (200 rpm/s acceleration) for 10 sec. and 2) 5000 rpm (2000 rpm/s acceleration) for 35 sec. The perovskite precursor solution was dropped in the beginning of the program and 5 seconds before the end of the spinning process, a solvent-quenching method was used by dropping 300 µL anisole onto the wet, spinning films. The method was previously reported in more detail.[36] Average film thicknesses of 495 and 550 nm for FACs and FAMACs, respectively was determined using a DekTak profilometer.

Preparation of $MAPbI_3$ (ACN/MA) thin films

MAI and sigma-PbI_2 were combined at a ratio of 1:1.06 with a solvent mixture of acetonitrile and methylamine to obtain a 0.5 M solution. The precuror solution was spincoated in a CDA dry box

using a one-step protocol: 2000 rpm for 45sec. The resulting thin films were then post-treated with MACl, by dynamically spincoating 100 µL of a 5 mg/mL solution of MACl in IPA. The samples were then annealed at 100 °C for 60 mins. The formation of the acetonitrile/methylamine solvent and the rest of the method is detailed in a previous study.[32] An average film thickness of 400 nm was determined using a DekTak profilometer.

Preparation of $MAPbI_{3-x}Cl_x$ (DMF) thin films

The perovskite precursor solution was made by combining MAI, $PbCl_2$ and sigma-PbI_2 with the stoichiometry $MA_3Pb(Cl_{0.98}I_{0.02})_3$ and dissolved in pure DMF to obtain a 0.76 M solution. The thin films were prepared in a drybox (CDA, 15% to 20% RH at 20 °C) by a two-step spin-coating process: 1) 1300 rpm for 25sec.and 2) 3000 rpm for 15sec. Crystallization was induced by quickly quenching the spinning film with a CDA gun for 30sec. The resulting films were dried at 20 °C for 15 min and then at 70 °C for 15 min on a hot plate. Then the films were annealed 100 °C for 90 min before the tamperature was ramped up to 120 °C for 10 min inside an oven at ambient conditions. Finally, the annleaing process was completed at 150 °C for 10 min to evaporate excess MAI and form the perovskite material. The method is detailed in a previous report.[38] An average film thickness of 405 nm was determined using a DekTak profilometer.

Preparation of $MAPbI_3$ (DMF/HPA) thin films

MAI and $PbAc_2{\cdot}3\,H_2O$ were combined with the stoichiometry of MA_3PbI_5 and dissolved in DMF to obtain a 0.43 to 0.73 M solution. Then, 0.05 to 0.1 mol% of HPA solution was added to the precursor solution. The thin films were fabricated in a nitrogen-filled glovebox by a one-step spin coating process: 2000 rpm for 45sec. Afterwards, the films were left at 25 °C for drying for 10 to 15 min. then annealed at 100 °C for 5 min. The procedure is based on a previous report.[34] An average film thickness of 340 nm was determined using a DekTak profilometer.

Preparation of $MAPbI_3$ single crystals

MAI and PbI_2 were combined at a 1:1 molar ratio and dissolved in fresh GBL at 55 °C for at least 30 min. to obtain a 1.2 M solution. To obtain a seed crystal, 200 µL of FAH were added to 5 mL of precursor solution and the mixture was filtered through a 0.45 µm filter. The solution was kept in a closed vial at 55 °C until a seed crystal formed. Then, another solution was prepared from precursor salts with the same stoichiometry and concentration, but this time only 150 µL of FAH

per 5 mL of precursor solution were added. A cleaned Si wafer was placed at the bottom of the vial and a small (approx. 500 µm) seed crystal was placed on top of it. Then the vial was closed and placed in an oil bath at 55 °C until the crystal size was sufficient. The protocol is described in more detail in previous reports.[183,184] To be able to use the crystals for photo-conductivity measurements a 75 nm layer of gold was evaporated onto the dried crystals using a Nano36 (Kurt J. Lesker) evaporator. A thin piece of tape was carefully used to mask part of the crystal surface and produce laterally spaced electrodes. The parameters of the $MAPbI_3$ single crystals used in **Chapter 4** are summarized in **Table 3.1**. They were determined using a digital caliper.

Table 3.1: Structural parameters of the $MAPbI_3$ single crystal devices for the TPC measurements in **Chapter 4**.

Crystal No.	**Crystal width** (mm)	**Crystal thickness** (mm)	**Electrode spacing** (mm)
1	3.2	0.22	2.8
2	2.8	0.30	3.3
2	3.6	0.35	4.5

Thin Film Samples for Chapter 5

Thin film samples for this work were deposited on glass substrates for UV-Vis absorption, TRPL, PLQE and TPC measurements and on z-cut quartz for OPTP and XRD experiments. Thicker samples were produced for all optical characterization, while in the case of the 2D perovskite samples, the UV-Vis absorption was obtained from thinner samples, to be able to resolve the excitonic absorption feature.

Preparation of $FA_{0.9}Cs_{0.1}PbI_3$ Thin Films

FAI, CsI and PbI_2 were combined with the stoichiometry of $FA_{0.9}Cs_{0.1}PbI_3$ and dissolved in a 3:1 solvent mixture of DMF and DMSO, to obtain a 1 M solution. The solution was stirred overnight. Then, the thin films were fabricated by spin-coating the precursor solution via a two-step program: 1) 1000 rpm (200 rpm/s acceleration) for 10 sec. and 2) 5000 rpm (2000 rpm/s acceleration) for 35 sec. 250 µL of precursor solution were dropped onto the spinning substrate 5 to 6 sec. after starting the program. Crystallization was induces by dropping 350 µL of anisole onto the spinning films 10 sec. before the end of the program. It took about 1 to 2 sec. to release

all of the antisolvent. The films were then annealed on a hotplate at 100 °C for 15 min. All processing was done inside a nitrogen-filled glovebox. An average film thickness of 370 nm was determined using a DekTak profilometer.

Preparation of two-dimensional perovskites A_2PbI_4 Thin Films

The same procedure was used for all ammonium iodides (AI) used in this thesis namely PEAI, F-PEAI, MeO-PEAI and Me-PEAI.

PbI_2 and the chosen AI were combined with the stoichiometry of A_2PbI_4 and dissolved in a 3:1 solvent mixture of DMF and DMSO, to obtain a 0.6 M solution. The solution was stirred overnight. Then, the thin-films were fabricated by spin-coating the precursor solution substrate via a two-step program: 1) 1000 rpm (200/s rpm acceleration) for 10 sec. and 2) 6000 rpm (2000 rpm/s acceleration) for 35 sec. 250 µL of precursor solution were dropped onto the substrate after 5 to 6 sec. starting the program. No anti-solvent was needed to induce crystallization. The films were then annealed on a hotplate at 100 °C for 15 min. All processing was done inside a nitrogen-filled glovebox. For the thicker films, an average film thickness of 590 nm was determined using a DekTak profilometer, while for the thinner ones used for UV-Vis absorption a thickness of 160 nm was determined.

Thin Films for Chapter 6

The $FAPbI_3$ thin films and $FAPbI_3$|Spiro samples were deposited on glass substrates, while the SnO_2+TiO_2|$FAPbI_3$ samples were depoited on FTO. All samples for this project were fabricated by Dr. Seongrok Seo (University of Oxford).

Preparation of $FAPbI_3$ Thin Films

Precursor salts were combined according to the $(FAPbI_3)_{0.99}(CsPbBr_3)_{0.01}$ stoichiometry with 35mol% excess MACl and were dissolved in a DMF:DMSO solvent mixture (4:1 by volume) to obtain a 1.5 M solution. It was stirred for 1 hr and filtered using a 0.45 µm PTFE filter before use. The spin was conducted in 2 steps: 1000 rpm for 10 sec. (500 rpm/s acceleration) and 5000 rpm for 35 sec. (1000 rpm/s acceleration). 100 µL of the precursor solution was dropped dynamically in the beginning of the program. Then 300 µL of anisole were used for the solvent quenching at 5 seconds before end the spin and annealed at 80 °C for 10 mins. Films were spin-coated in

a nitrogen-filled glovebox and then further annealed at 150 °C for 15 min. in a dry box (10 to 15%RH).

Preparation of SnO_2+TiO_2|$FAPbI_3$ Half-Stacks

Glass substrates were cleaned and UVO treated for 30 min. before the deposition of the ETL. 100 µL of TTIP solution (diluted 1:15 in 1-Butanol) were statistically spin-coated at 5000 rpm for 45 sec. (2000 rpm/s acceleration) then dried at 130 °C for 5 min. and 450 °C for 30 min. 100 µL of SnO_2 nanoparticle dispersion (2 wt% diluted in DI water) were statistically spin-coated at 4000 rpm for 30s (3000 rpm/s acceleration) and then annealed at 180 °C for 30min. Then the perovskite was processed on top, as described before.

Preparation of $FAPbI_3$|Spiro-OMeTAD Half-Stacks

Spiro-OMeTAD solution was prepared with the following composition: 60 mg of Spiro-OMeTAD, 25.5 µL of 4-tert-butylpyridine, 15.5 µL of Li-TFSI (520 $\mathrm{mg\,mL^{-1}}$ in acetonitrile), and 12.5 µL of Co-TFSI (375 $\mathrm{mg\,mL^{-1}}$ in acetonitrile) in 700 µL of chlorobenzene. 60 µL of the solution was dynamically spin-coated on top of the perovskite thin film at 4000 rpm for 30s, then dried overnight in dry air condition before characterization.

Preparation of Samples for Transient Photo-Conductivity Measurements

To prepare samples for TPC measurements, in-plane gold (Au) electrodes with a thickness of 75-100 nm were evaporated onto the perovskite thin films on glass using a Nano36 (Kurt J. Lesker) evaporator. The measurements of the channel dimensions are summarized in **Table 3.2**. There were two different pixel layouts used: a 300 µm-channel, which was used for **Chapter 4** and **5**, and a 500 µm-channel. For **Chapter 6** both channels were used. All evaporation masks were designed by Dr. Jongchul Lim (Chungnam National University).

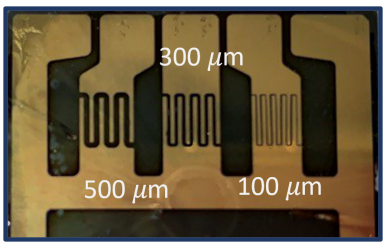

Figure 3.1: Photograph of the interdigitated Au electrode layout used throughout this thesis. The '300 µm' and '500 µm' pixels were used.

Table 3.2: Structural parameters of the two Au pixel layouts used for the TPC measurements in this thesis.

	'300 µm'	'500 µm"
Spacing (mm)	0.3	0.5
Length (mm)	31.6	23.2

3.4 STRUCTURAL MATERIALS CHARACTERIZATION

1D Thin Film X-ray Diffractometry

All X-ray diffractograms presented in this thesis have been measured on z-cut quartz, unless stated otherwise. They were obtained using an X'PERT Pro X-ray diffractometer (Panalytical) using a Cu-Kα1 X-ray source.

2D Thin Film X-ray Diffractometry

2D X-ray diffractograms were measured for thin film samples on z-cut quartz. The measurements were conducted in ambient air (30 to 50%RH, r.t.) with a Rigaku SmartLab X-ray diffractometer with a Cu-Kα1 X-ray source and a HyPix-3000 2D hybrid pixel array detector. All 2D X-ray diffractograms were measured and analyzed by Philippe J. Holzhey (University of Oxford).

Secondary Electron Microscopy (SEM)

The instrument used to image thin films using the secondary electron emission was an FEI Quanta 600 FEG electron microscope. The thin films were either deposited on glass or ITO-coated glass. The latter was necessary for two-dimensional perovskites (in **Chapter 5**) as they showed strong in-plane conductivity, which resulted in diffuse images. Measuring on ITO improved the image quality.

Kelvin probe Force Microscopy

The measurement was performed in a nitrogen-filled glovebox at room temperature using a Kelvin probe (KP technologies) with a 50 µm tip diameter, and with a micro-translation stage to move the sample under the tip. A bias voltage of < 0.01 V µm^{-1} was applied to the sample via the evaporated electrodes used for TPC. Samples were assessed with and without illumination.

3.5 CHARACTERIZATION OF ABSORPTION PROPERTIES

UV-Vis Absorption

Transmission and reflection spectra were measured for thin-film samples on microscope glass slides with a PerkinElmer 1050+ UV-Vis-NIR spectrophotometer equipped with an integrating sphere accessory. The absorption coefficient was calculated according to **Equation (2.10)** where the thickness d was determined using a DekTak profilometer.

It is worth mentioning at this point that for the analysis of data obtained from optoelectronic characterization methods it is crucial to know the number of photons absorbed by the sample. In this case the knowledge of the absorption coefficient is not sufficient, but the reflectance $r(h\nu)$ at the illuminated surface is needed as well. The absorptance can then be calculated as

$$A(h\nu) = (1 - r(h\nu)) \cdot \left(1 - e^{-\alpha(h\nu)d}\right) \tag{3.1}$$

For example, for perovskites illuminated with a 470 nm (2.64 eV) excitation laser, the absorption coefficient is approximately 1×10^5 cm^{-1}. At a film thickness of 500 nm, almost all photons should be absorbed. The measured absorptance is however only 75% to 85%, because it is limited by the reflectance the illuminated surface.

Ellipsometry

A JA Wollam RS2 ellipsometer was used to measure the dielectric constants of the thin films on glass. The constants of a reference glass substrate were measured and fit first, and then the glass/film sample was measured with the glass model held constant. The psi and delta values were measured at angles of 55,65 and 75 with respect to the sample normal. A b-spline model was used to determine the n and k values, with a transparent region past the band edge set to $k = 0$. All ellipsometry was measured and assessed by Akash Dasgupta (University of Oxford).

3.6 PHOTOLUMINESCENCE CHARACTERIZATION

Steady-State Photoluminescence Quantum Efficiency (PLQE)

PLQE measurements were carried out using a home-built setup. Over the course of this thesis, the previously used PLQE setup was upgraded with a different set of lasers and an optical fiber. For **Chapter 5** the 'old setup' was used. There, a 405 nm laser (Roithner laser MLL-III-405-200 mW), was used for the two-dimensional perovskite samples and a 532 nm laser (Roithner laser RTLMLL-532-1.5-3W) for the three-dimensional ones. An integrating sphere, and a calibrated grating spectrometer (QEPro, OceanInsight), were used to measure the PL spectra.
For **Chapter 6** the 'new setup' was used, where a 445 nm laser (Thorlabs L450P1600MM laser diode powered with a LTC56B current controller) was used to measure all samples.

Intensity-Dependent PLQE

Intensity-dependent PLQE measurements can help to understand the recombination properties of a material. The same setups as above were used. For **Chapters 4** and **5** the old setup was used, where the intensity was changed with a discrete filter wheel and the resulting power was measured with a powermeter. The small spot size and irregular illumination times made it necessary to measure many samples (typically 3 spots on 3 samples) in order to obtain a statistically significant dataset.

For **Chapter 6** the new setup was used, where the discrete filter wheel was replaced with a continuous one and the power of the laser was monitored by a photo-diode attached directly to a powermeter. The intensity was then changed by a protocol written in `python` by Akash Dasgupta (University of Oxford), which fixed both the illumination time before the measurements and the time the sample was in the dark. The new setup yielded more reproducible results, so only one spot was measured for each sample.

Time-Correlated Single-Photon Counting (TCSPC)

In order to investigate transient behaviour of photo-generated charge carriers, the transient photoluminescence can be studied using time-correlated single-photon counting. For this thesis, a TimeHarp300 (Picoquant) was used, which includes a PMT detector (dead time < 95 ps) coupled to single-photon counting electronics (TimeHarp260 nano). Two lasers were mainly used with emissions at 398 nm (LPD- P-C-405) and 505 nm (LDH-P-C-510). The laser spot sizes and fluence ranges are summarized in **Table 3.3** For each sample, multiple fluences were measured to enable extraction of physical parameters using global fit (see **Section 3**).

In TCSPC experiments, the sample is excited with a pulsed light source and photo-generated charge carriers form upon absorption. The charge carriers will decay via a multitude of pathways (see **Chapter 2**) and emit photons at the detected wavelength. The time-difference between excitation and emission of a photon is tracked using the time-correlation electronics. This only works efficiently, if the number of photons arriving at the detector is a stream of single photons. One measure to keep in mind, is the pile-up rate, which is defined as the ratio of rate of emission to the rate of excitation. A pile-up rate of 100% therefore means that each excitation pulse generates one photon. The pile-up rate is influence by two important processes: (a) long-lived photons that stem from previous pulse cycles and (b) multi-photon emission within one pulse cycle. If the pile-up rate is too high, there is a chance for two photons simultaneously arriving at the detector, whereas the detector cannot differentiate between them. Effectively, this leads to an underestimation of the number of emitted photons from the sample. It is generally advised to keep the pile-up rate as low as possible to reduce this effect. If the pile-up rate gets too high, either the repetition rate of the laser can be reduced or neutral density filters can be used to reduce the number of photons reaching the detector. In all TRPL measurements for this thesis, the pile-up rate was kept below 5% to ensure that these effects are minimized.

Table 3.3: Parameters of the two lasers used in this thesis for the TCSPC measurements.

Laser Wavelength	398 nm	505 nm
spot size ($\times 10^{-5}$ cm^2)	8	15
max. Fluence (m^2)	4.8×10^{11}	2.1×10^{10}

3.7 PHOTO-CONDUCTIVITY MEASUREMENTS

Optical-Pump Terahertz-Probe (OPTP) Conductivity

Optical-Pump THz-Probe experiments were performed as previously described.[17,185] A Spectra Physics Mai Tai-Empower-Spitfire Pro Ti:Sapphire regenerative amplifier provided 35 fs pulses centered at 800 nm at a repetition rate of 5 kHz. 400 nm (3.10 eV) photo-excitation is obtained by frequency doubling the fundamental laser output through a BBO crystal, and 520 nm (2.38 eV) photo-excitation is obtained using an Optical Parametric Amplifier (Spectra Physics TOPAS). THz probe pulses are generated by a spintronic emitter composed of 1:8nm of Co40Fe40B20 sandwiched between 2 nm of Tungsten and 2 nm of Platinum, all supported by a quartz substrate. Detection of the THz pulses was performed using electro-optic sampling in a ZnTe crystal (1 mm (110)-ZnTe). The samples studied were bare perovskite films deposited on z-cut quartz. The sample, THz emitter and THz detector were held under vacuum ($<10^{-2}$ mbar) during the measurements. For this technique, no electronic contact is made with the sample.

Transient photo-conductivity (TPC)

Using a home-built setup, the transient photo-conductivity (TPC) can be measured for the thin films on glass. Inter-digitated gold electrodes spaced were used to bias the sample with a weak electric field of < 0.01 V µm^{-1}. The sample was illuminated by a 10 Hz pulsed laser at 470 or 550 nm with power densities < 1 mW cm^{-2} neutral density filters are used to access multiple excitation fluences and a hazy lens in front of the sample was used to uniformly illuminate the sample between in-plane electrodes, with an excitation of up 0.25 cm^2. The excitation used during the TPC experiment has a pulse width σ_{FWHM} of 3.7 ns, and was used as an optical trigger for a digital oscilloscope (Tektronix DPO 3054), which measures the voltage across a terminal resistor. More details about the technique and post-processing of the acquired data is part of **Chapter 4**.

A Note on the Probed Length-Scales

Concerning the length-scale over which the charge transport will occur during the measurement, this will depend upon the charge carrier mobility, the charge carrier lifetime and the applied electric field. For instance, with a mobility of 1 $cm^2\,V^{-1}\,s^{-1}$ and a lifetime of 1000 ns, the charge carriers would drift 1000 nm in the applied electric field of 0.01 $V\,\mu m^{-1}$.

Similarly to the TPC measurement, the length-scale over which OPTP spectroscopy probes the charge carrier mobility is dependent upon the absolute value of the charge carrier mobility. It is not straight forward to precisely estimate this length-scale.[186] However, for metal halide perovskites it has been observed that the OPTP estimated charge carrier mobility reduces when reducing perovskite nanocrystal sizes from 9 to 5 nm, suggesting that the length-scale probed is on the order of 10 nm. Hence, this technique is considered short-range, in comparison to the length-scale of 100s to 1000s of nm probed by the TPC measurement.

3.8 COMPUTATIONAL METHODS

About Physical Models

A general consideration when using physical models is the maximum number of parameters needed to fully describe a set of experimental data. A physical model should be able to describe the entire data set, make falsifiable predictions about unseen data and contain physically meaningful parameters.[187] When using a physical model one hence needs to consider the effects of under- and over-fitting: An experimental data set will contain features that are caused by some underlying, physical process and random fluctuations known as measurement noise that depend on the nature of the measurement and the environment. The physical model should be able to accurately describe features, but neglect the random fluctuations. Both, the lack of (under-fitting) as well as the abundance of (over-fitting) parameters may lead to a model that lacks the ability to make predictions and from which no physically meaningful quantities can be extracted.[188]

Simultaneously one needs to pay close attention to the identifiability of the physical model: There should be enough parameters to describe the experimental data set, but not so many that degenerate parameter combinations are possible.[189] It should be noted at this point that both, over-fitting and non-identifiability may enable 'cherry picking', by which only one of the degenerate parameter combinations is reported to support the hypothesis of an experiment. At the same time, non-identifiability can also be a feature of an experimental data set.[190] These considerations should be kept in mind, when writing or assessing physical models and will be explored further in **Chapter 6**.

Elliott Fit

The exciton binding energy of semiconductor materials is commonly determined by fitting the absorption coefficient to Elliot's Model.[83] In brief, the absorption onset of a direct bandgap semiconductor can be characterised by a range of states that are influenced by the presence of excitonic states below the bandgap. Previous studies have demonstrated that the absorption spectrum of metal halide perovskites cannot be accurately captured by Elliott's model, primarily

due to the presence of a strong Coulomb interaction within the material.[81] Only the first few hundred meV above the absorption onset can be fitted by the model. For the purpose of the work presented in this thesis it is good enough to fit these first few hundred meV and extract the exciton binding energy E_{B} as the difference in energy between the excitonic state and the continuum of states. The absorption coefficient α, can be modelled by separating it into an excitonic component f_{ex} and a continuum component f_{c}

$$\alpha(h\nu) = B \cdot \frac{\sqrt{E_{\mathrm{B}}}}{h\nu} \cdot (f_{\mathrm{ex}}(h\nu) + f_{\mathrm{c}}(h\nu)) \,. \tag{3.2}$$

Here, $\frac{\sqrt{E_{\mathrm{B}}}}{h\nu} \cdot (f_{\mathrm{ex}}(h\nu) + f_{\mathrm{c}}(h\nu))$ is dimensionless and can also be used to fit the absorbance directly. To be able to fit the absorption coefficient instead, the factor B, is needed, which is on the order of $\frac{1}{d}$, with d being the thickness of the sample.

The excitonic part f_{ex} consists of a series of normalised Gaussian peaks, with the peak centres being $E_{\mathrm{g}} - E_{\mathrm{B}}$ and a broadening factor of σ_{ex}. The energetic spacing between the different excitonic states is denoted as $E_{\mathrm{x}m}$. In general, it is useful to split the excitonic part into the first (1s) and all the other (ms) Gaussian peaks.

$$f_{\mathrm{ex}}\,(h\nu) = \; f_{\mathrm{1s}}\,(h\nu) + f_{ms}\,(h\nu) \tag{3.3}$$

The advantage of this approach is that special attention can be given to the 1s excitonic peak. For confined systems, like the layered perovskites, the 1s excitonic peak has been observed to show an asymmetric peak shape.[191] Hence, two distinct broadening terms, $\sigma_{\mathrm{ex},1}$ and $\sigma_{\mathrm{ex},2}$ need to be used to characterize each side of the peak, with $\sigma_{\mathrm{ex},2} \geq \sigma_{\mathrm{ex},1}$ being associated with the high-energy side. In addition to the asymmetry, a strong exciton-lattice coupling of the 1s excitonic peak needs to be taken into account. It can be quantified by an additional dielectric confinement factor, denoted as b_{D}. More details on these corrections can be found in a recent study.[191,192] In the case of three-dimensional perovskites, the asymmetry of the 1s excitonic peak and its enhancement due to dielectric confinement didn't need to be taken into account.

$$f_{\mathrm{1s}}\,(h\nu) = 4\pi \cdot \; (E_{\mathrm{B}})^{3/2} \cdot \frac{1}{\sqrt{2\pi \cdot \sigma_{\mathrm{ex}}^2}} \cdot \; e^{-\frac{1}{2}\cdot\left(\frac{h\nu-(E_{\mathrm{g}}-E_{\mathrm{B}})}{\sigma_{\mathrm{ex}}}\right)^2}, \text{where } \begin{cases} h\nu \leq E_{\mathrm{g}} - E_{\mathrm{B}}, \sigma = \sigma_{\mathrm{ex},1} \\ h\nu > E_{\mathrm{g}} - E_{\mathrm{B}}, \sigma = \sigma_{\mathrm{ex},2} \end{cases} \tag{3.4}$$

All other excitonic peaks can then be described as a sum of Gaussian peaks with broadening σ_{ex}, where $\sigma_{\mathrm{ex}} = \sigma_{\mathrm{ex},1}$ in the case of an asymmetric 1s excitonic peak.

$$f_{ms}\left(h\nu\right) = \sum_{m=2}^{11} b_{\mathrm{D}} \cdot \frac{4\pi \cdot \left(E_{\mathrm{B}}\right)^{3/2}}{m^3} \cdot \frac{1}{\sqrt{2\pi \cdot \sigma_{\mathrm{ex}}^2}} \cdot \; e^{-\frac{1}{2}\cdot\left(\frac{h\nu - E_{\mathrm{x}m}}{\sigma_{\mathrm{ex}}}\right)^2}, \text{where } E_{\mathrm{x}m} = \frac{E_{\mathrm{g}} - E_{\mathrm{B}}}{m^2} \tag{3.5}$$

The continuum of states f_c can be modelled using a square-root function, which equals zero below the bandgap. To take the strong coulombic interactions of free charge carriers in a solid state lattice into account, one can use the Sommerfeld factor ($SF = \frac{2\pi \cdot x}{1 - e^{-2\pi \cdot x}}$).[193] Hence

$$f_{\mathrm{c},0}\left(h\nu\right) = \frac{2\pi \cdot x}{1 - e^{(-2\pi \cdot x)}} \cdot \sqrt{h\nu - E_{\mathrm{g}}}, \text{where } h\nu > E_{\mathrm{g}}, \; x = \sqrt{\frac{E_{\mathrm{B}}}{h\nu - E_{\mathrm{g}}}} \tag{3.6}$$

is a good estimation for the continuum of states. To include additional effects, like the influence of energetic disorder in the vicinity of the bandgap, it is necessary to introduce an additional broadening factor. In this case, the square-root function is augmented by a normalised Gaussian with a broadening parameter σ_{c}

$$b = \frac{\frac{1}{\sqrt{2\pi \cdot \sigma_{\mathrm{c}}^2}} \cdot e^{-\frac{1}{2}\cdot\left(\frac{h\nu}{\sigma_{\mathrm{c}}}\right)^2}}{\int_0^{\infty} \frac{1}{\sqrt{2\pi \cdot \sigma_{\mathrm{c}}^2}} \cdot e^{-\frac{1}{2}\cdot\left(\frac{h\nu}{\sigma_{\mathrm{c}}}\right)^2} d(h\nu)} \tag{3.7}$$

so that the continuum of states can then be modelled as

$$f_{\mathrm{c}}\left(h\nu\right) = \left(b * f_{\mathrm{c},0}\right)\left(h\nu\right) \tag{3.8}$$

Computationally, **Equations 3.6 to 3.8** are challenging, because they need to be modelled via convolution of the square-root function and broadening factor taking energetic disorder into account. The fitting therefore depends strongly on both σ_{c} and the fitting window in eV. To overcome this issue, both can be fixed and then changed manually to assess their impact on the overall fitting and the extracted parameters. For the data shown in **Chapter 5**, both both σ_{c} and the fitting window were manually changed by ± 1 meV for the $FA_{0.9}Cs_{0.1}PbI_3$ samples and ± 10 meV for the PEA_2PbI_4 samples. A better estimate for the exciton binding energy was then obtained by averaging four fits of the same dataset. The results are presented in **Chapter 5**.

The fitting algorithm was implemented in `python` (see **Appendix C** for details). The original code was written by Dr. Bernard Wenger (University of Oxford), but adapted for the work

presented in this thesis. Especially, the asymmetric excitonic 1s peak and the additional dielectric confinement factor needed to be implemented.

Estimation of Long-Range Mobility from Photo-Conductivity

A detailed description of the methodology and optimization is given in **Chapter 4**. The code was written in `python` and is shown in **Appendix C**.

PLQE

Under continuous illumination, the PLQE of a material can be estimated via **Equation 2.32**. It was calculated by solving the general recombination equation for the steady-state condition $\frac{dn}{dt} = 0$

$$0 = G - k_1 \cdot n_{\mathrm{ss}} - k_2 \cdot n_{\mathrm{ss}}^2 - k_3 \cdot n_{\mathrm{ss}}^3, \tag{3.9}$$

where G is the generation rate of the laser used and k_2 can be exchanged for $k_2 + \frac{k_{\mathrm{x}}}{n_{\mathrm{ss}}}$ to include excitonic behaviour. The equation was solved in `python` using the `root`-function from the `scipy.optimize` package. Then, the estimated steady-state carrier density n_{ss} could be used in **Equation 2.32** to calculate the PLQE. This approach was mainly used for the intensity-dependent PLQE. The code is shown in **Appendix C**.

Time-Resolved PL

General Considerations

The behaviour after pulsed excitation can be described using the continuity equation (**Equation 2.13**). There exists no analytical solution to the differential equation without several assumptions and approximations.

Analytical Solution to the Simplified Continuity Equation

Assuming fast charge carrier redistribution, $J(t, z)$ describing drift and diffusion of photo-excited charge carriers can be neglected. Additionally, the charge carrier generation rate $G(t, z)$ can be assumed to be a constant value at $t = 0$ ns for excitation pulses that are much shorter than the

charge carrier lifetime. Again, this assumption is valid for many metal halide perovskite materials. **Equation 2.13** then simplifies to

$$\frac{d\Delta n(t)}{dt} = R(t) = -k_1\Delta n(t) - k_2\Delta n(t)^2 - k_3\Delta n(t)^3 \tag{3.10}$$

where k_1, k_2 and k_3 are the to mono-, bi- and tri-molecular recombination processes, respectively and $\Delta n(t)$ is the photo-generated charge carrier density. Since negligible charge carrier redistribution is assumed, this equation is independent of z. For three-dimensional MHPs the k_3 rate is related to Auger recombination and has reported values between 10^{-27} and 10^{-29} $\mathrm{cm^6 s^{-1}}$. Under typical excitation densities reached during TRPL experiments (10^{13} to 10^{18} $\mathrm{cm^{-3}}$) the impact of Auger recombination is therefore also negligible. **Equation 3.10** can then be solved analytically. Multiple equivalent solutions have been reported, but in this thesis the one derived by Ohnesorge *et.al.* as been used[194]

$$PL_{\mathrm{norm}}(t) = B \cdot k_1 \cdot \frac{e^{-k_1 t}}{1 + \left(\frac{k_{2,\mathrm{eff}}}{k_1}\right) \cdot \Delta n_0 \cdot (1 - e^{-k_1 t})}, \tag{3.11}$$

where B is a scaling parameter, Δn_0 is the excitation density and $k_{2,\mathrm{eff}}$ is an effective, bi-molecular recombination rate. The latter is impacted by recombination and hence the escape probability of photons generated, as well as exciton formation. k_1 can be estimated with high accuracy by fitting the TRPL transients globally for different Δn_0 and sharing the parameters between them. The implementation of this model in `python` is summarized in **Appendix C**. It is worth noting that the parameter B is absolutely crucial for this model to fit typical TRPL data and that it cannot be shared between data sets for the global fitting. The reason for this is that this simple model assumes negligible early-time processes such as charge carrier redistribution and the impact of the excitation pulse width.

Numerical Simulation of the Simplified Continuity Equation

The fitting problems of the analytical model can be reduced, by directly modelling **Equation 2.13**, while assuming charge carrier redistribution to be negligible ($J(t,z) \approx 0$). The resulting differential equation is then again independent of z. In this approach, the generation rate $G(t,z)$ needs to be included to allow charge carrier generation during the numerical simulation of the

differential equation. It can be approximated as a Gaussian profile centered around $t = 0$. The resulting differential equation reads

$$\frac{d\Delta n(t)}{dt} = \frac{1}{\sigma_{\mathrm{ir}} \cdot \sqrt{2\pi}} \cdot e^{-\frac{1}{2}\cdot\left(\frac{t}{\sigma_{\mathrm{ir}}}\right)^2} - k_1\Delta n(t) - k_2\Delta n(t)^2 \tag{3.12}$$

where σ_{ir} is the width of the instrument response in time and Auger recombination is assumed to be negligible. σ_{ir} is related to the full-width at half-maximum broadening (σ_{FWHM}) via

$$\sigma_{\mathrm{ir}} = \frac{\sigma_{\mathrm{FWHM}}}{2 \cdot \sqrt{2 \cdot \ln(2)}} \tag{3.13}$$

In the case of the TRPL setup (see **Section**) used in throughout this work the σ_{FWHM} of the instrument response is approx. 400 ps (the laser excitation peak width is $<$ 100 ps). To solve **Equation 3.12** it was set to the time resolution of the data set. Using this model to globally fit a set of intensity-dependent TRPL transients is only possible, if the first 10 to 20 ns of the decay are neglected. This indicates that there are still some early-time effects apart from the impact of the excitation pulse width that are not described by this model. In a first instance these missing effects can be approximated by adding another exponential decay, here called 'additional early-time decay' (etd). It is added to the normalized solution of **Equation 3.12** in order to simulate the measured TRPL intensity as

$$PL_{\mathrm{norm}}(t) = (1 - A_{\mathrm{etd}}) \cdot \Delta n_{\mathrm{norm}}(t)^2 + A_{\mathrm{etd}} \cdot e^{-\frac{t}{\tau_{\mathrm{etd}}}} \tag{3.14}$$

where A_{etd} is a scaling factor for the additional early-time decay and τ_{etd} is the corresponding lifetime. It should be noted that this corresponds to **Equation 3.11** in the limit of $\frac{t}{\tau_{\mathrm{etd}}} = 0$, where $(1 - A_{\mathrm{etd}})$ becomes then equivalent to the scaling factor B in the analytical solution. Even though the physical nature of τ_{etd} is unknown here, it can be useful to extract the characteristic lifetime τ_{etd} for the underlying early-time processes. In the case of excitonic materials, such as two-dimensional systems, the early-time annihilation of excitons will dominate the TRPL transients as shown in more detail in **Chapter 5**. It should be re-emphasized here that underlying early-time processes leading to this additional decay are not defined for this model and strongly depend on the material composition and thin film morphology. Processes such as early-time trap filling, charge carrier redistribution, exciton annihilation, charge transfer processes, sample inhomogeneity or

the effects of reabsorption may all lead to similar results. The implementation of this model algorithm in `python` is shown in **Appendix C**.

Bayesian Inference

The limitations mentioned so far, including the problem of over-fitting and non-identifiability of the models, can be overcome by using Bayesian inference. This is the scope of **Chapter 6**, so it won't be detailed here. In short, Bayesian inference can be used to estimate a probability distribution for each parameter that best describes the experimental data set. The `pymc` (PyMC version 5.0) package was used in `python` (the code is shown in **Appendix C**) to do the inference part and the parameter space was explored using a Markov-Chain Monte-Carlo (MCMC) algorithm from the same package.[195] The MCMC algorithm used was Metropolis-Hastings running 10 chains in parallel with 10000 samples. The algorithm was run on a ThinkStation P620 (to allow parallel sampling of 10 chains) with a AMD Ryzen^{TM} Threadripper^{TM} PRO 5975WX Processor (3.60 GHz up to 4.50 GHz). A typical run with the optimized conditions shown in **Chapter 6** took < 2 hours.

CHAPTER

LONG RANGE MOBILITY OF THREE-DIMENSIONAL METAL HALIDE PEROVSKITES

4

The mobility of charge carriers is a fundamental property of semiconductor materials. Many different methods have reported widely varying charge carrier mobilities for metal halide perovskites, such as $MAPbI_3$. After pulsed photo-excitation and measurement of photo-conductivity using non-contact or contact techniques, mobilities are often estimated using transient methods that assume an initial charge carrier population. Early-time recombination and the exciton-to-free-carrier ratio make it difficult to precisely determine the free-carrier population following photo-excitation using transient methods that operate on timescales of nanoseconds to milliseconds. By taking into account both effects, transient photo-conductivity measurements can be used to estimate lateral, long-range charge carrier mobilities across a wide range of photo-excitation densities. Long-range mobilities between 0.3 and 6.7 $cm^2\,V^{-1}\,s^{-1}$ are calculated for $FA_{0.83}Cs_{0.17}Pb(I_{0.9}Br_{0.1})_3$, $(FA_{0.83}MA_{0.17})_{0.95}Cs_{0.05}Pb(I_{0.9}Br_{0.1})$, and $MAPbI_3$ polycrystalline thin films. The findings highlight the critical role that processing plays in determining the long-range mobility of polycrystalline thin films.

Some parts of the work presented in this chapter are adapted with permission from:

Jongchul Lim & Manuel Kober-Czerny, Yen-Hung Lin, James M. Ball, Nobuya Sakai, Elisabeth A. Duijnstee, Min Ji Hong, John G. Labram, Bernard Wenger and Henry J. Snaith, Long-range charge carrier mobility in metal halide perovskite thin-films and single crystals via transient photo-conductivity,
Nature Communications **2022**, 13, 4201.

4.1 INTRODUCTION

In order to further improve the performance of metal halide perovskite-based optoelectronic devices, such as light emitting diodes (LED), photovoltaic devices (PV), transistors or photodetectors, it is crucial to understand their long range optoelectronic properties and how these change in different carrier density regimes.[10,196–198] As introduced in **Chapter 2**, the mobility is determined by the interaction of charge carriers with the solid state lattice. Alongside other parameters, like light absorption, charge carrier lifetime, and photo-luminescence quantum efficiency it is an important material property and needed to understand the charge transport behaviour at different internal charge carrier densities.[95,138,197,199–203] It must be acquired carefully. For instance, for $MAPbI_3$, the archetypical metal halide perovskite composition, the reported mobility values span three orders of magnitude (see **Figure 4.1**).[17,40,95,199,204–210]

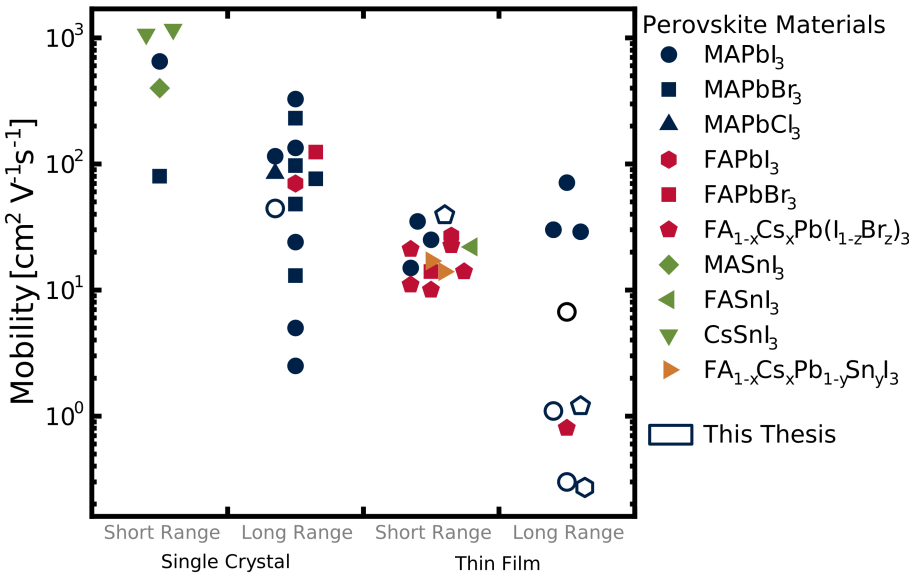

Figure 4.1: Overview of sum-mobility ($\Sigma\mu$) values reported in literature for common perovskite single crystal or thin film materials. For single crystals, the methods to obtain the mobility include OPTP or Hall measurement for short-range mobility and TPC, TRMC, SCLC or ToF for long-range mobility. For thin film samples the short-range mobility was measured only via OPTP and the long-range mobility via TPC, TRMC, SCLC or ToF. If only one of the two mobilities was reported (electrons or holes), its value was doubled for the plot. The perovskite materials include: $MAPbI_3$ (17, 40, 95, 204–210), $MAPbBr_3$ (95, 207, 211, 212), $MAPbCl_3$ (213), $FAPbI_3$ (214, 215), $FAPbBr_3$ (214, 215), $FA_{1-x}Cs_xPb(I_{1-y}Br_y)_3$ (36, 216, 217), $MASnI_3$ (218), $FASnI_3$ (219), $CsSnI_3$ (220, 221), and $FA_{1-x}Cs_xPb_{1-y}Sn_yI_3$ (222).

Some of these discrepancies are caused by real differences in the morphology of the material, for instance highly defective polycrystalline films versus improved-crystallinity thin-films or single crystals.[17,39,204,205] Other variations arise from the length scales probed (i.e. few nm versus many microns or mm), and from inappropriate application of measurement techniques based on false assumptions.[199,223]

There are a variety of techniques that can be used to determine the mobility of a material. They can generally be separated into transient, steady-state, contact, and non-contact methods.[39,95,122,201,202] Common approaches include, field effect transistors (FETs), space-charge-limited-current (SCLC), Hall-effect or time-of-flight (ToF) measurements, the charge extraction by linearly increasing voltage (CELIV) method, optical-pump terahertz-probe spectroscopy (OPTP), and time-resolved microwave conductivity (TRMC). In **2.2** metal halide perovskites were introduced as semiconductors with a soft, ionic lattice with mobile ionic species. Hence, not all of the above mentioned methods can be used with perovskites.

It is difficult to estimate bulk mobilities using FETs, due to the mobile ion displacement in the channel and the semiconductor-dielectric interface affecting electronic charge transport. Further, FETs can only operate in higher charge carrier density regimes, which exceed the operating conditions for most semiconductor devices.[148,202] The SCLC method assumes that there is an electric field across the semiconductor that is only influenced by the electronic space charge. However, in metal halide perovskites the ionic charge may also contribute. In recent years, pulsed SCLC measurements have been developed to decouple the ionic contribution to the electric field from the electronic one and allow extraction of bulk mobilities.[211,223,224] Both FETs and SCLC determine electronic transport via charge injection, which are dark methods and cannot determine photo-excited charge carrier transport properties. This is also true for Hall effect measurements and especially detrimental there, as the perovskite material is too resistive in the dark.[31] Additionally, the Hall effect measurements are steady-state measurements, so the redistribution of ionic species under the influence of an external magnetic field can also have an impact. Recent advances using a photo-Hall effect method with a pulsed AC magnetic field makes this approach more feasible.[225] Similarly, there are different CELIV methods, like dark-, photo- and injection-CELIV.[52,226,227]

In all cases, the charge transport is assessed via transient charge extraction. As such, the method can be influenced by interfacial effects. There are some methods, that can only determine the mobility of photo-excited species, such as the ToF measurement. There, photo-excited charge carriers move through an electric field that is assumed to be constant across the semiconductor layer, which is not true, when mobile ions are present.[95] All of the methods mentioned so far require the sample to be electronically contacted.

OPTP is a purely optical method and can determine bulk mobility values under high excitation density regimes.[39,200,228] The mobility is thereby estimated from the photo-conductivity peak within the first few tens of ps after excitation. Even though it is not straightforward to estimate the diffusion length at these time scales and carrier densities, a "short range" of 10s on nanometers is assumed.[138,186] In contrast, TRMC typically pulsed excitation with pulse widths in the nanosecond range.[229–231] As such, the photo-excited charge carriers can drift in the electric field generated via the microwaves for 100s or even 1000s of nanometers, making this a "long-range" method. The method only works reliable at lower internal charge carrier density regimes, because early-time recombination can occur during the long excitation pulses and skew the results.[172,231] Both OPTP and TRMC are non-contact methods.

In this project, transient photo-conductivity (TPC) was used to determine the long range bulk mobility of different metal halide perovskite compositions (see Chapter 3 for details). The method is most similar to TRMC, but the electric field is generated using electronic contacts and a battery. In addition, a post-treatment of the data is introduced that corrects for the early-time recombination during the long excitation pulses as also observed in TRMC. This allows for a more accurate estimation of the long range mobility. This parameter can then be linked to other material properties, such as the thin film morphology and quality, by comparing different fabrication routes for similar metal halide perovskite compositions.

4.2 PART I - METHOD DEVELOPMENT

The methodology presented here was co-developed by Dr. Bernard Wenger (University of Oxford) and Dr. Jongchul Lim (Chungnam National University).

Measuring the Sample Photo-Conductivity

To estimate the mobility of photo-excited charge carriers for a particular pump modulation frequency and laser fluence, the transient photo-conductivity can be measured using a pulsed laser, a voltage source, and a digital oscilloscope.[149,197,232,233] In this work, transient photo-conductivity (TPC) was measured using the home-built setup as described in **Chapter 3** in more detail. In short, the sample on a glass or quartz substrate was photo-excited with a 10 Hz, pulsed laser with a pulse full-width-half-maximum (FWHM) of 3.74 ns. The pulsed excitation was used as a trigger for a digital oscilloscope and was attenuated in order to illuminate the sample at different laser fluences. The illumination was uniform over the entire area of the sample (0.25 cm^2) leading to a homogeneous charge carrier density in between the two in-plane, gold electrodes. The photo-excited charge carriers were probed via a weak electric field (< 0.01 V µm^{-1}) induced by a DC voltage (V_{app}), which led to a displacement current within the electric circuit. This current could be measured as a voltage change across a terminal resistor (R_T, typically 1 kΩ), which was in parallel with a digital oscilloscope. A simplified schematic of the setup is shown in **Figure 4.2(a)**. Using the measured voltages at the oscilloscope (V_{osc}), the photo-conductivity σ_{photo} can be calculated as

$$\sigma_{photo}(t) = \frac{V_{osc}}{R_T \cdot (V_{app} - V_{osc})} \cdot \frac{s}{d \cdot l} \tag{4.1}$$

where s is the spacing between electrodes, l is the electrode length and d is the sample thickness.[13,197,234] The measures s and l for the different electrode designs used in this work are summarized in **Table 3.2**. A typical set of acquired photo-conductivity transients is shown for an $FA_{0.9}Cs_{0.1}PbI_3$ (here FACsPbI) thin film in **Figure 4.2(b)**.

The film was photo-excited with a 510 nm (2.4 eV) laser to generate charge carrier densities (excitation densities) of 9×10^{14} cm^{-3} to 3×10^{17} cm^{-3}.

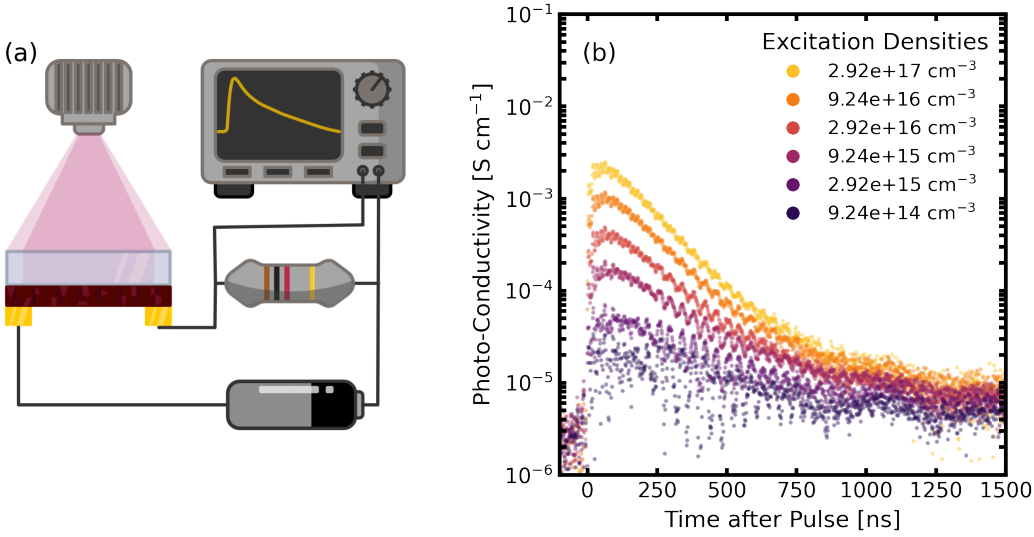

Figure 4.2: Measurement of transient photo-conductivity (TPC). (a) The simplified experimental setup is shown schematically. A 10 Hz pulsed laser with a 3.74 ns pulse width illuminates the sample through the substrate. Two in-plane, gold electrodes are connected to a battery (V_{app}) to generate a small electric bias of < 0.01 V µm^{-1}. It is important to note that the voltage per distance during typical solar cell characterization is on the order of 2 V µm^{-1}, which is roughly three orders of magnitude larger than the TPC bias voltage. The circuit is closed via a 1 kΩ resistor (R_T). The displacement current induced by the photo-excited charge carriers is measured as a voltage change across R_T with an oscilloscope. (b) The obtained transient photo-conductivity decays are shown for a $FA_{0.9}Cs_{0.1}PbI_3$ poly-crystalline perovskite thin film. The excitation densities are 9.2×10^{14} to 2.9×10^{17} cm^{-3} from dark to light color.

Even though photo-excited charge carriers can diffuse in z-direction (towards opposite side of illumination), the applied electric field between the electrodes results in charge carrier drift in the plane of the film. Due to the high aspect ratio between the in-plane electrode spacing (300 μm) and film thickness (approx. 500 nm), a negligible impact of the z-direction diffusion was assumed. In order to test this assumption, a sample of $FA_{0.83}Cs_{0.17}Pb(I_{0.9}Br_{0.1})_3$ (here: FACsPbIBr) was illuminated from both sides and the change in voltage across the terminal resistor was recorded with the oscilloscope (V_{osc}). The resulting voltage transients are shown in **Figure 4.3(a)**. It can be observed that both illumination directions yield the same V_{osc} signal. A small, but negligible difference in peak voltage shortly after the excitation pulse could be accounted for by a difference in reflectance from the two surfaces. Hence, the effect of charge carrier re-distribution was assumed to be negligible here.

Next, the electric field between the in-plane electrodes was investigated, as it is assumed to be uniform in **Equation 4.1**. This assumption needed to be verified, since metal halide perovskites contain mobile ionic species, which can screen the electric field, as was introduced in **Chapter 2.2**. To quantify the surface potential between the in-plane electrodes while subjecting them to an externally applied DC bias voltage, Dr. Jongchul Lim (Chungnam National University) used a Kelvin probe. The magnitude of the bias voltage used in this experiment was comparable to that in the TPC measurements (< 0.01 V µm^{-1}). The surface potential was measured as a function of the distance between the electrodes, both in the presence and absence of continuous-wave illumination. As seen in **Figure 4.3(b)** the potential exhibited a nearly linear decrease between the electrodes, suggesting a relatively homogeneous electric field throughout the entire channel spacing. It should be acknowledged that the presence of light did result in a slight decrease in potential in the vicinity of the electrodes. However, this reduction accounted for less than 10% of the overall potential drop across the channel. Consequently, its impact on the estimated photoconductivities was expected to be minimal. Thereby the use of **Equation 4.1** was validated for the TPC method presented in this chapter.

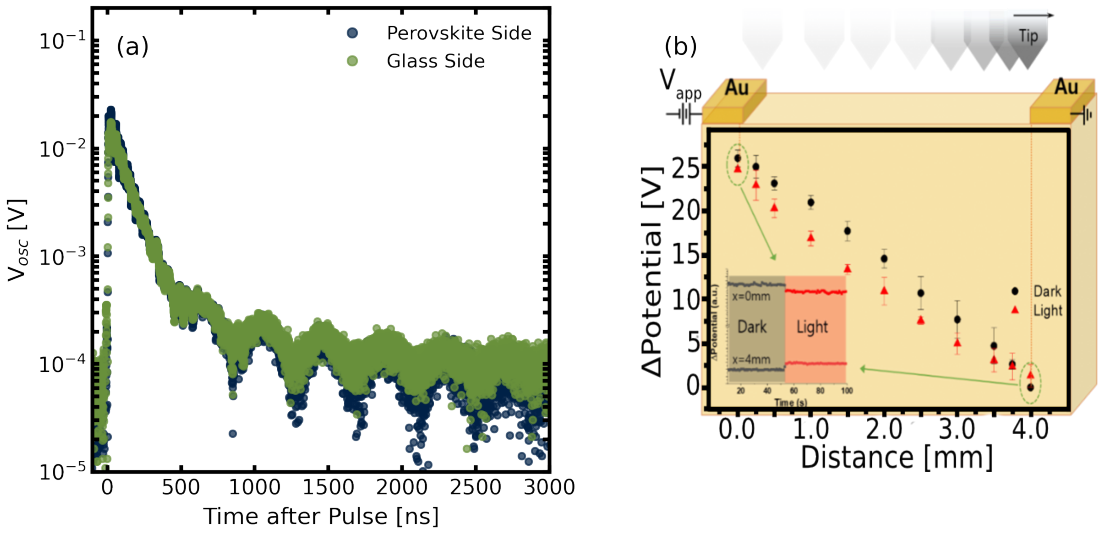

Figure 4.3: (a) V_{osc} is shown for a FACsPbIBr thin film illuminated from the perovskite side and glass side. (b) The surface potential differences of an FACsPbIBr thin between the in-plane electrodes under the externally applied bias voltage (< 0.01 V µm^{-1}) with and without light are shown. The Kelvin probe measurement was performed by Dr. Jongchul Lim (Chungnam National University).

The calculated photo-conductivity shows three distinct, transient features after pulsed photo-excitation: (1) an increase at $t = 0$; (2) a maximum value at $t = t_{\mathrm{R}}$; followed by (3) a long decay. It can be observed that the increase is not step-like, but rather a slow rise of photo-conductivity. This behaviour has been described before as being linked to the RC-time of the circuit, where R is R_{T} - the terminal resistor at the oscilloscope - and C_{geo} is the geometric capacitance of the sample architecture.[232,233] The impact of R_{T} was investigated first to make sure the TPC methods probes the changes in charge carrier density over time and not just a slow discharging of the capacitance. An FACsPbIBr sample was therefore illuminated with a 470 nm (2.64 eV) excitation wavelength and V_{osc} was measured for different R_{T} of 50 Ω, 1 kΩ, 10 kΩ, 50 kΩ, 100 kΩ and 250 kΩ. The results are shown in **Figure 4.4(a)**. The initial voltage increase after photo-excitation changed drastically with R_{T}: as R_{T} increased, the initial voltage change slowed down and the maximum reached voltage increased. The latter is expected from $V_{\mathrm{osc}} = R_{\mathrm{T}} \cdot I_{\mathrm{displ.}}$. As aforementioned, the rise-time scales with the RC-time, where C_{geo} is related to the capacitor formed by the perovskite (as a dielectric material) and the in-plane electrodes. A circuit schematic is shown in **Figure 4.4(b)** to illustrate this effect. Immediately after photo-excitation, a net current generated by the charge carriers can be measured as V_{osc} across R_{T}. The initial current is high and used to charge the capacitor, which is the sample in contact with the electrodes. Since this initial current is regulated by R_{T}, the charging time will also change with R_{T}. This effect is observed as the rise time. After the capacitor has charged, the charge carriers will still move inside the electric field, but the resulting current will be lower now and is known as the displacement current $I_{\mathrm{displ.}}$.

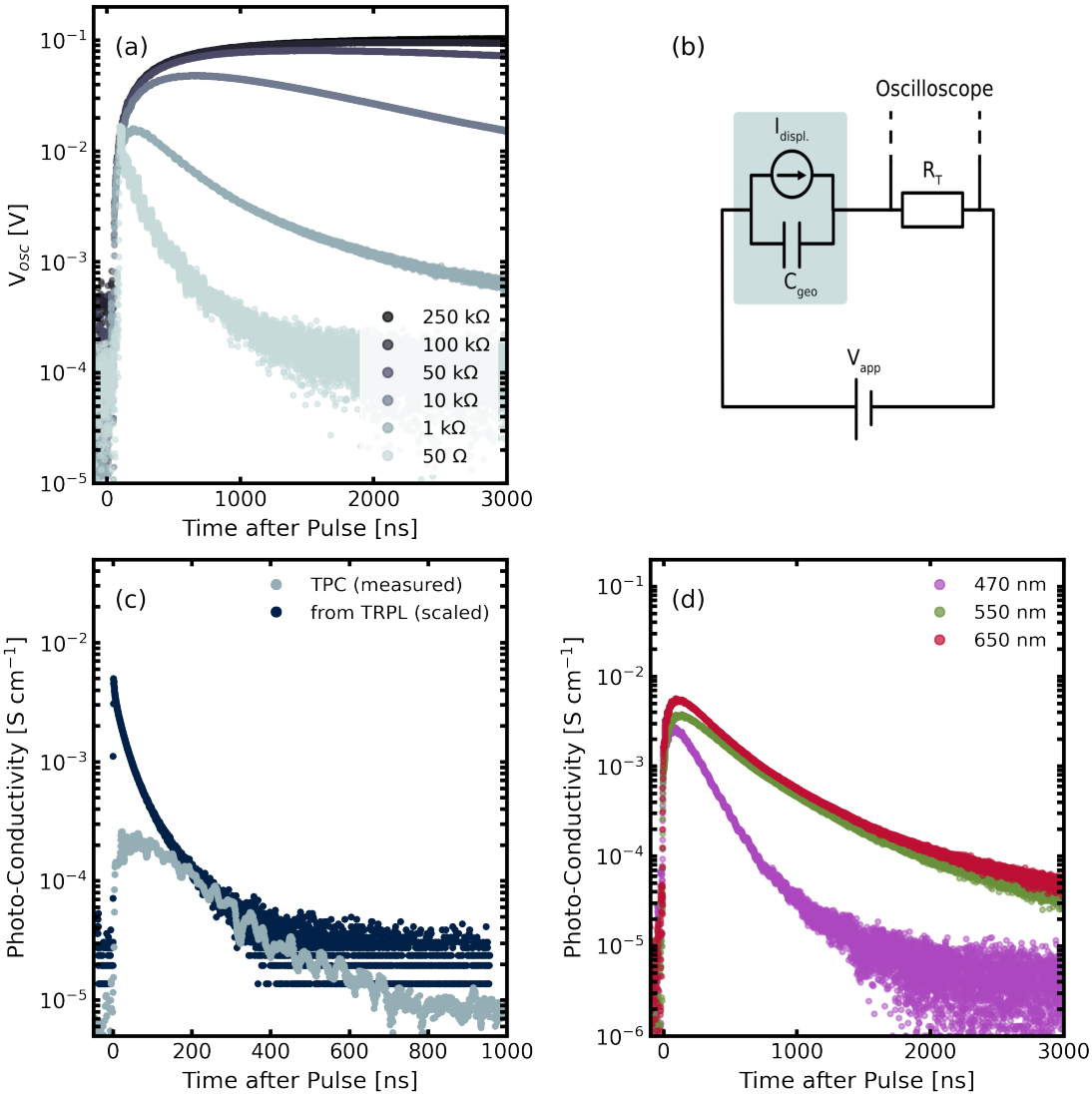

Figure 4.4: (a) V_{osc} is shown for different R_{T} between 50 Ω and 250 kΩ. (b) A simple circuit diagram, which can illustrate the RC behaviour observed in the TPC experiment. The coloured rectangle indicates properties of the sample. (c) The measured photo-conductivity of a FACsPbI sample is compared to a scaled TRPL decay trace of the same sample for an excitation density of approx.1×10^{16} cm^{-3}. (d) The photo-conductivity of a FACsPbI sample is shown for different excitation wavelengths of 470 nm (2.64 eV), 550 nm (2.25 eV) and 650 nm (1.91 eV), which resulted in excitation densities of 2.3×10^{16}, 2.5×10^{16} and 1.4×10^{16} cm^{-3}, respectively. (b) was adapted from 232.

It is interesting to observe that only the 50 Ω and 1 kΩ measurements show a reduction in V_{app} at the timescales probed here, even though the capacitor has been charged and the resulting current should be stabilized. The decay is most likely related to charge carrier recombination within the perovskite material, but before that can be investigated it first needs to be understood which R_{T} can be used for the TPC experiment.

For this, a TPC decay trace of a FACsPbI sample is compared to a TRPL decay trace of the same sample. Here, two things need to be kept in mind: 1) the fluences used during the TPC experiment are typically much higher than the ones used for the TRPL, so only the highest fluences used during the TRPL measurement overlap with the lowest fluences used during the TPC measurements. 2) The TRPL probes the photo-luminescence of the material, which scales with n^2 for a three-dimensional perovskite, as described in **Chapter 2**. The photo-conductivity in contrast scales with n. Thus, the square-root of the TRPL decay needed to be used to compare both data sets. The TPC decay measured through the 1 kΩ resistor is shown alongside a measured and then scaled TRPL decay in **Figure 4.4(c)**. A good agreement between the two could be seen, especially for times later than approx. 150 ns. It is worth acknowledging that an R_{T} of 50 Ω agreed even better with the TRPL decay, but the resulting V_{osc} is too low for most samples to allow for reproducible measurements. This is especially true, when low excitation fluences are used.

Lastly, the impact of the excitation wavelength on the resulting photo-conductivity was investigated by illuminating the FACsPbI sample with 470 nm (2.64 eV), 550 nm (2.25 eV), and 650 nm (1.91 eV) excitations. The resulting photo-conductivity transients are shown in **Figure 4.4(d)**. To make a comparison between the different excitations possible, it is important to accurately determine the excitation carrier density from the absorption properties of the film and the laser fluence (see **Equation 2.11**). Interestingly, the trace measured at 470 nm decays significantly faster than the ones at 550 and 650 nm, which could be due to the shorter penetration depth of the illumination making the technique more surface sensitive. It can also be noted that the photo-conductivity at t = 0 ns is more similar between the different excitation wavelengths. It should be re-emphasized here that the decay of the photo-conductivity can stem from three mechanisms: 1) the discharging of the geometric capacitor, 2) charge extraction at the electrodes, and 3) the recombination of charge carriers. 1) was shown to be negligible, when a smaller R_{T} of $\leq$ 1 kΩ was used. 2) The distance travelled by photo-generated charge carriers during the measurement period can be estimated from the drift current equation (**Equation 2.15**. For a mobility of 10 $\mathrm{cm^2\,V^{-1}\,s^{-1}}$ and an electric field of 0.01 $\mathrm{V\,\mu m^{-1}}$ a drift velocity of 10 $\mathrm{\mu m\,\mu s^{-1}}$ can be estimated. Due to the relatively large width of the channel (300 μm), a minimal amount of charge carrier sweep-out was expected during the decay period of a few hundred nanoseconds.

Thus, the primary source of the decaying photo-conductivity signal could be attributed to the recombination of charge carriers within the perovskite material. It is noted that the dropping mobility with increasing carrier density was previously attributed to higher order recombination processes, such as bi-molecular and Auger recombination, during the ns laser excitation.[230,235] However, no corrective measures were undertaken.

Accounting for early-time recombination and free-carrier fraction

The mobility can be estimated from σ_{photo} via **Equation 2.21**, which allows the extraction of $\Sigma\mu$, the sum-mobility of electrons and holes (assuming that $n = p$). It is important to note that **Equation 2.21** needs to be expanded here as:

$$\sigma_{\text{photo}}(t) = e \cdot n(t) \cdot \phi\Sigma\mu \tag{4.2}$$

where ϕ is the fraction of absorbed photons which generate mobile, free charge carriers. The reason for this is that excitonic species will be unaffected by the electric field and hence do not contribute to the measured displacement current. Here, ϕ will also be used to account for recombination during the duration of the excitation pulse.

A common assumption made during pulsed excitation is that all absorbed photons result in the generation of a free electron-hole pair at t = 0 ns. While this may be true, it can only be correlated to the photo-luminescence response (as seen in **Figure 4.4(c)**), where the laser pulse width is < 1 ns, but not for the TPC experiment, where a pulse width of approx. 4 ns is used and the RC-time of the sample further induces an initial build-up of photo-conductivity. To overcome this discrepancy and make the estimations of $\Sigma\mu$ more accurate, it was necessary to simulate the transient behaviour of ϕ during the initial 100 to 200 ns of the TPC experiment. In order to achieve this, the recombination properties of the perovskite material needed to be understood in detail first.

Early-time recombination can be accounted for by considering the radiative band-to-band and Auger recombination rates for the perovskite absorber layer, assuming a simple continuity equation without diffusion as:

$$\frac{dn(t)}{dt} = G(t) - k_{1,\text{nr}} \cdot \Delta n - k_{2,\text{rad}} \cdot \Delta n^2 - k_{\text{aug}} \cdot \Delta n^3 \tag{4.3}$$

similar to **Equation 2.13** shown before. Both the bi-molecular and Auger rate constants are intrinsic material properties and can often be obtained from other studies. Trap-assisted recombination, via the Shockley-Read-Hall mechanism, exhibits a strong dependence on the film fabrication process. Hence, the estimation of the recombination rate for the films employed in the photo-conductivity measurements holds considerable importance. All recombination parameters could be estimated by combining the time-resolved photo-luminescence (TRPL) of the sample with an intensity-dependent photo luminescence quantum efficiency (intensity-dependent PLQE) measurement. In **Figure 4.5(a)** a set of TRPL traces measured at different excitation fluences are shown alongside a global fit to the analytical model to **Equation 4.3** (see **Chapter 3**), in which $k_{1,\mathrm{nr}}$ and $k_{2,\mathrm{rad}}$ were shared parameters and the impact of k_{aug} was assumed to be negligible. It was important to ignore the first 25 ns during the fitting, which can be ascribed to early-time effects such as carrier redistribution. For the FACsPbIBr films employed here, the resulting $k_{1,\mathrm{nr}}$ was $(1.51 \pm 0.03) \times 10^6$ s^{-1} from the analytical model. While there is a high confidence in the accuracy of $k_{1,\mathrm{nr}}$ due to its impact on the tail of the TRPL decay, $k_{2,\mathrm{nr}}$ needed to be further refined using the intensity-dependent PLQE data shown in **Figure 4.5(b)**, where **Equation 2.32** was used. $k_{1,\mathrm{nr}}$ was fixed to the value obtained from the global fit to the TRPL traces and no non-radiative, bi-molecular recombination term was used. The parameters extracted were 3.4×10^{-11} $\mathrm{cm}^3\,\mathrm{s}^{-1}$ and 9.2×10^{-28} $\mathrm{cm}^6\mathrm{s}^{-1}$ for $k_{2,\mathrm{rad}}$ and k_{aug}, respectively.

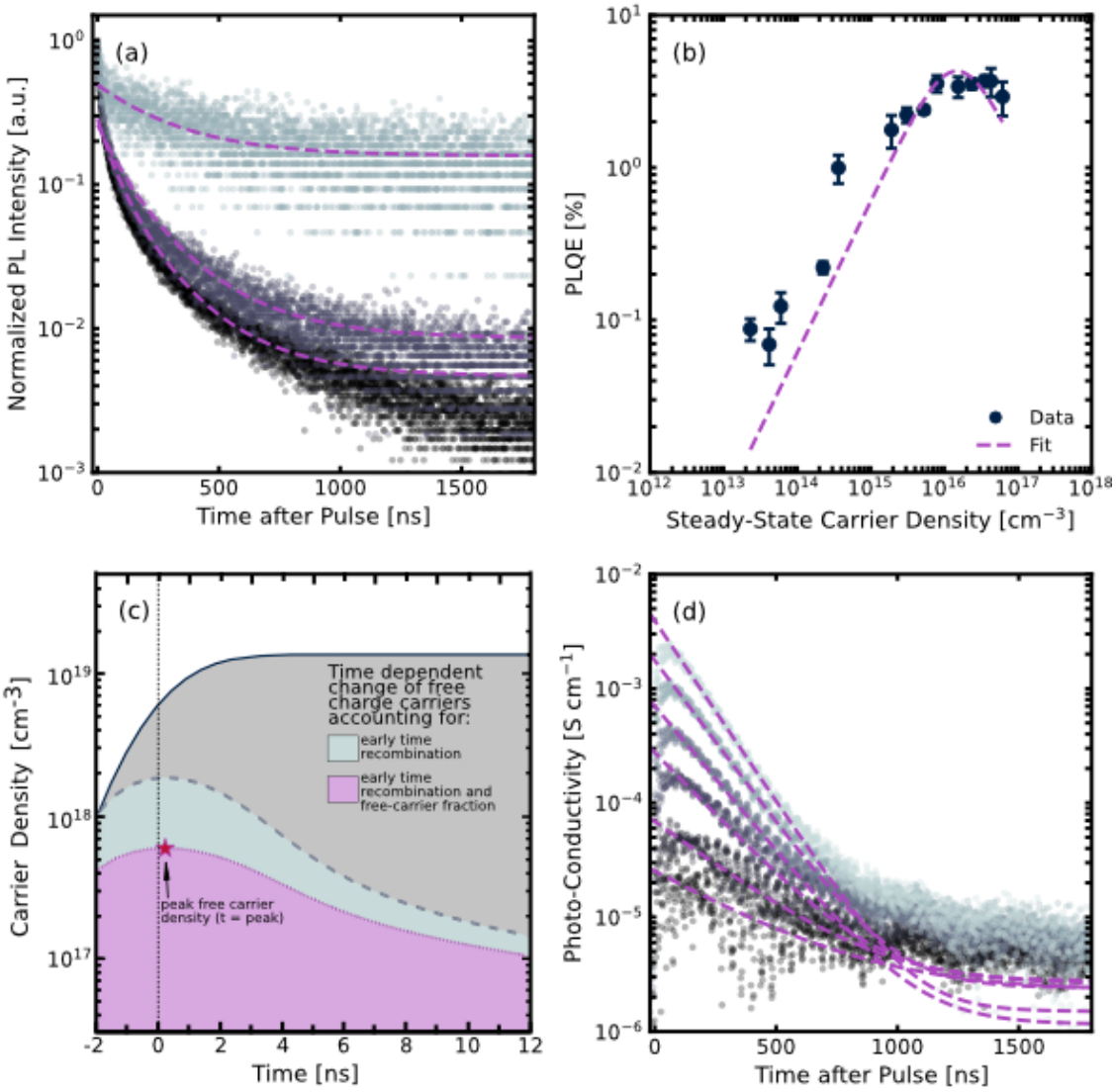

Figure 4.5: (a) TRPL transients are shown for fluences of 9.5×10^9, 5.4×10^{10} and 1.3×10^{11} cm^{-2}. The data normalized to the number of PL counts at $t = 0$ ns and was fitted globally with the analytical model described in **Chapter 3**. (b) The result of an intensity-dependent PLQE measurement is shown alongside a fit to **Equation 3.9**. (c) A schematic illustrating the effect of the charge carrier density for early-time recombination and exciton formation. An excitation density of 1.4×10^{19} cm^{-3} was used. A peak free carrier density can be obtained shortly after the photo-excitation pulse. (d) Photo-conductivity transients as obtained from the TPC measurement for a FACsPbIBr sample. The excitation fluences range from 7.4×10^{10} to 2.4×10^{13} cm^{-2}. The decays were fitted individually to a mono-exponential decay function.

Now, **Equation 4.3** could be used to simulate the transient charge carrier density with $G(t)$ now being a Gaussian peak pulse with a σ_{FWHM} of 3.74 ns. The resulting build-up of charge carrier density is shown in **Figure 4.5(c)** as a dark blue line. In addition to the early-time recombination, exciton formation can become important at higher charge carrier densities, even for low exciton binding energies of 10 meV (see **Figure 2.6**. It is important to mention here again that the Saha equation (**Equation 2.8**) is an equilibrium equation. It was used in this work to

simulate transient behaviour, which is valid under the assumption that the thermal equilibrium between free charge carriers and excitons is reached faster than recombination. The exciton binding energy (E_B) for the studied FACsPbIBr thin-film was estimated to be approx. 11 meV by fitting the absorption profile to the Elliot model (see **Chapter 3**). The obtained $\phi(t)$ was then be multiplied with $n(t)$ to acquire the transient free charge carrier density. In **Figure 4.5(c)** the simulated free carrier density for 1). Only early-time recombination ($E_B = 0$) and 2) early-time plus exciton formation ($E_B > 0$) are shown alongside the initial, simulated $n(t)$. It can be seen that in both cases, the free charge carrier density has a maximum value shortly after t = 0. This is the result of two competing mechanisms: As the charge carrier density is initially low, the exciton fraction and recombination are also low. As the charge carrier density increases, the exciton fraction and recombination increase, resulting in a lower ϕ. Hence, there is a maximum ϕ, at which most charge carriers have not recombined yet and the specific charge carrier density results in a low, relative exciton population.

It was now possible to estimate a more accurate $\phi\Sigma\mu$ with the knowledge of ϕ. The simplest approach to obtain $\phi\Sigma\mu$ is to estimate $\sigma_{\text{photo}}(t = 0)$, as the charge carrier density at this point is known to be $n(t = 0)$, the excitation density. As the radiative efficiency of perovskites is generally high for excitation energies above the bandgap (see **Chapter 2.4**), it can be assumed that each absorbed photon initially results in the creation of an electron-hole pair, denoted as ϕn. Then, the maximum ϕ extracted from the simulations described above is used to estimate $\Sigma\mu$. In **Figure 4.5(d)** the TPC decays for the FACsPbIBr sample are shown together with individual, mono-exponential fits that are used to extrapolate $\sigma_{\text{photo}}(t = 0)$.

Calculating Mobility from Photo-Conductivity Transients

In order to showcase the TPC technique, polycrystalline FACsPbI thin films were fabricated. The measurement of σ_{photo} was conducted using several excitation fluences on a single device. For each excitation fluence, a $\sigma_{\text{photo}}(t = 0)$ was extracted, as well as a $\sigma_{\text{photo}}(t = \phi_{\text{max}})$ and $\sigma_{\text{dark}}(t < 0)$. It should be noted that measurements were started after the sample had been illuminated for a full minute. This time frame was chosen so that a steady state could be reached, which is required if photo doping or light soaking effects are present.[197,236] The resulting data was then used to

create a plot of σ_{photo} as a function of charge carrier density. This is shown in **Figure 4.6(a)**. It shall be emphasized that for $\sigma_{\text{photo}}(t = 0)$ and $\sigma_{\text{dark}}(t < 0)$ the carrier density is $n(t = 0)$, the excitation density, but for $\sigma_{\text{photo}}(t = \phi_{\text{max}})$, it is $\phi_{\text{max}} n(t = 0)$, the maximum free carrier density. It can be observed that $\sigma_{\text{photo}}(t = 0)$ increased monotonically with charge carrier density, but the increase is sub-linear at higher carrier densities. This was corrected for $\sigma_{\text{photo}}(t = \phi_{\text{max}})$, which now showed a linear dependence on the carrier density, as expected from **Equations 4.2** and **2.21**. The dark conductivity $\sigma_{\text{dark}}(t < 0)$ also increased, but its impact on the total conductivity was negligible here. The small increase of $\sigma_{\text{dark}}(t < 0)$ with increasing charge carrier density could be ascribed to a build-up of charge carriers, due to a slow discharging of the electrodes.[237] This effect becomes more pronounced at higher charge carrier densities. It is noted that, over the range of excitation densities studied here, a super-linear increase in peak photo-conductivity with increasing excitation density was not observed at any point. This implied that the low charge density regime where trap filling may play a role was already surpassed.

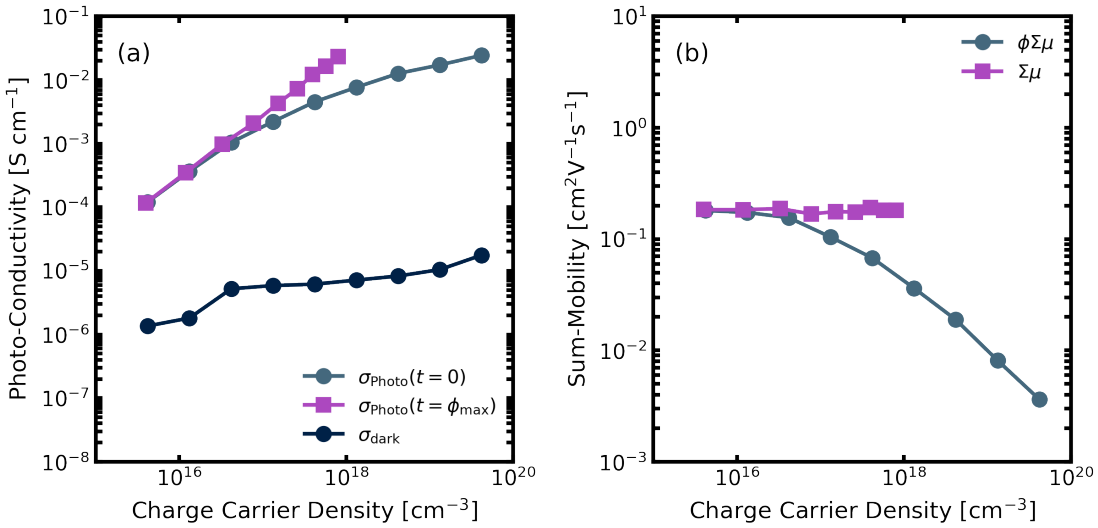

Figure 4.6: (a) All conductivities extracted from the TPC experiment are shown for a FACsPbI sample: $\sigma_{\text{photo}}(t = 0)$ was obtained from extrapolating the photo-conductivity decays to t=0, $\sigma_{\text{photo}}(t = \phi_{\text{max}})$ was obtained at the time point where the maximum free carrier fraction was reached, and $\sigma_{\text{dark}}(t < 0)$ is the median conductivity signal before the photo-excitation at t=0. (b) The mobility values estimated from the TPC experiment are shown for the FACsPbI sample: $\phi\Sigma\mu$ is the uncorrected mobility, by assuming $\phi = 1$, and $\Sigma\mu$ is the mobility after correcting for early-time recombination and exciton formation.

In **Figure 4.6(b)** the corresponding $\phi\Sigma\mu$ from $\sigma_{\text{photo}}(t = 0)$ and $\Sigma\mu$, where ϕ was taken into account are shown as a function of carrier density. Again, the carrier density $\phi\Sigma\mu$ is the excitation

density, while for $\Sigma\mu$, it is the free charge carrier density. It can be seen that the estimated $\phi\Sigma\mu$ values ranged from 3×10^{-3} to 0.2 $\mathrm{cm^2\,V^{-1}\,s^{-1}}$, spanning several orders of magnitude. Clearly, the estimated $\phi\Sigma\mu$ for the FACsPbI films is dependent on the excitation density, exhibiting a monotonous decrease as the excitation density increases. This behaviour is a result of the decrease in ϕ, due to recombination and exciton formation, rather than a decrease in long-range mobility. As a result, the corrected $\Sigma\mu$ was invariant across a wider range of charge carrier densities. The fact that the method presented here could sufficiently correct for the decrease in $\phi\Sigma\mu$ with increasing charge carrier density supported the notion that early-time recombination and exciton formation are the most relevant mechanisms limiting the free carrier density. It is important to note that the exciton to free-carrier branching ratio must be included in the corrections in order to observe a sum-mobility that is completely invariant with charge carrier density. It is also worth noting that recombination and exciton formation have not been accounted for in previous measurements of electronically contacted, transient mobility measurements. This indicates that the previously found apparent correlation between carrier mobility and charge density may be a methodological problem.[149]

Improving the Mobility Analysis

Having established that recombination and exciton formation are the dominating mechanisms that reduce ϕ, it was now possible to investigate the effect of over- or under-estimating parameters. In this case, specifically $k_{2,\mathrm{rad}}$ is full of uncertainties, which stem from the fact that intensity-dependent PLQE requires the use of a $k_{2,nr}$ and that the escape probability P_{esc} can further the observed $k_{2,\mathrm{rad}}$. Hence, $k_{2,\mathrm{rad}}$ was modulated for the same FACsPbI thin film as shown in **Figure 4.6(a)** and **(b)** between 10^{-13} and 10^{-6} $\mathrm{cm^3\,s^{-1}}$. Then, the above protocol was used to estimate $\Sigma\mu$ over a range of free carrier densities. The results are presented in **Figure 4.7(a)**, where the round data points show the uncorrected $\phi\Sigma\mu$. Clearly, $k_{2,\mathrm{rad}}$ has a significant impact on the shape of the charge carrier density-dependent $\Sigma\mu$: as $k_{2,\mathrm{rad}}$ increases, the change in $\Sigma\mu$ with increasing charge carrier densities is reduced. For an under-estimated $k_{2,\mathrm{rad}}$, $\Sigma\mu$ is also "under-corrected", while for an over-estimated $k_{2,\mathrm{rad}}$, the resulting $\Sigma\mu$ is over-estimated significantly. In the latter case, $\Sigma\mu$ is once again dependent on the charge carrier density.

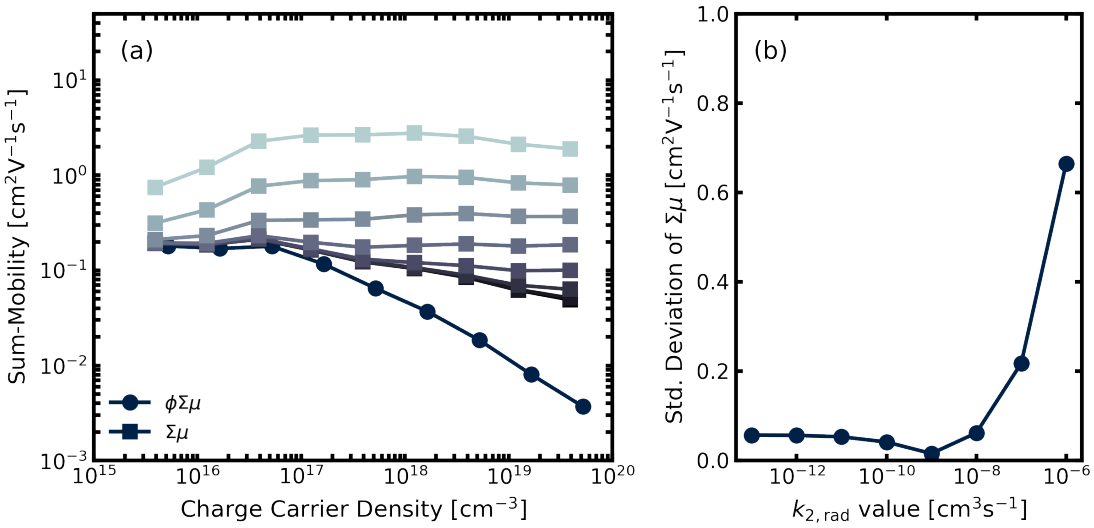

Figure 4.7: (a) The impact of changing $k_{2,\mathrm{rad}}$ on the resulting $\Sigma\mu$ is shown. The circles indicate the uncorrected mobility data, whereas the square data points indicate the correction where a lighter color corresponds to a higher $k_{2,\mathrm{rad}}$ value. (b) The standard deviation of the extracted mobility values is plotted as a function of $k_{2,\mathrm{rad}}$ values to reveal a minimum around 10^{-9} $\mathrm{cm}^3\,\mathrm{s}^{-1}$.

The standard deviation of all estimated $\Sigma\mu$ was used to quantify the accuracy of ϕ. In other words, if the standard deviation is smallest, the recombination should be fully taken into account and the resulting $\Sigma\mu$ should be independent of the charge carrier density. Thus, in **Figure 4.7(b)** the standard deviation of $\Sigma\mu$ is shown as a function of $k_{2,\mathrm{rad}}$. It becomes apparent that a minimum standard deviation is achieved for a $k_{2,\mathrm{rad}}$ of approx. 10^{-9} $\mathrm{cm}^3\,\mathrm{s}^{-1}$. This value is comparable to the intrinsic $k_{2,\mathrm{rad}}$ reported for metal halide perovskites.[81] In addition to $k_{2,\mathrm{rad}}$, $k_{1,\mathrm{nr}}$ can be estimated from the lowest-fluence measurement, which was shown to overlap with the TRPL decays in **Figure 4.4(c)**. As such, ϕ as well as $\Sigma\mu$ can be accurately determined without prior knowledge of $k_{1,\mathrm{nr}}$ or $k_{2,\mathrm{rad}}$ for materials which can be described by similar recombination dynamics as the three-dimensional perovskites shown here. Then, the TPC measurement can be used to also estimate the intrinsic $k_{2,\mathrm{rad}}$. Only the exciton binding energy is needed as an input as it significantly influences the outcome and is discussed in more detail in **Chapter 5**.

4.3 PART II - RESULTS AND DISCUSSION

Estimation of $\Sigma\mu$ from Wavelength-Dependent Transient Photo-Conductivity

Using the TPC measurements together with the established estimation of ϕ, the long-range mobility for the mixed cation mixed halide FACsPbIBr thin films could be assessed for different excitation wavelengths of 470 nm (2.64 eV), 550 nm (2.25 eV), and 650 nm (1.91 eV). The resulting $\phi\Sigma\mu$ as well as $\Sigma\mu$ are shown side-by-side in **Figure 4.8(a)** to **(c)**. Despite the fact that the photo-conductivity decays for this sample under these three excitation wavelengths was different in **Figure 4.4(d)**, the resulting $\Sigma\mu$ were in good agreement with one another. This coincidence of $\Sigma\mu$ for all three wavelengths encourages the claim that the diffusion of charge carriers in z-direction (throughout the film thickness) was negligible during the TPC experiment, as only charge carriers drifting parallel to the substrate will significantly contribute to $I_{\text{displ.}}$. The long-range, in-plane mobility for FACsPbIBr was found to be in the range of 1.5 $\text{cm}^2\,\text{V}^{-1}\,\text{s}^{-1}$ over a wide range of carrier densities and across all excitation wavelengths.

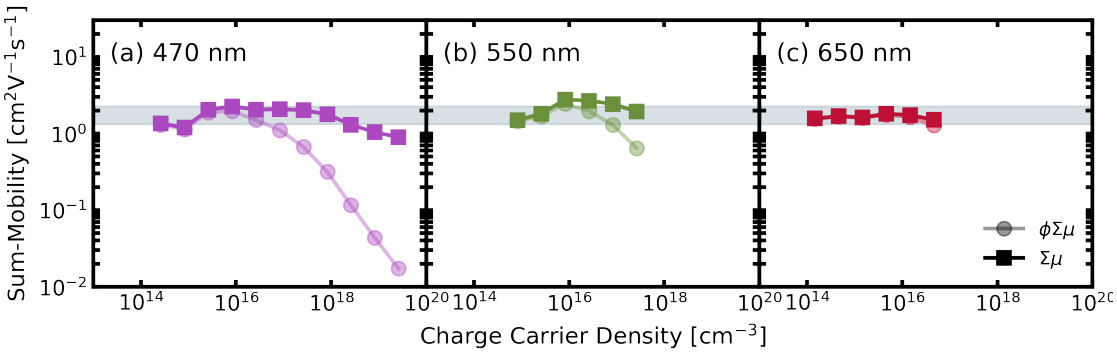

Figure 4.8: The extracted $\phi\Sigma\mu$ and $\Sigma\mu$ are shown for a FACsPbI sample under different excitation wavelengths of (a) 470 nm (2.64 eV), (b) 550 nm (2.25 eV), and (c) 650 nm (1.91 eV). All show a $\Sigma\mu$ value of approx. 1.5 $\text{cm}^2\,\text{V}^{-1}\,\text{s}^{-1}$.

Influence of composition and processing upon charge carrier mobility

In addition to the FACsPbIBr composition, the impact of sample processing and other perovskite compositions was investigated.

Perovskite films of $MAPbI_3$ were fabricated using three different fabrication processes. Additionally, mixed cation, mixed halide perovskite films, commonly employed in the perovskite research field, were prepared. The first set of samples consisted of single cation films based on MA, where $MAPbI_{3-x}Cl_x$ was coated using dimethylformamide (DMF) as the solvent (referred to as the DMF route).[38] The second set of samples involved $MAPbI_3$ thin films prepared from the acetonitrile solvent with the addition of methylamine (referred to as the ACN/MA route).[32] The third set of samples were $MAPbI_3$ films prepared from DMF as the solvent, using lead-acetate as the lead source precursor with the addition of hypophosphorous acid (referred to as the DMF/HPA route).[34] All $MAPbI_3$ samples were prepared by Dr. Nobya Sakai (University of Oxford). Two additional types of samples are included in the study: the previously measured $FA_{0.83}Cs_{0.17}Pb(I_{0.9}Br_{0.1})_3$ (referred to as FACsPbIBr) and $(FA_{0.83}MA_{0.17})_{0.95}Cs_{0.05}Pb(I_{0.9}Br_{0.1})_3$ (referred to as FAMACs). These samples were prepared using a mixed solvent of DMF and dimethylsulfoxide (DMSO) through the "anti-solvent quenching" technique. All mixed-cation samples were prepared by Dr. Yen-Hung Lin (University of Oxford). The specific deposition procedures for each sample can be found in **Chapter 3**. The resulting long-range mobilities $\Sigma\mu$ are shown in **Figure 4.9(a)**.

Compared to the DMF route film ($MAPbI_{3-x}Cl_x$), all other films showed lower long-range mobilities. The DMF/HPA route film, which has smaller crystalline grains, has the lowest mobilities of all the MA-based single cation samples fabricated by different methods.[34] The mixed cation samples demonstrated greater $\Sigma\mu$ for the FACs samples compared to the FAMACs film. The $\Sigma\mu$ of all perovskite films was nearly invariant with free charge carrier density, with average values of 6.7 ± 0.5, 1.1 ± 0.1, 0.3 ± 0.1, 0.60 ± 0.04, and $1.2\pm0.1\ cm^2\,V^{-1}\,s^{-1}$ for DMF, ACN/MA, DMF/HPA routes, FAMACs, and FACs films, respectively. Notably, it was observed that the long-range mobility of MA-single cation samples via different processing techniques, varied by approx. an order of magnitude. These variations may stem from trapping/detrapping processes, grain-boundary scattering, and charge at grain borders, along with other factors such as perovskite composition, grain sizes, crystallinity, and crystal orientation.[32,34,149,238,239] Ongoing research is targeted to-

wards determining which material qualities are most significantly affecting the long-range charge carrier transport properties.

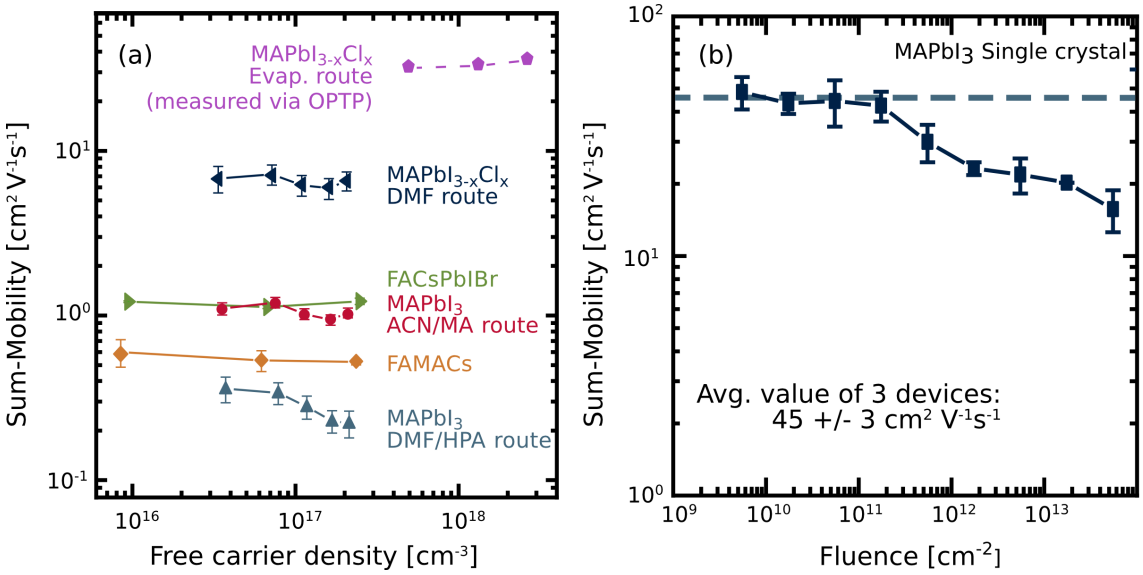

Figure 4.9: Mobility of metal halide perovskite thin-films prepared via different methodologies as a function of free-carrier density. For comparison, the mobilities of $CH_3NH_3PbI_{3-x}Clx$ (evaporation route) determined via non-contact OPTP are reproduced from 240. (b) Mobility of $MAPbI_3$ thin single crystals as a function of excitation fluence. All errors shown are statistical errors from three different devices.

These results represented the most accurate estimate of lateral, long-range charge carrier mobility within these perovskite thin films. It is a useful parameter to further the understanding of optoelectronic applications that rely on long-range charge transport.

The question of whether poly-crystalline thin films of metal halide perovskites exhibit properties similar to macroscopic single crystals, or if single crystals indeed possess superior attributes such as increased charge carrier mobility and diminished defect densities, was still unclear. One issue was that it was usually not possible to compare these different types of material using the same approach. As discussed in the introduction of this chapter, this can significantly impact the results obtained from such comparison. The effects of ionic diffusion and redistribution also introduce uncertainties into electronic measurements of single crystals, such as space-charge-limited-current.[211,223] The lateral mobility of a prepared $MAPbI_3$ single crystal was estimated using the TPC measurement technique in order to compare the long-range charge carrier mobility of single crystals and polycrystalline thin films.[183,184] The single crystal samples were produced by Elisabeth Duijnstee (University of Oxford). In-plane electrodes with roughly 3 mm channel lengths were deposited onto large area $MAPbI_3$ single crystals that were multiple millimetres in

thickness. The excitation fluence was varied over four orders of magnitude using TPC measurements, and the uncorrected plot of $\phi\Sigma\mu$ versus excitation fluence is shown in **Figure 4.9(b)**. Due to the large difference in distance between the in-plane electrodes and the thickness of the thin film, it was safe to assume a uniform out-of-plane charge density while ignoring the effect of carrier diffusion in the vertical (z) direction when dealing with thin films. On the other hand, it was necessary to account for charge carrier diffusion in the z-direction in order to correct the free-carrier population subsequent to photo-excitation in thick single crystals. This is particularly relevant in cases where photo-excitation predominantly takes place near a single surface, as it may reduce the observed bi-molecular recombination rate.[56,175] This was however outside the scope of this work. It was shown in **Figures 4.6** and **4.7** that bi-molecular recombination and the exciton fraction could be neglected at sufficiently low excitation fluence. Hence, below a certain fluence of 10^{11} cm^{-2}, the free carrier fraction ϕ was assumed to be close to 1, indicating that all charge carriers existed as free carriers. This allowed the estimation of the $\Sigma\mu$ of a $MAPbI_3$ single crystal as 45 ± 3 $cm^2\,V^{-1}\,s^{-1}$. This average is based on the TPC readings of three separate crystals (see Table 3.1). The results showed that further improvements were needed for polycrystalline thin films to match the long-range charge carrier mobility of single crystals.

As a further indication of the potential improvement in charge carrier mobility achievable for polycrystalline films, OPTP mobility values, which probe the short-range mobility within $MAPbI_3$ thin films, were found to be in the range of 10 to 30 $cm^2\,V^{-1}\,s^{-1}$, a full 2 orders of magnitude higher than the long-range mobility determined for state-of-the-art FACsPbIBr and FAMACs films.[17,39,240] One representative measurement of an evaporated $MAPbI_{3-x}Cl_x$ sample assessed via OPTP is shown in **Figure 4.9(a)** alongside the results from the TPC analysis.

4.4 SUMMARY AND OUTLOOK

In this chapter, the coupling of TPC measurements with post-measurement corrections has been presented as a powerful technique to assess lateral, long-range mobility. For this, a simulation of the transient free carrier density was performed, taking into account early-time recombination and the free-carrier versus exciton population. With the increased understanding gained in this chapter, only the exciton binding energy is needed as an input parameter in order to apply this method to any conventional semiconductor. The obtained mobility values in metal halide perovskite films were shown to be insensitive to changes in carrier density within the range relevant to most optoelectronic devices. The long-range mobility in $MAPbI_3$, $FA_{0.83}Cs_{0.17}Pb(I_{0.9}Br_{0.1})_3$, and $(FA_{0.83}MA_{0.17})_{0.95}Cs_{0.05}Pb(I_{0.9}Br_{0.1})_3$ thin films was evaluated with the presented methodology. Based on the composition and method of thin-film preparation, the calculated mobilities ranged from 0.3 to 6.7 $cm^2\,V^{-1}\,s^{-1}$, which was significantly lower than the estimated long-range sum-of-mobilities for $MAPbI_3$ single crystals, which was 45 ± 3 $cm^2\,V^{-1}\,s^{-1}$.

The crystal measurements, as well as comparisons to OPTP measurements, suggested that current "state-of-the-art" polycrystalline perovskite absorber materials still have significant room for improvement in terms of their long-range charge carrier transport properties. Notably, the importance of long-range charge carrier mobility, which has not been clearly derived until now, is most pronounced in optoelectronic device structures that require carrier transport over longer distances. Understanding the impact of long-range charge carrier mobility on the electronic properties of different devices and device configurations, as well as the parameters that can be tuned to increase this mobility, will need to be investigated in the future. Long-range mobilities in metal halide perovskites are postulated to approach the values of single crystals once the key limiting factors, such as charge trapping and scattering at grain boundaries, have been understood and can be controlled. The approach presented here is expected to be of particular interest for estimating the long-range charge carrier mobility in semiconductor materials where the long-range mobility is expected to vary considerably in comparison to the short-range mobility, as observed

in quantum dots, carbon materials, semiconducting organic molecules, and metal oxides, among others.

It is important to highlight that the long-range mobility obtained via this method is measured in the lateral direction (parallel to the substrate), which is not the direction of charge transport in a photovoltaic device. There is thus far no conclusive evidence showing if the vertical mobility in a perovskite thin film is closer to the short-range mobility as obtained from OPTP, or the longer-range mobility measured via the methodology presented here. This will be part of **Chapter 6**, where diffusion simulations indicate the importance of the long-range mobility on the vertical transport properties as well.

CHAPTER

CHARGE TRANSPORT PROPERTIES IN TWO-DIMENSIONAL METAL HALIDE PEROVSKITES

5

Layered, two-dimensional perovskites hold promise for enhancing the stability of metal halide perovskite thin film devices, yet their charge transport characteristics still remain largely unexplored. In this chapter, the sum of electron and hole mobilities ($\Sigma\mu$) in PEA_2PbI_4, a two-dimensional perovskite, is examined using two different photo-conductivity measurements, which are sensitive to short-distance and long-distance transport processes, respectively. A remarkable long-range mobility of 8.0 ± 0.6 $cm^2\,V^{-1}\,s^{-1}$ is determined. This mobility is found to be tenfold higher than that of a stereotypical three-dimensional perovskite, $FA_{0.9}Cs_{0.1}PbI_3$. These results are compared to optical-pump terahertz probe conductivity measurements to reveal that the two-dimensional, polycrystalline thin films exhibit single-crystal-like charge transport properties. It is then revealed in follow-up work that the long-range order of the two-dimensional materials strongly impacts their properties. Simultaneously, more and more evidence is shown, which supports the claim that the two-dimensional perovskite materials are not solely excitonic materials, but rather that their optoelectronic properties are governed by the interplay of free charge carriers and excitonic species. The results shown here offer fundamental insights into the class of two-dimensional, layered perovskites that will ultimately help to improve optoelectronic device performance.

The work presented in this chapter has in parts been adapted with permission from:
Manuel Kober-Czerny, Silvia G. Motti, Philippe Holzhey, Bernard Wenger, Jongchul Lim, Laura M. Herz, Henry J. Snaith, Excellent Long-Range charge carrier Mobility in 2D Perovskites, *Advanced Functional Materials* **2022**, 32, 2203064.

5.1 INTRODUCTION

Despite the rapid improvement of the PCE, industrial application of metal halide perovskite solar cells is still inhibited by their inherent instability under various environmental factors. Particularly, under operating conditions (heat and light), significant losses in PCE can be observed over time.[44,241,242] The soft lattice of the perovskite material leads to a multitude of degradation pathways via intrinsic defects, photo- and heat-induced ion migration, and surface reconstruction. Therefore, it has become the focus of the perovskite research field to understand and mitigate these degradation pathways and hence improve the overall long-term stability of the resulting photovoltaic devices.

One common approach to enhance the stability of metal halide perovskite-based photovoltaic devices is the use of bulky, organic cations. They can be added to the perovskite precursor solution during fabrication to improve material quality via controlling the crystallization and film formation. This has been shown to improve the PCE as well as long-term stability.[243–245] In this case, the inverted, p-type-intrinsic-n-type (p-i-n) device architecture is often used. There light travels through the hole-transport layer first, before being absorbed by the perovskite material. The main stability improvement is thought to come from the enhanced crystallinity and perovskite material quality.[118,245] Another approach is to use the organic cations as a post-treatment to passivate the top-surface of the perovskite films. In that case, two-dimensional perovskite phases, as introduced in **Chapter 2**, can form. As a surface passivation, this layer not only protects against environmental influences by the steric nature of the cations, but may also induce the formation of a heterojunction between the three-dimensional perovskite and a wider bandgap, two-dimensional perovskite.[118] Most studies using this approach report devices in a regular, n-type-intrinsic-p-type (n-i-p) architecture.[118,246–250] In this structure, the wide bandgap, two-dimensional perovskite may act as an electron-blocking layer if it becomes too thick. Hence, passivating the hole-transporting side of an n-i-p device can both passivate that surface and reduce interfacial recombination with electrons leading to near-zero losses in open-circuit voltage.[166,247,251,252] The reduction of interfa-

cial electron trapping may aid long-term stability via the suppression of interface reactions with mobile ions.[248] The exact role of the two-dimensional phase in the improvement of the long-term stability is still debated, as it can also be explained by simply reducing the direct contact between the perovskite material and the contact layer, as has been observed in other passivation strategies.[253,254] Nevertheless, some of the highest reported PCEs in perovskite-based solar cells have used a two-dimensional perovskite passivation layer.[246,249]

Significant research effort is directed towards the use of p-i-n devices as well,. They still report the best long-term stability values for perovskite-based solar cells, due to the use of organic transport materials, which avoid redox reactions at typically employed TiO_2/SnO_2 bottom transport layer materials and mobile dopants in the HTM , such as Li^+.[255,256] In this architecture, significant effort is needed to achieve improved device efficiencies via use of chloride-based additives or controlled two-dimensional perovskite layer formation.[251,252,257]

If the two-dimensional perovskite layer does completely cover the surface, the charges in both architectures will have to travel through it to get to the electronic contacts. This interaction will be governed by the inherent characteristics of the two-dimensional perovskite layer and the properties of the bulky, organic cation. Due to the anisotropy of the two-dimensional system, it is generally accepted that the out-of-plane (here out-/in-plane correspond to the crystallographic planes) charge carrier transport and mobility of two-dimensional perovskites is much lower than the in-plane mobility.[116,258] When charge carriers in two-dimensional perovskites have to move between different crystallographic planes, the performance of photovoltaic devices can be reduced.[250] Indeed, it is commonly believed that the two-dimensional perovskite phases‘ ability to increase the stability of a three-dimensional perovskite comes at the expense of both the conductivity and mobility of carriers.[6,116,245] In contrast, an increase in mobility, in this case the mobility of free charge carriers in the two-dimensional plane, was predicted by early studies of layered tin-halide perovskites, despite their reduced conductivity.[259] New developments in film fabrication have allowed for more precise control over layer orientation, and in some cases, complete conversion into vertically oriented two-dimensional layers, which makes transport along the two-dimensional perovskite sheets possible in a direction normal to the substrate, opening up the possibility of vertical device architectures.[110,119,260,261] Since PEA_2PbI_4 (n = 1) is one of the most studied layered perovskites and thus allows for best comparison of the results, it was first

studied as a model system to better understand the charge carrier transport in two-dimensional perovskites. Solution-processed n = 1 thin-films are typically more oriented with their planes parallel to the substrate and are not subjected to the same phase impurity challenges as seen for n > 1 two-dimensional perovskites.[123,201,262–267] In early work, PEA_2PbI_4 is described as a dielectrically confined system with exciton binding energies of 230 meV.[130] In a recent diffusivity study of PEA_2PbI_4, highly mobile excitonic species were observed.[134] Concurrently, free-carrier behaviour has been observed and is under investigation: in a recent report, a polaron model is proposed to account for free carrier transport in PEA_2PbI_4.[136]

In this work, the in-plane mobility and photo-physical properties of some two-dimensional perovskites were investigated by measuring the lateral long-range and short-range photo-conductivity of highly oriented thin films. A better understanding of the generation and transport properties of free charge carriers in PEA_2PbI_4 over both length-scales was gained. The initial findings allowed consideration of possible ways to make two-dimensional perovskites in general more useful in optoelectronic device applications. One possibility is to change the electronic nature of the bulky spacer cation, which was investigated at the end of this work.
For this work, a simple fabrication method (see **Chapter 3**) was developed to produce phase-pure, highly oriented PEA_2PbI_4 thin films of high quality.

5.2 PART I - MOBILITY OF "FREE" CHARGE CARRIERS

Understanding Transient Exciton and Free Charge Carrier Behaviour

To begin the investigation, the optoelectronic properties of PEA_2PbI_4 were assessed first. This was necessary in order to accurately describe the behaviour of both excitonic and free-carrier-like species. The absorption properties were probed using absolute transmittance and reflectance measurements, as well as an estimate for the thin film thickness using a profilometer (see **Chapter 3** for details). The absorption coefficient $\alpha(h\nu)$ could then be calculated using **Equation 2.10** and the results are shown in **Figure 5.1** for $FA_{0.9}Cs_{0.1}PbI_3$ and PEA_2PbI_4. As introduced in **Chapter 2**, the absorption of the two-dimensional material is shifted towards higher energies and exhibits a strong characteristic peak near the absorption onset associated with exciton formation.[123,131,134] It is important to note again that thinner films of approx. 160 nm were needed to resolve the excitonic absorption peak.

Both absorption spectra could be fitted individually with the "Elliott model" (as described in **Chapter 3**) to estimate the exciton binding energy (E_B), as well as the electronic bandgap of the continuum of states for each material (distinct from optical or Tauc estimates of the absorption onset energy).[83] From this exciton binding energies of approx. 7 meV (lit.: 5.3 meV) for $FA_{0.9}Cs_{0.1}PbI_3$ (bandgap of 1.55 eV, lit.: 1.51-1.57 eV) and approx. 230 meV (lit: 193-230 meV) for PEA_2PbI_4(bandgap of 2.63 eV, lit.: 2.36-2.63 eV) could be estimated.[268–273] **Figure 5.1** shows the excitonic and continuum components of the Elliott fit alongside the measured data. It can be noticed that the fit diverges from the data a few hundred meV above the absorption onset. As mentioned in **Chapter 3** this is expected due to strong Coulomb interactions within the materials, which are not part of the Elliott model.

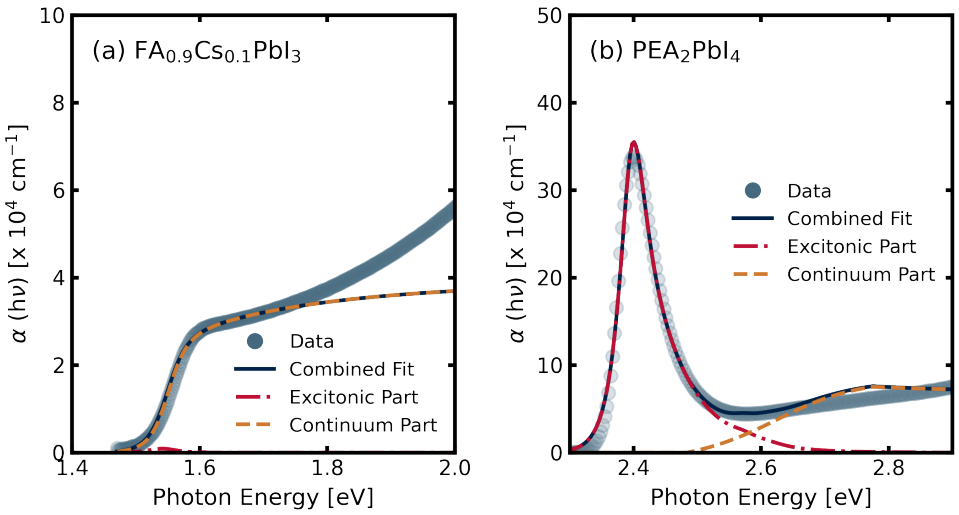

Figure 5.1: The absorption coefficients as obtained from total transmittance and reflectance measurements are shown for (a) $FA_{0.9}Cs_{0.1}PbI_3$ and (b) PEA_2PbI_4. For both, the Elliott model was used to fit the absorption onset and extract the exciton binding energy. The combined fit as well as the separated excitonic and continuum part are shown alongside the data.

Next, the recombination of photo-generated charge carriers was assessed via time-resolved photo-luminescence (TRPL) and intensity-dependent photo-luminescence quantum efficiency (intensity-dependent, external PLQE) measurements. In both experiments, the photo-luminescence (PL) was measured and physical models were used to extract information about the parameters related to recombination (k^*_{rad}, k_{nr}, and k_{x}, as introduced in **Chapters 2** and **3**). Therefore, it was important to first understand how the PL signal related to the charge carrier density. For this purpose, both materials were measured using a the TRPL setup. The maximum signal intensity scales linearly with the PL and is plotted as a function of excitation fluence in **Figure 5.2 (a)**. Since the photo-generated charge carrier density Δn also scaled linearly with the excitation fluence F (assuming negligible effects at the pico-second timescale), it allowed the extraction of factor b in the proportionality law

$$PL_{\mathrm{t=0}} \propto F^b \propto \Delta n^b \tag{5.1}$$

According to **Equation 2.22**, free-carrier recombination from intrinsic semiconductors with negligible equilibrium carrier concentration leads to $b = 2$, while pure excitonic recombination (as per **Equation 2.25**) results in $b = 1$. In **Figure 5.2 (a)** it can be observed that indeed PEA_2PbI_4 showed $b = 1$ behaviour indicative of the excitonic nature of the layered material. In contrast to

that, $FA_{0.9}Cs_{0.1}PbI_3$ showed a $b = 1.5$ behaviour. This behaviour had been previously observed in other three-dimensional perovskite thin films.[136,274] The explanation brought forward was polaron formation, as well as fast initial annihilation of a minority of excitons. For the work presented here, the exact mechanism of this was less important, since $b = 1$ behaviour was observed for PEA_2PbI_4 and the transient photo-conductivity (TPC) as well as terahertz spectroscopy (OPTP) could only probe the free-carrier mobility.

In **Figure 5.2 (b)**, the TRPL decays for both, $FA_{0.9}Cs_{0.1}PbI_3$ and the layered PEA_2PbI_4 are shown for a range of pulsed excitation fluences (notably the TCSPC pulse width is tens of ps, rather than ns for the TPC measurement). A stark difference in lifetimes between the two- and three-dimensional perovskites could be observed immediately: the three-dimensional material showed a long PL decay of a few hundred nanoseconds, which is indicative of mono-molecular, trap-assisted recombination dominating the PL dynamics. In contrast, the PL intensity of the two-dimensional material dropped by an order of magnitude within a few tens of nanoseconds. However, it still showed a significant PL signal after more than 200 ns, indicating the presence of longer-lived species. As mentioned in **Chapter 3**, during a TRPL experiment the generation rate G can be reduced to a constant generation of charge carriers at $t = 0$ ns and Auger recombination can generally be neglected at the fluences probed. The analytical model was used to fit TRPL data (see **Chapter 3**). A trap-assisted recombination constant $k_{1,\mathrm{nr}}$ as well as k^*_{rad} could be extracted. The resulting fits overlaid with the data are shown in **Figure 5.2 (b)** for all fluences. For $FA_{0.9}Cs_{0.1}PbI_3$, $k_{1,\mathrm{nr}}$ was determined to be 7.5×10^5 s^{-1}, while it increased to 6.3×10^6 s^{-1} for PEA_2PbI_4. As mentioned in **Chapter 2**, the mono-molecular exciton decay rate k_{ex} has a strong influence on k^*_{rad}, but cannot be disentangled from it through TRPL measurements.
To disentangle the two, intensity-dependent, external PLQE was measured for thin films of both materials. For $FA_{0.9}Cs_{0.1}PbI_3$ a monotonically increasing external PLQE up to a carrier density of 2×10^{16} cm^{-3} could be observed, while for PEA_2PbI_4, the thin films have an almost constant external PLQE of approx. 1%. This is a result of the excitonic nature of the PL emission as described previously, where the mono-molecular radiative recombination of excitons is insensitive to excitation fluence.[136,263] The data was fitted to **Equation 3.9** using a root-finding algorithm (see **Chapter 3** for details). To reduce the number of free parameters, k_{nr} was fixed to the

value obtained from the global TRPL fits and $k_x = 0$ s^{-1} for the three-dimensional perovskite $FA_{0.9}Cs_{0.1}PbI_3$. The resulting fits are shown alongside the data in **Figure 5.2 (c)**.

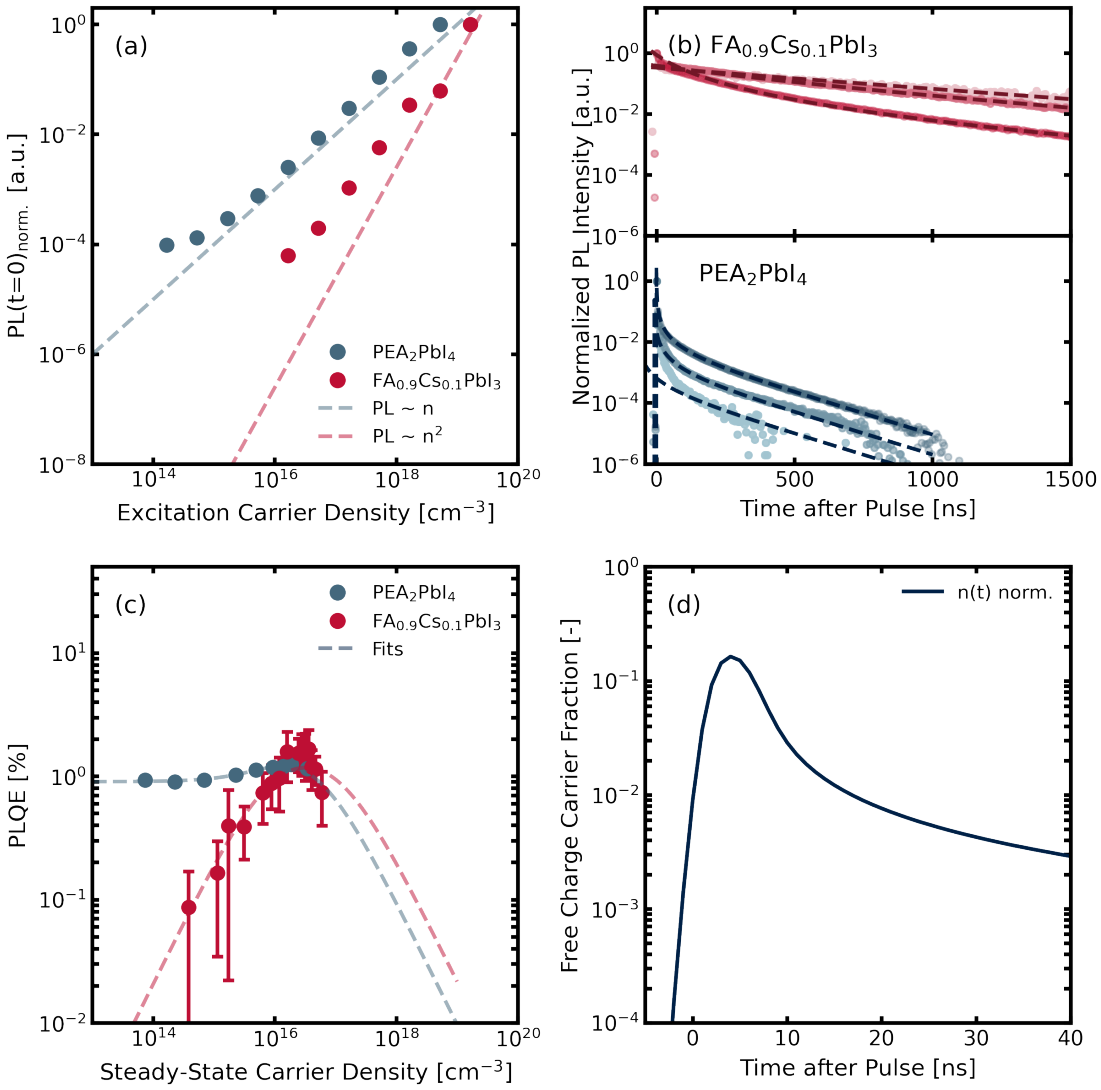

Figure 5.2: (a) The initial PL intensity after photo-excitation is shown as a function of excitation carrier density for both materials studied here. The dotted lines indicate the $PL \propto n$ and $PL \propto n^2$ behaviour. (b) TRPL transients of both materials are shown for three different fluences (light: 4.4×10^9cm^{-2} (2.2 nJ cm^{-2}), medium: 4.4×10^{10}cm^{-2} (22 nJ cm^{-2}), dark: 4.4×10^{11}cm^{-2} (220 nJ cm^{-2})). The data was normalized to the number of PL counts at $t = 0$ ns.(c) The intensity-dependent, external PLQE ($\eta_{QE,ext}$) for both materials is shown alongside a fit (dotted line) to extract the recombination parameters. (d) A representative, simulated evolution of n(t), the Saha fraction and ϕ during and after the 3.7 ns long pulse used during the TPC experiment. A maximum in ϕ is achieved after approx. 5 ns.

For $FA_{0.9}Cs_{0.1}PbI_3$ a $k_{2,rad}$ of 8.79×10^{-11} cm^3 s^{-1} and negligible k_{aug} of 7.22×10^{-28} cm^{6}s^{-1} were extracted. In contrast, for the PEA_2PbI_4 thin films $k_{2,rad}$ was determined as 3.3×10^{-10} cm^3 s^{-1}, k_{aug} as 10^{-32} cm^{6}s^{-1}, $k_{2,nr}$ as 2.5×10^{-8} cm^3 s^{-1}, and k_x as 7.4×10^5 s^{-1}. It is worth noting that the accuracy of k_x is relatively high, assuming that $k_{1,nr}$ as determined from the TRPL

decays is accurate. The accuracy of $k_{2,\mathrm{rad}}$ is also relatively high, since there is a small, but highly relevant increase in PLQE over the excitation range studied, due to the increasing competitiveness of the radiative $k_{2,\mathrm{rad}}$ process over the non-radiative $k_{1,\mathrm{nr}}$ process over the intensity range of measurement. The accuracy of k_{aug} is low, but its low value also makes its impact negligible.[121,263]

The same recombination constants were estimated by Dr. Silvia G. Motti (University of Oxford) using optical-pump terahertz probe (OPTP) spectroscopy. The OPTP experiment can record the photo-conductivity transients at higher charge carrier densities and with femtosecond resolution, thus allowing for more accurate determination of the higher-order decay rates, $k_{2,\mathrm{rad}}$ and k_{aug}. In **Table 5.1**, the values obtained by both methods are shown to be in good agreement with one another and with previously reported values. In **Appendix A.1**, the impact of an error in the recombination constants on the resulting mobility of PEA_2PbI_4 is shown. It was concluded that the recombination constants were determined with enough accuracy so that the resulting error was lower than the batch-to-batch variation of the TPC data and hence to allow for conclusive results.

Table 5.1: Recombination constants of$PEA_2PbI_4$and $FA_{0.9}Cs_{0.1}PbI_3$ as obtained from TRPL/intensity-dependent, external PLQE and OPTP measurements. They are compared to literature values.

Material	Method	$k_{1,\mathrm{nr}}$ [x 10^6 s^{-1}]	k_{x} [x 10^6 s^{-1}]	$k_{2,\mathrm{rad}}$ [x 10^{-10} cm^3s^{-1}]	k_{aug} [x 10^{-28} cm^6s^{-1}]
$FA_{0.9}Cs_{0.1}PbI_3$	TRPL, PLQE	1.1	NA	0.9	7.2
	OPTP	-	NA	3.1	0.7
	197, 215	0.5-7	NA	1.1	0.2
PEA_2PbI_4	TRPL, PLQE	6.3	0.7	3.3	-
	OPTP	5.0	-	900	3.1
	116, 263	0.9	50	20	10-200

Now, the Saha equation (**Equation 2.8**) could be used to estimate the fraction of free carriers (ϕ) with respect to the total density of photo-excited species. This was done by solving **Equation 2.8** at each time point as detailed in **Chapter 3** for the excitation pulse length of 3.74 ns used during the TPC experiment. The resulting transient free-carrier fraction is plotted in **Figure 5.2 (d)** for both sets of extracted parameters. It becomes apparent that the higher E_{B} of the layered material results in an overall lower free-carrier fraction as expected for excitonic materials.

Long-Range Mobility

To estimate the long-range, in-plane mobility, the TPC method was used. As two-dimensional perovskites are anisotropic materials, their orientation with respect to the substrate strongly impacts the TPC measurement, which is an in-plane method. It was hence important to have a pure two-dimensional perovskite phase with nearly perfectly oriented layers, in order to reduce the effects of both multiple phases and anisotropy on the measured conductivity. In order to assess the orientation of the thin films studied, in particular the PEA_2PbI_4, 2D XRD scans were taken by Philippe J. Holzhey (University of Oxford). In **Figure 5.3 (a)** and **(b)**, the 2D XRD scans for both materials are shown: for the three-dimensional perovskite films, the XRD peaks appear as semicircles in the q_y vs. q_z plot, indicative of a low degree of texturing and a random distribution of crystalline orientations. In contrast, the majority of the scattering intensity was along the q_z-direction for the two-dimensional perovskite film, consistent with highly textured films, with the perovskite two-dimensional planes lying parallel to the substrate.[123,268] Alongside the 2D XRD scans, a set of 1D XRD diffractograms is shown in **Figure 5.3 (c) and (d)** as well. In the case of thePEA_2PbI_4, a highly oriented film was obtained with a d-spacing of approx. 1.6 nm.

From these findings, it was expected that the TPC mostly probed the conductivity and mobility in the plane of the two-dimensional perovskite sheets, hence "in-plane" in this case did not only refer to the lateral arrangement of the electrodes, but also to the direction of the measurement within the layers of the two-dimensional perovskite. It is important to re-emphasize here that excitons, as pseudo particles with a net charge of zero, do not drift in an electric field and so do not contribute to the conductivity. The assumption of $\phi = 1$ was thus no longer true for excitonic materials such as two dimensional perovskites. This behaviour was shown in **Figure 5.2 (d)** as well. Without accurately determining the free-carrier fraction, there is a risk of presenting confusing, even contradictory results when studying excitons and mobile carriers, using long-range and short-range measurement techniques.

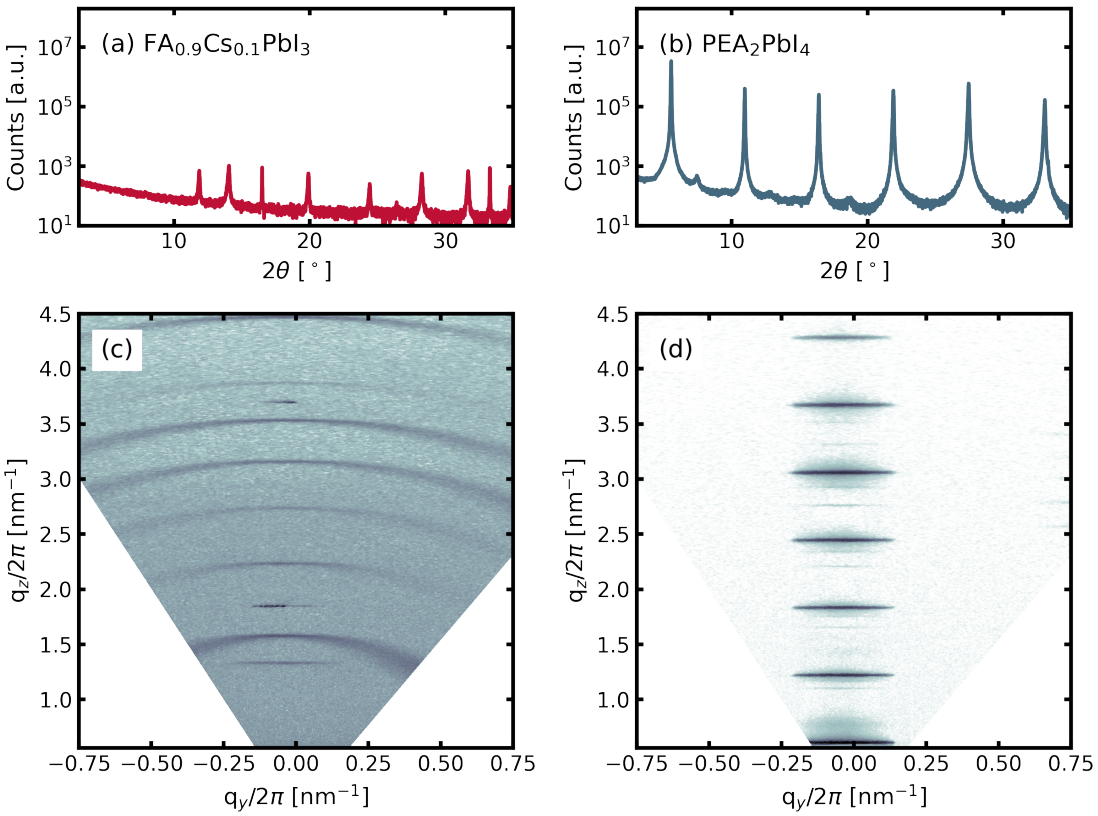

Figure 5.3: (a) and (b) show the 1D-XRD diffractograms for the two materials studied here. (c) and (d) show the 2D-XRD diffractograms for both materials and were measured by Philippe J. Holzhey (University of Oxford).

The obtained conductivity decays from the TPC measurements are shown in **Figure 5.4 (a)** for both PEA_2PbI_4 and $FA_{0.9}Cs_{0.1}PbI_3$. For both materials, the photo-conductivity traces again indicated the presence of long-lived species, with mono-exponential decay lifetimes of a few hundred nanoseconds, and peak conductivities between 10^{-4} to 10^{-2} S cm^{-1}. Using an approach similar to the one in **Chapter 4**, where early-time recombination during the photo-excitation pulse was neglected and $\phi = 1$ was assumed, the uncorrected sum-mobility $\phi\Sigma\mu$ could be extracted from the extrapolated $\sigma_{t=0}$ using **Equation 4.1**. The resulting $\phi\Sigma\mu$ values determined in this manner were 0.1 to 0.7 cm^2 V^{-1} s^{-1} in the case of PEA_2PbI_4 and 0.2 to 0.7 cm^2 V^{-1} s^{-1} for $FA_{0.9}Cs_{0.1}PbI_3$. It shall be noted that the uncorrected long-range mobility values were very similar for both materials. The drop off observed for $\phi\Sigma\mu$ determined in this manner with increasing excitation density was consistent with a reduction in ϕ due to early-time recombination and exciton formation with increasing intensity, as was already observed in **Chapter 4**. The transient free carrier fraction shown in **Figure 5.2 (d)** could now be used to obtain a corrected $\Sigma\mu$.

The uncorrected $\phi\Sigma\mu$ values are presented side by side with the corrected $\Sigma\mu$ values in **Figure 5.4**

and plotted against the fluence of the laser. The fully-corrected estimations of the mobilities are significantly different: in the case of the three-dimensional perovskite, the corrections affected the higher excitation densities more strongly with estimated free-carrier fractions at peak conductivity (with respect to the initial excitation density) of 0.84, 0.68, 0.49 and 0.33, for excitation fluences of 0.08, 0.25, 0.80, and 2.54 nJ cm^{-2}, respectively, with an average mobility of 0.8 ± 0.1 cm^2 V^{-1} s^{-1} (average of 3 samples from one batch, and across all excitation fluences). As shown in **Chapter 4** the long-range mobility of three-dimensional perovskites can be estimated as 0.2-6.7 cm^2 V^{-1} s^{-1}, similar to the values obtained in **Chapter 4**. For PEA_2PbI_4, the free-carrier fractions near peak conductivity were reduced to 0.11, 0.07, 0.04, and 0.03 for the same range of excitation energies, resulting in $\Sigma\mu$ of 8.0 ± 0.6 cm^2 V^{-1} s^{-1} (average of 18 samples from 6 batches and across all probed excitation energies). In both cases, the smaller relative errors of the estimated mobilities were consistent with the expectation that the mobility is widely independent of charge carrier densities in the regime measured in this work. It is worth emphasizing here that the low values of ϕ in the case of the layered perovskite could mainly be accounted for by the Saha equilibrium at the high exciton binding energy of 230 meV.

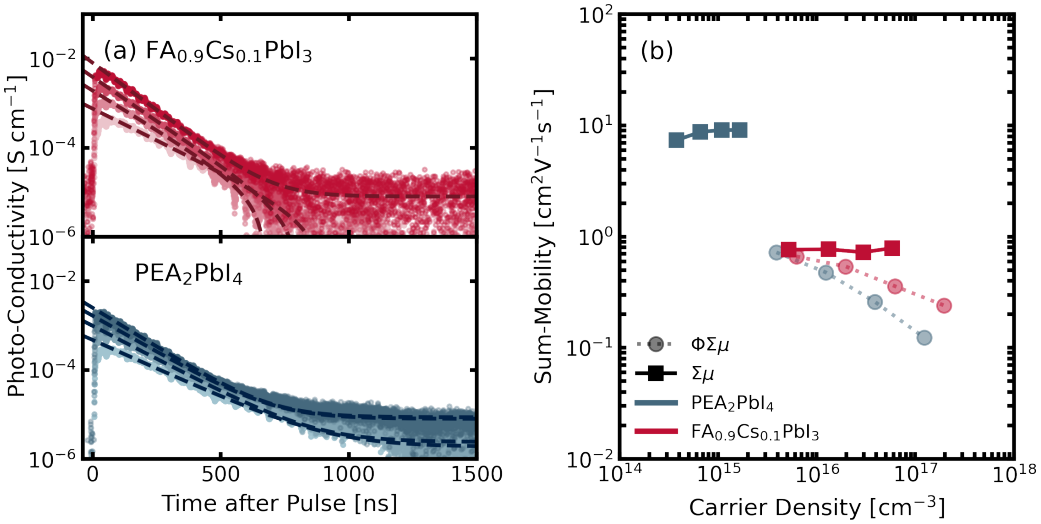

Figure 5.4: (a) TPC decay traces are shown for different laser fluences (1.9×10^{11}cm^{-2} (0.08 µJ cm^{-2}), 6.0×10^{11}cm^{-2} (0.25 µJ cm^{-2}), 1.9×10^{12}cm^{-2} (0.8 µJ cm^{-2}), 6.0×10^{12}cm^{-2} (2.5 µJ cm^{-2})) (b) The extracted $\phi\Sigma\mu$ and $\Sigma\mu$ are shown side-by-side for both materials studied here. In the case of $\phi\Sigma\mu$, the charge carrier density is the excitation density, while for $\Sigma\mu$ it is the simulated free charge carrier density.

Short-Range Mobility

To further investigate both the early-time recombination processes and to probe the early time "short-range" charge carrier mobility, optical-pump terahertz-probe (OPTP) spectroscopy was performed by Dr. Silvia G. Motti (University of Oxford). The time-scale probed is typical $<$ 1 ns, which is short enough, so that no equilibrium of free-carriers and excitons has formed yet and ϕ can be approximated as 1. The transient OPTP photo-conductivity decays are shown in **Figure 5.5 (a)** again for both the two- and three-dimensional perovskite thin films. The OPTP transients of PEA_2PbI_4 excited with 400 nm (3.10 eV) photo-excitation showed a very fast decay component (within the first few picoseconds), which was not present in the three-dimensional material. This early time decay was independent of excitation fluence for the transient OPTP signal in the PEA_2PbI_4 samples. It hence could not be ascribed to bi-molecular or Auger recombination. Similar to earlier studies, this behaviour was interpreted as due to the rapid exciton formation from an initial free-carrier population.[275,276]

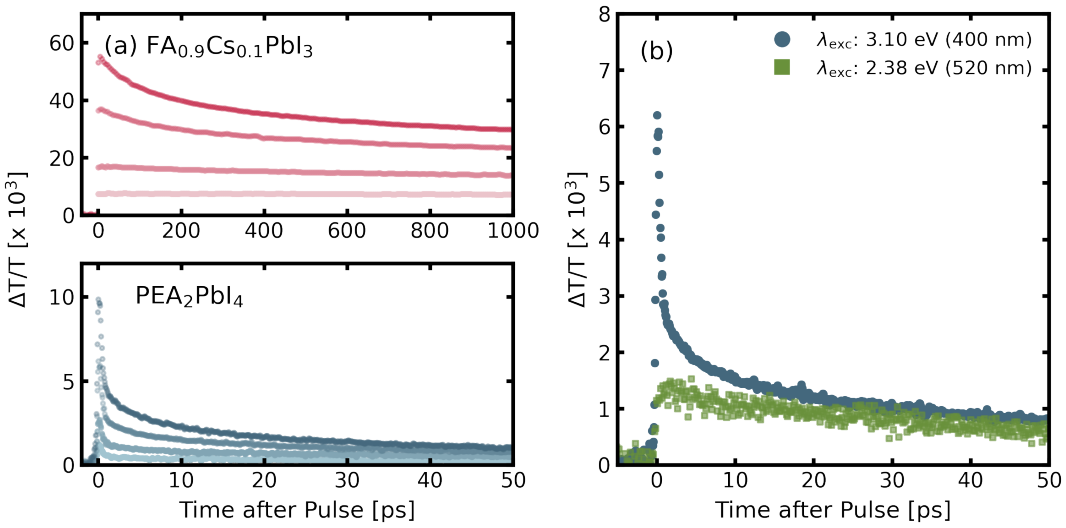

Figure 5.5: (a) The OPTP decays as measured with a 400 nm (3.1 eV) pulsed laser with different fluences (4.2 µJ cm^{-2}, 9.9 µJ cm^{-2}, 23.7 µJ cm^{-2}, 41.3 µJ cm^{-2}). (b) The OPTP decays are shown side-by-side for PEA_2PbI_4 excited at 400 nm (3.1 eV) and 520 nm (2.38 eV). All measurements presented here were done by Dr. Silvia G. Motti, University of Oxford.

In short, the initially formed free-carrier population, which is generated by photo-excitation energies significantly above the band gap, will relax to the conduction band edge and then into excitonic states, which are no longer sensed by the THz probe beam. This interpretation was further confirmed by photo-exciting the same sample with a photon energy chosen to be resonant with the excitonic states (520 nm, 2.38 eV). The results for both excitation energies are presented side-by-side in **Figure 5.5 (b)**. Consistently, when the excitonic states were excited directly, the early time drop in photo-conductivity could no longer be observed. It seemed that the enhanced temporal resolution of the OPTP experiment allowed for the probing of the free-carrier population before exciton formation took place, hence ϕ could again be assumed to be close to 1 for the peak of the conductivity.

The THz charge carrier mobility $\Sigma\mu$ from the peak photo-conductivity signals were determined to be 40 cm^2 V^{-1} s^{-1} for $FA_{0.9}Cs_{0.1}PbI_3$ and 8 cm^2 V^{-1} s^{-1} for PEA_2PbI_4. It is worth highlighting again that the mobility estimated from OPTP is a relatively short-range mobility, owing to the high frequency of the THz probe (see **Chapter 2** for details).[199,277] Notably, the THz mobility determined for the case for which the excitonic bandgap was excited directly ($\phi\Sigma\mu$ at 2.38 eV) was reduced by a factor of approximately 5.5, resulting in a $\phi\Sigma\mu$ of 1.5 cm^2 V^{-1} s^{-1}. This is much closer to the TPC mobility determined when the exciton fraction has not been accounted for.

High Quality Thin-Films

Comparing the longer-range mobility that was determined from the TPC measurements to the short-range mobility determined from the OPTP spectroscopy can yield valuable insights into the thin-film quality and device relevance of the different materials where longer range transport is required. Both data sets are summarized in **Figure 5.6 (a)**, including $\phi\Sigma\mu$ from the OPTP spectroscopy at 400 nm (3.10 eV) and 510 nm (2.38 eV). For the three-dimensional perovskite $FA_{0.9}Cs_{0.1}PbI_3$, the short-range and long-range mobility differed by a factor of 50, which had previously been reported in similar materials.[197,199] A detailed understanding of the mechanisms behind this observation is part of ongoing research, but it indicates that longer-range defects responsible for charge carrier scattering are present in these polycrystalline thin films.[40–42] Encouragingly, for the two-dimensional PEA_2PbI_4, the long range and short-range mobility (at 3.1 eV) were almost identical, indicating close to "single-crystal-like" charge transport in these polycrystalline thin-films. This agreement between the short-range THz and long-range TPC mobility was a first for metal halide perovskites. Interestingly, the short-range mobility estimated at 2.38 eV was much closer to the uncorrected long-range mobility. This is not a coincidence since a larger density of excitons are initially formed when the sample is photo-excited in resonance with the excitonic bandgap. According to **Equation 2.8**, the initial fraction of free carriers would be significantly closer to the equilibrium value of *phi*. The fact that the data were self-consistent and agreed with the existing literature, strongly supported the validity of the approach and interpretations here.

To tie together structure and morphology with the results obtained from long-and short-range photo-conductivity measurements, top view SEM images were taken for both materials **Figure 5.6 (b)** and **(c)**. Strikingly large grain sizes (as resolved in the top view SEM images) were observed for the layered perovskite thin films. Although the three-dimensional perovskite films appeared much rougher on the 100s nm length scale in the top view SEM image, with much smaller polycrystalline grain size than the layered perovskite thin films, both types of films appeared extremely smooth and specular (shiny) on the optical length-scale. Grain sizes in the tens to hundreds of nm length-scales are also typical for three-dimensional perovskite thin films processed from mixed solvent systems via the anti-solvent quenching method was used for the fabrication

here.[278] Even after careful optimization it was not possible to significantly enhance the grain size in the three-dimensional perovskite films without changing the stoichiometry significantly.

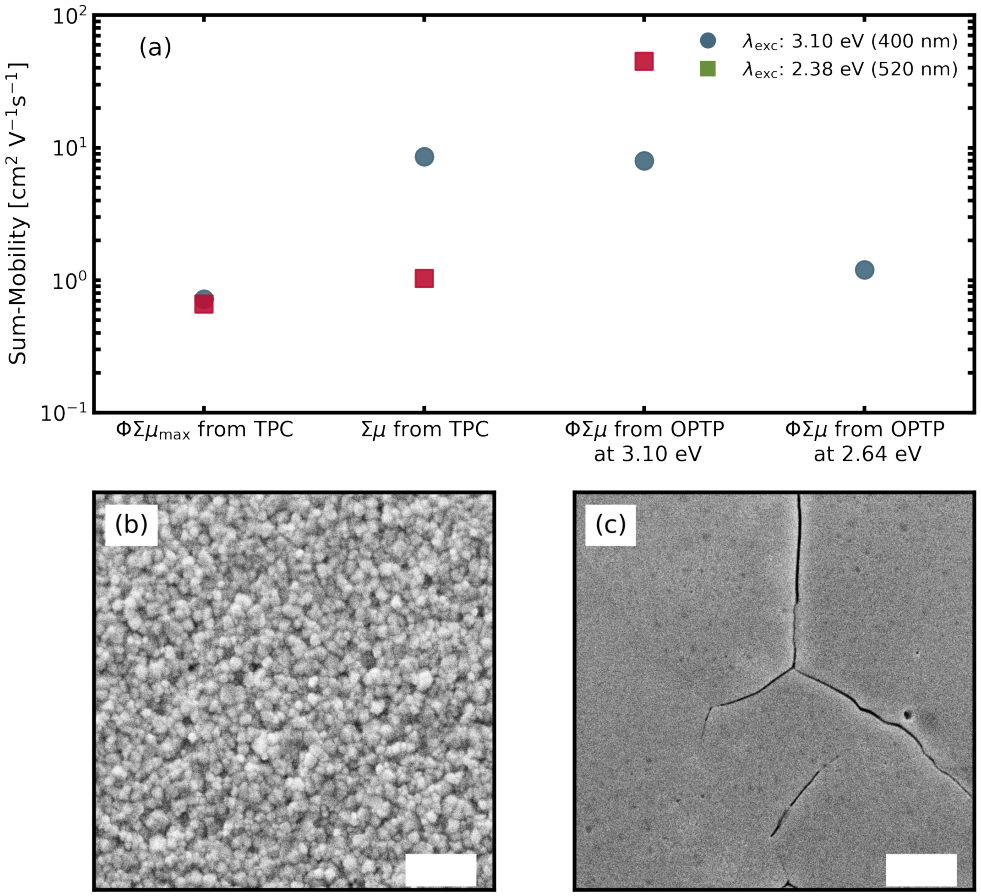

Figure 5.6: (a) All estimated mobilities are shown together for the different techniques (OPTP, TPC) and excitation wavelengths (400 nm, 510 nm). Only the PEA_2PbI_4 sample was excited with the 510 nm (2.64 eV) laser. (b) and (c) Top-view SEM images of $FA_{0.9}Cs_{0.1}PbI_3$ (b) and PEA_2PbI_4 (c) are shown to compare the material morphologies. The white scale bar is 1 µm in both cases.

The often-reported "underperformance" of two-dimensional perovskite photovoltaic devices, as compared to their three-dimensional counterparts could hence be ascribed to two main factors: 1) the increased exciton binding energy which leads to a low free carrier fraction of $\leq 10\%$ at room temperature under AM1.5 illumination (100 mW cm^{-2}), and 2) a lack of understanding of the impact of anisotropic charge carrier transport properties on the performance of the resulting photovoltaic devices. It became the focus of this project to explore ways to overcome the

limitations of the high exciton binding energy.

5.3 PART II - TOWARDS IMPROVED PROPERTIES

Functionalizing the Organic Moeity

A method to increase the free charge carrier fraction is to functionalize the organic spacer cation. Here a range of functionalized phenylethylethylammonium derivatives (4-fluorophenethylammonium iodide, 4-methoxyphenethylammonium iodide and 4-methylphenethylammonium iodide) were tested (see **Figure 5.7(a)** for chemical structures). To understand the impact of each molecule on the optoelectronic properties of the resulting two-dimensional perovskites, thin films of MeO$-PEA_2PbI_4$ (here: MeO-PEA), F$-PEA_2PbI_4$ (here: F-PEA) and Me$-PEA_2PbI_4$ (here: Me-PEA), were produced with the same, previously established recipe. First, the absorption properties were studied by measuring total transmittance and reflectance of the thin films on glass and calculating the absorption coefficient via **Equation 2.10**. As for PEA_2PbI_4, thinner films were needed in order to resolve the excitonic peak feature (see **Figure 5.7(b)**. The Elliott model was used to obtain exciton binding energies of 170, 190, and 200 eV for MeO-PEA, F-PEA, and Me-PEA, respectively.[83] It needs to be pointed out that the absorption coefficients $\alpha(h\nu)$ shown in **Figure 5.7(b)** are reduced with respect to the one for PEA_2PbI_4 shown in **Figure 5.1(b)**. This can be an artefact of the measurement and the fact that the estimation of $\alpha(h\nu)$ is highly dependent on an accurate estimate of the thickness. In fact, a new PEA_2PbI_4 reference sample measured alongside MeO-PEA, F-PEA and Me-PEA showed a similar peak absorption coefficient of approx. 2.5×10^5 cm^{-1}.

Next, the photo-luminescence properties of the two-dimensional perovskite thin films were investigated TRPL by exciting each sample with a 1 MHz pulsed laser at 3.12 eV (398 nm) from the substrate side. The resulting TRPL decay traces are shown in **Figure 5.7(c)**. Each showed a fast drop in the normalized PL intensity within the first 50 ns, indicative of an excitonic recombination behaviour. Then, a longer "tail" following a near-mono-exponential decay was observed. The TRPL traces were fitted with the "simplified continuity equation"-model as described in **Section 3**. The mono-molecular recombination rate k_1 was shared between two different fluences at 2.2 and 22 nJ cm^{-2}. To further understand the recombination behaviour, intensity-dependent,

external PLQE was measured using a 3.12 eV (398 nm) continuous-wave laser. The resulting external PLQE as a function of absorbed photon flux is shown in **Figure 5.7(d)**.

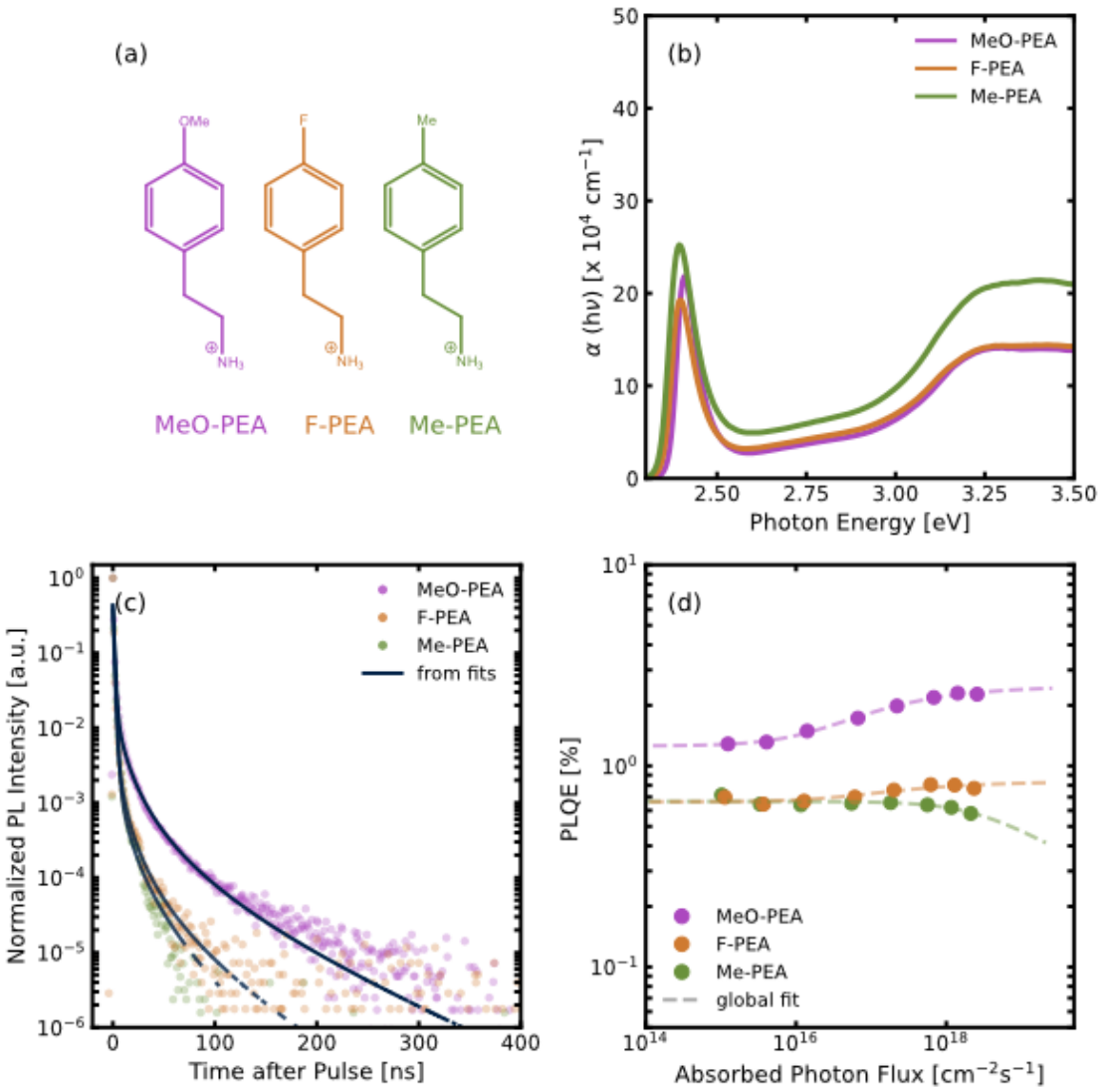

Figure 5.7: (a) Chemical structures of the organic spacer cations studied here: 4-methoxyphenethylammonium (MeO-PEA), 4-fluorophenethylammonium (F-PEA), and 4-methylphenethylammonium (Me-PEA). (b) Absorption coefficient of two-dimensional perovskite thin films made of the three organic spacer cations. The absorption coefficient was calculated from total reflectance and transmittance measurements. (c) TRPL decay traces of all two-dimensional perovskite thin films studied here. Only the traces for an excitation fluence of approx. 24 $\mathrm{nJ\,cm^{-2}}$ are shown here for clarity. The data was fitted with the "simplified continuity equation"-model, by using two fluences. (d) Intensity-dependent, external PLQE measurements of the three two-dimensional perovskites studied here are shown together with a global fit to extract the recombination parameters.

For all samples the external PLQE at lower excitation power densities converged towards a stable value, whereas a small increase could be observed at higher excitation power densities. Only MeO-PEA showed an overall higher PLQE when compared to PEA_2PbI_4. The data was fitted to **Equation 3.9** to estimate k_x, $k_{2,rad}$, $k_{2,nr}$ and k_{aug}. For the intensity-dependent, external PLQE

fitting, $k_{1,nr}$ was fixed to the value obtained from the TRPL fits, $k_{2,nr}$, k_{aug}, as well as P_{esc} were shared between all materials, which helped to make this model more identifiable. All results are summarized in **Table 5.2**. The extracted, shared parameters were k_{aug}: 10^{-32} cm^6s^{-1}, $k_{2,nr}$: 2.5×10^{-8} $cm^3\,s^{-1}$ and P_{esc}: 97.3%. All materials showed comparable $k_{1,nr}$, but differed slightly in the extracted $k_{2,rad}$ and k_x rates.

Table 5.2: Recombination constants obtained for MeO–PEA_2PbI_4, F–PEA_2PbI_4 and Me–PEA_2PbI_4 as obtained from TRPL/intensity-dependent, external PLQE measurements. $k_{1,nr}$ is obtained solely from TRPL, $k_{2,rad}$ and k_x are obtained from intensity-dependent, external PLQE.

Material	$k_{1,nr}$ [x 10^6 s^{-1}]	$k_{2,rad}$ [x 10^{-10} cm^3s^{-1}]	k_x [x 10^5 s^{-1}]
MeO–PEA_2PbI_4	7.7	6.5	1.0
F–PEA_2PbI_4	8.9	2.1	0.6
Me–PEA_2PbI_4	8.5	1.5	0.6

These results indicated that the Auger recombination was negligible under these conditions and instead $k_{2,nr}$ of unkown origin fitted the data better. It is also important to keep in mind that either process only affects the two data points measured at the highest fluences, for each material. Both the increase in $k_{2,rad}$ and k_x could explain the increase in the PLQE of the MeOPEA sample at all fluences. An increase in k_x would indicate faster exciton annihilation, while an increase in $k_{2,rad}$ might indicate enhanced carrier-carrier recombination. Looking at the initial PL drop observed during TRPL could give more insights: this drop had been previously assigned to fast exciton annihilation. In the case of the MeOPEA sample a less severe initial PL drop pointed towards an improvement in carrier-carrier recombination, rather than exciton annihilation. This would also be in agreement with a lower exciton binding energy as observed for the MeOPEA sample from the Elliott fit. Additionally the intensity-dependent, external PLQE shape itself could be used to indicate which process was the dominating one. As exciton annihilation is independent of the charge carrier density, the resulting intensity-dependent, external PLQE should be constant over a wide range of excitation fluences as previously mentioned. On the contrary, carrier-carrier recombination results in a monotonic increase of PLQE with excitation fluence until higher-order, non-radiative effects come into play. Only the MeOPEA sample showed an increasing PLQE with increasing excitation fluence, further indicating an increase in free charge carrier density.

To understand how this affected the photo-conductivity of the materials, TPC was measured with lateral electrodes as previously described. Again, a 470 nm (2.63 eV) pulsed excitation laser was used with a maximum fluence of 2.54 $\mu J\,cm^{-2}$. At the highest fluence, the photo-conductivities were measured as 4.4×10^{-3}, 3.6×10^{-3}, and 0.8×10^{-3} $S\,cm^{-1}$ for the MeO-PEA, F-PEA, and Me-PEA samples, respectively. In comparison, for PEA_2PbI_4 a photo-conductivity of 3.2×10^{-3} $S\,cm^{-1}$ was measured at the same fluence. As with the PEA_2PbI_4, both the short-range and long-range mobility were extracted from OPTP and TPC measurements, respectively. The OPTP measurements were performed by Dr. Silvia G. Motti (University of Oxford). They are shown side-by-side in **Figure 5.8(a)** and compared to the PEA_2PbI_4 from Part I of this chapter. The short-range mobility from OPTP did not differ, while the long-range mobility changes over an order of magnitude between the different materials. The extracted short-range mobilities were 6.7, 7.1, and 6.1 $cm^2\,V^{-1}\,s^{-1}$, while the long-range mobilities were 2.1 ± 0.4, 1.7 ± 0.6, and 0.6 ± 0.3 $cm^2\,V^{-1}\,s^{-1}$, for MeO-PEA, F-PEA, and Me-PEA, respectively. In contrast to the PEA_2PbI_4 reference sample, all studied two-dimensional materials showed a discrepancy between the long- and short-range mobility, indicative of reduced material quality. To test whether this was the case, 1D-XRD diffractograms were measured and are shown in **Figure 5.8(b)**. All organic spacers form highly oriented two-dimensional perovskite films along the (0 0 2) plane, which meant the inorganic planes were again oriented parallel to the underlying substrate. Despite all of them being phase-pure, oriented materials they showed different intensities of the initial XRD peaks. This can be indicative of structural disorder.[279]

The (0 0 2) peak was integrated for each material and used as a measure of structural disorder. Then, the difference in short- and long-range mobility were calculated as $\Delta\mu = \mu_{\mathrm{OPTP}} - \Sigma\mu_{\mathrm{TPC}}$ and plotted against the (0 0 2) peak area in **Figure 5.8(c)**. Surprisingly, the data showed a near-perfect linear trend. While this was just a crude approximation, it indicated that the long-range transport properties of the layered perovskites studied here were greatly impacted by the morphology and disorder within the thin films. The impact was even more pronounced than for three-dimensional perovskites, which have an already lower long-range mobility to begin with.

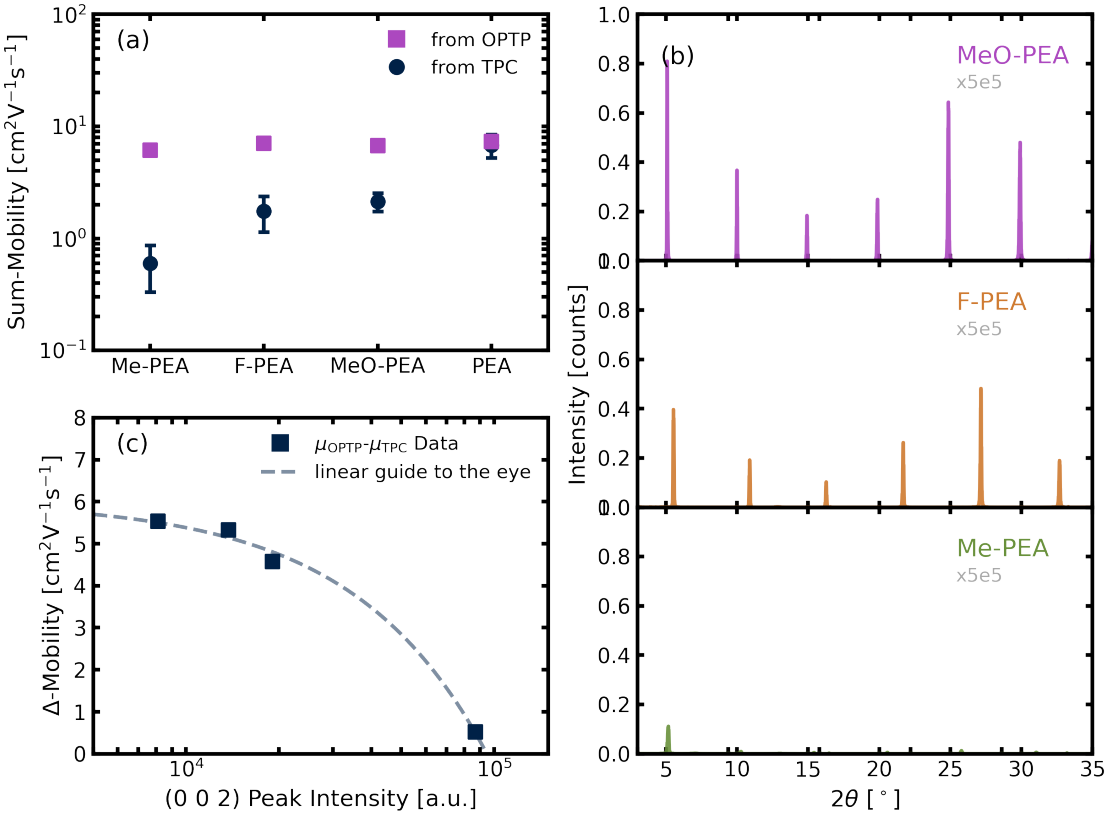

Figure 5.8: (a) Extracted long- and short-range mobilities from TPC/OPTP for all PEA-derivatives. The OPTP measurements were performed by Silvia G. Motti (University of Oxford). (b) 1D-XRD diffractograms of the three derivatives studied here. (c) A comparison of the difference in short- and long-range mobility to the (0 0 2) peak area is shown to illustrate the impact of structural changes on the discrepancy in mobility.

All results pointed towards MeO−PEA_2PbI_4 having improved optoelectronic properties. These were most likely achieved due to an increased free-carrier fraction. Even though the long-range mobility was lower than that of PEA_2PbI_4, the measured photo-conductivity was still higher. In contrast to that the structural disorder as approximated from the (0 0 2) peak area was reduced for MeO−PEA_2PbI_4. These results indicated that MeO−PEA_2PbI_4 could be more suitable for use in photovoltaic applications or even as a two-dimenional perovskite passivation layer, if the fabrication of the thin films was optimized for this specific material.[280,281] In fact, it had been used as a surface passivation in one recent report of a perovskite-based PV device with outstanding efficiency.[246]

5.4 SUMMARY AND OUTLOOK

It is worth mentioning that all results presented in this work may be impacted by the reduced number of grain boundaries, an increased crystallinity, as well as a combination of both and it is part of ongoing research to disentangle these effects.[40–42]

In conclusion, it was first shown that PEA_2PbI_4, as an excitonic, two-dimensional perovskite, also has a substantial free charge carrier density that affects its optoelectronic properties. At the same time, a considerably higher long-range mobility was measured than for a typical three-dimensional perovskite. Critically, in PEA_2PbI_4 thin-films, the sum of mobilities was the same as determined by measurements sensitive to both short-range and long-range transport. In contrast, the difference between short- and long-range mobility for three-dimensional perovskites was greater than a factor of ten, and in the example here, a factor of 50. This indicates that, for two-dimensional perovskite thin films, no extrinsic defects are responsible for charge carrier scattering, beyond those inducing short-range scattering events in the crystalline structure. Thus, the PEA_2PbI_4 thin-films studied here can be considered to have charge transport properties similar to those typically observed in single crystals.
These results indicate that employing two-dimensional perovskites, or using two-dimensional perovskites to direct the crystallisation of three-dimensional perovskites, may be a viable method to enhance the charge transport in optoelectronic devices. This is in contrast to their use as surface passivation for three-dimensional phases to induce stability enhancements. These passivations often lead to performance drops in certain architectures, which could now be ascribed to two main factors: 1) the higher exciton binding energy, which for a material such as PEA_2PbI_4 resulted in 90% exciton formation at room temperature under solar irradiance and 2) the anisotropic charge carrier transport and limited understanding of its impact on the resulting device performance.

The first point was then addressed in further work trying to enhance the density of free charge carriers within the material by introducing functional groups at the organic spacer cation. The

organic spacer cation phenylethylammonium was functionalized with three different groups on the aromatic ring. From this, it could be understood that the optoelectronic properties of the two-dimensional materials are greatly dependent on the interplay of excitons and free charge carriers. Thus, the intensity-dependent PLQE and TRPL measurements could only be understood conclusively, if both were taken into account. From this, an increased free carrier fraction could be postulated for the MeO–PEA_2PbI_4 two-dimensional perovskite. In agreement with this, an increased photo-conductivity and PLQE were measured. Despite these promising results for MeO–PEA_2PbI_4, its long-range mobility differed from the short-range mobility as obtained from OPTP. This effect could be connected to some structural disorder within the thin film. Most likely, this is a result of the fact that the original fabrication route was optimized for PEA_2PbI_4 and would need to be revised for MeO–PEA_2PbI_4 to make use of its potentially much improved properties.

Despite these promising findings, more work is needed - specifically in understanding how to control the orientation of the two-dimensional planes in perovskite thin films. Further research should prioritise improving the understanding of the interplay of excitons and free charge carriers in these materials. Being able to control exciton populations in two-dimensional perovskites, such as PEA_2PbI_4 or MeO–PEA_2PbI_4, will help to determine the optimal methods for integrating them into devices and establishing effective interfaces with charge extraction/injection materials.

CHAPTER

USING BAYES' THEOREM TO EVALUATE TIME-RESOLVED PHOTO-LUMINESCENCE DATA

6

In this chapter it is demonstrated that time-resolved PL data of metal halide perovskites can be effectively evaluated by combining Bayesian inference with a Markov-Chain Monte-Carlo algorithm. A thin film of $FAPbI_3$ is used to showcase the advantages of the approach, namely a high number of inferable parameters alongside their probability distributions as well as correlations among parameters. A set of half-stacks with SnO_2 and Spiro-OMeTAD is used to validate the inference of surface recombination velocities with high precision. From the probability distributions of all inferred parameters, an intensity-dependent PLQE measurement can be simulated and compared to the experimental data. A good agreement between the two can be found for all samples studied here. Finally, a mobility value obtained from the methodology presented here is compared to values obtained from transient photo-conductivity (TPC) measured on the same sample and optical-pump terahertz-probe spectroscopy from literature. The mobility values inferred from TRPL decays are close to those measured using the TPC method. It is postulated that the charge transport in thin-film-based photovoltaic devices is defined by the long-range mobility. Overall, this chapter demonstrates the effectiveness of coupling Bayesian inference with a Markov-Chain Monte-Carlo algorithm, an approach which can be expanded to a variety of other analysis techniques in the future.

6.1 INTRODUCTION

Time-resolved photo-luminescence (TRPL) is a powerful technique in which the sample is illuminated by a short laser pulse and the photo-luminescence is measured in a time-correlated fashion. The photo-luminescence intensity will quickly decay after the pulse, due to diffusion, recombination and trapping of charger carriers within the material.[204,282,283] As such, the shape of the decay can give insights into material properties to varying complexity. In the simplest case of a mono-exponential decay, the time at which the photo-luminescence intensity has reached 1/e (approx. 37%) of its initial value can be determined. This is a straight-forward method to compare different fabrication routes of similar semiconductor materials. Even this simple approach has the underlying "model" that the PL decay follows a mono-molecular rate equation. In reality the TRPL decay rarely follows a mono-molecular rate law, but rather a multiexponential decay. The most common approach is the use of a bi-exponential decay from which two lifetimes can be extracted.[282,284–286] This approach is only viable to determine an average decay time, however in literature physical meaning is often given to both extracted lifetimes, which can lead to confusing and even contradictory interpretations of results. Things become even more complicated, when a tri-exponential decay is used and physical meaning is imposed onto all three lifetimes.[287,288] None of the approaches presented thus far can accurately describe the observed change in TRPL decay kinetics with changing laser fluence.

The simplest physical model is the continuity equation without drift or diffusion (**Equation 2.13**). Analytical solutions have been described, however it can also be solved numerically and fitted to data using a least-squares approach (see **Chapter 3**). With this model, a change in decay kinetics with changing laser fluences can be accurately described and used to extract physically meaningful parameters. Still, the model is a simplification, as diffusion effects are completely neglected and there is no distinction made between non-radiative recombination occurring in the bulk or the surface of the material. The latter point is especially important when trying to assess the effectiveness of solar cell stacks, as surface recombination is a key limiting factor and engi-

neering the surface has been the topic of the most recent works which claim the highest efficiency. Measurements done on photovoltaic absorber materials interfaced with a charge transport layer (half-stack) may be used investigate the induced surface recombination at the interface, but the models in **Chapter 3** ignore this.

To overcome this issue, a full physical model needs to be used including diffusion, surface recombination at both interfaces as well as radiative and non-radiative recombination in the bulk of the sample. As mentioned in **Chapter 3** having many a large number of parameters can lead to non-identifiable models, meaning there are multiple, degenerate solutions which may describe the observations well. One common approach to overcome this limitation is to reduce the number of free parameters by fixing some of them to known values from literature or other experiments. For instance, a common approach is to use bare perovskite on glass to determine the bulk recombination parameters (assuming that the surface recombination is negligible) and then fix these when measuring a half-stack in order to estimate the surface recombination velocity (SRV) at the newly introduced interface.[47,143,181,289] This is a viable approach to get a good estimate for the SRV, however it has some limitations in the case of perovskite materials, as the underlying layer can affect the crystallization and final film morphology, which in turn will affect the recombination parameters and surface properties as well.[142,290]

To surpass these limitations, Bayesian inference implemented through a Markov-Chain Monte-Carlo algorithm is utilized in this chapter. Bayesian inference is a method in which Bayes' theorem is applied to compare a set of measured data to a modelled set, to infer knowledge about model parameters.[291] In the Bayesian approach, each parameter is described by a probability distribution. In the beginning, the initial belief about a parameter is encoded into an initial probability distribution, called the *prior*. Samples drawn from the prior will then be compared to some observed data with the help of a *likelihood function*, which determines, how well the parameters describe the data following some physical model. In this chapter, a Markov-Chain Monte-Carlo (MCMC) algorithm is used to select random samples from the prior distribution of the parameters. The MCMC algorithm takes an iterative approach: after an initial draw of samples from the parameter distributions a new set of samples is drawn where the parameters

are in close proximity to the previous ones. Only if some specific condition is met will the new set of samples be accepted as the next step by the MCMC algorithm.[292] To define this condition, the likelihood function and Bayes' theorem can be used, which states:

$$P(A|B) = \frac{P(B|A)P(A)}{P(B)} \tag{6.1}$$

where A can be the next sample and B the observed data.[291] The theorem then states that the probability that parameter A can describe a set of observations are correct is the probability of the observed data B being described by the parameter A (the likelihood function) multiplied by the prior of A ($P(A)$) and normalized by the probability of the observed being correct ($P(B)$). Thus, the *posterior* belief of a parameter depends on the likelihood that the observed data can be described by it. As the MCMC algorithm propagates, the sampled set will converge towards a state of high posterior probability or high likelihood of the parameters agreeing with the observed data. After many cycles the distribution of the sampled data will be identical to the true *posterior* probability distributions for each parameter.

This approach has been demonstrated to be effective, however the set of measurements was limited and the total time of calculation was quite long (multiple 10s of hours).[152,293] Here, an updated approach is shown in which a full physical model is used to describe the transient charge carrier density after pulsed photo-excitation, including diffusion, surface- and bulk-recombination as well as reabsorption effects and the impact of shallow traps. By improving the likelihood function and testing which parts of the model need to be included, the time of a typical calculation is cut down to two hours on a computer cluster or 8-10 hours on a regular, four-core computer. The new and versatile approach is then tested on a set of $FAPbI_3$ samples on glass or interfaced with SnO_2 or Spiro. The results give insights into the underlying, optoelectronic mechanisms that govern the transient charge carrier behaviour in this material.

6.2 PART I - METHOD DEVELOPMENT

The aim of the methodology used here was to be able to accurately infer a set of parameters from four measurements: two fluences from the substrate- and two from the material-side. As metal halide perovskites of varying quality might be encountered in a research situation, it was important to define such as minimal set of measurements. However, as will be seen in Part II of this chapter, this set already needed to be reduced when the perovskite material was interfaced with transport layers and significant quenching was induced.

The Physical Model

In order to estimate the time-resolved PL behaviour in a semiconductor, the radiative recombination rate needs to be calculated. Then the time-resolved PL response is

$$PL(t) \propto \int_0^d (1 - P_{\text{reab}}(z)) \cdot R_{\text{rad}}(t, z)\ dz + \epsilon_{\text{PL}} \tag{6.2}$$

where R_{rad} is the total, radiative recombination rate, as introduced in **Chapter 2** and ϵ_{PL} is the noise floor of the measurement. Since the radiative recombination is dependent on the charge carrier density (see **Equation 2.22**), the transient charge carrier density needs to be calculated as a function of t and z. This includes both band-to-band, radiative and trap-assisted, non-radiative recombination, as well as diffusion. The latter was included here by using the eigenvalue solution to the diffusion equation with the surface recombination velocities (SRV) as boundary conditions (see **Equations 2.16** and **2.19**).[150,151]

Assuming that both SRVs are different and non-zero, the solution is

$$n_0(t,z) = \sum_{k=1}^{\infty} A_k U_k(z) \cdot e^{-D\beta_k^2 \cdot t} \tag{6.3}$$

where A_k are matrix elements of the eigenvalue solutions and are proportional to the $G(t,z)$ as

$$A_k = \alpha(h\nu) \cdot \ F(h\nu) \cdot \frac{\int_0^d e^{-\alpha(h\nu)z} \cdot U_k(z) dz}{\int_0^d U_k(z)^2 dz} \tag{6.4}$$

with $U_k(z)$ being time-independent and describing the spatial evolution of carrier densities for the different eigenvalues β_k, which can be estimated from

$$U_k\left(z\right) = \cos\left(\beta_k \cdot z\right) + \ \frac{S_\mathrm{f}}{D \cdot \beta_k} \cdot \ \sin\left(\beta_k \cdot z\right) \tag{6.5}$$

where S_f is the SRV at the illuminated (front) surface of the sample. The eigenvalues β_k can be found by solving

$$\tan\left(\beta_k \cdot d\right) + \frac{D \cdot \beta_k \cdot S_\mathrm{sum}}{\left(\frac{S_\mathrm{sum}}{2}\right)^2 \cdot b - D^2 \cdot \beta_k^2} = 0 \tag{6.6}$$

The solutions β_k for $k \geq 1$ are used. D is the diffusion coefficient and is related to the mobility μ of the material via **Equation 2.17**. Typically, **Equation 6.6** is defined via the two surface recombination velocities S_1 and S_2.[150–152] However, this leads to degenerate solutions, simply by swapping the labels on S_1 and S_2. Degenerate solutions make it difficult for the MCMC to traverse the parameter space and thus should be avoided, if possible.[294]. To avoid this issue, the surface recombination was re-parameterized, by defining the sum and the product of S_1 and S_2: S_sum and S_prod. There existed now only one solution for $S_\mathrm{sum} = S_1 + S_2 = S_2 + S_1$. If the sum of two numbers is known, then the product of the two is constrained to be

$$S_\mathrm{prod} = b \cdot \left(\frac{S_\mathrm{sum}}{2}\right)^2 \ ; \ b \in [0,1] \tag{6.7}$$

Hence, using S_sum and b made the solutions of **Equation 6.6** to be non-degenerate. It is important to note that re-parameterization here did not introduce more parameters, but re-defined them to break the degeneracy. $F(h\nu)$, the fluence at the excitation wavelength, needed to be allowed to vary in a small error window ϵ_F of $\pm$ 10% in order to improve the overall likelihood of the

methodology. It is implemented as

$$F(h\nu) = F_{\mathrm{m}}(h\nu) \cdot \left(0.9 + \frac{\epsilon_{\mathrm{F}}}{5}\right) \tag{6.8}$$

where ϵ_{F} can vary between 0 and 1. The reason for this is that the measured PL response is highly dependent on the charge carrier generation and thus a slight change in alignment can change the measured response. A $\pm$ 10% error in excitation fluence can be accounted for by a $< 5\%$ error in the diameter of the excitation spot (assuming a circular spot). This error is reasonable since the laser spot size varies slightly, if different spots on the sample are measured and if the sample is illuminated from the material- or the substrate-side.

After having estimated the diffusion, the recombination could now be calculated as being dependent on t and z as well. This was done by a set of coupled rate equations, one for the electrons and one for the holes:

$$\begin{aligned}
\frac{\partial n(t,z)}{\partial t} =& -\frac{k_{2,\mathrm{rad}}}{P_{\mathrm{reab}}(z)} \cdot (n(t,z) \cdot p(n,t) + n(t,z) \cdot n_{\mathrm{eq}}) \\
& - k_{\mathrm{nr}} \cdot (n(t,z) \cdot (1 - f_{\mathrm{t}}) - f_{\mathrm{t}} \cdot n_{\mathrm{e,n}}) \\
\frac{\partial p(t,z)}{\partial t} =& -\frac{k_{2,\mathrm{rad}}}{P_{\mathrm{reab}}(z)} \cdot (n(t,z) \cdot p(n,t) + p(t,z) \cdot p_{\mathrm{eq}}) - k_{\mathrm{nr}} \cdot p(t,z) \cdot f_{\mathrm{t}}
\end{aligned} \tag{6.9}$$

where

$$f_{\mathrm{t}}(t,z) = \frac{n(t,z)}{n(t,z) + n_{\mathrm{e,n}} + p(t,z)} \tag{6.10}$$

is the relative trap occupancy in thermal equilibrium (pseudo steady-state).[164,165] A density of states in the conduction band of 10^{18} cm^{-3} was assumed. The set of equations was defined here for an electron trap, but is also true, if electrons and holes are swapped. **Equations 6.9** and **6.10** could be derived from **Equations 2.26(a)-(d)** by assuming: 1) a similar trap cross section for electrons and holes (yielding a single k_{nr}), 2) a trap between the middle of the bandgap and the edge of the conduction band (thus $n_{\mathrm{e,p}} \approx 0$), and 3) the trapping- and de-trapping processes being faster than the recombination, so that a pseudo-steady state, relative trap occupancy can be formulated. It is important to emphasize that f_{t} describes the fraction of filled traps relative to the empty traps at the beginning of the excitation pulse and can depend on previous pulses and the repetition rate.[295] The TRPL measurements typically took between one and three minutes,

so if charge carriers accumulated in shallow traps, they would continue to affect the recombination dynamics during the measurement. The definition of f_t tried to take that into account. In addition n_{eq} was used to estimate this "equilibrium" concentration of charge carriers that accumulated during the measurement. It is the sum of the background charge carrier density and the accumulated charge carrier density.

Equations 6.9 and **6.10** were solved iteratively using a Runge-Kutta algorithm. The solutions $n(t, z)$ and $p(t, z)$ then needed to be modulated to take the calculated diffusion into account. This was done via

$$n(t_i, z) = n(t_{i+1}, z) \cdot \frac{n_0(t_{i+1}, z)}{n_0(t_i, z)} \tag{6.11}$$

using $n(t_0, z) = n_0(t_0, z)$. An equivalent equation was used for the holes assuming the same diffusion as for the electrons ($n_0(t, z) = p_0(t, z)$).

The Eigenvalue Function

The eigenvalue function (Equation 6.6) is at the center of the model, thus a few difficulties that had to be overcome will be summarized here. The solution is dependent on D, S_{sum}, b and d. In **Figure 6.1(a)** and **(b)** the left hand side of Equation 6.6 is shown as a function of different values of $\beta \cdot d$, showcasing the dynamic nature of the equation. β_k are the roots of the equation and can be found numerically. However, common root-finding algorithms, like the ones from the `scipy.optimize` library struggled to find all roots. Especially, the fourth root in **Figure 6.1(b)** would be most likely missed, due to the high gradient at that point. The issue that arose from this is that the MCMC algorithm could not traverse this point, because the solution would change abruptly from close neighbouring ones. This effectively biased the MCMC walkers to avoid this area. To overcome this issue, the square of **Equation 6.6** was calculated instead, which turned all roots into local minima. Then, common algorithms could find all roots with much higher reproducibility and accuracy.

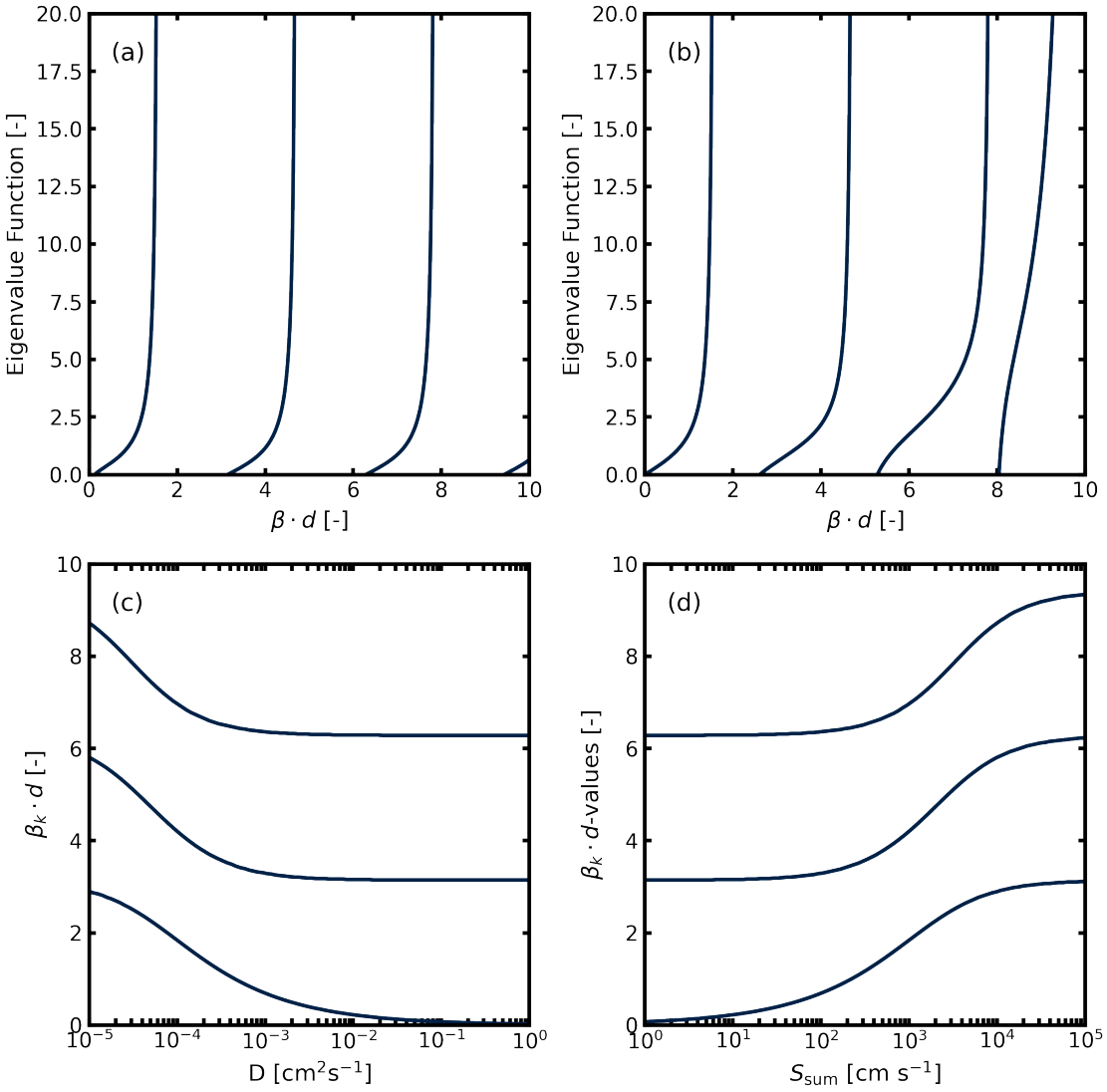

Figure 6.1: (a) and (b): The shape of the eigenvalue function is shown for different $\beta \cdot d$ values for the parameters (a) $D = 3 \times 10^{-2}$ cm^2 s^{-1}, $S_{\text{sum}} = 10$ cm s^{-1}, and $b = 0.95$; and (b) $D = 3 \times 10^{-3}$ cm^2 s^{-1}, $S_{\text{sum}} = 400$ cm s^{-1}, and $b = 0.95$. (c) and (d): The impact of D and S_{sum} on the solutions $\beta_k \cdot d$ are shown for a range of values where (c) $S_{\text{sum}} = 10$ cm s^{-1} and (d) $D = 3 \times 10^{-2}$ cm^2 s^{-1}.

To further emphasize the dynamic nature of the equation the first three non-zero roots were estimated for 1) a range of D with $S_{\text{sum}} = 10$ cm s^{-1} and $b = 0.95$, and 2) a range of S_{sum} with $D = 10^{-2}$ cm^2 s^{-1} and $b = 0.95$. The roots were multiplied by d for comparability and are shown in **Figure 6.1(c)** and **(d)**, respectively. It could be observed that there exist two limiting cases, one for small D or large S_{sum}, where $\beta_k \cdot d = k \cdot \pi$, and another for large D or small S_{sum}, where $\beta_k \cdot d = (k-1) \cdot \pi$.[150,152] The change from one limiting case to the other is highly dependent on D, S_{sum}, b and d and cannot be solved analytically. In the future, solving the eigenvalue solution could be replaced by a look-up table approach or an empirical correlation in the four-dimensional parameter space of D, S_{sum}, b and d, but this is beyond the scope of this chapter.

Taking Reabsorption into Account

Reabsorption of emitted photons can change the observed PL decay, as it delays the emission at later times, then the charge carrier density homogeneous across the sample thickness.[56,173–175] As mentioned in **Chapter 2**, its impact can be simulated by a full ray-tracing model.[173,175] This was however computationally too expensive for the approach presented here, were many thousands of calculations needed to be run for a representative Bayesian inference. Hence, several models to calculate P_{reab} of increasing complexity are compared here. As a reference, the calculation is also run without including any reabsorption. The simplest approach ("simple") assumed an exponentially decaying escape probability $P_{\text{esc}} = 1 - P_{\text{reab}}$ in z direction, thus:

$$P_{\text{esc}}(z) = e^{-\alpha_{\text{reab},i} \cdot z} \tag{6.12}$$

where $\alpha_{\text{reab},i}$ is the reabsorption factor of the two different surfaces (i = 1, 2) and is a product of the absorption coefficient at the emission wavelength and the number of internal reflections or scattering.[296] In this model the escape probability was assumed to be 100% at both surfaces. A higher order correction to this model ("separate") then took into account that the escape probability might not be the same for both surfaces. Thereby

$$\begin{aligned} P_{\text{esc},1}(z) =& e^{-\alpha_{\text{reab},1} \cdot z} \\ P_{\text{esc},2}(z) =& A_2 \cdot e^{-\alpha_{\text{reab},2} \cdot z} \end{aligned} \tag{6.13}$$

Lastly, the most complete model ("combined") included here considered that the escape probability relevant for **Equations 6.2** and **6.9** would not be the same, due to the fact that for the latter the generated photons could escape through the front and back surface, while for the estimation of $PL(t)$ only the surface directed at the detector would be important. The combined model is

$$\begin{aligned} P_{\text{esc,rec}}(z) =& e^{-\alpha_{\text{reab},1} \cdot z} + A_2 \cdot e^{\alpha_{\text{reab},2} \cdot (z-d)} \\ P_{\text{esc,PL}}(z) =& e^{-\alpha_{\text{reab},1} \cdot z} \end{aligned} \tag{6.14}$$

In **Figure 6.2** the P_{esc} is shown for each model as a function of z coordinate. In order to understand, which model describes the data the best the Akaike information criterion (AIC) was

calculated. It is defined as

$$AIC = \frac{\Sigma_1^{n=N} LL_n}{N} + 2 \cdot \frac{k_\mathrm{p}}{2} \cdot \sigma_\mathrm{L}^2 \tag{6.15}$$

for a gaussian distribution, where LL is the log-likelihood (defined below), N is the number of points and k_p the number of parameters.[297] In general, the smaller the AIC, the more appropriate the model. In **Figure 6.2(d)** the different AICs are shown for all three models. It can be seen that there is a significant difference between the models, which included reabsorption and the one without. Thus it was concluded that reabsorption had to be part of the model to improve the overall likelihood of the inference and hence the significance of its results. Among the three reabsorption models no significant difference could be determined. As such, the "simple" model with the lowest number of parameters was used for this chapter.

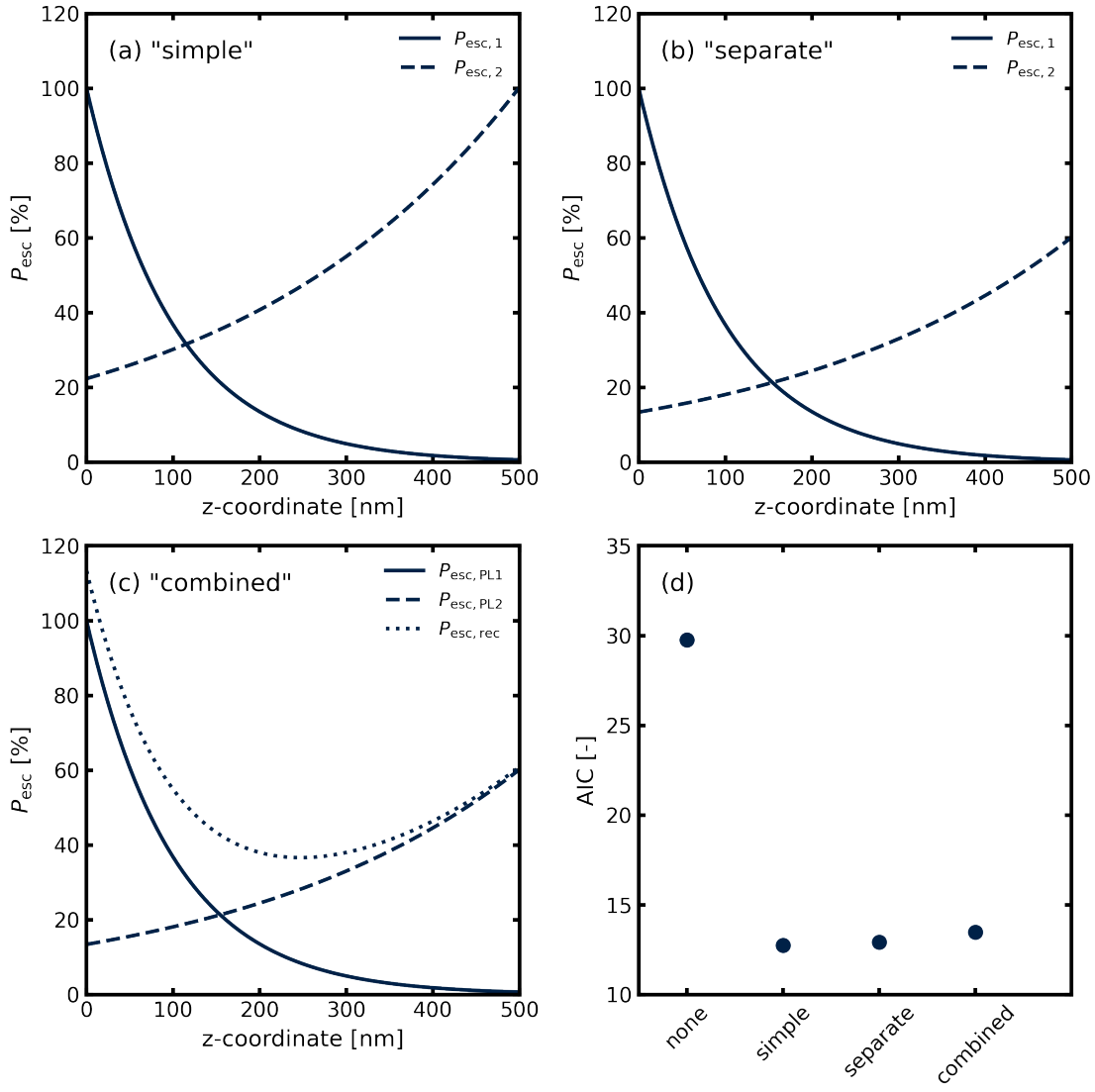

Figure 6.2: The different reabsorption models are illustrated as P_{esc} as a function of the z-coordinate up to a thickness of 500 nm, where (a) simple model, (b) separate model, and (c) combined model. (d): For a test data set of 4 TRPL decays measured at two excitation fluences and two illumination sides, the AIC is shown for all reabsorption models.

The Impact of the Parameters on the Final PL decay

Before using the algorithm on real data it was necessary to understand the impact of each parameter on the calculated photo-luminescence decay. For this, the PL model was run with all parameters fixed except one and the resulting, calculated PL is plotted in **Figures 6.3** and **6.4**. The parameters were fixed to values where their impact could be neglected: d: 500 nm, $F(h\nu)$: 5×10^{10} cm^{-2}, $\alpha(h\nu)$: 10^5 cm^{-1}, μ: 0.1 cm^2 V^{-1} s^{-1}, S_i: 0.1 cm s^{-1}, $k_{2,\mathrm{rad}}$: 10^{-10} cm^3 s^{-1}, k_{nr}: 10^5 s^{-1}, ΔE_t: 0.6 eV, n_{eq}: 10^{13} cm^{-3} and α_{reab}: 1 cm^{-1}. At this point it shall be noted that the parameters showed an effect on the PL decay in two time-frames: early- and later times.

First, $k_{2,\mathrm{rad}}$ was changed from 10^{-8} to 10^{-11} $\mathrm{cm^3\,s^{-1}}$. The resulting, simulated PL decays are shown in **Figure 6.3(a)**. It could be seen that changing $k_{2,\mathrm{rad}}$ affected both, the early- and later times of the PL decay as well as the curvature of the decay. In contrast, a change in k_{nr} from 10^5 to 10^8 $\mathrm{s^{-1}}$ only affected the later time decay, also often referred to as the "tail" of the decay (see **Figure 6.3(b)**). Thus in earlier chapters in this thesis, k_{nr} could be estimated with high accuracy by fitting the analytical model (see **Chapter 3**) to the later times of the PL decay. A change in μ between 0.01 and 10 $\mathrm{cm^2\,V^{-1}\,s^{-1}}$ affected only the very early decay times and controlled the time it took for the photo-generated charge carriers to redistribute across the film thickness (see **Figure 6.3(c)**). It is pointed out that a constant charge carrier density was reached around 40% of the initial value. Here, the inference algorithm could be unintentionally biased towards lower mobility values, if the initial drop of the PL is faster than the resolution between time points. To remove this bias, the observed and calculated PL was normalized to the second data point. To be able to see an effect of the trap-depth ΔE_{t}, k_{nr} had to be changed to 10^7 $\mathrm{s^{-1}}$. Then, the trap-depth changed from 0.8 to 0.1 eV affected the late times, by making the decay more shallow, the closer the trap was to the band edge (see **Figure 6.3(d)**).

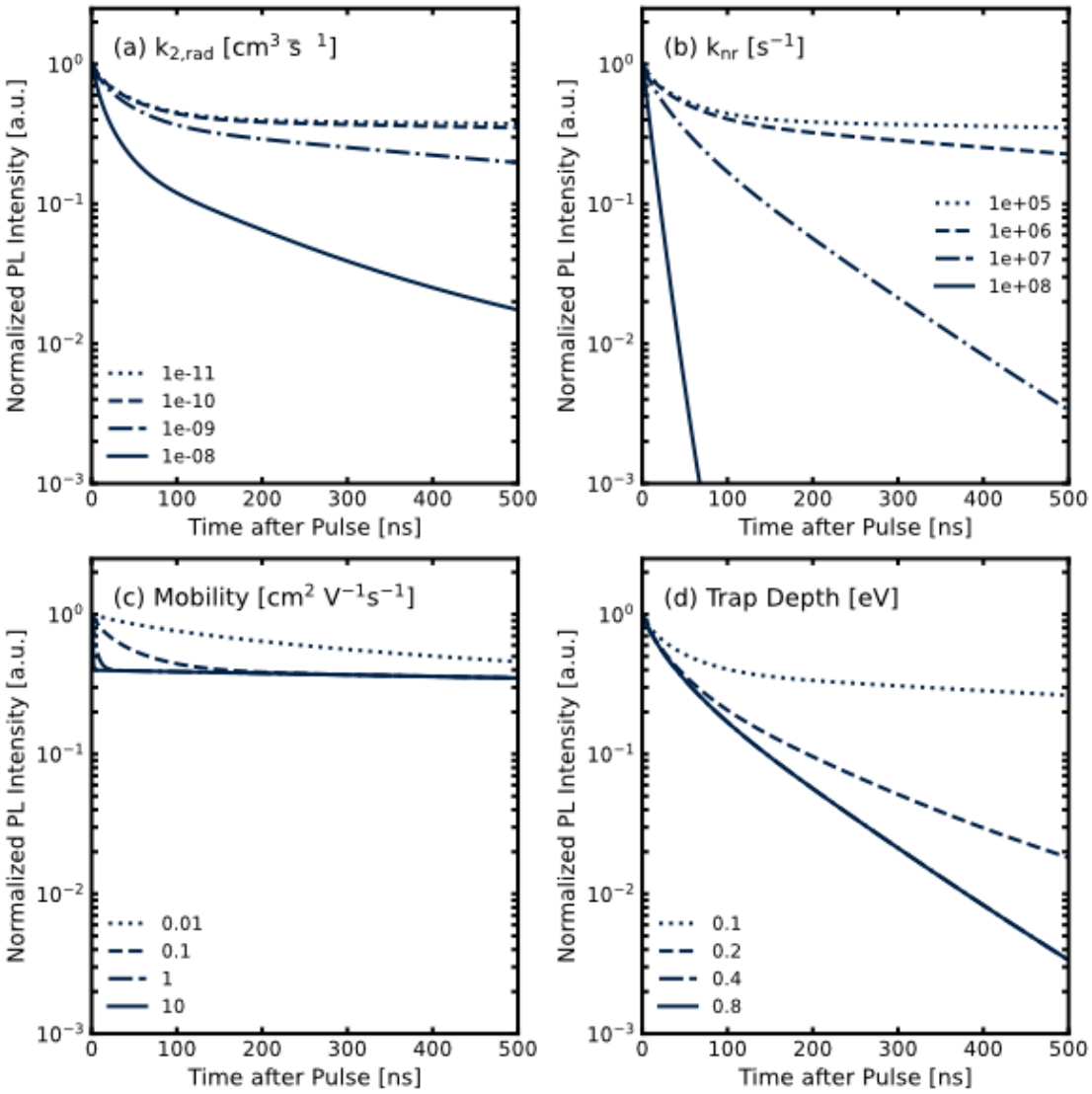

Figure 6.3: The PL decay is calculated for a fixed set of parameters (d: 500 nm, $F(h\nu)$: 5×10^{10} cm^{-2}, $\alpha(h\nu)$: 10^5 cm^{-1}, μ: 0.1 cm^2 V^{-1} s^{-1}, S_i: 0.1 cm s^{-1}, $k_{2,\mathrm{rad}}$: 10^{-10} cm^3 s^{-1}, k_{nr}: 10^5 s^{-1}, ΔE_{t}: 0.6 eV, n_{eq}: 10^{13} cm^{-3} and α_{reab}: 1 cm^{-1}), where one parameter is changed: (a) $k_{2,\mathrm{rad}}$, (b) k_{nr}, (c) μ, and (d) the trap-depth ΔE_{t}. For the latter, k_{nr} had to be changed to 10^7 s^{-1} to see the impact of the parameter ΔE_{t}. The calculated PL is normalized to the value at $t = 0$ ns.

Very little effect could be observed when n_{eq} was changed from 10^{13} to 10^{16} cm^{-3} (see **Figure 6.4(a)**). It is known to affect the change between "high-injection" and "low-injection" recombination regimes, which may not have been reached at the excitation fluence of 5×10^{10} cm^{-2}.[151,152] Reabsorption is known to affect the earlier PL decay times without affecting the shape of the later time decay.[56,173–175] This effect can also be observed in **Figure 6.4(b)**), where α_{reab} has been changed from 10^3 to 10^7 cm^{-1}.

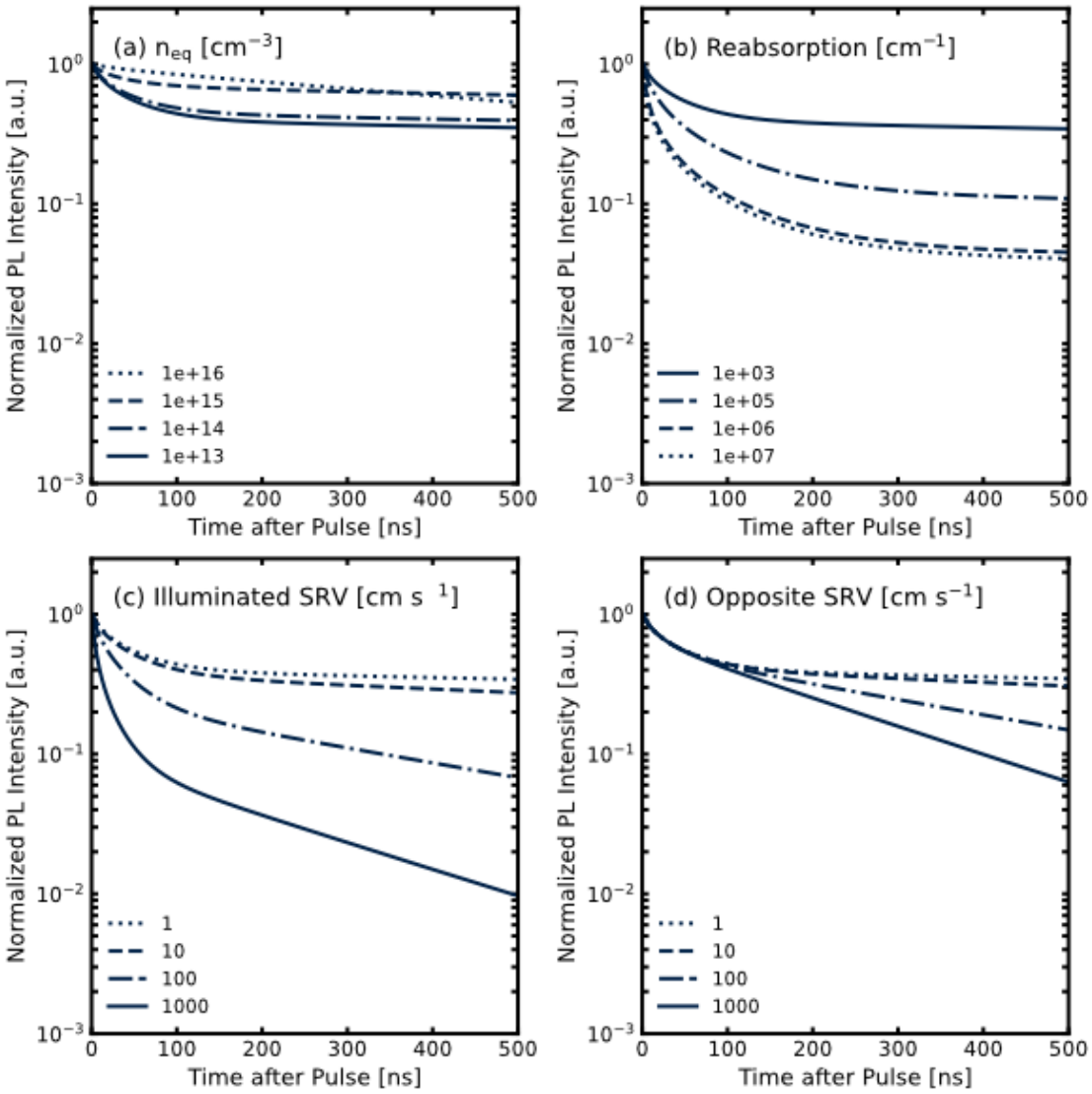

Figure 6.4: The PL decay is simulated for a fixed set of parameters (d: 500 nm, $F(h\nu)$: 5×10^{10} cm^{-2}, $\alpha(h\nu)$: 10^5 cm^{-1}, μ: 0.1 cm^2 V^{-1} s^{-1}, S_i: 0.1 cm s^{-1}, $k_{2,\mathrm{rad}}$: 10^{-10} cm^3 s^{-1}, k_{nr}: 10^5 s^{-1}, ΔE_{t}: 0.6 eV, n_{eq}: 10^{13} cm^{-3} and α_{reab}: 1 cm^{-1}), where one parameter is changed: (a) n_{eq}, (b) α_{reab}, (c) S_{front}, and (d) S_{back}. The calculated PL is normalized to the value at $t = 0$ ns.

The effect of changing either of the S_i between 1 and 1000 cm s^{-1} is shown in **Figure 6.4(c)**) and **(d)** for the illuminated and opposite surface, respectively. While both affected the later time decay equally, only the illuminated surface had an impact on the early times of the PL decay. The effects of each parameter on the PL decay are summarized in **Table 6.1**. Running the inference algorithm on the early- and later time data simultaneously over a range of fluences allowed the inference of all parameters.

Table 6.1: The effect of each parameter on the shape of the final PL decay.

Parameter	Effect on the PL Decay Shape		
	early time	late time	curvature
D or μ	x		
S_{front}	x	x	
S_{back}		x	
$k_{2,\text{rad}}$	x	x	x
n_{eq}	x		x
k_{nr}		x	
ΔE_{t}		x	x
$\alpha_{\text{reab, } i}$	x		x

Priors and their Impact on the Sampling Efficiency

The prior distribution of a parameter is the initial sampling probability distribution to start off the MCMC chains. A good prior includes all prior knowledge that is present about a parameter before any of the data is observed. It is not straightforward to construct good priors. A naïve choice for an uninformative prior, where nothing is known about the parameter, is a uniform distribution between two boundary values. This can however lead to issues at the boundaries of the distribution, where the probability drops to zero, which may result in biased posterior distributions.[294] Instead, weakly informative priors, like a wide normal distribution should be used. Imposing some weak prior knowledge is not a problem, because the impact of observing data on the likelihood and posterior distribution will always outweigh the prior.[294] In reality, some knowledge about a parameter is always present and an unbiased prior can be constructed.

In this work most parameters needed to be able to vary over multiple orders of magnitude and mainly three types of priors were constructed: 1) positive-free, 2) positive with an upper or lower boundary and 3) with two boundaries. Since most parameters in the physical model relate to densities or rates, they needed to be limited to positive values. The free prior used in this work

is a lognormal distribution with a σ_{LN} of 2.

$$p_{\mathrm{LN}}(x|\mu,\sigma_{\mathrm{LN}}) = \frac{1}{x\cdot\sigma_{\mathrm{LN}}\sqrt{2\pi}}\cdot e^{-\frac{(\ln(x)-\mu)^2}{2\sigma_{\mathrm{LN}}^2}} \tag{6.16}$$

The center value, μ was set to a realistic value for the parameter, for example in the case of the equilibrium carrier concentration (n_{eq}) $\mu = 25$, which corresponds to a value of 7.2×10^{10} cm^{-3} (see **Table 6.2**).

For some parameters a one-side-bounded-prior was needed to improve the efficiency of the sampling. The reason for this is that the time resolution of the data limits the the resolution of the sampling as well and for example recombination rates above a certain value all have a similar likelihood and posterior. This makes it difficult for the MCMC algorithm to traverse these regions, where the gradient in the posterior is low. The result is that chains with starting values in these regions often do not move at all for the first few 1000s of samples. To avoid this from happening, a realistic "upper bound"-prior can be defined as

$$p_{\mathrm{ub}}(x|\mu,\sigma_{\mathrm{LN}},ub) = \frac{ub}{1+p_{\mathrm{LN}}(x|\mu,\sigma_{\mathrm{LN}})} \tag{6.17}$$

where ub is the upper bound value. Similarly a "lower bound"-prior can be defined as

$$p_{\mathrm{lb}}(x|\mu,\sigma_{\mathrm{LN}},lb) = lb\cdot(1+p_{\mathrm{LN}}(x|\mu,\sigma_{\mathrm{LN}})) \tag{6.18}$$

Some parameters needed to be restrained to real physical limits and were described by a beta distribution prior with $\alpha=\beta=2$, which puts the highest probability of the distribution in the center.

$$p_{\mathrm{b}}(x|\alpha,\beta) = \frac{x^{\alpha-1}(1-x)^{\beta-1}}{B(\alpha,\beta)} \tag{6.19}$$

Here, B is the beta-function. Parameters that were describes as this included the trap depth, which is physically limited to be within 1 eV from the conduction or valence band (see **Table 6.2**). Alternatively, the same effect could also be achieved by an "upper-bound"-prior with $ub = 1$.

Lastly, the parameters related to the noise floor had a half-normal distribution prior. Again, this

parameter needed to have only positive values, but now zero had to be part of the value space:

$$p_{\mathrm{HN}}(x|\sigma_{\mathrm{HN}}) = \frac{1}{\sigma_{\mathrm{HN}}\sqrt{2\pi}} \cdot e^{-\frac{x^2}{2\sigma_{\mathrm{HN}}^2}} \tag{6.20}$$

A summary of all the parameters used is shown in **Table 6.2**.

The Likelihood Function

The statistics underlying the Bayesian inference algorithm are important to understand as well in order to maximize its efficiency during sampling. The likelihood function quantifies the probability of observing a given set of data under a set of parameters and is the way that data has an impact on the posterior distribution.[294] The choice of the likelihood function can greatly influence the outcome of the inference. Special care needs to be taken when dealing with data that spread over multiple orders of magnitude, as in the case of TRPL. The likelihood function used here was a normal distribution of the logarithm of the data and the calculation, so that both, early-time and late-time effects could contribute significantly to the posterior distribution.

$$\log(L(x_{\mathrm{s}}, \sigma_{\mathrm{L}}|x_{\mathrm{d}})) = -\log\left(\frac{1}{\sigma_{\mathrm{L}}\sqrt{2\pi}}\right) \cdot \frac{\left(\log(x_{\mathrm{d}}) - \log(x_{\mathrm{s}})\right)^2}{2\sigma_{\mathrm{L}}^2} \tag{6.21}$$

where x_{s} and x_{d} are the simulated and observed data points, respectively and σ_{L} is the standard deviation. In other words, $L(x_{\mathrm{s}}, \sigma_{\mathrm{L}}|x_{\mathrm{d}})$ is the likelihood that a simulated point x_{s} with standard deviation σ agrees with an observed data point x_{d}. In nuance, this is different from the probability of observing the data point x_{d} with a specific value x_{s} and standard deviation σ_{L} (which would be $P(x_{\mathrm{d}}|x_{\mathrm{s}}, \sigma_{\mathrm{L}})$)). In reality, both of them result in the same distribution hence in the rest of the chapter, "likelihood" is used when talking about the relation of the model calculation and data, while "probability" is used when parameters are assessed.

It has been described in previous work that the standard deviation σ_{L} affects the spread of the likelihood function and hence the efficiency of the sampling.[152,293] For a σ_{L} that is too large a lot of samples need to be taken to infer accurate parameters, while for a σ_{L} that is too small the MCMC algorithm will be unable to effectively explore the full parameter space. To overcome this issue, σ_{L} was also set a free parameter in this work (see **Table 6.2**).

The log-likelihood of a data set of simulated points is obtained by summing the log-likelihoods of the individual, simulated points. The log-likelihoods of the individual points needed to be weighed by the observed data (see **Equation 6.22**). This was necessary for good inference when using multiple data sets, where at least one decays faster than the other.

$$\log(L(S, \sigma_{\mathrm{L}}|D)) = \sum x_{\mathrm{d}} \cdot \log(L(x_{\mathrm{s}}, \sigma_{\mathrm{L}}|x_{\mathrm{d}})) \tag{6.22}$$

where S and D are the simulated and observed data set, respectively.

The number of datapoints used in **Equation 6.22** as well as their spacing of points where the likelihood is evaluated greatly affect the outcome of the Bayesian Inference. Thus, the impact of different spacings was tested here. First, a "linear" spacing was used, in which all time points were used for the calculation of the PL and evaluation of $\log(L(S, \sigma_{\mathrm{L}}|D))$. This was compared to four different spacings of evaluated data points: 1) "squared" spacing, where the next time point is $t_{i+1} = t_i^2$, 2) "golden ratio" spacing, where the next time point is $t_{i+1} = t_i + t_{i-1}$ and 3) "log-spaced" time points. In the latter case the number of time points were chosen to match either the "squared" ("log-85") or "golden ratio" ("log-20") spacing. Then, 10 MCMC chains were run in parallel with 10k samples each. The median calculated PL of the last 1000 samples of each chain is shown in **Figure 6.2(a)** alongside a set of measured TRPL data from the material- and substrate-side. It can be observed that both the "linear" and "squared" spacing over-estimate the initial drop in PL intensity, while "log-85", "log-20" and "golden ratio" spacing capture this much better.

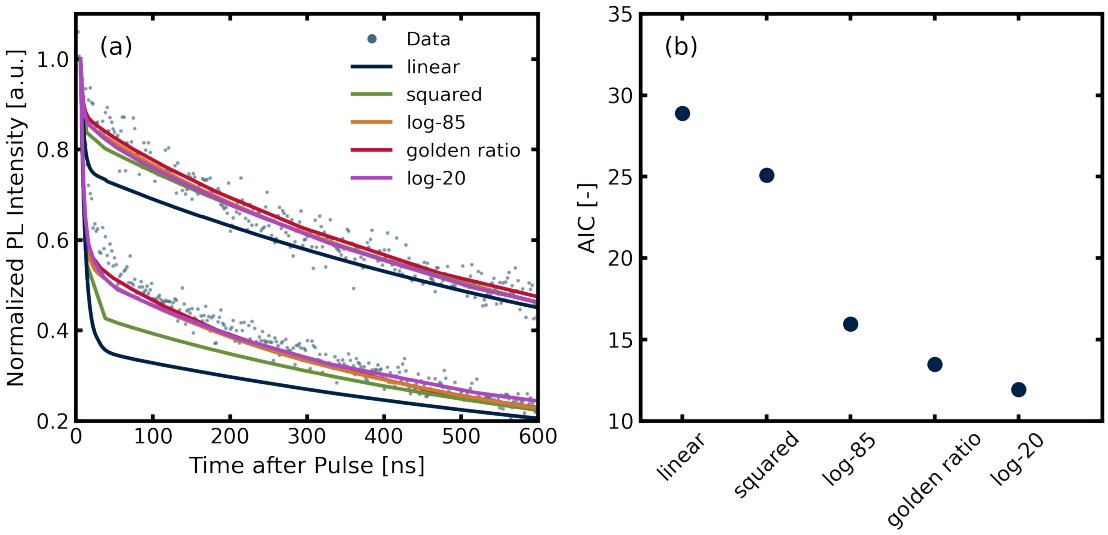

Figure 6.5: (a) The first 500 ns of a set of test data measured at one fluence from both sides of the sample is shown alongside the obtained median of the model assessments for each data point spacing. The data has been normalized to the number of PL counts at the second data point ($t = 4$ ns).(b) The corresponding AIC for each data point spacing is shown. The lower the AIC, the better suited the model to describe this set of data.

In order to quantify, how "well" the model calculations describe the data, the log-likelihood $\log(L(S, \sigma_L|D))$ can be used. It is important to understand that $\log(L(S, \sigma_L|D))$ will be highly dependent on the number of time points, as it is defined by the sum of all points. So, in order to be able to compare the different spacings, again, the AIC (**Equation** 6.15) was used. In **Figure 6.2(b)** the different AICs are shown for all the spacings tested here. It becomes apparent that the "log-20" spacing shows the lowest AIC, despite the fact that it has the lowest number of data points, due to the much improved agreement of the PL calculation and the data. In addition to this, the "log-20" is also nearly 20 times faster, due to the fact that only 20 time points need to be simulated instead of the full 9000. A typical run of 10 parallel MCMC chains with 10k samples, each would thus run in less than 2 hours. For the rest of this chapter "log-20" was used.

Table 6.2: The priors of parameters used in the final model are described here.

Parameter	Prior	
	Diffusion	
D	lower bound:	$\mu = 2$; $\sigma_{\mathrm{LN}} = 2$; $lb = 10^{-4}$
S_{sum}	lower bound:	$\mu = 0$; $\sigma_{\mathrm{LN}} = 2$; $lb = 1$
b	beta:	$\alpha = 2$; $\beta = 2$
	Recombination	
$k_{2,\mathrm{rad}}$	upper bound:	$\mu = 1$; $\sigma_{\mathrm{LN}} = 3$; $ub = 10^{-8}$
n_{eq}	lognormal:	$\mu = 25$; σ_{LN}=2
k_{nr}	lognormal:	$\mu = 11$; σ_{LN}=2
ΔE_{t}	beta:	$\alpha = 2$; $\beta = 2$
	Reabsorption	
$\alpha_{\mathrm{reab},i}$	lognormal:	$\mu = 4$; $\sigma_{\mathrm{LN}} = 2$
	Errors	
ϵ_{PL}	halfnormal:	σ_{HN}=10^{-3}
ϵ_{F}	beta:	$\alpha = 2$; $\beta = 2$
	Hyper-Parameters	
σ_{L}	upper bound:	$\mu = 1$; $\sigma_{\mathrm{LN}} = 2$; $ub = 0.05$

6.3 PART II - RESULTS AND DISCUSSION

$FAPbI_3$ Thin Films

After establishing the functionality of the method of combining Bayesian inference with a Markov-Chain Monte-Carlo algorithm (Bayes-MCMC), $FAPbI_3$ thin films were used as a model system to demonstrate the approach and understand the limitations of it. The $FAPbI_3$ thin films were optimized and fabricated by Dr. Seonrok Seo (University of Oxford). The recipe was optimized for the n-type-intrinsic-p-type (n-i-p) architecture, but the films were fabricated on glass for this chapter. The sample was measured from the substrate- and material-side (S1 and S2, respectively) with a 398 nm (3.12 eV) excitation laser at a repetition rate of 50 kHz at two fluences (1.5×10^{11} and 4.8×10^{11} cm^{-2}). The high energy excitation was used in order to obtain charge generation predominantly near the illuminated surface. Then, the assessment of a full set of front- and back-illuminated samples should allow for the inference of all parameters of the physical model. The film thickness was measured to be approx. 600 nm and $\alpha(3.12eV) = 3 \times 10^5$ cm^{-1} using spectroscopic ellipsometry. The ellipsometry measurement and analysis of the data was performed by Akash Dasgupta (University of Oxford).

The Bayes-MCMC algorithm was run with the "simple" reabsorption model. 10 MCMC chains were run in parallel for 10k samples. First, it needed to be established, if the MCMC algorithm had converged onto a region of high likelihood. For each sample taken, the log-likelihood was hence estimated following **Equation 6.22** and using the "log-20"- spacing. The maximized likelihood corresponds to the minimized, negative log-likelihood. In **Figure 6.6(a)** the negative log-likelihood is plotted as a function of sample number. Within the first 100 samples, the log-likelihood decreased by a factor of approx. 10^4. Over the rest of the samples it stabilized around a value of 1200 ± 220 (average over the last 1000 values of each chain). To reduce the number of results used for further investigations, only the last 1000 samples of each chain were saved. In order to assess the "fit" of the Bayes-MCMC approach to the data, the median TRPL decay ('median line') of these samples was calculated and plotted alongside the measured TRPL decay

traces in **Figure 6.6(b)**. A good agreement between the data and the median line can be observed across all timescales. It is worth mentioning, that this is the first time in this thesis, that a single, physical model could simultaneously "fit" to the early- and later times of a set of TRPL decay traces. For each parameter a probability distribution is obtained (the collection of all parameters is shown in **Appendix B**). The inferred parameters are summarized in **Table 6.3**.

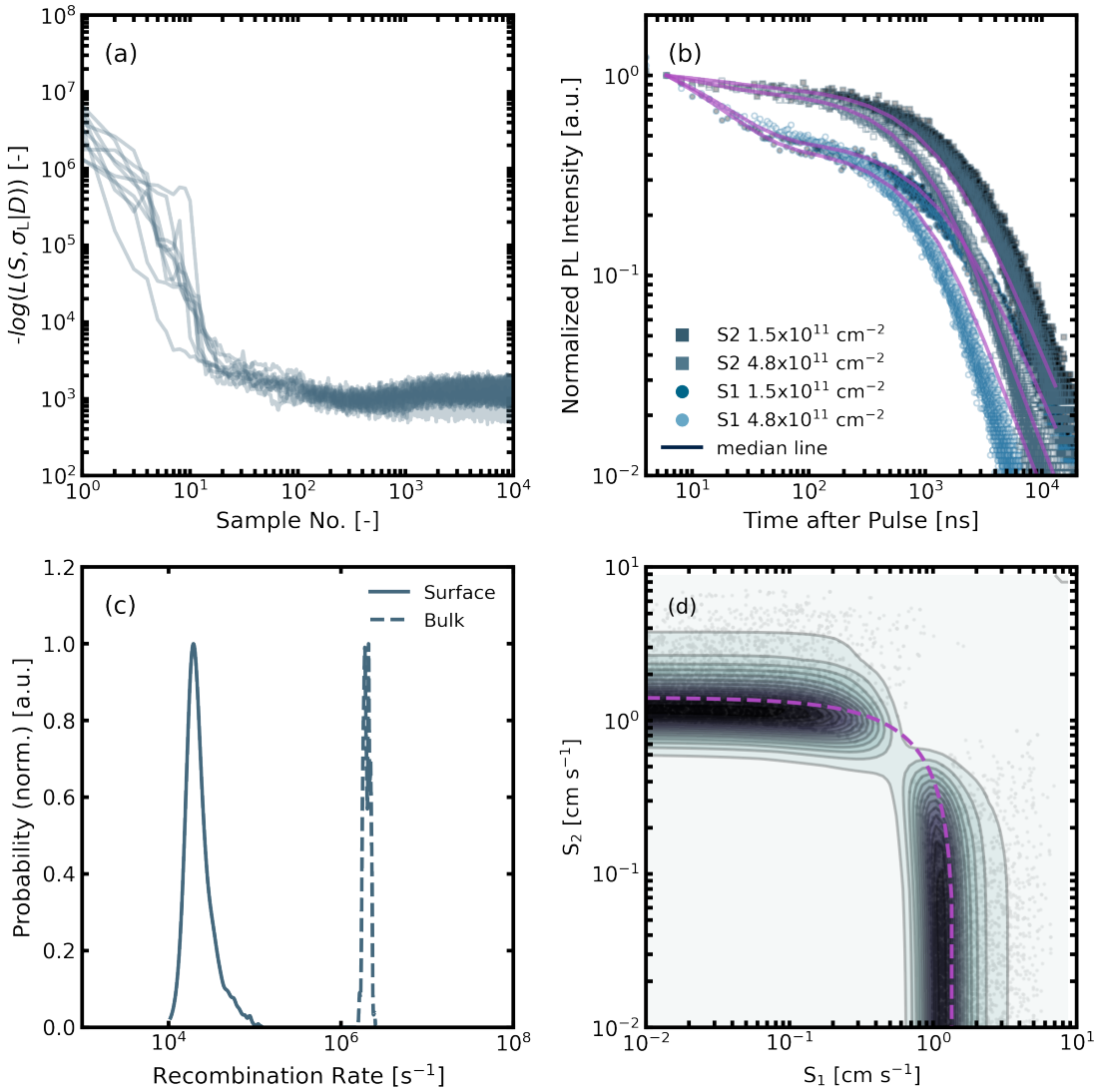

Figure 6.6: (a) Negative log-likelihood for the $FAPbI_3$ sample assessed here as a function of the sample number along 10 individual Markov chains (shown as individual lines). The lower the negative log-likelihood, the better the agreement between data and model. (b) The set of TRPL data measured from the substrate (S1) and perovskite (S2) side for two fluences (1.5×10^{11} and 4.8×10^{11} cm^{-2}), each. The data has been normalized to the number of PL counts at the second data point ($t = 4$ ns). The pink lines indicate the median TRPL calculated from the last 1000 samples of the 10 Markov chains ('median line'). (c) The normalized probability distributions of the surface- and bulk non-radiative recombination rate are shown side-by-side. (d) The two surface recombination velocities (S_1 and S_2) are shown in a 2D cornerplot. The darker the color, the higher the likelihood of this region. Faint, grey spots indicate the underlying, samples values. The dotted, pink line follows the relation $S_{sum} = S_1 + S_2$.

An initial drop in the PL intensity can be observed for the illumination from S1. A high SRV at the perovskite-glass interface has been observed in a previous study.[298] There, recombination at the illuminated surface, together with charge carrier diffusion was postulated to be the main reason for the observed early-time drop in PL intensity. Here, the same behaviour in PL was observed, so this was investigated in more detail as well.

First, the surface non-radiative recombination rate was calculated via[151]

$$k_{\mathrm{nr,S}} = \frac{S_{\mathrm{sum}}}{d} \tag{6.23}$$

where $k_{\mathrm{nr,S}}$ is typically associated with the long-term surface recombination rate after charge carrier homogenization. Hence, it impacts the later times of the decay, which are also influenced by k_{nr}. In **Figure 6.6(c)** the normalized probability density of the inferred $k_{\mathrm{nr,S}}$ (surface) is compared to that of k_{nr} (bulk). The recombination rate associated with the bulk of the material had a peak at $(2.0 \pm 0.2) \times 10^6$ s^{-1} and the one associated with the surface $(3.0 \pm 1.8) \times 10^4$ s^{-1}. This result indicated that the bulk recombination dominated the TRPL decay at the longer times. While this in itself was a useful result, it could also help to guide optimization process of a particular perovskite composition, for instance whether or not a surface passivation would improve the material properties. In the case presented here, an improvement of the bulk of the material might be the better strategy to reduce the non-radiative recombination. Overall, it is worth to mention that in this particular case, a S_{sum} of 1.8 ± 1.1 cm s^{-1} was inferred, which was already among the lowest reported values in the literature and is associated with high device performance.[47,254,299]

Despite this outstanding result, it does not further the understanding of how the surface recombination impacts the early-time decay. Thus, first the parameter b was assessed, which controls the difference of S_1 and S_2 (the smaller b, the larger the difference of the two SRVs). Here, a b- parameter of 0.09 ± 0.14 was inferred, indicating that the two surfaces are different. The two individual surface recombination rates S_{high} and S_{low} could then be calculated from the knowledge of S_{sum} and b via

$$S_{\mathrm{low/high}} = \frac{S_{\mathrm{sum}} +/- \sqrt{S_{\mathrm{sum}}^2 \cdot (1-b)}}{2} \tag{6.24}$$

The Markov chain chooses, if $S_1 = S_{\mathrm{low}}$ and $S_2 = S_{\mathrm{high}}$ or vice versa in accordance with Bayes‘

Theorem to maximize the likelihood. As the Markov-chain sampling had converged onto a high-likelihood region, a two-dimensional corner plot of S_1 and S_2 could reveal, which one was the surface with the higher SRV. The resulting 2D corner plot is shown in **Figure 6.6(d)**, where the darker color indicates higher probability. It can be seen that the plot is symmetric about a diagonal line. This behaviour had been previously reported for the case of one-sided illumination where S_1 and S_2 could not be differentiated.[152] The same effect was observed here, where the 2D cornerplot shows the limiting cases for $S_1 = S_{\text{sum}}$ or $S_2 = S_{\text{sum}}$. The pink, dotted line represents $S_{\text{sum}} = S_1 + S_2$. It became apparent that the set of data used here was not sufficient to resolve the individual SRVs. It should be noted that this statement is extremely impactful as it means that one could not determine which surface has which recombination velocity - it is non-identifiable. As mentioned in **Chapter 3** this can have implications when a frequentist approach, like a least-squares fit, is used instead. In that case, the initially guessed values of S_1 and S_2 will determine the outcome of the fitting algorithm. The Bayes-MCMC approach makes it possible to instead report the non-identifiability as a feature of this dataset.[190]

Still, the drop in PL intensity was observed, when the sample is illuminated from S1, but it would be naïve to therefore ascribe the higher SRV to S_1 as was just shown. Instead, other parameters might be different for the two surfaces. The errors on the fluence ϵ_{F} were estimated to be 1.9% for the S1-side and 3.1% for the S2-side. These values could hence not explain the observed PL behaviour. Instead, the reabsorption constants were compared, which were $(5.9 \pm 0.7) \times 10^5$ cm^{-1} and $(3.7 \pm 2.6) \times 10^4$ cm^{-1} for $\alpha_{\text{reab,1}}$ and $\alpha_{\text{reab,2}}$, respectively. As was shown in **Figure 6.4(b)** an increased α_{reab} could result in a more pronounced drop of the PL intensity at early times, while not affecting the decay at later times significantly. Therefore, the results of the Bayes-MCMC method indicated that it was reabsorption rather than surface recombination, which determined the early-time decay in this particular example. While both effects could result in an early-time drop of the PL intensity, taking the entire decay into account made the reabsorption the more likely mechanism.

Now it could be speculated, why the reabsorption would be different from the two surfaces. It could simply be due to a difference in internal reflectance at the two interfaces, but a detailed investigation was not part of this study. Instead this example was used to showcase the amount

of information that can be inferred from a simple, optical measurement and how the results of the Bayes-MCMC method may be used to inform further experiments.

Half-Stacks of $FAPbI_3$ Thin Films

The low surface recombination of < 2 cm s^{-1} inferred in the previous section made this material an ideal model system to investigate the impact of charge transport layers (TL), like SnO_2 and Spiro-OMeTAD (here: Spiro), which are common materials used in photovoltaic devices with the n-i-p architecture. The samples were made by Dr. Seongrok Seo (University of Oxford) after careful optimization for the n-i-p architecture. Each sample was illuminated from the substrate side with two fluences of 1.5×10^{11} and 4.8×10^{11}cm^{-2}, but for the illumination from the material side only the higher fluence could be measured sufficiently. The resulting data and calculated median TRPL decay of the last 1000 samples are shown in **Figure 6.7(a)** and **(b)** for SnO_2 and Spiro, respectively.

The SnO_2 sample showed long PL decays, while for the Spiro sample, the PL intensity was quickly reduced over the first few hundred nanoseconds for all fluences. The latter had been previously ascribed to PL quenching due to a high interfacial recombination rate at the perovskite-Spiro interface.[47] Again, the median of the calculated TRPL decay from the last 1000 samples of each chain is shown as a pink line alongside the data. All inferred parameters are summarized in **Table 6.3**. The non-radiative surface- and bulk recombination rates ($k_{\mathrm{nr,S}}$ and k_{nr}) of the two TL samples as well as the neat perovskite on glass are compared in **Figure 6.7(c)**. The inferred non-radiative bulk rates were $(2.0 \pm 3.1) \times 10^6$ and $(2.3 \pm 1.2) \times 10^7$ s^{-1}, for SnO_2 and Spiro, respectively. This time, the two surfaces (S1 and S2) could be differentiated by the Bayes-MCMC algorithm and are 4 ± 4 and 0.5 ± 0.8 cm s^{-1} for S_1 and S_2, respectively in the case of SnO_2 and 29 ± 52 and 328 ± 460 cm s^{-1} for S_1 and S_2, respectively in the case of Spiro. It is worth mentioning, that SnO_2 was indeed interfaced with the S_1 surface and Spiro with the S_2 surface. The Bayes-MCMC algorithm could correctly locate them from this set of measurements.

While these results are promising, they again required further investigation. For instance, the SRV at the perovskite-Spiro interface of a few hundred cm s^{-1} was significantly lower than previously

reported.[47] At the same time, an increase in the non-radiative bulk recombination k_{nr} for the Spiro sample seemed counter-intuitive for the fact that the Spiro was processed on top of the perovskite on glass. Hence, the validity of the model and the Bayes-MCMC approach had to be tested with another method at this point. intensity-dependent PLQE measurements were performed for each sample (glass, SnO_2 and Spiro) inside an integrating sphere as described in **Chapter 3**. The samples were illuminated with a 450 nm (2.76 eV) continuous-wave laser from the substrate side. The data is shown in **Figure 6.7(d)** as empty circles and triangles. All samples showed a monotonically increasing PLQE with increasing absorbed photon flux, as described by **Equation 3.9** for materials with a majority of free charge carriers. The "one-sun"-condition for this material can be found at an absorbed photon flux of around 10^{17} $\mathrm{cm^{-2}\,s^{-1}}$. There, a reduced PLQE for both the SnO_2 and Spiro sample with respect to the sample on glass could be observed. In addition, half-stack samples are often assessed via the slope of the intensity-dependent PLQE data (ideality factor), which was also linked to an enhanced interfacial recombination.[300]
From the inferred parameters from the Bayes-MCMC approach the expected PLQE response could be simulated. Under the continuous-wave illumination, recombination and charge generation lead to a steady-state ($\frac{dn}{dt} = 0$) charge carrier density n_{ss}, which can be estimated by solving:

$$\frac{dn(t)}{dt} = 0 = G - k_{2,\mathrm{rad}} \cdot \left(n_{\mathrm{ss}}^2 + n_{\mathrm{ss}} \cdot n_{\mathrm{eq}}\right) - k_{\mathrm{nr}} \cdot (n_{\mathrm{ss}} \cdot (1 - f_{\mathrm{t}}) + f_{\mathrm{t}} \cdot n_{\mathrm{e,n}}) - \frac{S_{\mathrm{sum}}}{d} \cdot n_{\mathrm{ss}} \qquad (6.25)$$

where G is the absorbed photon flux leading to charge carrier generation and $f_{\mathrm{t}} = \frac{n_{\mathrm{ss}}}{n_{\mathrm{ss}}+n_{\mathrm{e,n}}}$. The steady-state carrier density then needs to include the density of de-trapped charge carriers $n_{\mathrm{e,n}}$ as well. Thus, $n_{\mathrm{ss,eff}} = n_{\mathrm{ss}} + f_{\mathrm{t}} \cdot n_{\mathrm{e,n}}$. Then, the internal PLQE can be calculated via

$$\eta_{\mathrm{QE,calc}} = \frac{k_{2,\mathrm{rad}} \cdot \left(n_{\mathrm{ss,eff}}^2 + n_{\mathrm{ss,eff}} \cdot n_{\mathrm{eq}}\right)}{k_{2,\mathrm{rad}} \cdot \left(n_{\mathrm{ss,eff}}^2 + n_{\mathrm{ss,eff}} \cdot n_{\mathrm{eq}}\right) + \left(k_{\mathrm{nr}} + \frac{S_{\mathrm{sum}}}{d}\right) \cdot n_{\mathrm{ss,eff}}} \qquad (6.26)$$

In total, 500 random combinations of parameters were chosen from all tested parameter combinations during the Bayes-MCMC run. This allowed for the simulation of the internal PLQE including a statistical error. Since the observed escape probability P_{esc} is different in an integrating sphere and thus the reabsorption properties inferred from the TRPL data could not be used here, the simulated, internal PLQE was normalized to the measured, external PLQE at the "one-sun"-condition. The result is presented alongside the measured data in **Figure 6.7(d)** as

full circles and triangles where the errorbars correspond to the standard deviation of the PLQE simulated with 500 independent parameter combinations.

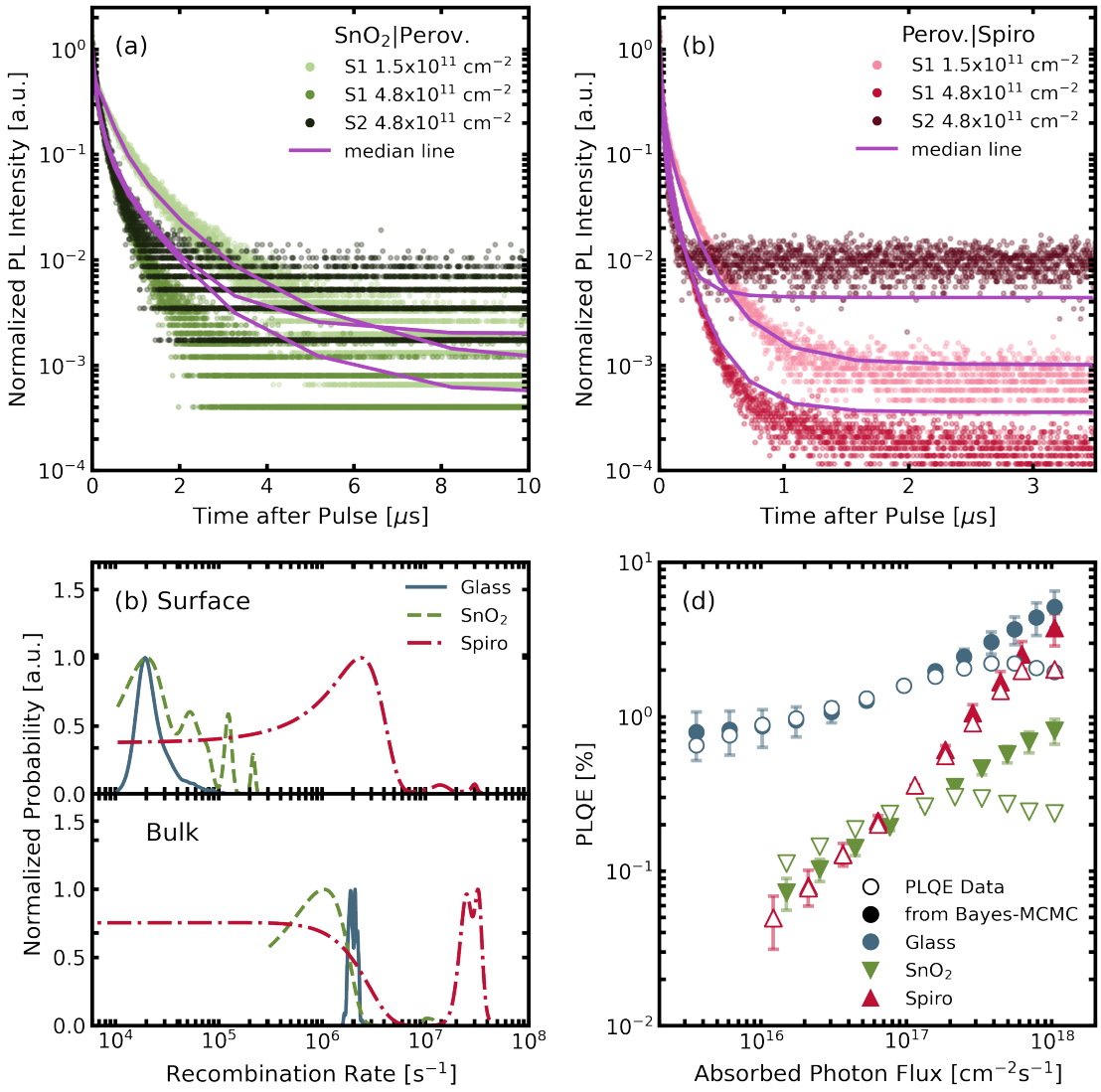

Figure 6.7: TRPL decays of a half-stacks of (a) SnO_2|$FAPbI_3$ and (b) $FAPbI_3$|Spiro-OMeTAD measured from the substrate (S1) and perovskite (S2) side with two excitation fluences (1.5×10^{11} and 4.8×10^{11} cm^{-2}). The data has been normalized to the number of PL counts at the second data point ($t = 4$ ns). (c): The surface (top) and bulk (bottom) non-radiative recombination rates are compared in the same plot for all samples. (d): The measured (empty) and simulated (full) intensity-dependent PLQE for all samples is shown. For the simulated PLQE, 500 random samples were drawn from the posterior distributions of the parameters. The PLQE was then normalized to the measured PLQE at 10^{17} cm^{-2} s^{-1}

A surprisingly good agreement between the simulated and measured PLQE could be observed for absorbed photon fluxes below the "one-sun"-condition. At higher fluences the simulation overestimated the PLQE, which indicated that there was an additional non-radiative decay mechanism, which was not included in the current physical model. Auger recombination could be one mecha-

nism, however the measured, external PLQE drop-off occurs at relatively low photon fluxes.[170,171] The good agreement for the lower photon fluxes indicated that a coupled methodology, in which the TRPL and intensity-dependent PLQE are used simultaneously to infer parameter values, could be a valuable tool to develop new physical models to understand the origin of this observed PLQE drop-off. This was however far beyond the scope of this work.

The comparison to the intensity-dependent PLQE data had increased the statistical significance of the parameter values inferred from the Bayes-MCMC methodology. Thus, the obtained parameters and their correlations were studied in more detail to help understand the discrepancy between them and the reported literature values. Upon close inspection it could be seen in **Figure 6.7(c)** that for the Spiro sample some probability density of the $k_{\mathrm{nr,S}}$ was at the same value of the k_{nr} and vice versa. This could be an indication for a mixture of both parameters within the frame of the physical model. To understand this, first a 2D corner plot of the surface $k_{\mathrm{nr,S}}$ and the bulk k_{nr} for the perovskite on glass was analyzed. It is shown in **Figure 6.8(a)** where a darker color indicates a higher probability. It can be seen that a region of high probability is very localized in both parameters.

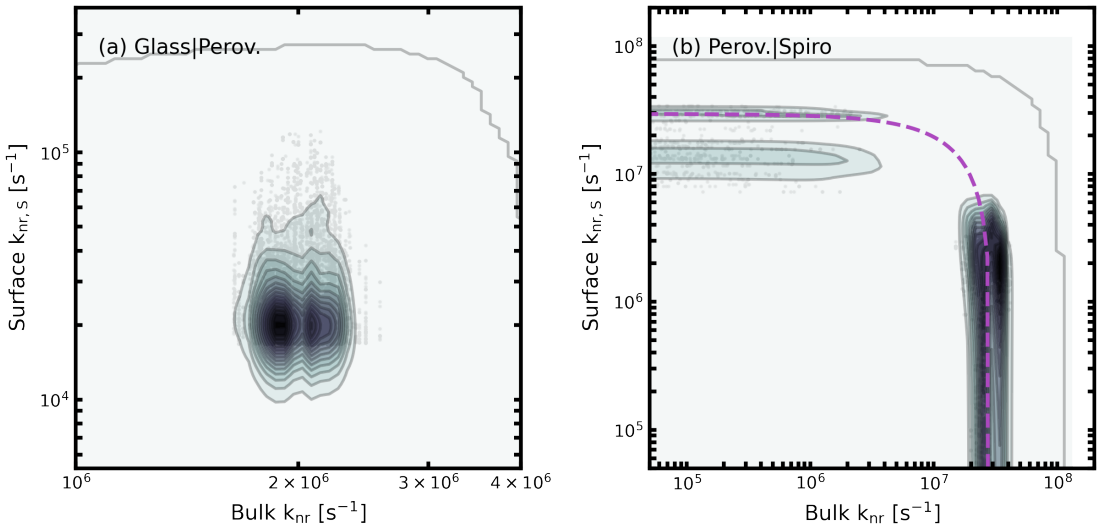

Figure 6.8: The non-radiative surface ($k_{\mathrm{nr,S}}$) and bulk (k_{nr}) recombination are shown in a 2D cornerplot. The darker the color, the higher the likelihood of this region. Faint, grey spots indicate the underlying, samples values. The plots are shown for the (a) perovskite sample on glass and (b) the perovskite-Spiro sample. The dotted, pink line follows the relation $k_{\mathrm{nr,tot}} = k_{\mathrm{nr}} + k_{\mathrm{nr,S}}$.

In contrast, the same 2D cornerplot is shown for the Spiro sample in **Figure 6.8(b)**. The proba-

bility distribution shows a similar shape to the one previously seen in **Figure 5.6(d)**, where two limiting cases exist that are linked by the sum of the individual parameters. Hence, the condition $k_{\mathrm{nr,tot}} = k_{\mathrm{nr}} + k_{\mathrm{nr,S}}$ is shown as a pink, dotted line **Figure 6.8(b)** as well. This correlation has been known to exist, as both non-radiative surface- and bulk recombination determine the longer time PL decay.[150,151,301] Thus, in the the two limiting cases the PL decay is either determined by the surface or the bulk. In this particular example a higher probability was found for the bulk-limiting case. Interestingly, if on the other hand the surface recombination would be the determining mechanism, then it would correspond to an SRV of 1503 ± 347 cm s^{-1}, which is much closer to the reported literature values.[47] This coincidence and the results presented here pointed towards a more general issue, where the assumptions made in the beginning overpower the observations and hence led to over-interpretation of the data.

In short, the model assumed a continuous block of material throughout the thickness of the sample with two distinct surfaces as boundary conditions. This is clearly no longer the case, when polycrystalline thin films are considered. The "surface" is then less clearly defined and grain boundaries are not part of the model. In such a case it could be possible that a top-surface layer, such as the Spiro-OMeTAD layer not only coats the "surface", but also penetrates into the "bulk" (as assumed by the model) via grain boundaries. In such a case the strict differentiation between surface and bulk might get more blurry and could lead to the correlation between the parameters that is observed in **Figure 6.8(b)**. It is however the part of future research to investigate this further and help understand the impact of other top-surface transport layers on the inferred correlation between "surface" and "bulk".

Table 6.3: All inferred parameter values are summarized here. The values are either presented as X (A,B), where X is the median of the posterior distribution and A and B are the 25% and 75% quantile, respectively or as $\leq$ X, when only an pper limit could be determined.

Parameter	Sample		
	Glass	SnO_2	Spiro
μ ($cm^2\,V^{-1}\,s^{-1}$)	0.75 (0.69, 0.86)	≤ 0.2	0.16 (0.13, 0.20)
S_1 ($cm\,s^{-1}$)	low: ≤ 0.03	≤ 8.2	≤ 16.0
S_2 ($cm\,s^{-1}$)	high: 1.38 (1.12, 2.04)	≤ 1.4	150 (114, 190)
Recombination			
$k_{2,rad}$ ($cm^3\,s^{-1}$)	7 (3, 12) x 10^{-13}	7 (6, 10) x 10^{-11}	$\leq 9 \times 10^{-10}$
n_{eq} ($cm\,s^{-1}$)	2.4 (1.9, 3.3) x 10^{16}	$\leq 1 \times 10^{12}$	$\leq 9 \times 10^{11}$
k_{nr} (s^{-1})	2.0 (1.9, 2.1) x 10^6	1.1 (0.6, 1.5) x 10^6	2.6 (2.1, 3.2) x 10^7
ΔE_t (eV)	160 (160, 170)	190 (180, 210)	140 (140, 160)
Reabsorption			
$\alpha_{reab,1}$ (cm^{-1})	6 (6, 6) x 10^4	$\leq 3 \times 10^3$	$\leq 7 \times 10^2$
$\alpha_{reab,2}$ (cm^{-1})	4 (3, 6) x 10^3	$\leq 8 \times 10^3$	$\leq 5 \times 10^3$

About the Mobility Relevant for Photovoltaic Devices

Another property, which could be inferred from the Bayes-MCMC methodology is the mobility, which was also measured with other methods presented in this thesis, namely TPC and OPTP. Hence, the same perovskite sample on glass that was used for the TRPL measurement was also used for a set of TPC measurements, by evaporating 80 nm gold electrodes on the top. Two additional samples of the same batch were added, in order to improve the statistical significance of the results. The sample was illuminated with a 550 nm (2.25 eV), pulsed laser from the substrate side to induce homogeneous charge carrier generation throughout the sample thickness. Both interdigitated mask layouts were used (see **Chapter 3** for details). The post-processing of the data developed in **Chapter 4** and refined in **Chapter 2.3** was used here as well and allowed the extraction of $\Sigma\mu$, $k_{1,\mathrm{nr}}$ and $k_{2,\mathrm{rad}}$.

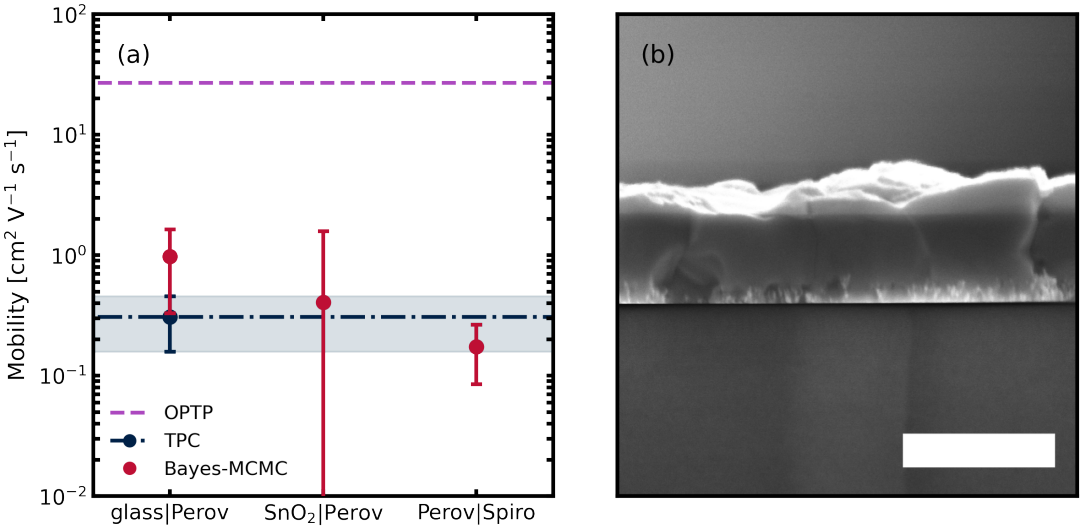

Figure 6.9: (a) Extracted mobility from the TPC method is shown as a dark-blue point and dotted line with the standard deviation shown as shaded area (the error is calculated for 9 fluences and 6 samples). The inferred values from the Bayes-MCMC algortihm is shown in red (the error is calculated from the last 1000 samples of 10 independent Markov-chains). The pink, dotted line represents the short-range mobility for $FAPbI_3$ as measured from OPTP and is taken from 215. (b) Cross-sectional SEM image of the $FAPbI_3$ thin film on a glass substrate is shown to illustrate the high quality of the sample. The white bar corresponds to 1 µm. The cross-sectional SEM was obtained by Heon Jin (University of Oxford).

The extracted parameters from TPC and TRPL are compared in **Table 6.4** and show good agreement between the two techniques. In **Figure 6.9(a)** the resulting mobility from the TPC is shown and compared to the values obtained from the inference of the TRPL data of all three

samples (glass, SnO_2, and Spiro). The results show a good overlap considering that the mobility can span multiple orders of magnitude. This indicated that the Bayes-MCMC method could be used to infer the mobility of the perovskite material while it is interfaced with transport layers. This reduces the effective number of samples needed for optoelectronic investigations. In addition, the perovskite material is believed to crystallize differently, depending on the underlying layer and this can sometimes lead to contradictory results, when comparing half-stack structures with the neat perovskite on glass or quartz.[290,302,303]

Table 6.4: Comparison of the parameters extracted from the TPC measurement with the ones inferred from the TRPL measurement and the Bayes-MCMC method for the $FAPbI_3$ sample on a glass substrate.

Parameter	from TRPL (average of all three samples)	from TPC (average of 54 measurements (3 samples, 9 fluences, 2 pixels))
$\Sigma\mu$ or μ_{TRPL} ($cm^2\,V^{-1}\,s^{-1}$)	0.52 ± 0.85	0.31 ± 0.15
$k_{1,nr}$ or k_{nr} (x10^6 unit)	8.9 ± 1.2	4.8 ± 2.8
$k_{2,rad}$ (x10^{-10} $cm^3\,V^{-1}\,s^{-1}$)	1 ± 2	5 ± 4

In **Figure 6.9a** the mobilities obtained from TPC and TRPL are also compared to the one obtained from optical-pump terahertz-probe spectroscopy (OPTP).[215] Interestingly, both the mobilities from TPC- and TRPL were much lower. It is a common practice in the field to use the mobility from OPTP, together with a measurement of the PL decay lifetime (TRPL) to estimate the diffusion length of charge carriers within the perovskite material.[304] If the results shown here are representative, then this approach would be false, as the mobility that is in better agreement with the TRPL decay is the long-range mobility, as obtained from TPC. To further confirm that this is not an issue of poor material quality, cross-sectional SEM images were taken for the $FAPbI_3$ thin films on glass by Heon Jin (University of Oxford). One representative image is shown in **Figure 6.9(b)**. Large grains spanning the entire thickness of the thin film could

be clearly seen. Nevertheless, the inferred mobility was not the one that is expected for single crystalline materials, which should agree more with the OPTP mobility. This initial result allows for further research into the underlying mechanisms that govern the charge carrier transport in the vertical direction as well.

6.4 SUMMARY AND OUTLOOK

In this chapter the combination of Bayesian inference with a Markov-Chain Monte-Carlo algorithm was shown as a powerful methodology to assess time-resolved photo-luminescence data of metal halide perovskites. A physical model was developed, based on previously reported theory and the hyper-parameters of the inference algorithm were optimized. This included a short study on the complexity of reabsorption that was needed to accurately model the TRPL response. It was shown that a simple exponential decay over the thickness of the sample was sufficient. Then, it could be shown that not all the time points would need to be assessed, but a subset of less than 1% was enough to accurately infer all parameters and in addition increased the overall likelihood of the model.

The newly optimized model and method were then tested on set of TRPL data for a $FAPbI_3$ thin film on glass. The experimental dataset consisted of two measurements at different excitation fluences from the material- and substrate side. Assessing the entire dataset at once allowed the in inference of up to 10 material-specific parameters that were in good agreement with already reported literature values. The results showed some indication that this specific sample was limited in its optoelectronic properties by non-radiative recombination in the bulk of the material rather than the surface. It could be demonstrated that the location of the surface recombination rates were non-identifiable.

The same material was then combined in half-stack structures with SnO_2 and Spiro-OMeTAD as electron- and hole-transporting materials, respectively. The methodology presented here could infer all parameters for these structures as well. Spiro-OMeTAD is known to induce photoluminescence quenching via interfacial surface recombination and the algorithm could correctly determine which surface of the perovskite material was interfaced with the transport layer. Additional investigations revealed a correlation between the surface and bulk recombination in the Spiro sample, which may be more mixed than previously assumed. The impact of the transport layers on the intensity-dependent behaviour of the PLQE was compared to the PLQE response

simulated for a sub-set of 500 parameter combinations drawn from the final probability distributions as obtained from the inference algorithm. The simulated PLQE showed a near-perfect agreement with the measured one for excitation densities around or below the one-sun condition for a bandgap of approx. 1.55 eV.

Lastly, a mobility value could be inferred for all samples measured here and was compared to transient photo-conductivity measurements on the same sample as well as values from literature obtained from optical-pump terahertz-probe spectroscopy. Surprisingly, the inferred mobility values from the TRPL decays were close to the ones measured via the TPC method, which is known to be a longer-range method. These result strongly indicate that the long-range mobility may be the relevant mobility to consider when assessing thin-film-based photovoltaic devices, where the charge transport is in the vertical direction with respect to the substrate.

Overall, the power of Bayesian inference coupled with a Markov-Chain Monte-Carlo algorithm was demonstrated here for TRPL measurements. In the future, this approach could be extended to other measurement techniques, where a multitude of parameters and models exist, but the measurement response is limited, such as for intensity-dependent PLQE or absorption measurements. The TRPL method enhanced with the Bayesian inference algorithm is a powerful technique, which will enable faster assessment of material parameters from a single optical measurement. It is part of ongoing research, to extend this methodology to complete photovoltaic devices, which are otherwise highly complex to investigate.

LIST OF PUBLICATIONS

1. Ultra-narrow room-temperature emission from single $CsPbBr_3$ perovskite quantum dots

Gabriele Rainò, Nuri Yazdani, Simon C. Boehme, **Manuel Kober-Czerny**, Chenglian Zhu, Franziska Krieg, Marta D. Rossell, Rolf Erni, Vanessa Wood, Ivan Infante & Maksym V. Kovalenko

Nature Communications **2022**, 13, 2587. (doi: 10.1038/s41467-022-30016-0)

2. Long-range charge carrier mobility in metal halide perovskite thin-films and single crystals via transient photo-conductivity

Jongchul Lim & **Manuel Kober-Czerny**, Yen-Hung Lin, James M. Ball, Nobuya Sakai, Elisabeth A. Duijnstee, Min Ji Hong, John G. Labram, Bernard Wenger & Henry J. Snaith

Nature Communications **2022**, 13, 4201. (doi: 10.1038/s41467-022-31569-w)

3. Excellent Long-Range Charge-Carrier Mobility in 2D Perovskites

Manuel Kober-Czerny, Silvia Genaro Motti, Philippe Holzhey, Bernard Wenger, Jongchul Lim, Laura Maria Herz, Henry James Snaith

Advanced Functional Materials **2022**, 32, 2203064. (doi: 10.1002/adfm.202203064)

4. Excitons at the Phase Transition of 2D Hybrid Perovskites

Jonas D. Ziegler, Kai-Qiang Lin, Barbara Meisinger, Xiangzhou Zhu, **Manuel Kober-Czerny**, Pabitra K. Nayak, Cecilia Vona, Takashi Taniguchi, Kenji Watanabe, Claudia Draxl, Henry J.

Snaith, John M. Lupton, David A. Egger & Alexey Chernikov

ACS Photonics **2022**, 9, 11, 3609. (doi: 10.1021/acsphotonics.2c01035)

5. Organic solvent free PbI_2 recycling from perovskite solar cells using hot water

Felix Schmidt, Meret Amrein, Sebastian Hedwig, **Manuel Kober-Czerny**, Adriana Paracchino, Ville Holappa, Riikka Suhonen, Andreas Schäffer, Edwin C. Constable, Henry J. Snaith, Markus Lenz

Journal of Hazardous Materials **2023**, 447, 130829. (doi: 10.1016/j.jhazmat.2023.130829)

6. Understanding the Degradation of Methylenediammonium and Its Role in Phase-Stabilizing Formamidinium Lead Triiodide

Elisabeth A. Duijnstee, Benjamin M. Gallant, Philippe Holzhey, Dominik J. Kubicki, Silvia Collavini, Bernd K. Sturdza, Harry C. Sansom, Joel Smith, Matthias J. Gutmann, Santanu Saha, Murali Gedda, Mohamad I. Nugraha, **Manuel Kober-Czerny**, Chelsea Xia, Adam D. Wright, Yen-Hung Lin, Alexandra J. Ramadan, Andrew Matzen, Esther Y.-H. Hung, Seongrok Seo, Suer Zhou, Jongchul Lim, Thomas D. Anthopoulos, Marina R. Filip, Michael B. Johnston, Robin J. Nicholas, Juan Luis Delgado & Henry J. Snaith

J. Am. Chem. Soc **2023**, 145, 18, 10275. (doi: 10.1021/jacs.3c01531)

7. Exciton Formation Dynamics and Band-Like Free Charge-Carrier Transport in 2D Metal Halide Perovskite Semiconductors

Silvia G. Motti, **Manuel Kober-Czerny**, Marcello Righetto, Philippe Holzhey, Joel Smith, Hans Kraus, Henry J. Snaith, Michael B. Johnston & Laura M. Herz

Advanced Functional Materials **2023**, 33, 2300363. (doi: 10.1002/adfm.202300363)

8. Hydrogen Bond-Assisted Dual Passivation for Blue Perovskite Light-Emitting Diodes

Zhongkai Yu, Xinyu Shen, Xiangyang Fan, Young-Kwang Jung, Woo Hyeon Jeong, Akash Dasgupta, **Manuel Kober-Czerny**, Pietro Caprioglio, Sung Heum Park, Hyosung Choi, Henry J. Snaith, Samuel D. Stranks & and Bo Ram Lee

ACS Energy Lett. **2023**, 8, 4296â4303. (doi: 10.1021/acsenergylett.3c01323)

REFERENCES

1. ""Web of Science"-Search based on "Metal Perovskite Solar " OR "Perovskite Photvoltaics" OR "Halide Perovskite Cells" OR "Perovskite Optoelectronics" NOT "LED" NOT "Photodetector Halide Perovskites"."
2. H. L. Wells, "Über die Cäsium- und Kalium-Bleihalogenide," *Zeitschrift für anorganische Chemie*, vol. 3, no. 1, pp. 195–210, 1893.
3. D. Weber, "CH3NH3PbX3, ein Pb(II)-System mit kubischer Perowskitstruktur / CH3NH3PbX3, a Pb(II)-System with Cubic Perovskite Structure," *Zeitschrift für Naturforschung B*, vol. 33, no. 12, pp. 1443–1445, 1978.
4. D. Weber, "CH3NH3SnBrxI3-x (x = 0-3), ein Sn(II)-System mit kubischer Perowskitstruktur / CH3NH3SnBrxI3-x(x = 0-3), a Sn(II)-System with Cubic Perovskite Structure," *Zeitschrift für Naturforschung B*, vol. 33, no. 8, pp. 862–865, 1978.
5. C. K. Møller, "Crystal Structure and Photoconductivity of Caesium Plumbohalides," *Nature*, vol. 182, no. 4647, pp. 1436–1436, 1958.
6. C. R. Kagan, D. B. Mitzi, and C. D. Dimitrakopoulos, "Organic-inorganic hybrid materials as semiconducting channels in thin- film field-effect transistors," *Science*, vol. 286, no. 5441, pp. 945–947, 1999.
7. D. B. Mitzi, K. Chondroudis, and C. R. Kagan, "Organic-inorganic electronics," 2001.
8. A. Kojima, K. Teshima, Y. Shirai, and T. Miyasaka, "Organometal halide perovskites as visible-light sensitizers for photovoltaic cells," *Journal of the American Chemical Society*, vol. 131, no. 17, pp. 6050–6051, 2009.
9. J. H. Im, C. R. Lee, J. W. Lee, S. W. Park, and N. G. Park, "6.5% efficient perovskite quantum-dot-sensitized solar cell," *Nanoscale*, vol. 3, no. 10, pp. 4088–4093, 2011.
10. M. M. Lee, J. Teuscher, T. Miyasaka, T. N. Murakami, and H. J. Snaith, "Efficient hybrid solar cells based

on meso-superstructured organometal halide perovskites," *Science*, vol. 338, no. 6107, pp. 643–647, 2012.

11. L. Loo and P. Patel, "Perovskite photovoltaics: David Mitzi addresses the promises and challenges," *MRS Bulletin*, vol. 40, no. 8, pp. 636–637, 2015.

12. F. Brivio, A. B. Walker, and A. Walsh, "Structural and electronic properties of hybrid perovskites for high-efficiency thin-film photovoltaics from first-principles," *APL Materials*, vol. 1, no. 4, p. 042111, 2013.

13. S. D. Stranks, G. E. Eperon, G. Grancini, C. Menelaou, M. J. P. Alcocer, T. Leijtens, L. M. Herz, A. Petrozza, and H. J. Snaith, "Electron-hole diffusion lengths exceeding 1 micrometer in an organometal trihalide perovskite absorber," *Science*, vol. 342, no. 6156, pp. 341–344, 2013.

14. G. Xing, N. Mathews, S. Sun, S. S. Lim, Y. M. Lam, M. Gräzel, S. Mhaisalkar, and T. C. Sum, "Long-range balanced electron-and hole-transport lengths in organic-inorganic CH3NH3PbI3," *Science*, vol. 342, no. 6156, pp. 344–347, 2013.

15. F. Deschler, M. Price, S. Pathak, L. E. Klintberg, D.-D. Jarausch, R. Higler, S. Hüttner, T. Leijtens, S. D. Stranks, H. J. Snaith, M. Atatüre, R. T. Phillips, and R. H. Friend, "High Photoluminescence Efficiency and Optically Pumped Lasing in Solution-Processed Mixed Halide Perovskite Semiconductors," *The Journal of Physical Chemistry Letters*, vol. 5, no. 8, pp. 1421–1426, 2014.

16. V. D'Innocenzo, G. Grancini, M. J. Alcocer, A. R. S. Kandada, S. D. Stranks, M. M. Lee, G. Lanzani, H. J. Snaith, and A. Petrozza, "Excitons versus free charges in organo-lead tri-halide perovskites," *Nature Communications*, vol. 5, no. 1, p. 3586, 2014.

17. C. Wehrenfennig, G. E. Eperon, M. B. Johnston, H. J. Snaith, and L. M. Herz, "High charge carrier mobilities and lifetimes in organolead trihalide perovskites," *Advanced Materials*, vol. 26, no. 10, pp. 1584–1589, 2014.

18. S. D. Wolf, J. Holovsky, S.-J. Moon, P. Löper, B. Niesen, M. Ledinsky, F.-J. Haug, J.-H. Yum, and C. Ballif, "Organometallic Halide Perovskites: Sharp Optical Absorption Edge and Its Relation to Photovoltaic Performance," *The Journal of Physical Chemistry Letters*, vol. 5, no. 6, pp. 1035–1039, 2014.

19. J. M. Ball, M. M. Lee, A. Hey, and H. J. Snaith, "Low-temperature processed meso-superstructured to thin-film perovskite solar cells," *Energy & Environmental Science*, vol. 6, no. 6, p. 1739, 2013.

20. H.-S. Kim, I. Mora-Sero, V. Gonzalez-Pedro, F. Fabregat-Santiago, E. J. Juarez-Perez, N.-G. Park, and J. Bisquert, "Mechanism of carrier accumulation in perovskite thin-absorber solar cells," *Nature Communications*, vol. 4, no. 1, p. 2242, 2013.

21. G. E. Eperon, S. D. Stranks, C. Menelaou, M. B. Johnston, L. M. Herz, and H. J. Snaith, "Formamidinium lead trihalide: A broadly tunable perovskite for efficient planar heterojunction solar cells," *Energy and Environmental Science*, vol. 7, no. 3, pp. 982–988, 2014.

22. M. R. Filip, G. E. Eperon, H. J. Snaith, and F. Giustino, "Steric engineering of metal-halide perovskites with tunable optical band gaps," *Nature Communications*, vol. 5, no. 1, p. 5757, 2014.

23. A. Walsh, "Principles of Chemical Bonding and Band Gap Engineering in Hybrid OrganicâInorganic Halide Perovskites," *The Journal of Physical Chemistry C*, vol. 119, no. 11, pp. 5755–5760, 2015.

24. "A Conversation with Tsutomu (Tom) Miyasaka," *ACS Energy Letters*, vol. 4, no. 4, pp. 832–833, 2019.

25. F. Brivio, K. T. Butler, A. Walsh, and M. v. Schilfgaarde, "Relativistic quasiparticle self-consistent electronic structure of hybrid halide perovskite photovoltaic absorbers," *Physical Review B*, vol. 89, no. 15, p. 155204, 2014.

26. R. E. Brandt, V. StevanoviÄ, D. S. Ginley, and T. Buonassisi, "Identifying defect-tolerant semiconductors with high minority-carrier lifetimes: beyond hybrid lead halide perovskites," *MRS Communications*, vol. 5, no. 2, pp. 265–275, 2015.

27. K. X. Steirer, P. Schulz, G. Teeter, V. Stevanovic, M. Yang, K. Zhu, and J. J. Berry, "Defect Tolerance in Methylammonium Lead Triiodide Perovskite," *ACS Energy Letters*, vol. 1, no. 2, pp. 360–366, 2016.

28. G.-J. A. H. Wetzelaer, M. Scheepers, A. M. Sempere, C. Momblona, J. Ávila, and H. J. Bolink, "Trap-Assisted Non-Radiative Recombination in Organic-Inorganic Perovskite Solar Cells," *Advanced Materials*, vol. 27, no. 11, pp. 1837–1841, 2015.

29. Y. Shao, Z. Xiao, C. Bi, Y. Yuan, and J. Huang, "Origin and elimination of photocurrent hysteresis by fullerene passivation in CH3NH3PbI3 planar heterojunction solar cells," *Nature Communications*, vol. 5, no. 1, p. 5784, 2014.

30. S. V. Reenen, M. Kemerink, and H. J. Snaith, "Modeling Anomalous Hysteresis in Perovskite Solar Cells," *Journal of Physical Chemistry Letters*, vol. 6, no. 19, pp. 3808–3814, 2015.

31. B. Chen, M. Yang, S. Priya, and K. Zhu, "Origin of J-V Hysteresis in Perovskite Solar Cells," *Journal of Physical Chemistry Letters*, vol. 7, no. 5, pp. 905–917, 2016.

32. N. K. Noel, S. N. Habisreutinger, B. Wenger, M. T. Klug, M. T. Hörantner, M. B. Johnston, R. J. Nicholas, D. T. Moore, and H. J. Snaith, "A low viscosity, low boiling point, clean solvent system for the rapid crystallisation of highly specular perovskite films," *Energy & Environmental Science*, vol. 10, no. 1, pp. 145–152, 2016.

33. S. Bai, P. Da, C. Li, Z. Wang, Z. Yuan, F. Fu, M. Kawecki, X. Liu, N. Sakai, J. T.-W. Wang, S. Huettner, S. Buecheler, F. Gao, and H. J. Snaith, "Planar perovskite solar cells with long-term stability using ionic liquid additives," *Nature*, vol. 571, no. 7764, pp. 245–250, 2019.

34. W. Zhang, M. Saliba, D. T. Moore, S. K. Pathak, M. T. Hörantner, T. Stergiopoulos, S. D. Stranks, G. E. Eperon, J. A. Alexander-Webber, A. Abate, A. Sadhanala, S. Yao, Y. Chen, R. H. Friend, L. A. Estroff, U. Wiesner, and H. J. Snaith, "Ultrasmooth organic-inorganic perovskite thin-film formation and crystallization for efficient planar heterojunction solar cells," *Nature Communications*, vol. 6, no. 1, p. 6142, 2015.

35. W. Zhang, S. Pathak, N. Sakai, T. Stergiopoulos, P. K. Nayak, N. K. Noel, A. A. Haghighirad, V. M.

Burlakov, D. W. deQuilettes, A. Sadhanala, W. Li, L. Wang, D. S. Ginger, R. H. Friend, and H. J. Snaith, "Enhanced optoelectronic quality of perovskite thin films with hypophosphorous acid for planar heterojunction solar cells," *Nature Communications*, vol. 6, no. 1, p. 10030, 2015.

36. D. P. McMeekin, G. Sadoughi, W. Rehman, G. E. Eperon, M. Saliba, M. T. Hörantner, A. Haghighirad, N. Sakai, L. Korte, B. Rech, M. B. Johnston, L. M. Herz, and H. J. Snaith, "A mixed-cation lead mixed-halide perovskite absorber for tandem solar cells," *Science*, vol. 351, no. 6269, pp. 151–155, 2016.

37. P. Gratia, I. Zimmermann, P. Schouwink, J. H. Yum, J. N. Audinot, K. Sivula, T. Wirtz, and M. K. Nazeeruddin, "The Many Faces of Mixed Ion Perovskites: Unraveling and Understanding the Crystallization Process," *ACS Energy Letters*, vol. 2, no. 12, pp. 2686–2693, 2017.

38. N. Sakai, Z. Wang, V. M. Burlakov, J. Lim, D. McMeekin, S. Pathak, and H. J. Snaith, "Controlling Nucleation and Growth of Metal Halide Perovskite Thin Films for HighâEfficiency Perovskite Solar Cells," *Small*, vol. 13, no. 14, p. 1602808, 2017.

39. R. L. Milot, G. E. Eperon, H. J. Snaith, M. B. Johnston, and L. M. Herz, "Temperature-Dependent Charge-Carrier Dynamics in CH3NH3PbI3 Perovskite Thin Films," *Advanced Functional Materials*, vol. 25, no. 39, pp. 6218–6227, 2015.

40. O. G. Reid, M. Yang, N. Kopidakis, K. Zhu, and G. Rumbles, "Grain-Size-Limited Mobility in Methylammonium Lead Iodide Perovskite Thin Films," *ACS Energy Letters*, vol. 1, no. 3, pp. 561–565, 2016.

41. T. A. S. Doherty, A. J. Winchester, S. Macpherson, D. N. Johnstone, V. Pareek, E. M. Tennyson, S. Kosar, F. U. Kosasih, M. Anaya, M. Abdi-Jalebi, Z. Andaji-Garmaroudi, E. L. Wong, J. Madéo, Y.-H. Chiang, J.-S. Park, Y.-K. Jung, C. E. Petoukhoff, G. Divitini, M. K. L. Man, C. Ducati, A. Walsh, P. A. Midgley, K. M. Dani, and S. D. Stranks, "Performance-limiting nanoscale trap clusters at grain junctions in halide perovskites," *Nature*, vol. 580, no. 7803, pp. 360–366, 2020.

42. S. Jariwala, H. Sun, G. W. Adhyaksa, A. Lof, L. A. Muscarella, B. Ehrler, E. C. Garnett, and D. S. Ginger, "Local Crystal Misorientation Influences Non-radiative Recombination in Halide Perovskites," *Joule*, vol. 3, no. 12, pp. 3048–3060, 2019.

43. F. D. Angelis and P. Kamat, "A Conversation with Michael Grätzel," *ACS Energy Letters*, vol. 2, no. 7, pp. 1674–1676, 2017.

44. K. Domanski, E. A. Alharbi, A. Hagfeldt, M. Grätzel, and W. Tress, "Systematic investigation of the impact of operation conditions on the degradation behaviour of perovskite solar cells," *Nature Energy*, vol. 3, no. 1, pp. 61–67, 2018.

45. J. A. Christians, P. Schulz, J. S. Tinkham, T. H. Schloemer, S. P. Harvey, B. J. T. D. Villers, A. Sellinger, J. J. Berry, and J. M. Luther, "Tailored interfaces of unencapsulated perovskite solar cells for >1,000 hour operational stability," *Nature Energy*, vol. 3, no. 1, pp. 68–74, 2018.

46. N. T. P. Hartono, H. Köbler, P. Graniero, M. Khenkin, R. Schlatmann, C. Ulbrich, and A. Abate, "Stability follows efficiency based on the analysis of a large perovskite solar cells ageing dataset," *Nature Communications*, vol. 14, no. 1, p. 4869, 2023.

47. J. Wang, W. Fu, S. Jariwala, I. Sinha, A. K.-Y. Jen, and D. S. Ginger, "Reducing Surface Recombination Velocities at the Electrical Contacts Will Improve Perovskite Photovoltaics," *ACS Energy Letters*, vol. 4, no. 1, pp. 222–227, 2019.

48. M. U. Rothmann, J. S. Kim, J. Borchert, K. B. Lohmann, C. M. OâLeary, A. A. Sheader, L. Clark, H. J. Snaith, M. B. Johnston, P. D. Nellist, and L. M. Herz, "Atomic-scale microstructure of metal halide perovskite," *Science*, vol. 370, no. 6516, 2020.

49. K. Frohna, M. Anaya, S. Macpherson, J. Sung, T. A. S. Doherty, Y.-H. Chiang, A. J. Winchester, K. W. P. Orr, J. E. Parker, P. D. Quinn, K. M. Dani, A. Rao, and S. D. Stranks, "Nanoscale chemical heterogeneity dominates the optoelectronic response of alloyed perovskite solar cells," *Nature Nanotechnology*, vol. 17, no. 2, pp. 190–196, 2022.

50. A. Dasgupta, S. Mahesh, P. Caprioglio, Y.-H. Lin, K.-A. Zaininger, R. D. Oliver, P. Holzhey, S. Zhou, M. M. McCarthy, J. A. Smith, M. Frenzel, M. G. Christoforo, J. M. Ball, B. Wenger, and H. J. Snaith, "Visualizing Macroscopic Inhomogeneities in Perovskite Solar Cells," *ACS Energy Letters*, vol. 7, no. 7, pp. 2311–2322, 2022.

51. J. Diekmann, F. Peña Camargo, N. Tokmoldin, J. Thiesbrummel, J. Warby, E. Gutierrez-Partida, S. Shah, D. Neher, and M. Stolterfoht, "Determination of Mobile Ion Densities in Halide Perovskites via Low-Frequency Capacitance and Charge Extraction Techniques," *The Journal of Physical Chemistry Letters*, vol. 14, no. 18, pp. 4200–4210, 2023.

52. J. Thiesbrummel, V. M. L. Corre, F. PeñaâCamargo, L. Perdigó nâToro, F. Lang, F. Yang, M. Grischek, E. GutierrezâPartida, J. Warby, M. D. Farrar, S. Mahesh, P. Caprioglio, S. Albrecht, D. Neher, H. J. Snaith, and M. Stolterfoht, "Universal Current Losses in Perovskite Solar Cells Due to Mobile Ions," *Advanced Energy Materials*, vol. 11, no. 34, p. 2101447, 2021.

53. V. M. L. Corre, J. Diekmann, F. Peña Camargo, J. Thiesbrummel, N. Tokmoldin, E. Gutierrez-Partida, K. P. Peters, L. Perdigó n Toro, M. H. Futscher, F. Lang, J. Warby, H. J. Snaith, D. Neher, and M. Stolterfoht, "Quantification of Efficiency Losses Due to Mobile Ions in Perovskite Solar Cells via Fast Hysteresis Measurements," *Solar RRL*, vol. 6, no. 4, 2022.

54. F. D. Angelis and P. V. Kamat, "A Conversation with Henry Snaith," *ACS Energy Letters*, vol. 2, no. 11, pp. 2552–2554, 2017.

55. X. Y. Chin, D. Turkay, J. A. Steele, S. Tabean, S. Eswara, M. Mensi, P. Fiala, C. M. Wolff, A. Paracchino, K. Artuk, D. Jacobs, Q. Guesnay, F. Sahli, G. Andreatta, M. Boccard, Q. Jeangros, and C. Ballif, "Interface passivation for 31.25%-efficient perovskite/silicon tandem solar cells.," *Science (New York, N.Y.)*, vol. 381,

no. 6653, pp. 59–63, 2023.

56. F. Staub, I. Anusca, D. C. Lupascu, U. Rau, and T. Kirchartz, "Effect of reabsorption and photon recycling on photoluminescence spectra and transients in lead-halide perovskite crystals," *Journal of Physics: Materials*, vol. 3, no. 2, p. 025003, 2020.

57. Y. Yuan, G. Yan, C. Dreessen, M. Hülsbeck, B. Klingebiel, U. Rau, and T. Kirchartz, "Shallow Defects and Ultralong Photoluminescence Decay Times up to 280 Â$\mu sin Triple - Cation Perovskites$,″ 2023.

58. P. Würfel and U. Würfel, *Physics of Solar Cells - From Basic Principles to Advanced Concepts*. Weinheim, Germany: Wiley-VCH Verlag GmbH & Co. KGaA, 3rd ed., 2016.

59. M. PLANCK, "The Old Quantum Theory," *PART 2*, pp. 82–90, 1967.

60. W. Shockley and H. J. Queisser, "Detailed balance limit of efficiency of p-n junction solar cells," *Journal of Applied Physics*, vol. 32, no. 3, pp. 510–519, 1961.

61. J. Mooney and P. Kambhampati, "Get the Basics Right: Jacobian Conversion of Wavelength and Energy Scales for Quantitative Analysis of Emission Spectra," *The Journal of Physical Chemistry Letters*, vol. 4, no. 19, pp. 3316–3318, 2013.

62. "Reference Solar Spectral Irradiance: Air Mass 1.5."

63. J. Fraunhofer, "Bestimmung des Brechungsâ und des FarbenzerstreungsâVermögens verschiedener Glasarten, in Bezug auf die Vervollkommnung achromatischer Fernröhre," *Annalen der Physik*, vol. 56, no. 7, pp. 264–313, 1817.

64. G. Kirchhoff, "Über die Fraunhofer'schen Linien," *Annalen der Physik*, vol. 185, no. 1, p. 148â150, 1860.

65. J. Li, B. E. Carlson, Y. L. Yung, D. Lv, J. Hansen, J. E. Penner, H. Liao, V. Ramaswamy, R. A. Kahn, P. Zhang, O. Dubovik, A. Ding, A. A. Lacis, L. Zhang, and Y. Dong, "Scattering and absorbing aerosols in the climate system," *Nature Reviews Earth & Environment*, vol. 3, no. 6, pp. 363–379, 2022.

66. M. A. Green, "Solar cell fill factors: General graph and empirical expressions," *Solid-State Electronics*, vol. 24, no. 8, pp. 788–789, 1981.

67. P. K. Nayak, S. Mahesh, H. J. Snaith, and D. Cahen, "Photovoltaic solar cell technologies: analysing the state of the art," *Nature Reviews Materials*, vol. 4, no. 4, pp. 269–285, 2019.

68. NREL, "NREL Efficiency Chart," 2021.

69. B. Saparov and D. B. Mitzi, "Organic-Inorganic Perovskites: Structural Versatility for Functional Materials Design," *Chemical Reviews*, vol. 116, no. 7, pp. 4558–4596, 2016.

70. Q. A. Akkerman and L. Manna, "What Defines a Halide Perovskite?," *ACS Energy Letters*, vol. 5, no. 2, pp. 604–610, 2020.

71. J. C. Thomas, J. S. Bechtel, A. R. Natarajan, and A. V. d. Ven, "Machine learning the density functional

theory potential energy surface for the inorganic halide perovskite CsPbBr 3," *Physical Review B*, vol. 100, no. 13, 2019.

72. T. Umebayashi, K. Asai, T. Kondo, and A. Nakao, "Electronic structures of lead iodide based low-dimensional crystals," *Physical Review B*, vol. 67, no. 15, p. 155405, 2003.

73. M. Kepenekian and J. Even, "Rashba and Dresselhaus Couplings in Halide Perovskites: Accomplishments and Opportunities for Spintronics and SpinâOrbitronics," *The Journal of Physical Chemistry Letters*, vol. 8, no. 14, pp. 3362–3370, 2017.

74. J. Even, L. Pedesseau, J.-M. Jancu, and C. Katan, "Importance of Spin-Orbit Coupling in Hybrid Organic/Inorganic Perovskites for Photovoltaic Applications," *The Journal of Physical Chemistry Letters*, vol. 4, no. 17, pp. 2999–3005, 2013.

75. D. Ghosh, A. R. Smith, A. B. Walker, and M. S. Islam, "Mixed A-Cation Perovskites for Solar Cells: Atomic-Scale Insights into Structural Distortion, Hydrogen Bonding, and Electronic Properties," *Chemistry of Materials*, vol. 30, no. 15, pp. 5194–5204, 2018.

76. R. Prasanna, A. Gold-Parker, T. Leijtens, B. Conings, A. Babayigit, H. G. Boyen, M. F. Toney, and M. D. McGehee, "Band Gap Tuning via Lattice Contraction and Octahedral Tilting in Perovskite Materials for Photovoltaics," *Journal of the American Chemical Society*, vol. 139, no. 32, pp. 11117–11124, 2017.

77. H. Turren-Cruz, A. Hagfeldt, and M. Saliba, "Methylammonium-free, high-performance, and stable perovskite solar cells on a planar architecture,"

78. M. Jansen and U. Wedig, "A Piece of the Picture-Misunderstanding of Chemical Concepts," *Angewandte Chemie International Edition*, vol. 47, no. 52, pp. 10026–10029, 2008.

79. J. N. Wilson, J. M. Frost, S. K. Wallace, and A. Walsh, "Dielectric and ferroic properties of metal halide perovskites," *APL Materials*, vol. 7, no. 1, p. 010901, 2019.

80. P. Y. Yu and M. Cardona, *Fundamentals of Semiconductors, Physics and Materials Properties*, vol. 4th Edition of *Graduate Texts in Physics*. 2010.

81. C. L. Davies, M. R. Filip, J. B. Patel, T. W. Crothers, C. Verdi, A. D. Wright, R. L. Milot, F. Giustino, M. B. Johnston, and L. M. Herz, "Bimolecular recombination in methylammonium lead triiodide perovskite is an inverse absorption process," *Nature Communications*, vol. 9, no. 1, p. 293, 2018.

82. K. P. Goetz, A. D. Taylor, F. Paulus, and Y. Vaynzof, "Shining Light on the Photoluminescence Properties of Metal Halide Perovskites," *Advanced Functional Materials*, vol. 30, no. 23, p. 1910004, 2020.

83. R. J. Elliott, "Intensity of Optical Absorption by Excitons," *Physical Review*, vol. 108, no. 6, pp. 1384–1389, 1957.

84. K. Galkowski, A. Mitioglu, A. Miyata, P. Plochocka, O. Portugall, G. E. Eperon, J. Tse, W. Wang, T. Stergiopoulos, S. D. Stranks, H. J. Snaith, and R. J. Nicholas, "Determination of the exciton binding energy and

effective masses for methylammonium and formamidinium lead tri-halide perovskite semiconductors," *This journal is Cite this: Energy Environ. Sci*, vol. 9, no. 3, p. 962, 2016.

85. M. Dyksik, H. Duim, X. Zhu, Z. Yang, M. Gen, Y. Kohama, S. Adjokatse, D. K. Maude, M. A. Loi, D. A. Egger, M. Baranowski, and P. Plochocka, "Broad Tunability of Carrier Effective Masses in Two-Dimensional Halide Perovskites," *ACS Energy Letters*, vol. 5, no. 11, pp. 3609–3616, 2020.

86. T. Ishihara, J. Takahashi, and T. Goto, "Optical properties due to electronic transitions in two-dimensional semiconductors (CnH2n+1NH3)2PbI4," *Physical Review B*, vol. 42, no. 17, pp. 11099–11107, 1990.

87. J. Frenkel, "Über die Wärmebewegung in festen und flüssigen Körpern," *Zeitschrift für Physik*, vol. 35, no. 8-9, pp. 652–669, 1926.

88. W. Jost, "Diffusion and Electrolytic Conduction in Crystals (Ionic Semiconductors)," *The Journal of Chemical Physics*, vol. 1, no. 7, pp. 466–475, 1933.

89. W. Schottky, "Über den Mechanismus der Ionenbewegung in festen Elektrolyten," *Zeitschrift für Physikalische Chemie*, vol. 29B, no. 1, pp. 335–355, 1935.

90. A. Zakutayev, C. M. Caskey, A. N. Fioretti, D. S. Ginley, J. Vidal, V. Stevanovic, E. Tea, and S. Lany, "Defect Tolerant Semiconductors for Solar Energy Conversion.," *The journal of physical chemistry letters*, vol. 5, no. 7, pp. 1117–25, 2014.

91. R. E. Brandt, J. R. Poindexter, P. Gorai, R. C. Kurchin, R. L. Z. Hoye, L. Nienhaus, M. W. B. Wilson, J. A. Polizzotti, R. Sereika, R. ZÌaltauskas, L. C. Lee, J. L. MacManus-Driscoll, M. Bawendi, V. StevanovicÌ, and T. Buonassisi, "Searching for "Defect-Tolerant" Photovoltaic Materials: Combined Theoretical and Experimental Screening," *Chemistry of Materials*, vol. 29, no. 11, pp. 4667–4674, 2017.

92. D. Meggiolaro, S. G. Motti, E. Mosconi, A. J. Barker, J. Ball, C. A. R. Perini, F. Deschler, A. Petrozza, and F. D. Angelis, "Iodine chemistry determines the defect tolerance of lead-halide perovskites," *Energy & Environmental Science*, vol. 11, no. 3, pp. 702–713, 2018.

93. X. Zhang, M. E. Turiansky, and C. G. V. d. Walle, "Correctly Assessing Defect Tolerance in Halide Perovskites," *The Journal of Physical Chemistry C*, vol. 124, no. 11, pp. 6022–6027, 2020.

94. Q. Zhou, B. Wang, R. Meng, J. Zhou, S. Xie, X. Zhang, J. Wang, S. Yue, B. Qin, H. Zhou, and Y. Zhang, "Understanding Temperature-Dependent Charge Extraction and Trapping in Perovskite Solar Cells," *Advanced Functional Materials*, vol. 30, no. 22, 2020.

95. D. Shi, V. Adinolfi, R. Comin, M. Yuan, E. Alarousu, A. Buin, Y. Chen, S. Hoogland, A. Rothenberger, K. Katsiev, Y. Losovyj, X. Zhang, P. A. Dowben, O. F. Mohammed, E. H. Sargent, and O. M. Bakr, "Low trap-state density and long carrier diffusion in organolead trihalide perovskite single crystals," *Science*, vol. 347, pp. 519–522, 2015.

96. Z. Lian, Q. Yan, T. Gao, J. Ding, Q. Lv, C. Ning, Q. Li, and J.-l. Sun, "Perovskite CH3NH3PbI3(Cl)

Single Crystals: Rapid Solution Growth, Unparalleled Crystalline Quality, and Low Trap Density toward 10^8 cm^{-3}," *Journal of the American Chemical Society*, vol. 138, no. 30, pp. 9409–9412, 2016.

97. E. M. Tennyson, T. A. S. Doherty, and S. D. Stranks, "Heterogeneity at multiple length scales in halide perovskite semiconductors," *Nature Reviews Materials*, vol. 4, no. 9, pp. 573–587, 2019.

98. N. E. Courtier, J. M. Cave, J. M. Foster, A. B. Walker, and G. Richardson, "How transport layer properties affect perovskite solar cell performance: insights from a coupled charge transport/ion migration model," *Energy & Environmental Science*, vol. 12, no. 1, pp. 396–409, 2018.

99. H. J. Snaith, A. Abate, J. M. Ball, G. E. Eperon, T. Leijtens, N. K. Noel, S. D. Stranks, J. T.-W. Wang, K. Wojciechowski, and W. Zhang, "Anomalous Hysteresis in Perovskite Solar Cells.," *The journal of physical chemistry letters*, vol. 5, no. 9, pp. 1511–5, 2014.

100. A. Guerrero, J. You, C. Aranda, Y. S. Kang, G. Garcia-Belmonte, H. Zhou, J. Bisquert, and Y. Yang, "Interfacial Degradation of Planar Lead Halide Perovskite Solar Cells," *ACS Nano*, vol. 10, no. 1, pp. 218–224, 2016.

101. H. Lee and C. Lee, "Analysis of Ion-Diffusion-Induced Interface Degradation in Inverted Perovskite Solar Cells via Restoration of the Ag Electrode," *Advanced Energy Materials*, vol. 8, no. 11, 2018.

102. M. H. Futscher, J. M. Lee, L. McGovern, L. A. Muscarella, T. Wang, M. I. Haider, A. Fakharuddin, L. Schmidt-Mende, and B. Ehrler, "Quantification of ion migration in CH 3 NH 3 PbI 3 perovskite solar cells by transient capacitance measurements," *Materials Horizons*, vol. 6, no. 7, pp. 1497–1503, 2019.

103. G. Y. Kim, A. Senocrate, T.-Y. Yang, G. Gregori, M. Grätzel, and J. Maier, "Large tunable photoeffect on ion conduction in halide perovskites and implications for photodecomposition," *Nature Materials*, vol. 17, no. 5, pp. 445–449, 2018.

104. A. Senocrate, G. Y. Kim, M. Grätzel, and J. Maier, "Thermochemical Stability of Hybrid Halide Perovskites," *ACS Energy Letters*, vol. 4, no. 12, pp. 2859–2870, 2019.

105. L. Lanzetta, T. Webb, N. Zibouche, X. Liang, D. Ding, G. Min, R. J. E. Westbrook, B. Gaggio, T. J. Macdonald, M. S. Islam, and S. A. Haque, "Degradation mechanism of hybrid tin-based perovskite solar cells and the critical role of tin (IV) iodide," *Nature Communications*, vol. 12, no. 1, p. 2853, 2021.

106. S. Chen, X. Xiao, H. Gu, and J. Huang, "Iodine reduction for reproducible and high-performance perovskite solar cells and modules," *Science Advances*, vol. 7, no. 10, p. eabe8130, 2021.

107. C. Eames, J. M. Frost, P. R. F. Barnes, B. C. O'Regan, A. Walsh, and M. S. Islam, "Ionic transport in hybrid lead iodide perovskite solar cells," *Nature Communications*, vol. 6, no. 1, p. 7497, 2015.

108. A. Bercegol, F. J. Ramos, A. Rebai, T. Guillemot, J. B. Puel, J. F. Guillemoles, D. Ory, J. Rousset, and L. Lombez, "Spatial Inhomogeneity Analysis of Cesium-Rich Wrinkles in Triple-Cation Perovskite," *Journal of Physical Chemistry C*, vol. 122, no. 41, pp. 23345–23351, 2018.

109. Q. Chang, D. Bao, B. Chen, H. Hu, X. Chen, H. Sun, Y. M. Lam, J.-X. Zhu, D. Zhao, and E. E. M. Chia, "Tracking carrier and exciton dynamics in mixed-cation lead mixed-halide perovskite thin films," *Communications Physics*, vol. 5, no. 1, p. 187, 2022.

110. C. G. Bischak, C. L. Hetherington, H. Wu, S. Aloni, D. F. Ogletree, D. T. Limmer, and N. S. Ginsberg, "Origin of Reversible Photoinduced Phase Separation in Hybrid Perovskites," *Nano Letters*, vol. 17, no. 2, pp. 1028–1033, 2017.

111. M. C. Brennan, A. Ruth, P. V. Kamat, and M. Kuno, "Photoinduced Anion Segregation in Mixed Halide Perovskites," *Trends in Chemistry*, vol. 2, no. 4, pp. 282–301, 2020.

112. L. A. Muscarella, E. M. Hutter, F. Wittmann, Y. W. Woo, Y.-K. Jung, L. McGovern, J. Versluis, A. Walsh, H. J. Bakker, and B. Ehrler, "Lattice Compression Increases the Activation Barrier for Phase Segregation in Mixed-Halide Perovskites," *ACS Energy Letters*, vol. 5, no. 10, p. acsenergylett.0c01474, 2020.

113. A. J. Knight, J. Borchert, R. D. J. Oliver, J. B. Patel, P. G. Radaelli, H. J. Snaith, M. B. Johnston, and L. M. Herz, "Halide Segregation in Mixed-Halide Perovskites: Influence of A-Site Cations," *ACS Energy Letters*, vol. 6, no. 2, pp. 799–808, 2021.

114. S. G. Motti, J. B. Patel, R. D. J. Oliver, H. J. Snaith, M. B. Johnston, and L. M. Herz, "Phase segregation in mixed-halide perovskites affects charge-carrier dynamics while preserving mobility," *Nature Communications*, vol. 12, no. 1, p. 6955, 2021.

115. S. G. Motti, D. Meggiolaro, A. J. Barker, E. Mosconi, C. A. R. Perini, J. M. Ball, M. Gandini, M. Kim, F. D. Angelis, and A. Petrozza, "Controlling competing photochemical reactions stabilizes perovskite solar cells," *Nature Photonics*, vol. 13, no. 8, pp. 532–539, 2019.

116. R. L. Milot, R. J. Sutton, G. E. Eperon, A. A. Haghighirad, J. M. Hardigree, L. Miranda, H. J. Snaith, M. B. Johnston, and L. M. Herz, "Charge-Carrier Dynamics in 2D Hybrid Metal-Halide Perovskites," *Nano Letters*, vol. 16, no. 11, pp. 7001–7007, 2016.

117. I. C. Smith, E. T. Hoke, D. Solis-Ibarra, M. D. McGehee, and H. I. Karunadasa, "A Layered Hybrid Perovskite Solar-Cell Absorber with Enhanced Moisture Stability," *Angewandte Chemie - International Edition*, vol. 53, no. 42, pp. 11232–11235, 2014.

118. G. Grancini, C. Roldán-Carmona, I. Zimmermann, E. Mosconi, X. Lee, D. Martineau, S. Narbey, F. Oswald, F. D. Angelis, M. Grätzel, and M. K. Nazeeruddin, "One-Year stable perovskite solar cells by 2D/3D interface engineering," *Nature Communications*, vol. 8, no. 1, p. 15684, 2017.

119. Y. Yang, C. Liu, A. Mahata, M. Li, C. Roldán-Carmona, Y. Ding, Z. Arain, W. Xu, Y. Yang, P. A. Schouwink, A. Züttel, F. D. Angelis, S. Dai, and M. K. Nazeeruddin, "Universal approach toward high-efficiency two-dimensional perovskite solar cells: Via a vertical-rotation process," *Energy and Environmental Science*, vol. 13, no. 9, pp. 3093–3101, 2020.

120. A. Krishna, S. Gottis, M. K. Nazeeruddin, and F. Sauvage, "Mixed Dimensional 2D/3D Hybrid Perovskite Absorbers: The Future of Perovskite Solar Cells?," *Advanced Functional Materials*, vol. 29, no. 8, p. 1806482, 2019.

121. L. R. Buizza, T. W. Crothers, Z. Wang, J. B. Patel, R. L. Milot, H. J. Snaith, M. B. Johnston, and L. M. Herz, "Charge-Carrier Dynamics, Mobilities, and Diffusion Lengths of 2Dâ3D Hybrid ButylammoniumâCesiumâFormamidinium Lead Halide Perovskites," *Advanced Functional Materials*, vol. 29, no. 35, p. 1902656, 2019.

122. H. Tsai, W. Nie, J. C. Blancon, C. C. Stoumpos, R. Asadpour, B. Harutyunyan, A. J. Neukirch, R. Verduzco, J. J. Crochet, S. Tretiak, L. Pedesseau, J. Even, M. A. Alam, G. Gupta, J. Lou, P. M. Ajayan, M. J. Bedzyk, M. G. Kanatzidis, and A. D. Mohite, "High-efficiency two-dimensional ruddlesden-popper perovskite solar cells," *Nature*, vol. 536, no. 7616, pp. 312–317, 2016.

123. D. H. Cao, C. C. Stoumpos, O. K. Farha, J. T. Hupp, and M. G. Kanatzidis, "2D Homologous Perovskites as Light-Absorbing Materials for Solar Cell Applications," *Journal of the American Chemical Society*, vol. 137, no. 24, pp. 7843–7850, 2015.

124. C. Otero-Martinez, J. Ye, J. Sung, I. PastorizaâSantos, J. PérezâJuste, Z. Xia, A. Rao, R. L. Z. Hoye, and L. Polavarapu, "Colloidal MetalâHalide Perovskite Nanoplatelets: ThicknessâControlled Synthesis, Properties, and Application in LightâEmitting Diodes," *Advanced Materials*, vol. 34, no. 10, p. e2107105, 2022.

125. C. C. Stoumpos, D. H. Cao, D. J. Clark, J. Young, J. M. Rondinelli, J. I. Jang, J. T. Hupp, and M. G. Kanatzidis, "Ruddlesden-Popper Hybrid Lead Iodide Perovskite 2D Homologous Semiconductors," *Chemistry of Materials*, vol. 28, no. 8, pp. 2852–2867, 2016.

126. J. V. Milić, J. H. Im, D. J. Kubicki, A. Ummadisingu, J. Y. Seo, Y. Li, M. A. Ruiz-Preciado, M. I. Dar, S. M. Zakeeruddin, L. Emsley, and M. Grätzel, "Supramolecular Engineering for Formamidinium-Based Layered 2D Perovskite Solar Cells: Structural Complexity and Dynamics Revealed by Solid-State NMR Spectroscopy," *Advanced Energy Materials*, vol. 9, no. 20, p. 1900284, 2019.

127. C. J. Dahlman, R. A. DeCrescent, N. R. Venkatesan, R. M. Kennard, G. Wu, M. A. Everest, J. A. Schuller, and M. L. Chabinyc, "Controlling Solvate Intermediate Growth for Phase-Pure Organic Lead Iodide RuddlesdenâPopper (C4H9NH3)2(CH3NH3) n-1Pb n I3n+1 Perovskite Thin Films," *Chemistry of Materials*, vol. 31, no. 15, pp. 5832–5844, 2019.

128. C. Liang, H. Gu, Y. Xia, Z. Wang, X. Liu, J. Xia, S. Zuo, Y. Hu, X. Gao, W. Hui, L. Chao, T. Niu, M. Fang, H. Lu, H. Dong, H. Yu, S. Chen, X. Ran, L. Song, B. Li, J. Zhang, Y. Peng, G. Shao, J. Wang, Y. Chen, G. Xing, and W. Huang, "Two-dimensional Ruddlesden-Popper layered perovskite solar cells based on phase-pure thin films," *Nature Energy*, vol. 6, no. 1, pp. 38–45, 2021.

129. D. B. Straus and C. R. Kagan, "Electrons, Excitons, and Phonons in Two-Dimensional Hybrid Perovskites: Connecting Structural, Optical, and Electronic Properties," *Journal of Physical Chemistry Letters*, vol. 9,

no. 6, pp. 1434–1447, 2018.

130. X. Hong, T. Ishihara, and A. U. Nurmikko, "Dielectric confinement eff'ect on excitons in PbI4-based layered semiconductors," *PHYSICAL REVIEW B*, vol. 45, p. 6961, 1992.

131. T. Ishihara, J. Takahashi, and T. Goto, "EXCITON STATE IN TWO-DIMENSIONAL PEROVSKITE SEMICONDUCTOR (CIoH21NH3)2PbI4," *Solid State Communications*, vol. 69, pp. 933–936, 1989.

132. D. Pariari, S. Mehta, S. Mandal, A. Mahata, T. Pramanik, S. Kamilya, A. Vidhan, T. N. G. Row, P. K. Santra, S. K. Sarkar, F. D. Angelis, A. Mondal, and D. D. Sarma, "Realizing the Lowest Bandgap and Exciton Binding Energy in a Two-Dimensional Lead Halide System," *Journal of the American Chemical Society*, 2023.

133. M. Seitz, A. J. Magdaleno, N. Alcázar-Cano, M. Meléndez, T. J. Lubbers, S. W. Walraven, S. Pakdel, E. Prada, R. Delgado-Buscalioni, and F. Prins, "Exciton diffusion in two-dimensional metal-halide perovskites," *Nature Communications*, vol. 11, no. 1, pp. 1–8, 2020.

134. J. D. Ziegler, J. Zipfel, B. Meisinger, M. Menahem, X. Zhu, T. Taniguchi, K. Watanabe, O. Yaffe, D. A. Egger, and A. Chernikov, "Fast and Anomalous Exciton Diffusion in Two-Dimensional Hybrid Perovskites," *Nano Letters*, vol. 20, no. 9, pp. 6674–6681, 2020.

135. M. N. Saha, "On a physical theory of stellar spectra," *Proceedings of the Royal Society of London. Series A, Containing Papers of a Mathematical and Physical Character*, vol. 99, no. 697, pp. 135–153, 1921.

136. A. Simbula, R. Pau, Q. Wang, F. Liu, V. Sarritzu, S. Lai, M. Lodde, F. Mattana, G. Mula, A. G. Lehmann, I. D. Spanopoulos, M. G. Kanatzidis, D. Marongiu, F. Quochi, M. Saba, A. Mura, and G. Bongiovanni, "Polaron Plasma in Equilibrium with Bright Excitons in 2D and 3D Hybrid Perovskites," *Advanced Optical Materials*, vol. 9, no. 16, p. 2100295, 2021.

137. G. W. Drake, ed., *Springer Handbook of Atomic, Molecular, and Optical Physics*. Springer Handbooks, 2023.

138. L. M. Herz, "Charge-Carrier Dynamics in Organic-Inorganic Metal Halide Perovskites," *Annual Review of Physical Chemistry*, vol. 67, no. 1, pp. 65–89, 2016.

139. J. Singleton, *Band Theory and Electronic Properties of Solids*, vol. 2 of *Oxford Master Series in Condensed Matter Physics Series*. Oxford University Press, Incorporated, 2001.

140. E. Ugur, M. Ledinský, T. G. Allen, J. Holovský, A. Vlk, and S. D. Wolf, "Life on the Urbach Edge," *The Journal of Physical Chemistry Letters*, vol. 13, no. 33, pp. 7702–7711, 2022.

141. T. G. Mayerhöfer, S. Pahlow, and J. Popp, "The BouguerâBeerâLambert Law: Shining Light on the Obscure," *ChemPhysChem*, vol. 21, no. 18, pp. 2029–2046, 2020.

142. K. P. Goetz and Y. Vaynzof, "The Challenge of Making the Same Device Twice in Perovskite Photovoltaics," *ACS Energy Letters*, vol. 7, no. 5, pp. 1750–1757, 2022.

143. T. Kirchartz, J. A. Márquez, M. Stolterfoht, and T. Unold, "PhotoluminescenceâBased Characterization of Halide Perovskites for Photovoltaics," *Advanced Energy Materials*, vol. 10, no. 26, p. 1904134, 2020.

144. H. J. Snaith, "How should you measure your excitonic solar cells?," *Energy & Environmental Science*, vol. 5, no. 4, pp. 6513–6520, 2012.

145. H. Meng, L. Xiong, J. Zhang, Y. He, B. Zhang, and C. Cai, "Accurate Measurement of New Type Non-silicon Solar Cellsâ Photoelectric Conversion Efficiency," *Journal of Physics: Conference Series*, vol. 972, no. 1, p. 012017, 2018.

146. H. Ibach and H. Lüth, *Solid-State Physics*, vol. 4th Edition. Springer-Verlag, 4th ed., 2009.

147. O. Flender, J. R. Klein, T. Lenzer, and K. Oum, "Ultrafast photoinduced dynamics of the organolead trihalide perovskite CH3NH3PbI3 on mesoporous TiO2 scaffolds in the 320-920 nm range.," *Physical chemistry chemical physics : PCCP*, vol. 17, no. 29, pp. 19238–46, 2015.

148. J. Zaumseil and H. Sirringhaus, "Electron and Ambipolar Transport in Organic Field-Effect Transistors," *Chemical Reviews*, vol. 107, no. 4, pp. 1296–1323, 2007.

149. T. Leijtens, S. D. Stranks, G. E. Eperon, R. Lindblad, E. M. J. Johansson, I. J. McPherson, H. Rensmo, J. M. Ball, M. M. Lee, and H. J. Snaith, "Electronic Properties of Meso-Superstructured and Planar Organometal Halide Perovskite Films: Charge Trapping, Photodoping, and Carrier Mobility," *ACS Nano*, vol. 8, no. 7, pp. 7147–7155, 2014.

150. R. Ahrenkiel, "Measurement of minority-carrier lifetime by time-resolved photoluminescence," *Solid-State Electronics*, vol. 35, no. 3, pp. 239–250, 1992.

151. M. Maiberg and R. Scheer, "Theoretical study of time-resolved luminescence in semiconductors. II. Pulsed excitation," *Journal of Applied Physics*, vol. 116, no. 12, p. 123711, 2014.

152. C. Fai, A. J. Ladd, and C. J. Hages, "Machine learning for enhanced semiconductor characterization from time-resolved photoluminescence," *Joule*, vol. 6, no. 11, pp. 2585–2610, 2022.

153. K. W. Cassel, "Matrix, Numerical, and Optimization Methods in Science and Engineering," pp. 466–526, 2021.

154. A. H.-D. Cheng and D. T. Cheng, "Heritage and early history of the boundary element method," *Engineering Analysis with Boundary Elements*, vol. 29, no. 3, pp. 268–302, 2005.

155. P. Kaienburg, L. Krückemeier, D. Lübke, J. Nelson, U. Rau, and T. Kirchartz, "How solar cell efficiency is governed by the Î±Î»Ï*product*,″ *PhysicalReviewResearch*, *vol*. 2, *no*. 2, *p*. 023109, 2020.

156. T. Leijtens, J. Lim, J. Teuscher, T. Park, and H. J. Snaith, "Charge Density Dependent Mobility of Organic HoleâTransporters and Mesoporous TiO2 Determined by Transient Mobility Spectroscopy: Implications to DyeâSensitized and Organic Solar Cells," *Advanced Materials*, vol. 25, no. 23, pp. 3227–3233, 2013.

157. M. Burgelman, P. Nollet, and S. Degrave, "Modelling polycrystalline semiconductor solar cells," *Thin Solid Films*, vol. 361-362, pp. 527–532, 2000.

158. N. E. Courtier, J. M. Cave, A. B. Walker, G. Richardson, and J. M. Foster, "IonMonger: a free and fast planar perovskite solar cell simulator with coupled ion vacancy and charge carrier dynamics," *Journal of Computational Electronics*, vol. 18, no. 4, pp. 1435–1449, 2019.

159. W. v. Roosbroeck and W. Shockley, "Photon-Radiative Recombination of Electrons and Holes in Germanium," *Physical Review*, vol. 94, no. 6, pp. 1558–1560, 1954.

160. K. Oki, B. Ma, and Y. Ishitani, "Population decay time and distribution of exciton states analyzed by rate equations based on theoretical phononic and electron-collisional rate coefficients," *Physical Review B*, vol. 96, no. 20, p. 205204, 2017.

161. J. Szczytko, L. Kappei, J. Berney, F. Morier-Genoud, M. T. Portella-Oberli, and B. Deveaud, "Determination of the Exciton Formation in Quantum Wells from Time-Resolved Interband Luminescence," *Physical Review Letters*, vol. 93, no. 13, p. 137401, 2004.

162. Q. Sun, C. Zhao, Z. Yin, S. Wang, J. Leng, W. Tian, and S. Jin, "Ultrafast and High-Yield Polaronic Exciton Dissociation in Two-Dimensional Perovskites," *Journal of the American Chemical Society*, vol. 143, no. 45, pp. 19128–19136, 2021.

163. N. Spitha, D. D. Kohler, M. P. Hautzinger, J. Li, S. Jin, and J. C. Wright, "Discerning between Exciton and Free-Carrier Behaviors in RuddlesdenâPopper Perovskite Quantum Wells through Kinetic Modeling of Photoluminescence Dynamics," *J. Phys. Chem. C*, vol. 124, no. 31, p. 41, 2020.

164. W. Shockley and W. T. Read, "Statistics of the Recombinations of Holes and Electrons," *Physical Review*, vol. 87, no. 5, pp. 835–842, 1952.

165. J. G. Simmons and G. W. Taylor, "Nonequilibrium Steady-State Statistics and Associated Effects for Insulators and Semiconductors Containing an Arbitrary Distribution of Traps," *Physical Review B*, vol. 4, no. 2, pp. 502–511, 1970.

166. Q. Jiang, Y. Zhao, X. Zhang, X. Yang, Y. Chen, Z. Chu, Q. Ye, X. Li, Z. Yin, and J. You, "Surface passivation of perovskite film for efficient solar cells," *Nature Photonics*, vol. 13, no. 7, pp. 460–466, 2019.

167. Q. Cai, Z. Lin, W. Zhang, G. Shen, X. Wen, H. Dong, X. Xu, D. Zhu, and C. Mu, "Improvement Performance of Planar Perovskite Solar Cells by Bulk and Surface Defect Passivation," *ACS Sustainable Chemistry & Engineering*, vol. 9, no. 38, pp. 13001–13009, 2021.

168. A. R. Bowman, S. Macpherson, A. Abfalterer, K. Frohna, S. Nagane, and S. D. Stranks, "Extracting Decay-Rate Ratios From Photoluminescence Quantum Efficiency Measurements in Optoelectronic Semiconductors," *Physical Review Applied*, vol. 17, no. 4, p. 044026, 2022.

169. J. M. Richter, M. Abdi-Jalebi, A. Sadhanala, M. Tabachnyk, J. P. Rivett, L. M. Pazos-Outó n, K. C. Gödel,

M. Price, F. Deschler, and R. H. Friend, "Enhancing photoluminescence yields in lead halide perovskites by photon recycling and light out-coupling," *Nature Communications*, vol. 7, no. 1, p. 13941, 2016.

170. P. T. Landsberg, C. Rhys-Roberts, and P. Lal, "Auger recombination and impact ionization involving traps in semiconductors," *Proceedings of the Physical Society*, vol. 84, no. 6, pp. 915–931, 1964.

171. F. Staub, U. Rau, and T. Kirchartz, "Statistics of the Auger Recombination of Electrons and Holes via Defect Levels in the Band GapâApplication to Lead-Halide Perovskites," *ACS Omega*, vol. 3, no. 7, pp. 8009–8016, 2018.

172. M. B. Johnston and L. M. Herz, "Hybrid Perovskites for Photovoltaics: Charge-Carrier Recombination, Diffusion, and Radiative Efficiencies," *Accounts of Chemical Research*, vol. 49, no. 1, pp. 146–154, 2016.

173. T. W. Crothers, R. L. Milot, J. B. Patel, E. S. Parrott, J. Schlipf, P. Müller-Buschbaum, M. B. Johnston, and L. M. Herz, "Photon Reabsorption Masks Intrinsic Bimolecular Charge-Carrier Recombination in CH3NH3PbI3 Perovskite," *Nano Letters*, vol. 17, no. 9, pp. 5782–5789, 2017.

174. M. Ansari-Rad and J. Bisquert, "Insight into Photon Recycling in Perovskite Semiconductors from the Concept of Photon Diffusion," *Physical Review Applied*, vol. 10, no. 3, p. 034062, 2018.

175. P. Fassl, V. Lami, F. J. Berger, L. M. Falk, J. Zaumseil, B. S. Richards, I. A. Howard, Y. Vaynzof, and U. W. Paetzold, "Revealing the internal luminescence quantum efficiency of perovskite films via accurate quantification of photon recycling," *Matter*, vol. 4, no. 4, pp. 1391–1412, 2021.

176. R. Graaff and J. J. T. Bosch, "Diffusion coefficient in photon diffusion theory.," *Optics letters*, vol. 25, no. 1, pp. 43–5, 2000.

177. Z. Gan, X. Wen, W. Chen, C. Zhou, S. Yang, G. Cao, K. P. Ghiggino, H. Zhang, and B. Jia, "The Dominant Energy Transport Pathway in Halide Perovskites: Photon Recycling or Carrier Diffusion?," *Advanced Energy Materials*, vol. 9, no. 20, 2019.

178. T. Yamada, Y. Yamada, Y. Nakaike, A. Wakamiya, and Y. Kanemitsu, "Photon Emission and Reabsorption Processes in CH3NH3PbBr3 Single Crystals Revealed by Time-Resolved Two-Photon-Excitation Photoluminescence Microscopy," *Physical Review Applied*, vol. 7, no. 1, p. 014001, 2017.

179. P. Caprioglio, S. Caicedo-Dávila, T. C.-J. Yang, C. M. Wolff, F. Peña Camargo, P. Fiala, B. Rech, C. Ballif, D. Abou-Ras, M. Stolterfoht, S. Albrecht, Q. Jeangros, and D. Neher, "Nano-emitting Heterostructures Violate Optical Reciprocity and Enable Efficient Photoluminescence in Halide-Segregated Methylammonium-Free Wide Bandgap Perovskites," *ACS Energy Letters*, vol. 6, no. 2, pp. 419–428, 2021.

180. C. Barugkin, J. Cong, T. Duong, S. Rahman, H. T. Nguyen, D. Macdonald, T. P. White, and K. R. Catchpole, "Ultralow Absorption Coefficient and Temperature Dependence of Radiative Recombination of CH 3 NH 3 PbI 3 Perovskite from Photoluminescence," *The Journal of Physical Chemistry Letters*, vol. 6, no. 5, pp. 767–772, 2015.

181. R. D. J. Oliver, P. Caprioglio, F. Peña Camargo, L. R. V. Buizza, F. Zu, A. J. Ramadan, S. G. Motti, S. Mahesh, M. M. McCarthy, J. H. Warby, Y.-H. Lin, N. Koch, S. Albrecht, L. M. Herz, M. B. Johnston, D. Neher, M. Stolterfoht, and H. J. Snaith, "Understanding and suppressing non-radiative losses in methylammonium-free wide-bandgap perovskite solar cells," *Energy & Environmental Science*, vol. 15, no. 2, pp. 714–726, 2021.

182. P. Caprioglio, J. A. Smith, R. D. J. Oliver, A. Dasgupta, S. Choudhary, M. D. Farrar, A. J. Ramadan, Y.-H. Lin, M. G. Christoforo, J. M. Ball, J. Diekmann, J. Thiesbrummel, K.-A. Zaininger, X. Shen, M. B. Johnston, D. Neher, M. Stolterfoht, and H. J. Snaith, "Open-circuit and short-circuit loss management in wide-gap perovskite p-i-n solar cells," *Nature Communications*, vol. 14, no. 1, p. 932, 2023.

183. P. K. Nayak, D. T. Moore, B. Wenger, S. Nayak, A. A. Haghighirad, A. Fineberg, N. K. Noel, O. G. Reid, G. Rumbles, P. Kukura, K. A. Vincent, and H. J. Snaith, "Mechanism for rapid growth of organicâinorganic halide perovskite crystals," *Nature Communications*, vol. 7, no. 1, p. 13303, 2016.

184. B. Wenger, P. K. Nayak, X. Wen, S. V. Kesava, N. K. Noel, and H. J. Snaith, "Consolidation of the optoelectronic properties of CH3NH3PbBr3 perovskite single crystals," *Nature Communications*, vol. 8, no. 1, p. 590, 2017.

185. C. Wehrenfennig, M. Liu, H. J. Snaith, M. B. Johnston, and L. M. Herz, "Charge-carrier dynamics in vapour-deposited films of the organolead halide perovskite CH 3 NH 3 PbI 3âx Cl x," *Energy & Environmental Science*, vol. 7, no. 7, pp. 2269–2275, 2014.

186. B. Zhang, L. Goldoni, C. Lambruschini, L. Moni, M. Imran, A. Pianetti, V. Pinchetti, S. Brovelli, L. D. Trizio, and L. Manna, "Stable and Size Tunable CsPbBr3 Nanocrystals Synthesized with Oleylphosphonic Acid.," *Nano letters*, vol. 20, no. 12, pp. 8847–8853, 2020.

187. F.-G. Wieland, A. L. Hauber, M. Rosenblatt, C. Tönsing, and J. Timmer, "On structural and practical identifiability," *Current Opinion in Systems Biology*, vol. 25, pp. 60–69, 2021.

188. J. Lever, M. Krzywinski, and N. Altman, "Model selection and overfitting," *Nature Methods*, vol. 13, no. 9, pp. 703–704, 2016.

189. F. Grabowski, P. Nałłęcz-Jawecki, and T. Lipniacki, "Predictive power of non-identifiable models," *Scientific Reports*, vol. 13, no. 1, p. 11143, 2023.

190. A. Sjölander and S. Vansteelandt, "Frequentist versus Bayesian approaches to multiple testing," *European Journal of Epidemiology*, vol. 34, no. 9, pp. 809–821, 2019.

191. J. V. Passarelli, C. M. Mauck, S. W. Winslow, C. F. Perkinson, J. C. Bard, H. Sai, K. W. Williams, A. Narayanan, D. J. Fairfield, M. P. Hendricks, W. A. Tisdale, and S. I. Stupp, "Tunable exciton binding energy in 2D hybrid layered perovskites through donorâacceptor interactions within the organic layer," *Nature Chemistry*, vol. 12, no. 8, pp. 672–682, 2020.

192. S. Neutzner, F. Thouin, D. Cortecchia, A. Petrozza, C. Silva, A. Ram, and S. Kandada, "Exciton-polaron spectral structures in two-dimensional hybrid lead-halide perovskites," *Physical Review Materials*, vol. 2, no. 6, p. 64605, 2018.

193. M. Cirelli, T. Hambye, P. Panci, a. , M. Aoki, T. Toma, A. V. , J. Chen, Z.-L. Liang, and Y.-L. Wu, "Self-consistent calculation of the Sommerfeld enhancement," *Journal of Cosmology and Astroparticle Physics OPEN ACCESS*, vol. 2016, no. 06, p. 021, 2016.

194. B. Ohnesorge, R. Weigand, G. Bacher, A. Forchel, W. Riedl, and F. H. Karg, "Minority-carrier lifetime and efficiency of solar cells," *Cite as: Appl. Phys. Lett*, vol. 73, no. 9, p. 1224, 1998.

195. O. Abril-Pla, V. Andreani, C. Carroll, L. Dong, C. J. Fonnesbeck, M. Kochurov, R. Kumar, J. Lao, C. C. Luhmann, O. A. Martin, M. Osthege, R. Vieira, T. Wiecki, and R. Zinkov, "PyMC: a modern, and comprehensive probabilistic programming framework in Python," *PeerJ Computer Science*, vol. 9, p. e1516, 2023.

196. S. D. Stranks and H. J. Snaith, "Metal-halide perovskites for photovoltaic and light-emitting devices," *Nature Nanotechnology*, vol. 10, no. 5, pp. 391–402, 2015.

197. J. Lim, M. T. Hörantner, N. Sakai, J. M. Ball, S. Mahesh, N. K. Noel, Y. H. Lin, J. B. Patel, D. P. McMeekin, M. B. Johnston, B. Wenger, and H. J. Snaith, "Elucidating the long-range charge carrier mobility in metal halide perovskite thin films," *Energy and Environmental Science*, vol. 12, no. 1, pp. 169–176, 2019.

198. W. F. Pasveer, J. Cottaar, C. Tanase, R. Coehoorn, P. A. Bobbert, P. W. M. Blom, D. M. d. Leeuw, and M. A. J. Michels, "Unified Description of Charge-Carrier Mobilities in Disordered Semiconducting Polymers," *Physical Review Letters*, vol. 94, no. 20, p. 206601, 2004.

199. L. M. Herz, "Charge-Carrier Mobilities in Metal Halide Perovskites: Fundamental Mechanisms and Limits," *ACS Energy Letters*, vol. 2, no. 7, pp. 1539–1548, 2017.

200. J. J. Yoo, G. Seo, M. R. Chua, T. G. Park, Y. Lu, F. Rotermund, Y.-K. Kim, C. S. Moon, N. J. Jeon, J.-P. Correa-Baena, V. BuloviÄ, S. S. Shin, M. G. Bawendi, and J. Seo, "Efficient perovskite solar cells via improved carrier management," *Nature*, vol. 590, no. 7847, pp. 587–593, 2021.

201. C. Li, J. Yang, F. Su, J. Tan, Y. Luo, and S. Ye, "Conformational disorder of organic cations tunes the charge carrier mobility in two-dimensional organic-inorganic perovskites," *Nature Communications*, vol. 11, no. 1, p. 5481, 2020.

202. X. Y. Chin, D. Cortecchia, J. Yin, A. Bruno, and C. Soci, "Lead iodide perovskite light-emitting field-effect transistor," *Nature Communications*, vol. 6, no. 1, p. 7383, 2015.

203. X. Gong, Z. Huang, R. Sabatini, C.-S. Tan, G. Bappi, G. Walters, A. Proppe, M. I. Saidaminov, O. Voznyy, S. O. Kelley, and E. H. Sargent, "Contactless measurements of photocarrier transport properties in perovskite single crystals," *Nature Communications*, vol. 10, no. 1, p. 1591, 2019.

204. D. A. Valverde-Chávez, C. S. Ponseca, C. C. Stoumpos, A. Yartsev, M. G. Kanatzidis, V. Sundström, and D. G. Cooke, "Intrinsic femtosecond charge generation dynamics in single crystal CH3NH3PbI3," *Energy and Environmental Science*, vol. 8, no. 12, pp. 3700–3707, 2015.

205. O. E. Semonin, G. A. Elbaz, D. B. Straus, T. D. Hull, D. W. Paley, A. M. V. D. Zande, J. C. Hone, I. Kymissis, C. R. Kagan, X. Roy, and J. S. Owen, "Limits of Carrier Diffusion in n-Type and p-Type CH3NH3PbI3 Perovskite Single Crystals," *Journal of Physical Chemistry Letters*, vol. 7, no. 17, pp. 3510–3518, 2016.

206. Q. Dong, Y. Fang, Y. Shao, P. Mulligan, J. Qiu, L. Cao, and J. Huang, "Electron-hole diffusion lengths > 175 ÎŒm in solution-grown CH3NH3PbI3 single crystals," *Science*, vol. 347, no. 6225, pp. 967–970, 2015.

207. M. I. Saidaminov, A. L. Abdelhady, B. Murali, E. Alarousu, V. M. Burlakov, W. Peng, I. Dursun, L. Wang, Y. He, G. Maculan, A. Goriely, T. Wu, O. F. Mohammed, and O. M. Bakr, "High-quality bulk hybrid perovskite single crystals within minutes by inverse temperature crystallization," *Nature Communications*, vol. 6, no. 1, p. 7586, 2015.

208. C. S. Ponseca, T. J. Savenije, M. Abdellah, K. Zheng, A. Yartsev, T. Pascher, T. Harlang, P. Chabera, T. Pullerits, A. Stepanov, J. P. Wolf, and V. Sundström, "Organometal halide perovskite solar cell materials rationalized: Ultrafast charge generation, high and microsecond-long balanced mobilities, and slow recombination," *Journal of the American Chemical Society*, vol. 136, no. 14, pp. 5189–5192, 2014.

209. E. M. Hutter, G. E. Eperon, S. D. Stranks, and T. J. Savenije, "Charge Carriers in Planar and Meso-Structured Organic-Inorganic Perovskites: Mobilities, Lifetimes, and Concentrations of Trap States," *Journal of Physical Chemistry Letters*, vol. 6, no. 15, pp. 3082–3090, 2015.

210. D. H. Kim, J. Park, Z. Li, M. Yang, J. Park, I. J. Park, J. Y. Kim, J. J. Berry, G. Rumbles, and K. Zhu, "300% Enhancement of Carrier Mobility in Uniaxial-Oriented Perovskite Films Formed by Topotactic-Oriented Attachment," *Advanced Materials*, vol. 29, no. 23, 2017.

211. V. M. L. Corre, E. A. Duijnstee, O. E. Tambouli, J. M. Ball, H. J. Snaith, J. Lim, and L. J. A. Koster, "Revealing Charge Carrier Mobility and Defect Densities in Metal Halide Perovskites via Space-Charge-Limited Current Measurements.," *ACS energy letters*, vol. 6, no. 3, pp. 1087–1094, 2020.

212. X. Cheng, J. Ma, Y. Zhou, C. Fang, J. Wang, J. Li, X. Wen, and D. Li, "Optical anisotropy of one-dimensional perovskite C4N2H14PbI4 crystals," *Journal of Physics: Photonics*, vol. 2, no. 1, 2020.

213. G. Maculan, A. D. Sheikh, A. L. Abdelhady, M. I. Saidaminov, M. A. Haque, B. Murali, E. Alarousu, O. F. Mohammed, T. Wu, and O. M. Bakr, "CH3NH3PbCl3 Single Crystals: Inverse Temperature Crystallization and Visible-Blind UV-Photodetector," *The Journal of Physical Chemistry Letters*, vol. 6, no. 19, pp. 3781–3786, 2015.

214. A. A. Zhumekenov, M. I. Saidaminov, M. A. Haque, E. Alarousu, S. P. Sarmah, B. Murali, I. Dursun, X.-H. Miao, A. L. Abdelhady, T. Wu, O. F. Mohammed, and O. M. Bakr, "Formamidinium Lead Halide

Perovskite Crystals with Unprecedented Long Carrier Dynamics and Diffusion Length," *ACS Energy Letters*, vol. 1, no. 1, pp. 32–37, 2016.

215. W. Rehman, R. L. Milot, G. E. Eperon, C. Wehrenfennig, J. L. Boland, H. J. Snaith, M. B. Johnston, and L. M. Herz, "Charge-Carrier Dynamics and Mobilities in Formamidinium Lead Mixed-Halide Perovskites," *Advanced Materials*, vol. 27, no. 48, pp. 7938–7944, 2015.

216. W. Rehman, D. P. McMeekin, J. B. Patel, R. L. Milot, M. B. Johnston, H. J. Snaith, and L. M. Herz, "Photovoltaic mixed-cation lead mixed-halide perovskites: links between crystallinity, photo-stability and electronic properties," *Energy & Environmental Science*, vol. 10, no. 1, pp. 361–369, 2016.

217. D. P. McMeekin, Z. Wang, W. Rehman, F. Pulvirenti, J. B. Patel, N. K. Noel, M. B. Johnston, S. R. Marder, L. M. Herz, and H. J. Snaith, "Crystallization Kinetics and Morphology Control of Formamidinium-Cesium Mixed-Cation Lead Mixed-Halide Perovskite via Tunability of the Colloidal Precursor Solution," *Advanced Materials*, vol. 29, no. 29, p. 1607039, 2017.

218. Y. Takahashi, H. Hasegawa, Y. Takahashi, and T. Inabe, "Hall mobility in tin iodide perovskite CH3NH3SnI3: Evidence for a doped semiconductor," *Journal of Solid State Chemistry*, vol. 205, pp. 39–43, 2013.

219. R. L. Milot, G. E. Eperon, T. Green, H. J. Snaith, M. B. Johnston, and L. M. Herz, "Radiative Monomolecular Recombination Boosts Amplified Spontaneous Emission in HC(NH2)2SnI3 Perovskite Films," *The Journal of Physical Chemistry Letters*, vol. 7, no. 20, pp. 4178–4184, 2016.

220. I. Chung, J.-H. Song, J. Im, J. Androulakis, C. D. Malliakas, H. Li, A. J. Freeman, J. T. Kenney, and M. G. Kanatzidis, "CsSnI3: Semiconductor or Metal? High Electrical Conductivity and Strong Near-Infrared Photoluminescence from a Single Material. High Hole Mobility and Phase-Transitions," *Journal of the American Chemical Society*, vol. 134, no. 20, pp. 8579–8587, 2012.

221. C. C. Stoumpos, C. D. Malliakas, and M. G. Kanatzidis, "Semiconducting Tin and Lead Iodide Perovskites with Organic Cations: Phase Transitions, High Mobilities, and Near-Infrared Photoluminescent Properties," *Inorganic Chemistry*, vol. 52, no. 15, pp. 9019–9038, 2013.

222. G. E. Eperon, T. Leijtens, K. A. Bush, R. Prasanna, T. Green, J. T.-W. Wang, D. P. McMeekin, G. Volonakis, R. L. Milot, R. May, A. Palmstrom, D. J. Slotcavage, R. A. Belisle, J. B. Patel, E. S. Parrott, R. J. Sutton, W. Ma, F. Moghadam, B. Conings, A. Babayigit, H.-G. Boyen, S. Bent, F. Giustino, L. M. Herz, M. B. Johnston, M. D. McGehee, and H. J. Snaith, "Perovskite-perovskite tandem photovoltaics with optimized band gaps.," *Science (New York, N.Y.)*, vol. 354, no. 6314, pp. 861–865, 2016.

223. E. A. Duijnstee, J. M. Ball, V. M. L. Corre, L. J. A. Koster, H. J. Snaith, and J. Lim, "Toward Understanding Space-Charge Limited Current Measurements on Metal Halide Perovskites," *ACS Energy Letters*, vol. 5, no. 2, pp. 376–384, 2020.

224. E. A. Duijnstee, V. M. L. Corre, M. B. Johnston, L. J. A. Koster, J. Lim, and H. J. Snaith, "Understanding Dark Current-Voltage Characteristics in Metal-Halide Perovskite Single Crystals," *Physical Review Applied*,

vol. 15, no. 1, p. 014006, 2021.

225. S. Lee and J. H. Noh, "Steady-State Transporting Properties of Halide Perovskite Thin Films under 1 sun through Photo-Hall Effect Measurement," *The Journal of Physical Chemistry C*, vol. 126, no. 22, pp. 9559–9566, 2022.

226. M. D. Khan and V. R. Nikitenko, "On the charge mobility in disordered organics from photo-CELIV measurements," *Chemical Physics*, vol. 539, p. 110954, 2020.

227. J. Lorrmann, B. H. Badada, O. Inganäs, V. Dyakonov, and C. Deibel, "Charge carrier extraction by linearly increasing voltage: Analytic framework and ambipolar transients," *Journal of Applied Physics*, vol. 108, no. 11, p. 113705, 2010.

228. P. Tiwana, P. Parkinson, M. B. Johnston, H. J. Snaith, and L. M. Herz, "Ultrafast Terahertz Conductivity Dynamics in Mesoporous TiO2: Influence of Dye Sensitization and Surface Treatment in Solid-State Dye-Sensitized Solar Cells," *The Journal of Physical Chemistry C*, vol. 114, no. 2, pp. 1365–1371, 2010.

229. C. L. Watts, L. Aspitarte, Y.-H. Lin, W. Li, R. Elzein, R. Addou, M. J. Hong, G. S. Herman, H. J. Snaith, and J. G. Labram, "Light soaking in metal halide perovskites studied via steady-state microwave conductivity," *Communications Physics*, vol. 3, no. 1, p. 73, 2020.

230. J. G. Labram, N. R. Venkatesan, C. J. Takacs, H. A. Evans, E. E. Perry, F. Wudl, and M. L. Chabinyc, "Charge transport in a two-dimensional hybrid metal halide thiocyanate compound," *Journal of Materials Chemistry C*, vol. 5, no. 24, pp. 5930–5938, 2017.

231. M. J. Hong and J. G. Labram, "Role of A-Site Composition in Charge Transport in Lead Iodide Perovskites," *Advanced Energy and Sustainability Research*, vol. 3, no. 11, p. 2200120, 2022.

232. J. Kniepert and D. Neher, "Effect of the RC time on photocurrent transients and determination of charge carrier mobilities," *Journal of Applied Physics*, vol. 122, no. 19, p. 195501, 2017.

233. S. W. Kettlitz, J. Mescher, N. S. Christ, M. Nintz, S. Valouch, A. Colsmann, and U. Lemmer, "Eliminating RC-Effects in Transient Photocurrent Measurements on Organic Photodiodes," *IEEE Photonics Technology Letters*, vol. 25, no. 7, pp. 682–685, 2013.

234. A. Petrozza, C. Groves, and H. J. Snaith, "Electron Transport and Recombination in Dye-Sensitized Mesoporous TiO2 Probed by Photoinduced Charge-Conductivity Modulation Spectroscopy with Monte Carlo Modeling," *Journal of the American Chemical Society*, vol. 130, no. 39, pp. 12912–12920, 2008.

235. H. Oga, A. Saeki, Y. Ogomi, S. Hayase, and S. Seki, "Improved Understanding of the Electronic and Energetic Landscapes of Perovskite Solar Cells: High Local Charge Carrier Mobility, Reduced Recombination, and Extremely Shallow Traps," *Journal of the American Chemical Society*, vol. 136, no. 39, pp. 13818–13825, 2014.

236. K. Sveinbjörnsson, K. Aitola, X. Zhang, M. Pazoki, A. Hagfeldt, G. Boschloo, and E. M. J. Johansson,

"Probing Photocurrent Generation, Charge Transport, and Recombination Mechanisms in Mesostructured Hybrid Perovskite through Photoconductivity Measurements," *The Journal of Physical Chemistry Letters*, vol. 6, no. 21, pp. 4259–4264, 2015.

237. L. Krückemeier, Z. Liu, T. Kirchartz, and U. Rau, "Quantifying Charge Extraction and Recombination Using the Rise and Decay of the Transient Photovoltage of Perovskite Solar Cells," *Advanced Materials*, vol. 35, no. 35, p. e2300872, 2023.

238. J. Steinhauser, S. Faÿ, N. Oliveira, E. Vallat-Sauvain, and C. Ballif, "Transition between grain boundary and intragrain scattering transport mechanisms in boron-doped zinc oxide thin films," *Applied Physics Letters*, vol. 90, no. 14, p. 142107, 2007.

239. A. A. Paraecattil, J. D. Jonghe-Risse, V. Pranculis, J. Teuscher, and J.-E. Moser, "Dynamics of Photocarrier Separation in MAPbI3 Perovskite Multigrain Films under a Quasistatic Electric Field," *The Journal of Physical Chemistry C*, vol. 120, no. 35, pp. 19595–19602, 2016.

240. C. Wehrenfennig, M. Liu, H. J. Snaith, M. B. Johnston, and L. M. Herz, "Homogeneous Emission Line Broadening in the Organo Lead Halide Perovskite CH3NH3PbI3-xClx.," *The journal of physical chemistry letters*, vol. 5, no. 8, pp. 1300–6, 2014.

241. L. T. Schelhas, Z. Li, J. A. Christians, A. Goyal, P. Kairys, S. P. Harvey, D. H. Kim, K. H. Stone, J. M. Luther, K. Zhu, V. Stevanovic, and J. J. Berry, "Insights into operational stability and processing of halide perovskite active layers," *Energy and Environmental Science*, vol. 12, no. 4, pp. 1341–1348, 2019.

242. W. Tress, K. Domanski, B. Carlsen, A. Agarwalla, E. A. Alharbi, M. Graetzel, and A. Hagfeldt, "Performance of perovskite solar cells under simulated temperature-illumination real-world operating conditions," *Nature Energy*, vol. 4, no. 7, pp. 568–574, 2019.

243. L. Zhu, H. Cao, C. Xue, H. Zhang, M. Qin, J. Wang, K. Wen, Z. Fu, T. Jiang, L. Xu, Y. Zhang, Y. Cao, C. Tu, J. Zhang, D. Liu, G. Zhang, D. Kong, N. Fan, G. Li, C. Yi, Q. Peng, J. Chang, X. Lu, N. Wang, W. Huang, and J. Wang, "Unveiling the additive-assisted oriented growth of perovskite crystallite for high performance light-emitting diodes," *Nature Communications*, vol. 12, no. 1, p. 5081, 2021.

244. G. Jang, S. Ma, H.-C. Kwon, S. Goh, H. Ban, J. S. Kim, J.-H. Kim, and J. Moon, "Elucidation of the Formation Mechanism of Highly Oriented Multiphase RuddlesdenâPopper Perovskite Solar Cells," *ACS Energy Letters*, vol. 6, no. 1, pp. 249–260, 2021.

245. Z. Wang, Q. Lin, F. P. Chmiel, N. Sakai, L. M. Herz, and H. J. Snaith, "Efficient ambient-air-stable solar cells with 2D-3D heterostructured butylammonium-caesium-formamidinium lead halide perovskites," *Nature Energy*, vol. 2, no. 9, p. 17135, 2017.

246. H. Min, D. Y. Lee, J. Kim, G. Kim, K. S. Lee, J. Kim, M. J. Paik, Y. K. Kim, K. S. Kim, M. G. Kim, T. J. Shin, and S. I. Seok, "Perovskite solar cells with atomically coherent interlayers on SnO2 electrodes," *Nature*, vol. 598, no. 7881, pp. 444–450, 2021.

247. A. A. Sutanto, P. Caprioglio, N. Drigo, Y. J. Hofstetter, I. Garcia-Benito, V. I. Queloz, D. Neher, M. K. Nazeeruddin, M. Stolterfoht, Y. Vaynzof, and G. Grancini, "2D/3D perovskite engineering eliminates interfacial recombination losses in hybrid perovskite solar cells," *Chem*, vol. 7, no. 7, pp. 1903–1916, 2021.

248. K. Ma, J. Sun, H. R. Atapattu, B. W. Larson, H. Yang, D. Sun, K. Chen, K. Wang, Y. Lee, Y. Tang, A. Bhoopalam, L. Huang, K. R. Graham, J. Mei, and L. Dou, "Holistic energy landscape management in 2D/3D heterojunction via molecular engineering for efficient perovskite solar cells," *Science Advances*, vol. 9, no. 23, p. eadg0032, 2023.

249. S. Sidhik, Y. Wang, M. D. Siena, R. Asadpour, A. J. Torma, T. Terlier, K. Ho, W. Li, A. B. Puthirath, X. Shuai, A. Agrawal, B. Traore, M. Jones, R. Giridharagopal, P. M. Ajayan, J. Strzalka, D. S. Ginger, C. Katan, M. A. Alam, J. Even, M. G. Kanatzidis, and A. D. Mohite, "Deterministic fabrication of 3D/2D perovskite bilayer stacks for durable and efficient solar cells," *Science*, vol. 377, no. 6613, pp. 1425–1430, 2022.

250. B. P. Kore, W. Zhang, B. W. Hoogendoorn, M. Safdari, and J. M. Gardner, "Moisture tolerant solar cells by encapsulating 3D perovskite with long-chain alkylammonium cation-based 2D perovskite," *Communications Materials*, vol. 2, no. 1, p. 100, 2021.

251. H. Li, C. Zhang, C. Gong, D. Zhang, H. Zhang, Q. Zhuang, X. Yu, S. Gong, X. Chen, J. Yang, X. Li, R. Li, J. Li, J. Zhou, H. Yang, Q. Lin, J. Chu, M. Grätzel, J. Chen, and Z. Zang, "2D/3D heterojunction engineering at the buried interface towards high-performance inverted methylammonium-free perovskite solar cells," *Nature Energy*, pp. 1–10, 2023.

252. M. Degani, Q. An, M. Albaladejo-Siguan, Y. J. Hofstetter, C. Cho, F. Paulus, G. Grancini, and Y. Vaynzof, "23.7% Efficient inverted perovskite solar cells by dual interfacial modification," *Science Advances*, vol. 7, no. 49, p. eabj7930, 2021.

253. R. J. E. Westbrook, W. Xu, X. Liang, T. Webb, T. M. Clarke, and S. A. Haque, "2D Phase Purity Determines Charge-Transfer Yield at 3D/2D Lead Halide Perovskite Heterojunctions," *The Journal of Physical Chemistry Letters*, vol. 12, no. 13, pp. 3312–3320, 2021.

254. Y. Shi, E. Rojas-Gatjens, J. Wang, J. Pothoof, R. Giridharagopal, K. Ho, F. Jiang, M. Taddei, Z. Yang, E. M. Sanehira, M. D. Irwin, C. Silva-Acuña, and D. S. Ginger, "(3-Aminopropyl)trimethoxysilane Surface Passivation Improves Perovskite Solar Cell Performance by Reducing Surface Recombination Velocity," *ACS Energy Letters*, vol. 7, no. 11, pp. 4081–4088, 2022.

255. T. Leijtens, G. E. Eperon, S. Pathak, A. Abate, M. M. Lee, and H. J. Snaith, "Overcoming ultraviolet light instability of sensitized TiO2 with meso-superstructured organometal tri-halide perovskite solar cells," *Nature Communications*, vol. 4, no. 1, p. 2885, 2013.

256. Z. Li, C. Xiao, Y. Yang, S. P. Harvey, D. H. Kim, J. A. Christians, M. Yang, P. Schulz, S. U. Nanayakkara, C.-S. Jiang, J. M. Luther, J. J. Berry, M. C. Beard, M. M. Al-Jassim, and K. Zhu, "Extrinsic ion migration

in perovskite solar cells," *Energy & Environmental Science*, vol. 10, no. 5, pp. 1234–1242, 2017.

257. R. Azmi, E. Ugur, A. Seitkhan, F. Aljamaan, A. S. Subbiah, J. Liu, G. T. Harrison, M. I. Nugraha, M. K. Eswaran, M. Babics, Y. Chen, F. Xu, T. G. Allen, A. u. Rehman, C.-L. Wang, T. D. Anthopoulos, U. Schwingenschlögl, M. D. Bastiani, E. Aydin, and S. D. Wolf, "Damp heatâstable perovskite solar cells with tailored-dimensionality 2D/3D heterojunctions," *Science*, vol. 376, no. 6588, pp. 73–77, 2022.

258. M. Yu, C. Yi, N. Wang, L. Zhang, R. Zou, Y. Tong, H. Chen, Y. Cao, Y. He, Y. Wang, M. Xu, Y. Liu, Y. Jin, W. Huang, and J. Wang, "Control of Barrier Width in Perovskite Multiple Quantum Wells for High Performance Green LightâEmitting Diodes," *Advanced Optical Materials*, vol. 7, no. 3, p. 1801575, 2019.

259. D. B. Mitzi, C. A. Feild, W. T. Harrison, and A. M. Guloy, "Conducting tin halides with a layered organic-based perovskite structure," *Nature*, vol. 369, no. 6480, pp. 467–469, 1994.

260. F. Huang, P. Siffalovic, B. Li, S. Yang, L. Zhang, P. Nadazdy, G. Cao, and J. Tian, "Controlled crystallinity and morphologies of 2D Ruddlesden-Popper perovskite films grown without anti-solvent for solar cells," *Chemical Engineering Journal*, vol. 394, p. 124959, 2020.

261. G. Grancini and M. K. Nazeeruddin, "Dimensional tailoring of hybrid perovskites for photovoltaics," *Nature Reviews Materials*, vol. 4, no. 1, pp. 4–22, 2019.

262. J. Liu, J. Leng, K. Wu, J. Zhang, and S. Jin, "Observation of internal photoinduced electron and hole separation in hybrid two-dimentional perovskite films," *Journal of the American Chemical Society*, vol. 139, no. 4, pp. 1432–1435, 2017.

263. G. Xing, B. Wu, X. Wu, M. Li, B. Du, Q. Wei, J. Guo, E. K. Yeow, T. C. Sum, and W. Huang, "Transcending the slow bimolecular recombination in lead-halide perovskites for electroluminescence," *Nature Communications*, vol. 8, no. 1, p. 14558, 2017.

264. M. E. Kamminga, H. H. Fang, M. R. Filip, F. Giustino, J. Baas, G. R. Blake, M. A. Loi, and T. T. Palstra, "Confinement Effects in Low-Dimensional Lead Iodide Perovskite Hybrids," *Chemistry of Materials*, vol. 28, no. 13, pp. 4554–4562, 2016.

265. N. R. Venkatesan, J. G. Labram, and M. L. Chabinyc, "Charge-Carrier Dynamics and Crystalline Texture of Layered Ruddlesden-Popper Hybrid Lead Iodide Perovskite Thin Films," *ACS Energy Letters*, vol. 3, no. 2, pp. 380–386, 2018.

266. S. Shao, H. Duim, Q. Wang, B. Xu, J. Dong, S. Adjokatse, G. R. Blake, L. Protesescu, G. Portale, J. Hou, M. Saba, and M. A. Loi, "Tuning the Energetic Landscape of Ruddlesden-Popper Perovskite Films for Efficient Solar Cells," *ACS Energy Letters*, vol. 5, no. 1, pp. 39–46, 2020.

267. J. Hu, I. W. Oswald, S. J. Stuard, M. M. Nahid, N. Zhou, O. F. Williams, Z. Guo, L. Yan, H. Hu, Z. Chen, X. Xiao, Y. Lin, Z. Yang, J. Huang, A. M. Moran, H. Ade, J. R. Neilson, and W. You, "Synthetic control over orientational degeneracy of spacer cations enhances solar cell efficiency in two-dimensional perovskites,"

Nature Communications, vol. 10, no. 1, pp. 1–11, 2019.

268. J. Gebhardt, Y. Kim, and A. M. Rappe, "Influence of the Dimensionality and Organic Cation on Crystal and Electronic Structure of Organometallic Halide Perovskites," *J. Phys. Chem. C*, vol. 121, no. 12, p. 121, 2017.

269. X. Xia, W. Wu, H. Li, B. Zheng, Y. Xue, J. Xu, D. Zhang, C. Gao, and X. Liu, "Spray reaction prepared FA 1-x Cs x PbI 3 solid solution as a light harvester for perovskite solar cells with improved humidity stability â ," *RSC Advances*, vol. 6, no. 18, pp. 14792–14798, 2016.

270. C. L. Davies, J. Borchert, C. Q. Xia, R. L. Milot, H. Kraus, M. B. Johnston, and L. M. Herz, "Impact of the Organic Cation on the Optoelectronic Properties of Formamidinium Lead Triiodide," *The Journal of Physical Chemistry Letters*, vol. 9, no. 16, pp. 4502–4511, 2018.

271. B. Subedi, L. Guan, Y. Yu, K. Ghimire, P. Uprety, Y. Yan, and N. J. Podraza, "Formamidinium + cesium lead triiodide perovskites: Discrepancies between thin film optical absorption and solar cell efficiency," *Solar Energy Materials and Solar Cells*, vol. 188, pp. 228–233, 2018.

272. Y. Q. Zhao, Q. R. Ma, B. Liu, Z. L. Yu, J. Yang, and M. Q. Cai, "Layer-dependent transport and optoelectronic property in two-dimensional perovskite: (PEA)2PbI4," *Nanoscale*, vol. 10, no. 18, pp. 8677–8688, 2018.

273. M. Dyksik, S. Wang, W. Paritmongkol, D. K. Maude, W. A. Tisdale, M. Baranowski, and P. Plochocka, "Tuning the Excitonic Properties of the 2D (PEA)2(MA)n-1PbnI3 n+1Perovskite Family via Quantum Confinement," *Journal of Physical Chemistry Letters*, vol. 12, no. 6, pp. 1638–1643, 2021.

274. W. Wang, Y. Li, X. Wang, Y. Liu, Y. Lv, S. Wang, K. Wang, Y. Shi, L. Xiao, Z. Chen, and Q. Gong, "Interplay between Exciton and Free Carriers in Organolead Perovskite Films," *Scientific Reports*, vol. 7, no. 1, p. 14760, 2017.

275. A. A. Burgos-Caminal, E. Socie, M. E. F. Bouduban, and J.-E. Moser, "Exciton and Carrier Dynamics in Two-Dimensional Perovskites," *J. Phys. Chem. Lett*, vol. 11, no. 18, p. 18, 2020.

276. V. A. Hintermayr, L. Polavarapu, A. S. Urban, and J. Feldmann, "Accelerated Carrier Relaxation through Reduced Coulomb Screening in Two-Dimensional Halide Perovskite Nanoplatelets," *ACS Nano*, vol. 12, no. 10, pp. 10151–10158, 2018.

277. A. Kumar, A. Solanki, M. Manjappa, S. Ramesh, Y. K. Srivastava, P. Agarwal, T. C. Sum, and R. Singh, "Excitons in 2D perovskites for ultrafast terahertz photonic devices," *Science Advances*, vol. 6, no. 8, p. eaax8821, 2020.

278. R. D. J. Oliver, Y.-H. Lin, A. J. Horn, C. Q. Xia, J. H. Warby, M. B. Johnston, A. J. Ramadan, and H. J. Snaith, "Thermally Stable Passivation toward High Efficiency Inverted Perovskite Solar Cells," *ACS Energy Letters*, vol. 5, no. 11, pp. 3336–3343, 2020.

279. A. S. Tutantsev, E. I. Marchenko, N. N. Udalova, S. A. Fateev, E. A. Goodilin, and A. B. Tarasov, "Structural Disorder in Layered Hybrid Halide Perovskites: Types of Stacking Faults, Influence on Optical Properties and Their Suppression by Crystallization Engineering," *Nanomaterials*, vol. 11, no. 12, p. 3333, 2021.

280. W. Fu, H. Liu, X. Shi, L. Zuo, X. Li, and A. K. Jen, "Tailoring the Functionality of Organic Spacer Cations for Efficient and Stable Quasi-2D Perovskite Solar Cells," *Advanced Functional Materials*, vol. 29, no. 25, p. 1900221, 2019.

281. F. Meng, X. Shang, D. Gao, W. Zhang, and C. Chen, "Functionalizing phenethylammonium by methoxy to achieve low-dimensional interface defects passivation for efficient and stable perovskite solar cells," *Nanotechnology*, vol. 33, no. 6, p. 065201, 2022.

282. J. Chen, J. Lv, X. Liu, J. Lin, and X. Chen, "A study on theoretical models for investigating time-resolved photoluminescence in halide perovskites," *Physical Chemistry Chemical Physics*, vol. 25, no. 11, pp. 7574–7588, 2023.

283. J. Shi, Y. Li, Y. Li, D. Li, Y. Luo, H. Wu, and Q. Meng, "From Ultrafast to Ultraslow: Charge-Carrier Dynamics of Perovskite Solar Cells," *Joule*, vol. 2, no. 5, pp. 879–901, 2018.

284. J. I. H. Haggar, S. S. Ghataora, V. Trinito, J. Bai, and T. Wang, "Study of the Luminescence Decay of a Semipolar Green Light-Emitting Diode for Visible Light Communications by Time-Resolved Electroluminescence," *ACS Photonics*, vol. 9, no. 7, pp. 2378–2384, 2022.

285. G. Han, H. D. Hadi, A. Bruno, S. A. Kulkarni, T. M. Koh, L. H. Wong, C. Soci, N. Mathews, S. Zhang, and S. G. Mhaisalkar, "Additive Selection Strategy for High Performance Perovskite Photovoltaics," *The Journal of Physical Chemistry C*, vol. 122, no. 25, pp. 13884–13893, 2018.

286. E. A. Alharbi, M. I. Dar, N. Arora, M. H. Alotaibi, Y. A. Alzhrani, P. Yadav, W. Tress, A. Alyamani, A. Albadri, S. M. Zakeeruddin, and M. Grätzel, "Perovskite Solar Cells Yielding Reproducible Photovoltage of 1.20 V," *Research*, vol. 2019, pp. 1–9, 2019.

287. W. Chen, N. D. Pham, H. Wang, B. Jia, and X. Wen, "Spectroscopic Insight into Efficient and Stable Hole Transfer at the Perovskite/Spiro-OMeTAD Interface with Alternative Additives," *ACS Applied Materials & Interfaces*, vol. 13, no. 4, pp. 5752–5761, 2021.

288. K. P. Chiu, "The influence of a trap state on the photoluminescence decay times under single pulse excitation," *Optical and Quantum Electronics*, vol. 55, no. 2, p. 163, 2023.

289. L. Krückemeier, B. Krogmeier, Z. Liu, U. Rau, and T. Kirchartz, "Understanding Transient Photoluminescence in Halide Perovskite Layer Stacks and Solar Cells," *Advanced Energy Materials*, 2021.

290. M. D. Bastiani, V. D'Innocenzo, S. D. Stranks, H. J. Snaith, and A. Petrozza, "Role of the crystallization substrate on the photoluminescence properties of organo-lead mixed halides perovskites," *APL MATERIALS*, vol. 2, no. 8, p. 081509, 2014.

291. BAYES, "AN ESSAY TOWARDS SOLVING A PROBLEM IN THE DOCTRINE OF CHANCES," *Biometrika*, vol. 45, no. 3-4, pp. 296–315, 1958.

292. C. P. Robert and G. Casella, "Monte Carlo Statistical Methods," *Springer Texts in Statistics*, pp. 267–320, 2004.

293. C. Fai, C. J. Hages, and A. J. Ladd, "Rapid Optoelectronic Characterization of Semiconductors by Combining Bayesian Inference with Metropolis Sampling," *PRX Energy*, vol. 2, no. 3, p. 033013, 2023.

294. A. Gelman, J. B. Carlin, H. S. Stern, D. B. Dunson, A. Vehtari, and D. B. Rubin, *Bayesian Data Analysis*. 3rd edition ed., 2014.

295. A. Kiligaridis, P. A. Frantsuzov, A. Yangui, S. Seth, J. Li, Q. An, Y. Vaynzof, and I. G. Scheblykin, "Are Shockley-Read-Hall and ABC models valid for lead halide perovskites?," *Nature Communications*, vol. 12, no. 1, p. 3329, 2021.

296. J. M. Borrego, S. Saroop, R. J. Gutmann, G. W. Charache, T. Donovan, P. F. Baldasaro, and C. A. Wang, "Photon recycling and recombination processes in 0.53 eV p-type InGaAsSb," *Journal of Applied Physics*, vol. 89, no. 7, pp. 3753–3759, 2001.

297. T. Hastie, J. Friedman, and R. Tibshirani, "The Elements of Statistical Learning," *Springer Series in Statistics*, pp. 257–298, 2001.

298. P. Zeng, G. Feng, X. Cui, and M. Liu, "Revealing the Role of Interfaces in Photocarrier Dynamics of Perovskite Films by Alternating Front/Back Side Excitation Time-Resolved Photoluminescence," *The Journal of Physical Chemistry C*, vol. 124, no. 11, pp. 6290–6296, 2020.

299. Y. Yang, Y. Yan, M. Yang, S. Choi, K. Zhu, J. M. Luther, and M. C. Beard, "Low surface recombination velocity in solution-grown CH3NH3PbBr3 perovskite single crystal," *Nature Communications*, vol. 6, no. 1, p. 7961, 2015.

300. P. Caprioglio, C. M. Wolff, O. J. Sandberg, A. Armin, B. Rech, S. Albrecht, D. Neher, and M. Stolterfoht, "On the Origin of the Ideality Factor in Perovskite Solar Cells," *Advanced Energy Materials*, vol. 10, no. 27, 2020.

301. T. P. Weiss, B. Bissig, T. Feurer, R. Carron, S. Buecheler, and A. N. Tiwari, "Bulk and surface recombination properties in thin film semiconductors with different surface treatments from time-resolved photoluminescence measurements," *Scientific Reports*, vol. 9, no. 1, p. 5385, 2019.

302. A. Al-Ashouri, M. Marčinskas, E. Kasparavičius, T. Malinauskas, A. Palmstrom, V. Getautis, S. Albrecht, M. D. McGehee, and A. Magomedov, "Wettability Improvement of a Carbazole-Based Hole-Selective Monolayer for Reproducible Perovskite Solar Cells," *ACS Energy Letters*, vol. 8, no. 2, pp. 898–900, 2023.

303. S. Chen, X. Dai, S. Xu, H. Jiao, L. Zhao, and J. Huang, "Stabilizing perovskite-substrate interfaces for high-performance perovskite modules," *Science*, vol. 373, no. 6557, pp. 902–907, 2021.

304. G. Hodes and P. V. Kamat, "Understanding the Implication of Carrier Diffusion Length in Photovoltaic Cells," *The Journal of Physical Chemistry Letters*, vol. 6, no. 20, pp. 4090–4092, 2015.

APPENDIX

ERROR ANALYSIS FOR CHAPTER 5

A

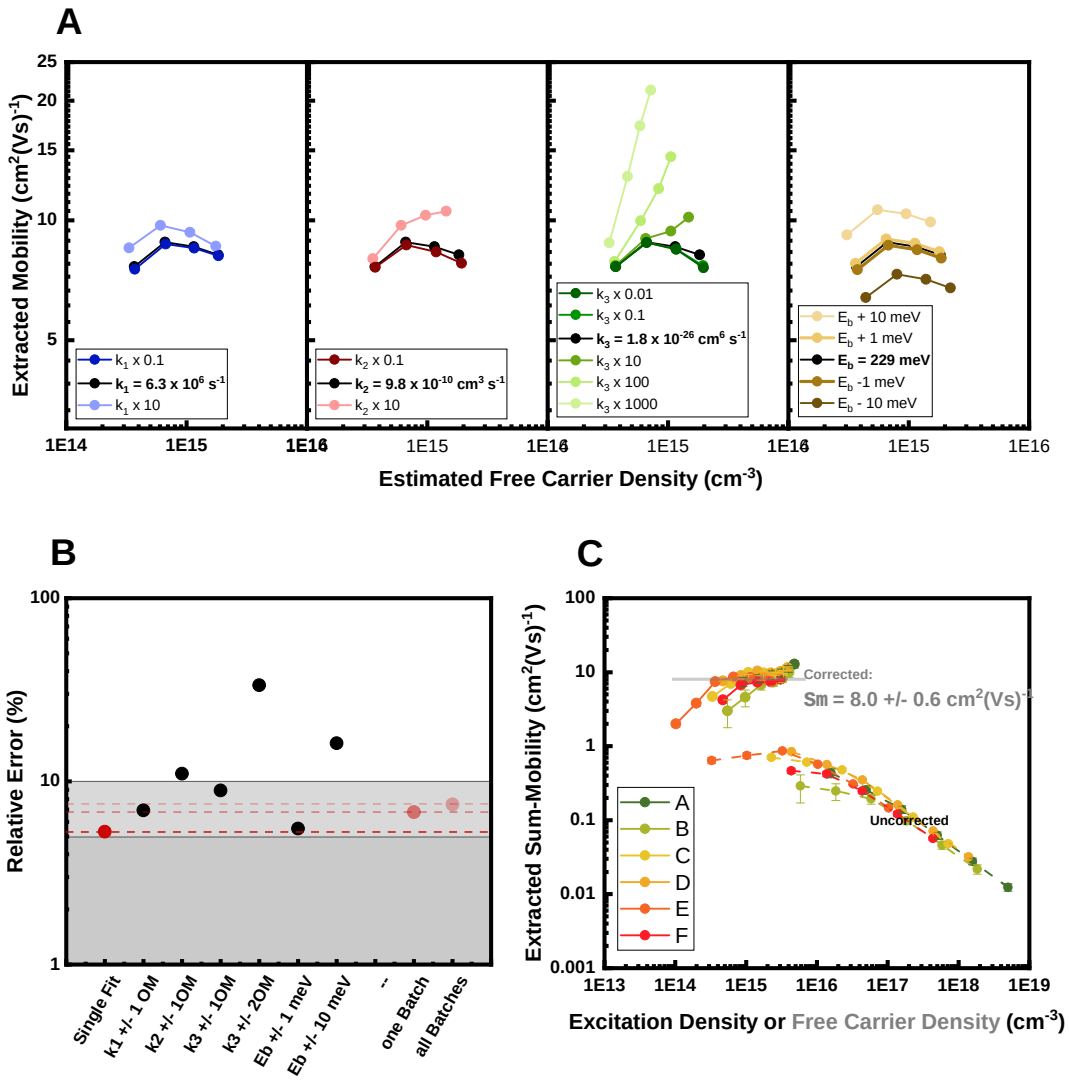

Figure A.1: **A**: Error estimation for the TPC corrections of PEA_2PbI_4. Each parameter is changed with respect to the best estimates summarized in **Table 5.1**. **B**: The data in A are averaged over all carrier densities, and the relative error in the sum of the charge carrier mobilities is calculated (for example $k_1 \pm 1$ OM means range of estimated mobility, using the range of k_1). The red data points with corresponding lines show the errors estimated by a single fit, three films within one batch and all batches from this study. The dark and light grey areas represent the 5% and 10% relative error regions respectively. **C**: Summarized mobility data of all the PEA_2PbI_4 batches used in this study. The uncorrected as well as corrected data are presented side-by-side.

APPENDIX

B

FULL DATA ANALYSIS FOR CHAPTER 6

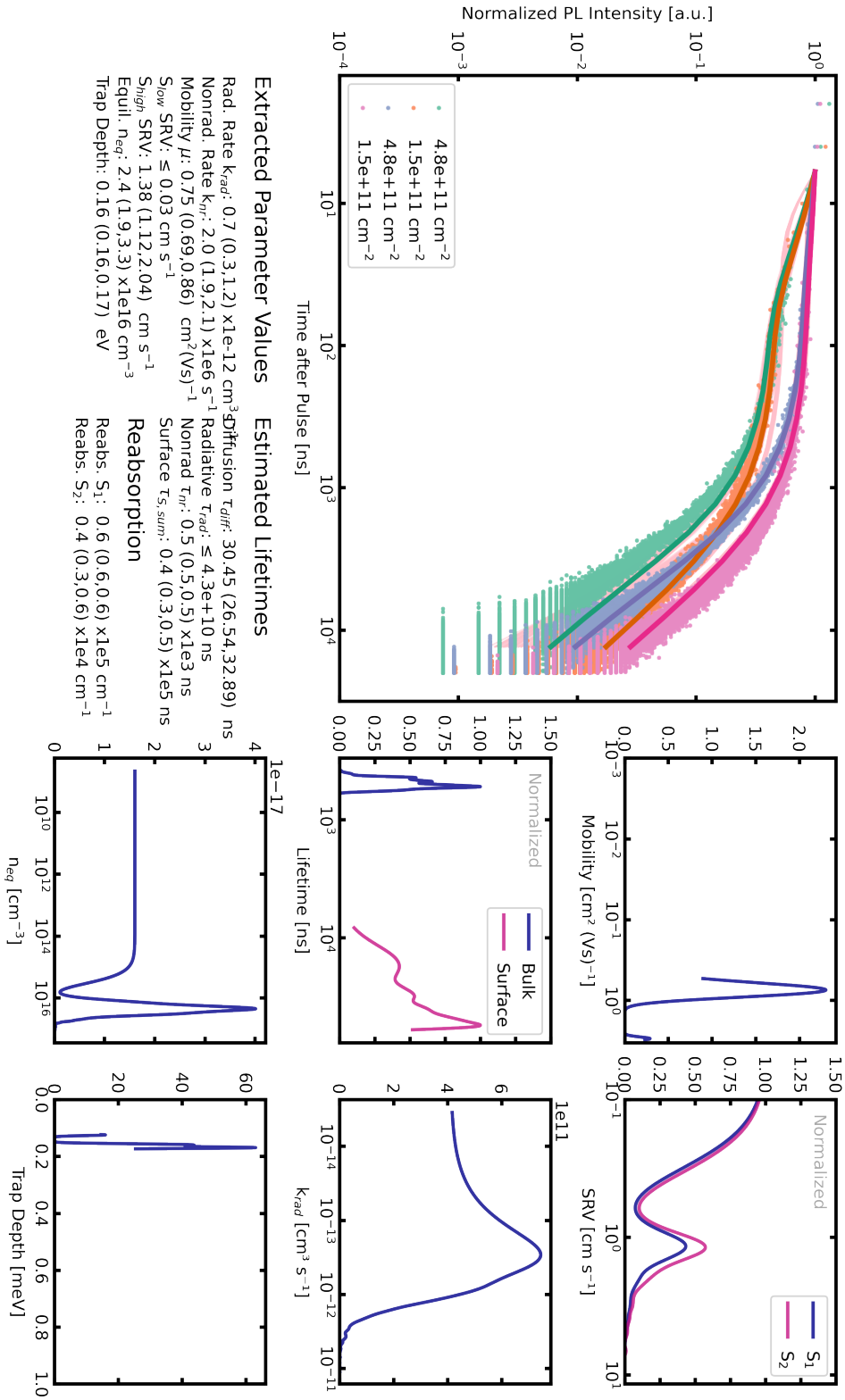

Figure B.1: $FAPbI_3$ on glass from **Chapter 6**.

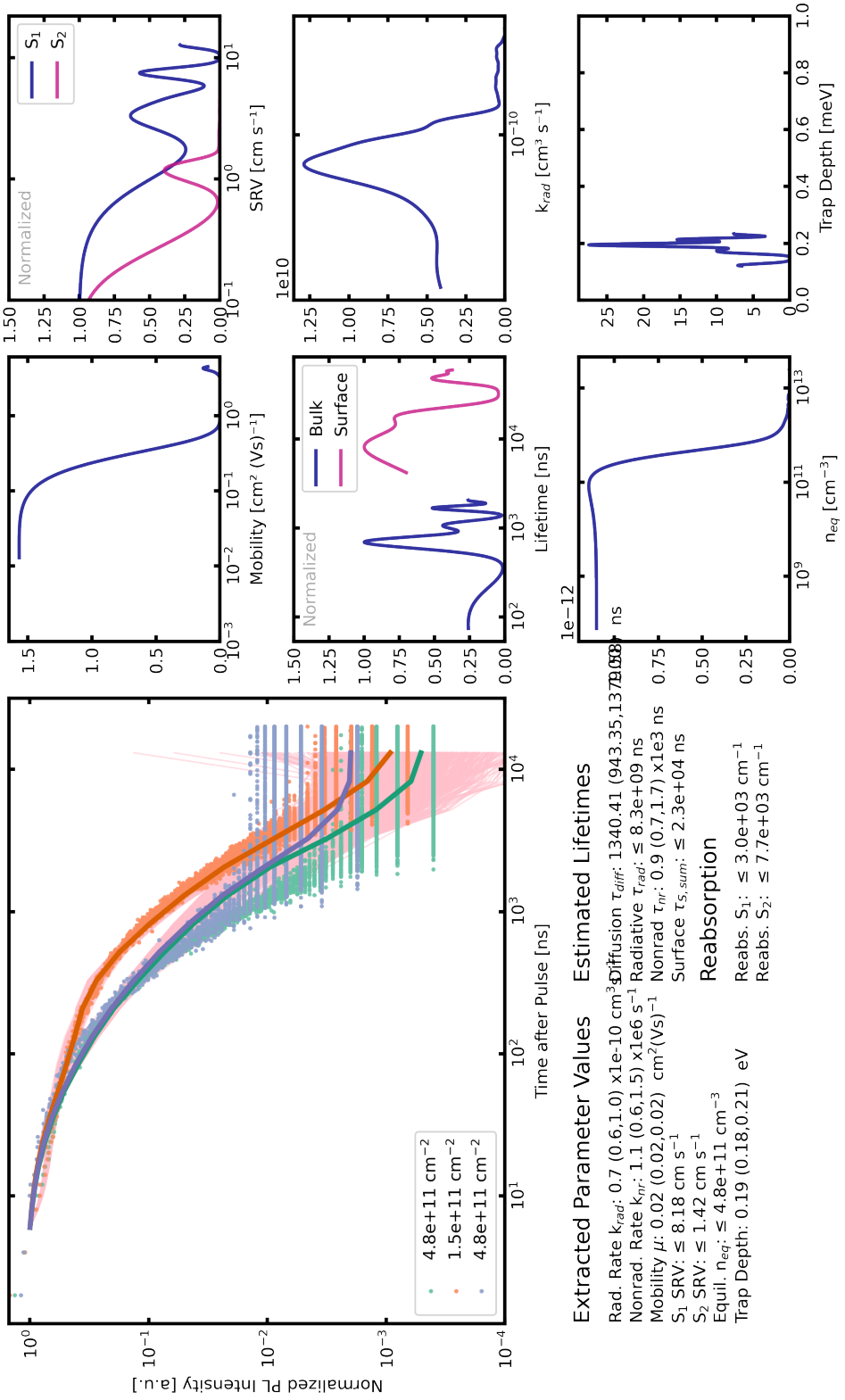

Figure B.2: $FAPbI_3$ on SnO_2 from **Chapter 6**.

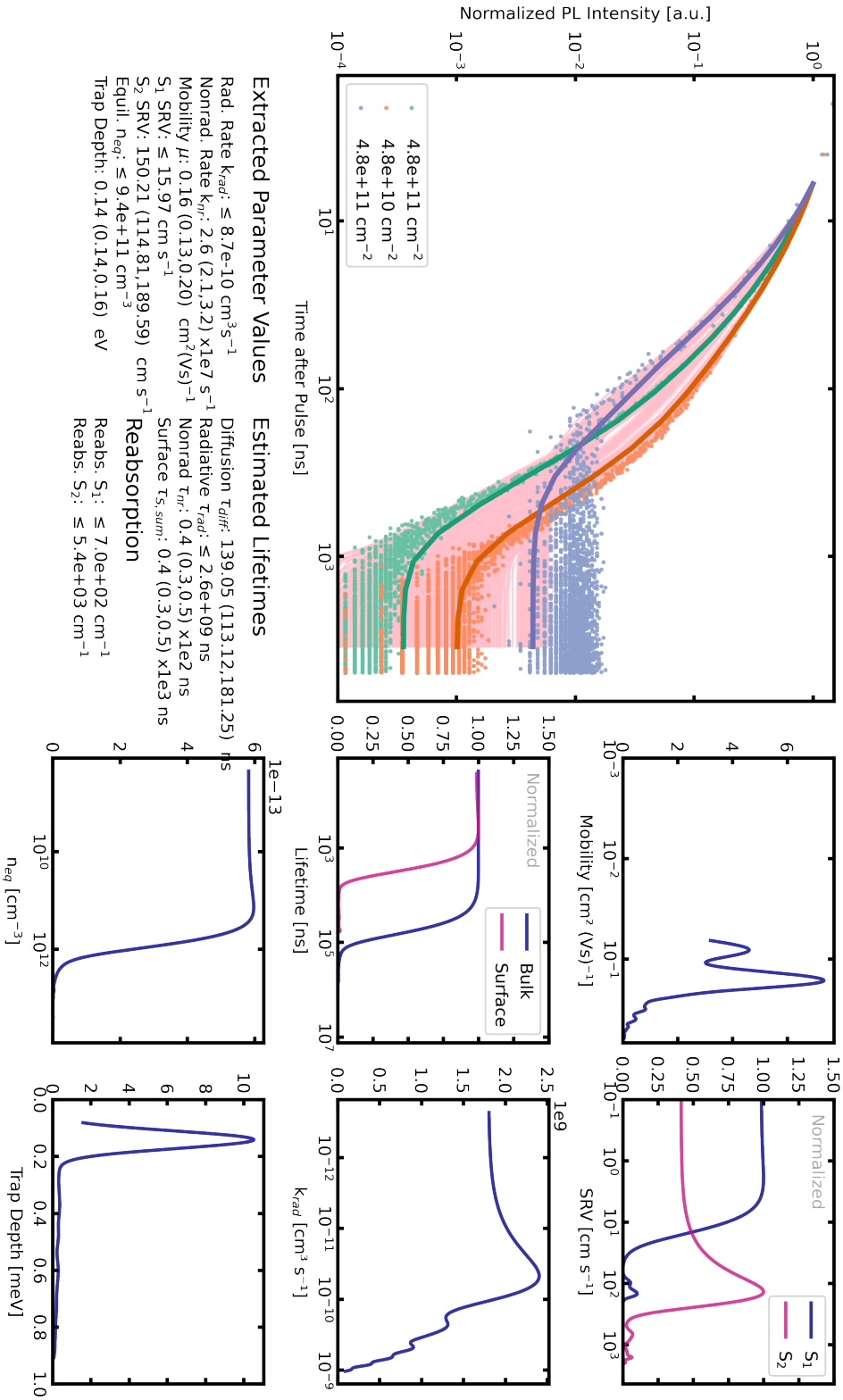

Figure B.3: $FAPbI_3$ on glass coated with Spiro from **Chapter 6**.

APPENDIX C

PYTHON CODES

In this appendix all `python` codes that were written for or adapted during this thesis are summarized. It is stated, who the original author was, if they were adapted or who co-authored them when they were newly written. In all cases only the core functionalities of the code are shown, which correspond to the equations from **Chapter 3**. This excludes the import of the raw data and the final plotting of the results, as well as exporting of extracted parameters.

ELLIOTT MODEL TO FIT ABSORPTION DATA

This `python` code was used to estimate the exciton binding energy of perovskite samples from the absorption coefficient measured via UV-Vis absorption. The input is a text-document with the photon energies and calculated absorption coefficient. Details of the equations can be found in **Chapter 3**. The code was written by Dr. Bernard Wenger (University of Oxford), but adapted during this thesis. The adapted parts are commented as such.

```
import numpy as np
import matplotlib.pyplot as plt
from scipy import signal
from scipy.stats import lognorm
from lmfit import Model

##############
# Functions #
##############

# Gauss function
def gauss(x, sig, mu):
        return np.exp(-((x-mu)/sig)**2/2)


## ELLIOTT MODEL
# Excitonic part
# --------------
def alpha_x(E, p):
    [b0, Ex, Eg, sigma_exc, mu_lognorm, sigma_cont,Ex_split, Ex_broad,
    ↪  Dielectric_Factor] = p

    alpha = np.zeros(len(E))

    mu = Eg-Ex

    # this part was adapted to account for an asymmetric peak broadening
    mua = mu - 0.5*Ex_split
    mub = mu + 0.5*Ex_split
    sigma_exc2 = Ex_broad*sigma_exc
```

```
30
31      bf = gauss(E, sigma_exc, mua) + np.where(E > mub, gauss(E, sigma_exc2,
        ↪  mub), gauss(E, sigma_exc, mub))
32
33      alpha += (4 * np.pi * Ex**(3/2)) * bf
34
35      for n in np.arange(2,11):
36          mu = Eg-Ex/n**2
37          bf = gauss(E, sigma_exc, mu)
38
39          # the Delta function is the identity in a convolution
40          alpha += (Dielectric_Factor**4 * np.pi * Ex**(3/2) / n**3) * bf
41      return alpha
42
43
44  # Continuum part
45  # # --------------
46  def alpha_c(E, p):
47      [b0, Ex, Eg, sigma_exc, mu_lognorm, sigma_cont, Ex_split, Ex_broad,
        ↪  Dielectric_Factor] = p
48
49      x = np.where(E > Eg, np.sqrt(Ex / (E - Eg), where=E>Eg), 0)
50      # Sommerfeld factor
51      xi = 2 * np.pi * x / (1 - np.exp(-2 * np.pi * x, where=x!=0))
52      # free continuum without exciton
53      free = np.where(E > Eg, np.sqrt(E-Eg, where = E>Eg), 0)
54      return np.where(E > Eg, xi * free, 0)
55
56  def alpha_c_conv(E, Erange, p): # Broadening of the continuum part
57      [b0, Ex, Eg, sigma_exc, mu_lognorm, sigma_cont, Ex_split, Ex_broad,
        ↪  Dielectric_Factor] = p
58
59      # build kernel
60      # works with evenly distributed abscissa
61      dx = E[1] - E[0]
62      kernel = np.arange(-8*sigma_exc, 8*sigma_exc, dx)
63      E_pad = np.pad(E, (E.size, E.size), 'edge')
64
65      res = np.convolve(alpha_c(E_pad, p),
66      gauss(kernel, sigma_cont, 0, 1), mode='same')/np.sum(gauss(kernel,
        ↪  sigma_cont, 0))
```

```
67
68      res = res[np.max(np.where(E_pad <= Erange[0])):
69      np.min(np.where(E_pad >= Erange[1]))+1]
70
71      # division by the sum is required to keep the scale
72      return res
73
74  def alpha_sum(E, Erange, b0, Ex, Eg, sigma_exc, mu_lognorm, sigma_cont,
    ↪  Ex_split, Ex_broad, Dielectric_Factor):
75      p = [b0, Ex, Eg, sigma_exc, mu_lognorm, sigma_cont,Ex_split, Ex_broad,
        ↪  Dielectric_Factor]
76
77      Esub = E[np.max(np.where(E <= Erange[0])): np.min(np.where(E >=
        ↪  Erange[1]))+1]
78
79      return b0 * Ex**0.5 / Esub * (alpha_x(Esub, p) + alpha_c_conv(Esub,
        ↪  Erange, p))
80
81  def dofit(eV, abscoef, guess, eVrange):
82      # need to have evenly spaced data for the convolution
83      eV_interp = np.linspace(eV[0], eV[-1], 600)
84      data_interp = np.interp(eV_interp, eV, absCoef)
85
86      # Fit range
87      eVsub = eV_interp[np.max(np.where(eV_interp < eVrange[0])):
        ↪  np.min(np.where(eV_interp > eVrange[1]))+1]
88      data = data_interp[np.max(np.where(eV_interp < eVrange[0])):
        ↪  np.min(np.where(eV_interp > eVrange[1]))+1]
89
90      # Using LMfit
91      ## 'Ex_split', 'Ex_broad' as well as 'Dielectric_Factor' were added to
        ↪  the original code
92      myMod = Model(alpha_sum, independent_vars=['E', 'Erange'])
93      print(myMod.param_names)
94      myMod.set_param_hint('b0',value=guess[0], vary = True)
95      myMod.set_param_hint('Ex', value=guess[1], min=0., vary=True)
96      myMod.set_param_hint('Eg', value=guess[2], min=0., vary=True)
97      myMod.set_param_hint('sigma_exc', value=guess[3], vary=True)#, min=0)
98      myMod.set_param_hint('sigma_cont', value=guess[4], min=0.0001,vary=False)
99      myMod.set_param_hint('mu_lognorm', value=guess[5], vary=True)
```

```
100     myMod.set_param_hint('Ex_split', value=guess[6], min = 0,max = 80,
        ↪  vary=False)
101     myMod.set_param_hint('Ex_broad', value=guess[7], min = 1,max = 10,
        ↪  vary=True)
102     myMod.set_param_hint('Dielectric_Factor', value=guess[8], min = 1, max =
        ↪  10, vary=True)
103
104     result = myMod.fit(data, E=eV_interp, Erange=eVrange)
105     print(result.fit_report())
106
107     best_params = result.best_values
108     bp = [best_params['b0'], best_params['Ex'], best_params['Eg'],
        ↪  best_params['sigma_exc'], best_params['mu_lognorm'],
        ↪  best_params['sigma_cont'],best_params['Ex_split'],
        ↪  best_params['Ex_broad'], best_params['Dielectric_Factor']]
109
110     fit_exc = bp[0] * bp[1]**0.5 / eV_interp * alpha_x(eV_interp, bp)
111     fit_cont = bp[0]  * bp[1]**0.5 / eV_interp * alpha_c_conv(eV_interp,
        ↪  [eV_interp[0], eV_interp[-1]], bp)
112     fit_y = bp[0] * bp[1]**0.5 / eV_interp * ( alpha_x(eV_interp, bp) +
        ↪  alpha_c_conv(eV_interp, [eV_interp[0], eV_interp[-1]], bp)
113
114
115
116 ##############
117 # Main Part #
118 ##############
119 # load and convert data
120 loaded = np.loadtxt('Mat1.txt', skiprows = 0, delimiter='\t', unpack=False)
121
122 absCoef = loaded[:, 1] # for scaling but needs to be appropriately
    ↪  calculateds
123 #absCoef -= 2100 # Remove baseline
124
125 scale = 1e4
126 absCoef /= scale # rescale
127 eV = loaded[:, 0]
128
129 # Guess parameters
130 b0 = 400000
```

```
Ex = 600 # meV
Eg = 3.0# eV
sigma_exc = 20 # meV
sigma_cont = 115# meV
mu_lognorm = -0.2 # eV

fit_range = [2.3, 3.2]

############################################################
# This part was adapted to account for confined systems #
############################################################

Ex_split = 1#meV  (only used, if > 0)

#Factor that simluates an asymmetric broadening of the 1s excitonic peak
Ex_broad = 2

#enhances excitonic peak (set to 1 for 3D)
Dielectric_Factor = 10

############
# Fitting #
############
guess = [b0 / scale, Ex*1e-3, Eg, sigma_exc*1e-3, sigma_cont*1e-3, mu_lognorm,
 ↪  Ex_split*1e-3, Ex_broad, Dielectric_Factor]
dofit(eV, absCoef, guess, fit_range)

```

TPC CODE 1.0

This `python` code was used to tuen the data measured from the oscilloscope into transient photoconductivity, fit them with a monoexponential decay to be able to estimate σ_{photo} at $t = 0$ ns and simulate the transient free carrier fraction. The input data is a text file containing the measurement time in s and then all V_{osc} measurements for the different ND filters used. The filter number is saved in the header. Details of the equations can be found in **Chapters 3** and **4**. The code was co-written by Dr. Bernard Wenger (University of Oxford) and Dr. Jongchul Lim (Chungnam National University). In this code the inclusion of an RC-type increase of the measured voltage or photo-conductivity was included, which was not part of the previous version.

This improved the overall fit and reproducibility of the method.

```
import numpy as np
import pandas as pd
from lmfit import Parameters, minimize
from scipy.integrate import odeint
from scipy.optimize import root


##############################
# Some Important Constants #
##############################

frequency = 10.0 #Hz
pulse_fwhm = 3.74e-9        #s
T = 292  # temp in K
mu_ex = 0.1 * 9.10938356e-31          # kg reduced mass
Resistance_System = 1000 #Ohm (terminal resistance on oscilloscope)
Fit_range = np.array([0, 1000])

#############
# Functions #
#############

def monoexponential(params, time):
    A1 = params['A'].value
    tau1 = params['tau'].value
    y0 = params['y0'].value
    RC = params['RC'].value

    biexp = (1-np.exp(-time/RC))*(A * np.exp(-(time / tau)))
    return biexp


def residual(params, time, Data, args):
   resid = residual2(params, time, Data, args)
   return resid*time


```

```
def residual2(params, time, Data, args):
    model = monoexponential(params, time)
    return (model - Data)


def Fitting_Cond(photo_cond, time, time_RC_max_old, args):
    Data_fit = photo_cond
    Data_fit[Data_fit <= 0] = np.nan
    if np.isnan(np.nanmean(Data_fit[0:400])):
        data_sort = np.sort(Data_fit[~np.isnan(Data_fit)])
        darkc = np.nanmedian(data_sort[0:100])
    else:
        darkc = np.nanmean(Data_fit[0:400])
    dark_cond_value = np.nan_to_num(darkc)

    limit = np.where((time > Fit_range[0]) & (time < Fit_range[1]))

    Data_fit_cut = Data_fit[limit] - dark_cond_value
    Data_fit_cut[Data_fit_cut <= 0] = np.nan

    #Data_fit = medfilt(Data_fit, 75)        # Good fit results, without
    ↪ changing the final estimated value

    time_fit = time[limit]

    time_RC_max_new = time_fit[np.nanargmax(Data_fit_cut)]

    if time_RC_max_new < time_RC_max_old:
        time_RC_max_fit = time_RC_max_new
    else:
        time_RC_max_fit = time_RC_max_old

    params = Parameters()
    params.add('A', value=0.001, min=0, max=1)
    params.add('tau', value=2000, min=10)
    params.add('y0', value=dark_cond_value, vary=False )
    params.add('RC', value=time_RC_max_fit , min=3.74, max=time_RC_max_fit,
    ↪ vary=True)

    results_Model = minimize(residual, params, method='leastsq',
    ↪ args=(time_fit, Data_fit_cut, args), nan_policy='omit')
```

```
    photo_cond_zero_value = results_Model.params['A'].value

    tau_value = results_Model.params['tau1'].value

    pseudo_k1_value = 1/(tau_avg_value*1e-9)

    RC_Fit = results_Model.params['RC'].value
    sigma_fit_value = (results_Model.params['A'].value * np.exp(-(time /
     ↪  results_Model.params['tau'].value))) + dark_cond_value


    return dark_cond_value, photo_cond_zero_value, tau_value,
     ↪  sigma_fit_value, pseudo_k1_value, RC_Fit


def gauss(t, mu, sig):
    return 1/(sig*np.sqrt(2*np.pi)) * np.exp(-(1/2)*((t-mu)/sig)**2)


def df(c0,t,p, sigma, mu):
    ne = c0

    k1, k2, k3, ntot = p
    G = gauss(t, mu, sigma)
    dnedt = ntot*G -k1*ne - k2*ne**2 #- k3*ne**3
    return dnedt


def a(n, E_B, mu_ex):
    # Solve the Saha equation to find the exciton density
    n_free = ()
    for m in n:

        k = 1.38064852e-23
        h = 6.62607004e-34
        e = 1.60217662e-19
        saha_const = (2*np.pi*mu_ex*k*T / h**2)**(3 / 2) * np.exp(-(e * E_B) /
         ↪  (k * T))

        phi_x =
         ↪  2*np.sqrt(saha_const)/(np.sqrt(saha_const+4*m)+np.sqrt(saha_const))
```

```
        n_free = np.append(n_free, phi_x)

    return n_free


######################
# Main Part of Code #
######################
args = get_args()

time, Data, OD_Filter = unpack_Data(args)
time = time*1e9

photo_cond, width, depth, spacing = photocond_dec(args)
num_rows, num_cols = photo_cond.shape

dark_cond = []
photo_cond_zero = []
tau_avg = []
pseudo_k1 = []
RC_value = []
sigma_fit = pd.DataFrame(time, columns=['Time (ns)'])


## Estimate Initial Carrier Density ##

Fluence, Exc_Density, PowerDens, Absorption = Exc_Density_Calc(OD_Filter,
↪  args)


## Fitting Photoconductivity ##

for i in range(num_rows):

    dark_cond_value, photo_cond_zero_value, tau_avg_value, sigma_fit_value,
    ↪  pseudo_k1_value, RC_Fit = Fitting_Cond(photo_cond[i], time,
    ↪  time_RC_max,  args)
```

```
150
151     dark_cond = np.append(dark_cond, dark_cond_value)
152     tau_avg = np.append(tau_avg, tau_avg_value)
153     RC_value = np.append(RC_value, RC_Fit)
154     photo_cond_zero = np.append(photo_cond_zero,photo_cond_zero_value)
155     pseudo_k1 = np.append(pseudo_k1,pseudo_k1_value)
156     sigma_fit[str('Filter_'+ str(OD_Filter[i]))] = sigma_fit_value
157
158     time_RC_max = RC_Fit
159
160
161
162 ## Estimation of Phi-Mobility ##
163 Phi_SMu = photo_cond_zero/(Exc_Density*1.602176634e-19)
164
165
166 ######################################
167 # Simulating Free Carrier Fraction #
168 ######################################
169
170 # Kinetik Equation Fitting #
171
172
173 if args.k1:
174     k1_const = args.k1 * 1e6  # in s-1
175     pseudo_k1_marker = "set"
176 else:
177     k1_const = pseudo_k1_value
178     pseudo_k1_marker = "pseudo"
179
180
181 exciton_binding = args.Exciton_Binding_Energy / 1000  # in eV
182 k2_const = args.k2 * 1e-10  # in cm3 s-1
183 k3_const = args.k3 * 1e-28  # in cm6 s-1
184
185 I0 =  0
186
187 sigma = pulse_fwhm / (2 * np.sqrt(2 * np.log(2)))
188 mu = pulse_fwhm
189 res = pd.DataFrame()
```

```
190
191 # Kinetik Model Preparation #
192
193 kinetik_range =[-10,1000]
194 for i in range(num_rows):
195     corr_param = [k1_const, k2_const, k3_const, Exc_Density[i]]
196
197     num_pnts = 1000  # number of points in the simulation
198
199
200     t = time[np.where((time > kinetik_range[0]) & (time <
    ↪  kinetik_range[1]))]*1e-9  # in ns
201     sol = odeint(df, I0, t, args=(corr_param,sigma, mu))
202     sol = sol.reshape(-1)
203     res['OD-Filter'+str(OD_Filter[i])] = sol#/np.max(sol)*Exc_Density[i]
204
205
206 # Solving the Saha Equation #
207
208 t_max = []
209 Max_Carr = []
210 free_carr_dens = np.zeros(shape=num_rows)
211 SCond = np.zeros(shape=num_rows)
212
213 a1_val = pd.DataFrame()
214 sol_saha_df = pd.DataFrame()
215 # Calculate free-carrier fraction as a function of charge density
216 # and exciton binding energy
217 for i in range(num_rows):
218     sol = res['OD-Filter' + str(OD_Filter[i])]
219
220     a1 = a(sol * 1e6, exciton_binding, mu_ex)  # Saha's equation is
    ↪  calculated in m3 not cm3, hence 1e6
221     a1_val['OD-Filter'+str(OD_Filter[i])] = a1
222     sol_saha = np.nan_to_num(sol * a1)
223     sol_saha_df['OD-Filter'+str(OD_Filter[i])] = sol_saha
224     free_carr_value = sol_saha/Exc_Density[i]
225
226     biexp_val = np.array(sigma_fit[str('Filter_'+
    ↪  str(OD_Filter[i]))])[np.where((time > kinetik_range[0]) & (time <
    ↪  kinetik_range[1]))]
```

```
227
228     t_max = np.append(t_max, t[np.nanargmax(sol_saha)] * 1e9)
229     free_carr_dens[i] =
        ↪  np.median(sol_saha[np.where(np.isclose(t*1e9,t_max[i]))])#np.nanmax(sol_saha)
230     SCond[i] =
        ↪  np.median(biexp_val[np.where(np.isclose(t*1e9,t_max[i]))])#biexp_val[np.nanargm
231
232
233
234 # Calculating Corrected Mobility #
235
236 SMu = SCond/(free_carr_dens*1.602176634e-19)
```

TPC CODE 2.0

This code is an upgraded version of TPC Code 1.0. Hence, only the changed parts are shown: the monoexponential fitting is the same and only the part `Simulating Free Carrier Fraction` has been changed into a `minimize` function.

```
1  import ... # as before
2  from scipy.optimize import root, minimize_scalar
3
4
5  ######################################
6  # Simulating Free Carrier Fraction #
7  ######################################
8
9  def Kinetik_Fit(k2x, time,sigma_fit, pseudo_k1_value, photo_cond_zero, args):
10     if args.k1:
11         k1_const = args.k1 * 1e6  # in s-1
12         pseudo_k1_marker = "set"
13     else:
14         k1_const = pseudo_k1_value
15         pseudo_k1_marker = "pseudo"
16
17
18     exciton_binding = args.Exciton_Binding_Energy / 1000  # in eV
19     k2_const = 10**(k2x) * 1e-10  # in cm3 s-1
```

```
    k3_const = args.k3 * 1e-28  # in cm6 s-1

    I0 =  0

    sigma = pulse_fwhm / (2 * np.sqrt(2 * np.log(2)))
    mu = pulse_fwhm
    res = pd.DataFrame()

    ## Kinetik Model Preparation

    kinetik_range =[-10,1000]
    for i in range(num_rows):
        corr_param = [k1_const, k2_const, k3_const, Exc_Density[i]]

        num_pnts = 1000  # number of points in the simulation


        t = time[np.where((time > kinetik_range[0]) & (time <
        ↪  kinetik_range[1]))]*1e-9  # in ns
        sol = odeint(df, I0, t, args=(corr_param,sigma, mu))
        sol = sol.reshape(-1)
        res['OD-Filter'+str(OD_Filter[i])] = sol#/np.max(sol)*Exc_Density[i]


    # Saha Equation Fitting #

    t_max = []
    Max_Carr = []
    free_carr_dens = np.zeros(shape=num_rows)
    SCond = np.zeros(shape=num_rows)

    a1_val = pd.DataFrame()
    sol_saha_df = pd.DataFrame()
    # Calculate free-carrier fraction as a function of charge density
    # and exciton binding energy
    for i in range(num_rows):
        sol = res['OD-Filter' + str(OD_Filter[i])]

        a1 = a(sol * 1e6, exciton_binding)  # Saha's equation is calculated
        ↪  in m3 not cm3, hence 1e6
```

```
        a1_val['OD-Filter'+str(OD_Filter[i])] = a1
        sol_saha = np.nan_to_num(sol * a1)
        sol_saha_df['OD-Filter'+str(OD_Filter[i])] = sol_saha
        free_carr_value = sol_saha/Exc_Density[i]

        biexp_val = np.array(sigma_fit[str('Filter_'+
        ↪  str(OD_Filter[i]))])[np.where((time > kinetik_range[0]) & (time <
        ↪  kinetik_range[1]))]

        t_max = np.append(t_max, t[np.nanargmax(sol_saha)] * 1e9)
        free_carr_dens[i] =
        ↪  np.median(sol_saha[np.where(np.isclose(t*1e9,t_max[i]))])#np.nanmax(sol_sah

    SMu = photo_cond_zero / (free_carr_dens * 1.602176634e-19)
    return SMu, t_max, free_carr_dens, SCond, pseudo_k1_marker


def residual_kin(k2x, time, sigma_fit,pseudo_k1_value, photo_cond_zero, args):

    SMu, t_max, free_carr_dens, SCond, pseudo_k1_marker = Kinetik_Fit(k2x,
    ↪  time, sigma_fit, pseudo_k1_value, photo_cond_zero, args)
    SMu_std = np.std(SMu[2:]) # The first two points are excluded due to the
    ↪  noise level

    return SMu_std



results_Model_kin = minimize_scalar(residual_kin, bounds=(-3, 5),
↪  method='bounded', args=(time, sigma_fit, pseudo_k1_value, photo_cond_zero,
↪  args))


# Calculating Corrected Mobility/Conductivity #

SMu, t_max, free_carr_dens, SCond, pseudo_k1_marker = Kinetik_Fit(k2_val,
↪  time, sigma_fit,pseudo_k1_value, photo_cond_zero, args)
```

```

```

INTENSITY-DEPENDENT PLQE CODE

The general approach shown here was used in **Chapters 4** and **5**. The input is a text file containing the power densities (the units can vary, but typically in $\mathrm{W\,cm^{-2}}$) and the calculated PLQE.

```
import numpy as np
import pandas as pd
from lmfit import Parameters, minimize
from scipy.integrate import odeint
from scipy.optimize import root

##############
# Functions #
##############

def equil_conc(G, params, i):
    k1 = 10**params[f'k1_{i + 1}'].value
    kex = 10**params[f'kex_{i + 1}'].value
    k2 = 10**params[f'k2_{i + 1}'].value
    k2_non = 10 ** params[f'k2non_{i + 1}'].value
    k3 = 10**params[f'k3_{i + 1}'].value
    n_dop = params[f'n_dop_{i + 1}'].value


    def recombination_model(n_eq0, k1, kex, k2, k2_non, k3, G, n_dop):

        n_eq0 += n_dop

        return G - k1*n_eq0 - (k2 + k2_non + kex/n_eq0)*n_eq0**2 -
        ↪  k3*n_eq0**3

    n_eq_sim = root(recombination_model, 1e15, method='hybr', args=(k1, kex,
    ↪  k2, k2_non, k3, G, n_dop))

    return n_eq_sim.x[0]
```

```
29
30
31  def plqe(params, n, i):
32      A = params[f'A_{i + 1}'].value
33      k1 = 10**params[f'k1_{i + 1}'].value
34      kex = 10**params[f'kex_{i + 1}'].value
35      k2 = 10**params[f'k2_{i + 1}'].value
36      k2_non = 10 ** params[f'k2non_{i + 1}'].value
37      k3 = 10**params[f'k3_{i + 1}'].value
38
39
40      plqe_int = (k2 * n+ kex)/(k1 + (k2 + k2_non) * n + kex+ k3 * n**2)
41
42
43      plqe_ext = (A*plqe_int)/((1-plqe_int)+(A*plqe_int))
44
45      return plqe_ext*100
46
47  def residual2(params, G, Data, i):
48      n_eq = []
49      for a in range(len(G)):
50          n_eq1 = equil_conc(G[a],params, i)
51          n_eq.append(n_eq1)
52
53      n_eq = np.array(n_eq)
54      model = plqe(params, n_eq, i)
55
56      return (model - Data)
57
58
59
60  def resid_global(params, generation_rate, Data, resid):
61
62      for i in range(num_rows):
63          k3_fact = np.abs(params[f'k3_{i + 1}'].value)
64          resid[:,i] = residual2(params, generation_rate[str(i)], Data[str(i)],
            ↪  i)/k3_fact
65
66
67      return resid.flatten()
```

```
68
69
70
71  ##############
72  # Main Part #
73  ##############
74  args = get_args()
75
76  df = pd.read_csv(args.data_path, header=None)
77  df = df.rename(columns={0: 'Filenames', 1: 'Thicknesses', 2: 'Wavelengths',
    ↪  3:'Reflectances', 4:'k1_values', 5:'k2_values', 6:'alpha'})
78
79  global num_rows
80  num_rows = len(df['Filenames'])
81
82  Power_dens = pd.DataFrame()
83  G_rate = pd.DataFrame()
84  PLQY_Data = pd.DataFrame()
85
86  for i in range(num_rows):
87      powerdens, generation_rate, Data = unpack_Data(df, i)
88
89      Power_dens[str(i)] = powerdens
90      G_rate[str(i)] = generation_rate
91      PLQY_Data[str(i)] = Data
92
93
94
95  ## Fitting PLQE Data ##
96  params = Parameters()
97
98  for i in range(num_rows):
99      params.add(f'A_{i + 1}', value=args.A, min=0, max=1)
100     params.add(f'n_dop_{i + 1}', value=args.Doping_n, min=0, max=1e18)
101     params.add(f'k1_{i + 1}', value=np.log10(df['k1_values'][i]), min=0,
        ↪  max=10)
102     params.add(f'neq_{i + 1}', value=12, min=1, max=18)
103     params.add(f'kex_{i + 1}', value=np.log10(args.kex), min=0, max=9)
104     params.add(f'k2_{i + 1}', value=np.log10(df['k2_values'][i]), min=-11,
        ↪  max=-7)
```

```
    params.add(f'k2non_{i + 1}', value=-11, min=-14, max=-7)
    params.add(f'k3_{i + 1}', value=np.log10(args.k3), min=-32, max=-24)

for y in range(num_rows - 1):
    if args.share_k1 == True:
        params[f'k1_{y + 2}'].expr = 'k1_1'
    if args.share_k2 == True:
        params[f'k2_{y + 2}'].expr = 'k2_1'

    if args.share_k3 == True:
        params[f'k3_{y + 2}'].expr = 'k3_1'
        params[f'k2non_{y + 2}'].expr = 'k2non_1'
    if args.share_kex == True:
        params[f'kex_{y + 2}'].expr = 'kex_1'
    if args.share_A == True:
        params[f'A_{y + 2}'].expr = 'A_1'
    if args.share_ndop == True:
        params[f'n_dop_{y + 2}'].expr = 'n_dop_1'

for i in range(num_rows):
    if args.fix_k1 == True:
        params[f'k1_{i + 1}'].vary = False
    if args.fix_k2 == True:
        params[f'k2_{i + 1}'].vary = False
    if args.fix_k3 == True:
        params[f'k3_{i + 1}'].vary = False
    if args.fix_kex == True:
        params[f'kex_{i + 1}'].vary = False
    if args.fix_A == True:
        params[f'A_{i + 1}'].vary = False
    if args.fix_Dn == True:
        params[f'n_dop_{i + 1}'].vary = False

resid = np.empty(shape = PLQY_Data.shape)
results_Model = minimize(resid_global, params, method='least_squares',
 ↪  args=(G_rate, PLQY_Data, resid), nan_policy='omit')


```

SIMPLIFIED CONTINUITY EQUATION FOR TRPL

This code uses the simplified differential equation and solves it numerically. Then the solution is fitted to the observed data. The input file is the output of picoquant's EasyTau software and contains all the measurement settings and the measured PL counts as a function of time.

```
import os
import numpy as np
import pandas as pd
from lmfit import Parameters, minimize
from scipy.integrate import odeint


###################
# Laser Settings #
###################

Ref_Files = os.listdir(str(folder + '\TRPL_Files'))

##############
# Functions #
##############

def unpack_Info(args):
    names, info = np.loadtxt(args, unpack=True, skiprows=1, max_rows=24,
    ↪  delimiter=' : ', dtype=str)
    sample_name = str(info[np.where(names == '  Sample')])[2:-2]

    wavelength = float(str(info[np.where(names == '  Exc_Wavelength')])[2:-4])
    ↪  # in nm

    sync_frequency = float(str(info[np.where(names == '
    ↪  Sync_Frequency')])[2:-4])  # in Hz
    signal_rate = float(str(info[np.where(names == '  Signal_Rate')])[2:-5])
    ↪  # in cps
    pile_up = signal_rate / sync_frequency * 100  # in %

    attenuation = str(info[np.where(names == '  Exc_Attenuation')])[2:-6]
    if attenuation == 'open':
```

```
        attenuation = 1
    else:
        attenuation = float(attenuation[0:-1]) / 100

    return pile_up, attenuation, wavelength, sync_frequency, sample_name


def Fluence_Calc(wavelength, args):
    # Unpack Ref Data File
    wl400, wl505, wl630 = np.loadtxt(str(folder + '\TRPL_Files\\' +
    ↪  args.laser_reference_file), unpack=True, skiprows=1)

    intensity = args.laser_intensity

    if wavelength == 397.7:

        laser_fluence = wl400[0] * intensity + wl400[1]

    elif wavelength == 505.5:

        laser_fluence = wl505[0] * intensity + wl505[1]

    elif wavelength == 633.8:

        laser_fluence = wl630[0] * intensity + wl630[1]

    return laser_fluence


def unpack_Data(FileName):

    # First the data is imported, the background removed, the maximum
    ↪  shifted to t=0 and everything is normalized

    time1, Data1 = np.loadtxt(FileName, unpack=True, skiprows=76)
    Data1 = np.array(Data1)
    len_Data = len(Data1)

    # Cut Data into Shape
    Data2, max_locator, time2 = cut_data(Data1, time1)
```

```
68
69      # Remove Background from before Pulse
70
71      Data3 = remove_bckg(Data2, max_locator)
72
73      # Normalize Data
74      data_max = Data3[max_locator]
75      Data5 = Data3 / np.max(Data3)
76      Data5[Data5 < 0] = np.nan
77
78      return time2, Data5, max_locator, len_Data, data_max
79
80
81  def cut_data(Data, time):
82      max_locator = np.argmax(Data)
83      dtime = time[2] - time[1]
84      pre_zero_time = np.linspace(max_locator, 1, max_locator)
85      pre_zero_time = pre_zero_time * dtime * -1
86      time = np.append(pre_zero_time, time)
87
88      Data = np.append(Data, pre_zero_time * 0)
89
90      return Data, max_locator, time
91
92
93  def remove_bckg(Data, max_locator):
94      # To remove the background the median of the 30% of the highest values
        ↪  before the pulse are substracted
95      Data_mask = np.array(Data[1:max_locator - 3])
96      Bckg = np.nanmedian(Data_mask)
97      Data = Data - Bckg
98
99      return Data
100
101
102 def make_Dataframe(time, data_raw, len_Data, max_locator):
103     Data = pd.DataFrame()
104
105
106     ## The data is cut to the correct lengths and stored in a pd.Dataframe
```

```
    Data['Time'] = time[0]
    Data['0'] = data_raw[0]

    i = 1
    while i < len(len_Data):

        Data2 = data_raw[i]

        if max_locator[i] != max_locator[0]:
            if max_locator[i] > max_locator[0]:
                a = max_locator[i] - max_locator[0]
                Data2 = Data2[a:]

            elif max_locator[i] < max_locator[0]:
                Data2 = np.append(np.zeros(max_locator[0] - max_locator[i]),
                 ↪  Data2)

        if len(Data2) != len(np.array(Data['Time'])):
            if len(Data2) > len(np.array(Data['Time'])):
                a = np.abs(len(Data2)-len(np.array(Data['Time'])))
                Data2 = Data2[0:-a]
            else:
                a = np.abs(len(Data2) - len(np.array(Data['Time'])))
                Data2 = np.append(Data2, np.zeros(a))

        Data[str(i)] = Data2

        i += 1

    max_locator = max_locator[0]

    return Data, max_locator


def one_over_e_Lifetime(Data):
    marker = np.where(Data[str(i)] < 1 / np.e)
    marker = np.array(Data['Time'])[marker]
    marker = marker[np.where(marker > 0)]
    marker = marker[0:5]
    marker1 = np.median(marker)
```

```
    marker_err1 = 0#abs(np.quantile(marker, 0.25) - marker1)
    marker_err2 = 0#abs(np.quantile(marker, 0.75) - marker1)

    return marker1, marker_err1, marker_err2


def time_range(Fit_range, Data):
    time = np.array(Data['Time'])
    limit = np.where((time > -10) & (time < Fit_range[1]))

    time_fit = time[limit]

    limit_i = Fit_range[0]
    limit_inner = np.where((time_fit >= limit_i))[0][0]

    nan_beg = np.empty(np.min(limit))
    nan_beg[:] = np.nan
    nan_end = np.empty(len(time) - np.amax(limit))
    nan_end[:] = np.nan


    return time_fit, nan_beg, nan_end, limit, limit_inner


def df_sigma(n0, time, params, i):
    def gaussian(t, mu, sig):
        return 1 / (sig * np.sqrt(2 * np.pi)) * np.exp(-(1 / 2) * ((t - mu) /
        ↪  sig) ** 2)

    k1 = params[f'k1_{i + 1}'].value
    k2 = params[f'k2_{i + 1}'].value
    k3 = params[f'k3_{i + 1}'].value

    sig = pulse_fwhm / (2 * np.sqrt(2 * np.log(2)))

    mu = 0
    ne = n0

    gauss_dat = gaussian(time, mu, sig)

```

```
    dnedt = Exc_Density[i] * gauss_dat - k1 * ne - k2 * ne ** 2 - k3 * ne ** 3
    return dnedt


def residual2(params_ode, time_fit, Counts, limit, limit2a, i):
    I0 = 0

    Data_fit = np.array(Counts[str(i)])[limit]
    A_ct = params_ode[f'A_ct_{i + 1}'].value
    tau_ct = params_ode[f'tau_ct_{i + 1}'].value

    dnedt = odeint(df_sigma, I0, time_fit*1e-9, args=(params_ode, i,))
    dndt = dnedt.reshape(-1)


    CT = np.where(time_fit > 0, (np.exp(-time_fit / tau_ct)), 0)
    dndt = ((dndt / Exc_Density[i]))**x_Parameter * (1 - A_ct) + (A_ct * CT)

    dndt = dndt/np.nanmax(dndt)
    resid = (Data_fit - dndt)

    return resid[limit2a+1:]


def resid_global(params_ode, time_fit, photo_cond, limit, limit2a, resid, i):
    while i < num_rows:
        resid[i, :] = np.abs(residual2(params_ode, time_fit, photo_cond,
        ↪  limit, limit2a, i)) * (time_fit[limit2a:-1]*1e9)
        i += 1

    return resid.flatten()


def post_Fitting(results_Model2, Data, limit, limit_inner, time_fit,
↪  empty_dat, i, nan_beg, nan_end):
    yfit = -residual2(results_Model2.params, time_fit, empty_dat, limit, 0, i)

    yfit = np.append(yfit, nan_end)
    yfit = np.append(nan_beg, yfit)

```

```
    return yfit



######################
# Main Part of Code #
######################

# This part of the code gets the filename(s) and makes a list out of it for later use

args = get_args()

FileName = args.data_path
global num_rows
num_rows = len(FileName)

global Exc_Density
Exc_Density = []

global x_Parameter
x_Parameter = args.x_Parameter

global pulse_fwhm  # ~ 372 ps
pulse_fwhm = 2e-9


pile_up = []
sample_name = []

time = []
data = []
max_locator = []
data_max = []
len_Data = []
laser_fluence_old = []

### Here, the additional information included in the Data header is imported and used to calculate the first important numbers
```

```
262
263 for i in range(num_rows):
264     pile_up_1, attenuation, wavelength, frequency, sample_name_1 =
        ↪ unpack_Info(FileName[i])
265     pile_up.append(pile_up_1)
266     sample_name.append(sample_name_1)
267
268     ## Steps to calculate Laser Fluence and Excitation Density
269     laser_fluence = Fluence_Calc(wavelength, args)  # in cm-2
270     laser_fluence = laser_fluence * attenuation * 10 ** (- args.OD_extra)  #
        ↪ in cm-2
271     laser_fluence_old.append(laser_fluence * (299792458 * 6.6261e-34) /
        ↪ (wavelength * 1e-9) * 1e9)  # in nJ cm-2
272     Exc_Density.append(laser_fluence * args.sample_absorbtance /
        ↪ (args.Thickness * 1e-7))  # in cm-3
273
274
275
276     ### Here, the data is combined into a dataframe
277     time1, Data3, max_locator1, len_Data1, data_max1 =
        ↪ unpack_Data(FileName[i])
278     data.append(Data3)
279     time.append(time1)
280     data_max.append(data_max1)
281     max_locator.append(max_locator1)
282     len_Data.append(len_Data1)
283
284
285 ### Length of Data is changed so it fits into a single Dataframe
286 i = 1
287 while i < num_rows:
288     len_Data[i] = len_Data[i] + len_Data[i - 1]
289     i += 1
290
291 ### The Dataframe is created
292 Data, max_locator = make_Dataframe(time, data, len_Data, max_locator)
293
294 ########################
295 # Fitting starts here #
296 ########################
```

```
297
298 ### Define most important Fitting Parameters
299 Fit_range = np.array([args.fit_start, args.fit_end])
300
301 time_fit, nan_beg, nan_end, limit, limit_inner = time_range(Fit_range, Data)
302
303 resid = np.empty(shape = (num_rows, len(time_fit)-limit_inner-1))
304 empty_dat = Data * 0
305 empty_dat[empty_dat == np.nan] = 0
306
307 params_ode = Parameters()
308 for i in range(num_rows):
309     params_ode.add(f'k1_{i + 1}', value=args.k1, min=1e5, max=1e10,
    ↪  vary=True)
310     params_ode.add(f'k2_{i + 1}', value=args.k2, min=1e-13, max=1e-3,
    ↪  vary=True)
311     params_ode.add(f'k3_{i + 1}', value=1e-28, max=1e-24, vary=True)
312     params_ode.add(f'A_ct_{i + 1}', value=0, min=0, max=1.000, vary=False)
313     params_ode.add(f'tau_ct_{i + 1}', value=0, min=1, max=50, vary=False)
314
315
316 if args.k1_shared == True:
317     for y in range(num_rows - 1):
318         params_ode[f'k1_{y + 2}'].expr = 'k1_1'
319
320 if args.k2_shared == True:
321     for y in range(num_rows - 1):
322         params_ode[f'k2_{y + 2}'].expr = 'k2_1'
323
324
325 if args.k1_fixed == True:
326     params_ode[f'k1_1'].vary = False
327     if args.k1 == 0:
328         params_ode[f'k1_1'].min = 0
329         params_ode[f'k1_1'].value = 0
330
331 if args.k2_fixed == True:
332     params_ode[f'k2_1'].vary = False
333     if args.k2 == 0:
334         params_ode[f'k2_1'].min = 0
```

```
        params_ode[f'k2_1'].value = 0

if args.additional_early_decay == True:
    for i in range(num_rows):
        params_ode[f'A_ct_{i+1}'].vary = True
        params_ode[f'A_ct_{i+1}'].value = 0.2
        params_ode[f'tau_ct_{i+1}'].vary = True
        params_ode[f'tau_ct_{i+1}'].value = 50


### Fitting the Data
results_Model2 = minimize(resid_global, params_ode, method='leastsq',
                          args=(time_fit, Data, limit, limit_inner, resid, 0),
                          ↪  nan_policy='omit')



k1_val = []
k2_val = []
k3_val = []
A_ct = []
tau_ct = []
R2_val = []

### Extract important Parameters from Fit
for i in range(num_rows):
    yfit = post_Fitting(results_Model2, Data[str(i)], limit, limit_inner,
    ↪  time_fit, empty_dat, i, nan_beg, nan_end)
    R2_val.append(R2_val_calc)
    Data[str('Fit_' + str(i))] = yfit1
    tau_ct.append(results_Model2.params[f'tau_ct_{i + 1}'].value)
    A_ct.append(results_Model2.params[f'A_ct_{i + 1}'].value)
    k1_val.append(results_Model2.params[f'k1_{i+1}'].value)
    k2_val.append(results_Model2.params[f'k2_{i + 1}'].value)
    k3_val.append(results_Model2.params[f'k3_{i + 1}'].value)

```

The input data is the same as for the simplified continuity code. The preparation of the raw data is the same, except that the line `Data = Data - Bckg` is skipped, because the measurement background is now the parameter ϵ_{PL}. To use `pymc`, the entire model had to be written in PyTensor notation, which has limited functionality when compared to the `numpy` library. For instance, it cannot be easily integrated with `scipy.optimize.root` or `scipy.integrate.odeint`. As such, these things had to be integrated manually.

```
1
2  import numpy as np
3  import pandas as pd
4  import pymc as pm
5  from scipy.optimize import shgo
6  import pytensor.tensor as at
7  from pytensor import *
8  from pytensor.graph.op import Op
9  from pytensor.graph.basic import Apply
10
11 ##############
12 # Functions #
13 ##############
14
15 def root_finder_loop_perform(D, a, b, thickness, noroots):
16     # Define an Aesara expression for the function to be rooted
17     def f(x, D, a, b, thickness):
18         #return (np.tan(x*thickness)+(D*(a)*x)/(b-D**2*x**2))**2
19         return (np.tan(x*thickness)+(D*(a)*x)/((a/2)**2*b-D**2*x**2))**2
20
21     x_sol1 = shgo(f,bounds=[(0,(noroots-0.5)*np.pi/(thickness))], args = (D,
       ↪  a, b, thickness), sampling_method='sobol', n=noroots*200).xl
22     x_sol = np.sort(x_sol1.flatten())
23
24
25
26     if x_sol[0] == 0:
27         return x_sol[1:noroots+1]
28     else:
29         return x_sol[0:noroots]
30
```

```
31
32  class RootFinder(Op):
33
34      def __init__(self, thickness, noroots):
35
36          self.thickness = thickness*1e-7
37          self.noroots = noroots
38
39      def make_node(self, D, a, b):
40
41          outputs = [at.vector(dtype='float64')]
42          return Apply(self, [D, a, b], outputs)
43
44      def perform(self, node, inputs, outputs_storage):
45          D, a, b = inputs
46
47          outputs_storage[0][0] = root_finder_loop_perform(D, a, b,
            ↪  self.thickness, self.noroots)
48
49
50  def beta_rootfinder(thickness, a, b, Diffusion_value, no_of_roots):
51
52      rootfinder = RootFinder(thickness=thickness, noroots = no_of_roots)
53
54      beta = rootfinder(Diffusion_value, a, b)
55
56      return beta
57
58
59  """This is the Diffusion model in PyTensor
60
61  It is mainly based on:  J. Appl. Phys. 116, 123711 (2014).
62  The important equations are marked.
63  In addition I took inspiration from:
64  https://www.nature.com/articles/s41598-019-41716-x#Sec16
65  https://static-content.springer.com/esm/art%3A10.1038%2Fs41467-017-02670-2/MediaObject
66  and
67  https://www.sciencedirect.com/science/article/pii/S2542435122004202#sec6.2
68
69  """
```

```
70
71  def diffusion_carrier_density_all(time, Fluence, Surface, thickness,
    ↪  Absorption_coeff, PL_err_init):
72
73      ### I - Diffusion Part
74      # I model the diffusion by using an approach described by R.K.
        ↪  Ahrenkiehl (Solid-State Electronics Vol. 35, No. 3, pp. 239-250,
        ↪  1992)
75      # as well as M Maiberg & R. Scheer (Journal of Applied Physics 116,
        ↪  123711 (2014)).
76      # To improve reproducability with the NUTS algorithm, I define the
        ↪  surface recombination in terms of their sum (S_sum) and the factor
        ↪  S_b, which
77      # relates the product as: S_prod = (S_sum/2)^2*S_b.
78      ## Define the spacial domains
79      # I use a tanh-spaced grid here, as it has more points close to the
        ↪  boundaries (surfaces) and allows the use of less datapoints overall
80
81      x = np.arange(0,thickness,5)
82
83      z_array_np = x*1e-7
84
85      z_array = at.as_tensor_variable(z_array_np)
86      z_array_4d = z_array.dimshuffle('x','x',0, 'x')
87      z_array_4d.broadcastable
88      (True, True, False, True)
89
90      z_array_diff = at.as_tensor_variable(np.diff(z_array_np))
91      z_array_diff_4d = z_array_diff.dimshuffle('x', 'x', 0, 'x')
92      z_array_diff_4d.broadcastable
93      (True, True, False, True)
94
95      z_array_diff_2d = z_array_diff.dimshuffle('x', 0)
96      z_array_diff_2d.broadcastable
97      (True, False)
98
99
100
101
102     ## Define Parameters
```

```
    # Surface recombination velocities are defined as the sum (S_sum), the
    ↪  ratio of sum and product (S_sumprod_ratio) and
    #
    S_sum_factor = pm.LogNormal('S_sum_model', 0, 2)
    S_sum_model = 1*(1+S_sum_factor)

    S_sumprod_ratio_factor = pm.Beta('S_sumprod_ratio_model', 2,2)
    S_sumprod_ratio_model = 10**(-3*S_sumprod_ratio_factor+0.01)


    S_mix = pm.Bernoulli('S_mix',0.5)


    ## Calculate both surface recombination velocities from S_sum and S_b
    S_a = (S_sum_model - at.sqrt(S_sum_model**2 *(1 -
    ↪  S_sumprod_ratio_model)))/2
    S_b = (S_sum_model + at.sqrt(S_sum_model**2 *(1 -
    ↪  S_sumprod_ratio_model)))/2

    # Effective S_front
    S_front_value = at.switch(at.eq(Surface, 1),  S_a*(1-S_mix) + S_b*S_mix,
    ↪  S_a*S_mix + S_b*(1-S_mix))

    S_front = S_front_value.dimshuffle(0,'x','x','x')
    S_front.broadcastable
    (False, True, True, True)

    # Reabsorption
    alpha_N_RV_fact = pm.LogNormal('alpha_N_RV', 4, 2, shape=2)
    alpha_N_RV_val_front =
    ↪  at.switch(at.eq(Surface,1),alpha_N_RV_fact[0],alpha_N_RV_fact[1])

    Reabs_front = at.exp(-at.outer(alpha_N_RV_val_front,z_array))

    # Diffusion Coeffient in cm2 s-1
    Diffusion_factor = pm.LogNormal('Diffusion_coefficient', 2, 2)
    Diffusion_coefficient = 1e-4*(1+Diffusion_factor)

    ## Calculate 'beta'-values of the Eigenvalue function
    a = S_sum_model
```

```
    b = S_sumprod_ratio_model

    beta_model = beta_rootfinder(thickness, a, b, Diffusion_coefficient, 5)
    beta_4d = beta_model.dimshuffle('x', 0 ,'x','x')
    beta_4d.broadcastable
    (True, False, True, True)



    ## Here the U_z function is calculates, which will impact the actual
     ↪  diffusion of the charge carriers in the model
    U_z = at.cos(beta_4d*z_array_4d) +
     ↪  S_front/(Diffusion_coefficient*beta_4d)*at.sin(beta_4d*z_array_4d)
    U_z.broadcastable
    (False, False, False, True)


    ## This part calculates the A_param, which will take care of the ratios
     ↪  of U_z functions, so the total sum ends up in cm-3
    Abs_coeff_4d = (Absorption_coeff).dimshuffle(0,'x','x','x')
    Abs_coeff_4d.broadcastable
    (False, True, True, True)

    Fluence_error = 0.9+pm.Beta('Fluence_error', 2,2,shape=len(Surface))/5

    Fluence_3d =
     ↪  (Fluence_error*Fluence*Absorption_coeff*(1-Reflectance)).dimshuffle(0,'x','x')
    Fluence_3d.broadcastable
    (False,  True, True)

    A_param = Fluence_3d *
     ↪  at.sum((((at.exp(-Abs_coeff_4d*z_array_4d)*U_z)[:,:,1:,:]+(at.exp(-Abs_coeff_4d*
    A_param_4d = A_param.dimshuffle(0, 1, 2, 'x')
    A_param_4d.broadcastable
    (False, False, True, True)



    ## Now the time-domain is introduced with the same resolution as the
     ↪  data
    time_4d = time.dimshuffle('x', 'x', 'x', 0)
```

```
    time_4d.broadcastable
    (True, True, True, False)

    ## n_tz0 is the 'initial' carrier density distribution from diffusion
    ↪  and surface recombination alone
    n_tz0 = (A_param_4d * U_z *
    ↪  at.exp(-(Diffusion_coefficient*at.power(beta_4d,2))*time_4d)
    ↪  ).sum(axis=1) # sum over all beta values


    ##########################################################################
    ##########################################################################

    ### II - Recombination Part
    ## Define Parameters
    # Radiative Recombination Rate
    k_rad_fact = pm.LogNormal('k_rad_model',1, 3)
    k_rad_model = 1e-8*1/(1+k_rad_fact)

    n_eq_model = pm.LogNormal('n_eq_model', 25,2)

    kc_n_factor = pm.LogNormal("kc_n_rates", 11, 2)
    kc_n = kc_n_factor



    trap_depth = pm.Beta('trap_depth', 2, 2)  # in eV
    Nc_power = 18
    n_em_1 = at.power(10, Nc_power)*
    ↪  at.exp(-trap_depth*1.60218e-19/(1.380649e-23 * 292))


    ## turn diffusion/surface recombination into a correctoin factor
    dt = at.extra_ops.diff(time).T#at.abs(time[1]-time[0])
    n_tz0_1 = n_tz0[:,:,:-1]
    n_tz0_2 = n_tz0[:,:,1:]

    print(dt.eval())
```

```
208
209     ### Looping over time-domain
210     def total_recombination_rate(n_tz0_1, n_tz0_2, dt_cuttent, n_dens, p_dens,
        ↪  PL_z, kc_n, ne_1, krad, n_eq, z_diff, PL_0, PL_err, reabs_front,
        ↪  reabs_recomb):
211
212         ### First: Define Rate equations
213         def rate_equations(n_dens, p_dens, kc_n, ne_1, krad, n_eq, m_phr):
214             ### Pseudo-Equilibrium at each time-point
215             f_trap = (n_dens)/(n_dens + ne_1 + p_dens)
216
217             dn_dt = - krad*reabs_front*(n_dens*p_dens + n_dens*n_eq) -
                ↪  kc_n*((n_dens)*(1-f_trap) - f_trap*ne_1)
218             dp_dt = - krad*reabs_front*(p_dens*n_dens + p_dens*n_eq) -
                ↪  kc_n*(p_dens)*f_trap
219
220             return dn_dt, dp_dt
221
222         # Runge-Kutta Algorithm
223         n_ds = n_tz0_2/n_tz0_1
224
225         n_dens = n_dens*n_ds
226         p_dens = p_dens*n_ds
227
228         RuKu1_n, RuKu1_p = rate_equations(n_dens, p_dens, kc_n, ne_1, krad,
            ↪  n_eq, reabs_recomb)
229         RuKu2_n, RuKu2_p = rate_equations(n_dens + RuKu1_n*dt_cuttent/2,
            ↪  p_dens + RuKu1_p*dt_cuttent/2, kc_n, ne_1, krad, n_eq,
            ↪  reabs_recomb)
230         RuKu3_n, RuKu3_p = rate_equations(n_dens + RuKu2_n*dt_cuttent/2,
            ↪  p_dens + RuKu2_p*dt_cuttent/2, kc_n, ne_1, krad, n_eq,
            ↪  reabs_recomb)
231         RuKu4_n, RuKu4_p = rate_equations(n_dens + RuKu3_n*dt_cuttent, p_dens
            ↪  + RuKu3_p*dt_cuttent, kc_n, ne_1, krad, n_eq, reabs_recomb)
232
233
234
235         n_next = (n_dens + dt_cuttent/6*(RuKu1_n + 2*RuKu2_n + 2*RuKu3_n +
            ↪  RuKu4_n))
236         p_next = (p_dens + dt_cuttent/6*(RuKu1_p + 2*RuKu2_p + 2*RuKu3_p +
            ↪  RuKu4_p))
```

```
237
238
239         Rad_next = reabs_front*(n_next*p_next + n_next*n_eq + p_next*n_eq)
240         PL_next = (at.sum(((Rad_next[1:,:] +
            ↪  Rad_next[:-1,:])/2*z_diff),axis=0)/PL_0)+PL_err
241
242         return n_next, p_next, PL_next
243
244
245     n_0z = p_0z = n_tz0[:,:,0]
246
247     PL_err = pm.HalfNormal('PL_err', 1e-3, shape=len(Surface))
248     PL_err_2d = PL_err.dimshuffle('x',0)
249     PL_err_2d.broadcastable
250     (True, False)
251
252
253     PL_0_calc1 =
        ↪  Reabs_front*((n_0z+n_eq_model)*(p_0z+n_eq_model)-n_eq_model**2)
254     PL_0_calc2 = at.sum(((PL_0_calc1[:,1:] +
        ↪  PL_0_calc1[:,:-1])/2*z_array_diff_2d),axis=1)
255     PL_0_calc2_2d = PL_0_calc2.dimshuffle('x',0)
256     PL_0_calc2_2d.broadcastable
257     (True, False)
258
259     PL_0z = PL_0_calc2#*(1 - PL_err)
260
261     result, updates = pytensor.scan(fn=total_recombination_rate,
262                                             sequences=[n_tz0_1.T, n_tz0_2.T,
                                                ↪  dt],
263                                             outputs_info=[n_0z.T, p_0z.T,
                                                ↪  PL_0z],
264                                             non_sequences=[kc_n, n_em_1,
                                                ↪  k_rad_model, n_eq_model,
                                                ↪  z_array_diff_2d.T, PL_0_calc2,
                                                ↪  PL_err, Reabs_front.T, 1])
265
266     #n_0z = n_0z.dimshuffle('x',1, 0)
267     #p_0z = p_0z.dimshuffle('x',1, 0)
268     PL_0z = (PL_0z/PL_0_calc2).dimshuffle('x', 0)
```

```
    #n_tz1 = at.concatenate([n_0z, result[0]], axis=0).T
    #p_tz1 = at.concatenate([p_0z, result[1]], axis=0).T
    PL_final = at.concatenate([PL_0z, result[2]], axis=0)
    #n_tz3 = (n_tz1*p_tz1)# + n_tz1*n_eq_model + p_tz1*n_eq_model)

    return PL_final




def glm_mcmc_inference_diffusion_full(Data_fit, a, a2, Fluence, Surface,
↪   Thickness, Absorption_coeff):



    #### Setting up the Data and Timeframe
    time = np.array(Data_fit['Time'])[a+2]*1e-9    #s

    y_combined = np.zeros((len(time),len(Surface)))
    PL_err_init = np.zeros(len(Surface))

    for s in range(len(Surface)):
        y_combined[:,s] = np.array(Data_fit[str(s)])[a+2]


    with pm.Model() as model:



        #### Simulation of Time-Resolved PL
        N_calc = diffusion_carrier_density_all(shared(time), Fluence, Surface,
        ↪   Thickness, shared(Absorption_coeff), PL_err_init)

        ## Likelihood Function Student-T Distribution)
        sigma_width_val = pm.LogNormal('sigma_width', 1, 2,
        ↪   shape=len(Surface))
        sigma_width = 0.05*1/(1+sigma_width_val)

```

```
306         sigma_width = at.outer(at.ones(shape=len(time)), sigma_width)
307 
308         y_combined = at.as_tensor_variable(y_combined)
309         y_combined = at.switch(at.le(y_combined,0), np.nan, y_combined)
310 
311         N_calc_collect = pm.Deterministic('N_calc_collect', N_calc)
312 
313 
314         Logp = pm.Deterministic('Logp',
            ↪  pm.logp(rv=pm.Normal.dist(mu=at.log(N_calc), sigma=sigma_width),
            ↪  value=at.log(y_combined)))
315 
316         Y_obs = pm.Potential('Y_obs', y_combined*Logp)
317 
318 
319 
320         #### Draw Samples from the Posterior Distribution
321         trace = pm.sample(step=pm.Metropolis(),  chains=10, draws=10000,
            ↪  cores=10, tune=0)
322 
323     return trace
324 
325 
326 
327 
328 ##############
329 # Main Part #
330 ##############
331 
332 if __name__ == '__main__':
333 
334     tmax = 20000
335     tmin = 0
336     amax = np.where(np.array(df['Time']) <= tmax )[0][-1]
337 
338     ## Choose time-point spacing
339     #a = lin_time(amax)
340     a = log_time(amax, 21)
341 
```

```
    trace = glm_mcmc_inference_diffusion_full(df, a, amax, Fluence, Surface,
    ↪  Thickness, Absorption_coeff)
```